Schweizerische Eidgenossenschaft
Confédération suisse
Confederazione Svizzera
Confederaziun svizra

Federal Department of the Environment,
Transport, Energy and Communications DETEC

Swiss Federal Office of Energy
Energy Research and Cleantech

Final report from 30 April 2026

Dig-A-Plan

Tool for Distribution Grid Asset Planning under Uncertainties of Load Configuration and Flexibility Provision

---

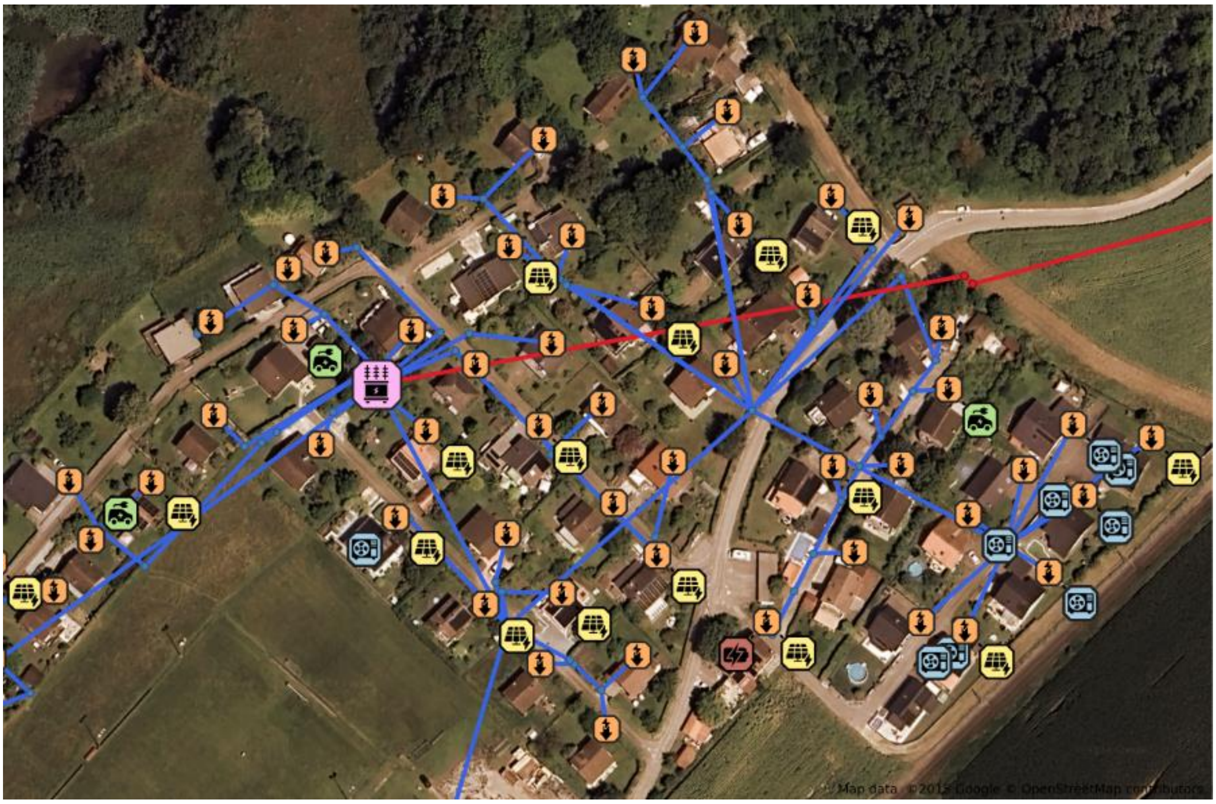

Source : © Groupe E / HEIG-VD, 2026

Publisher:
Swiss Federal Office of Energy SFOE
Energy Research and Cleantech
CH-3003 Berne
www.energy-research.ch

Co-financing: In-kind contributions provided by
- Groupe e, 1763 Granges-Paccot
- Services Industriels Lausanne (SiL), 1003 Lausanne
- Yverdon Energies, 1400 Yverdon

Subsidy recipients:
Haute École d'Ingénierie et de Gestion du Canton de Vaud (HEIG-VD), Institute of Energies (IE)
1400 Yverdon-les-Bains
https://heig-vd.ch/recherche/instituts/ie/ c

Université de Genève (UNIGE), Institute for Environnemental Sciences (ISE)
1205 Genève
https://www.unige.ch/energy/

EPFL, photovoltaic research laboratory (PV-LAB)
2002 Neuchâtel
https://www.epfl.ch/labs/pvlab/

Authors:
Mokhtar Bozorg, HEIG-VD, mokhtar.bozorg@heig-vd.ch
Mohammad Rayati, HEIG-VD, mohammad.rayiati@heig-vd.ch
Adeleh Mokhles-Gerami, HEIG-VD, adeleh.gerami@heig-vd.ch
Luca Tomasini, HEIG-VD, luca.tomasini@heig-vd.ch
Arbogast Nyandwi, UNIGE, arbogast.nyandwi@unige.ch
Martin Patel, UNIGE, martin.patel@unige.ch
Alejandro Pena-Bello, EPFL, alejandro.penabello@epfl.ch
Gerard Marias Gonzalez, EPFL, gerard.mariasgonzalez@epfl.ch
Nicolas Wyrsch, EPFL, nicolas.wyrsch@epfl.ch

SFOE project coordinators:
Dr Michael Moser, Michael.moser@bfe.ch

SFOE contract number: SI/502666-01

Summary

In this project, a comprehensive grid planning tool based on risk assessment has been developed, which helps the Distribution System Operators (DSOs) to deal with uncertainties of the energy transition. Since a massive rollout of photovoltaics (PV), electric vehicles (EV) and heat pumps (HP) is expected until 2050, a two-layer optimization framework has been implemented. With this architecture, the long-term capacity expansion planning has related to short-term operational flexibility, and in this way test the NOVA principle (giving priority to flexibility and optimization before expansion) in a rigorous manner.

High-resolution simulations are performed on real networks from Groupe E and Services Industriels de Lausanne, and from this several important insights were obtained. *First*, although electrification of heating and mobility changes the seasonal load patterns, it is the high PV penetration that is the main reason for thermal stress of transformers. Moreover, our analysis showed that time-of-use tariffs, if there is no capacity constraint, can create very volatile and synchronized demand peaks which are dangerous for the grid stability. At the end, the project demonstrated that the standard expectation-based risk models are quite robust for grid planning; in fact, accurate forecasting of the local demand and resource profiles is more critical for reliable planning than using very complex mathematical risk formulations.

Zusammenfassung

Im Rahmen dieses Projekts wurde ein umfassendes, auf einer Risikobewertung basierendes Netzplanungsinstrument entwickelt, das den Verteilernetzbetreibern (VNB) eine Entscheidungshilfe beim Umgang mit den Unsicherheiten der Energiewende an die Hand gibt. Da bis 2050 ein massiver Ausbau von Photovoltaikanlagen (PV), Elektrofahrzeugen (EV) und Wärmepumpen (HP) erwartet wird, wurde ein zweistufiges Optimierungsmodell implementiert. Mit dieser Architektur wird die langfristige Planung des Netzausbaus mit der kurzfristigen betrieblichen Flexibilität verknüpft, wodurch das NOVA-Prinzip (Vorrang für Flexibilität und Optimierung vor Ausbau) einer gründlichen praktischen Anwendung unterzogen wird.

An realen Netzen der Groupe E und der Services Industriels de Lausanne wurden hochauflösende Simulationen durchgeführt, aus denen sich mehrere wichtige Erkenntnisse ergaben. Erstens: Während die Elektrifizierung von Heizung und Mobilität die saisonalen Lastmuster verändert, ist der hohe PV-Anteil der Hauptgrund für die thermische Belastung der Transformatoren. Zudem ergibt unsere Analyse, dass zeitabhängige Tarife – sofern keine Kapazitätsengpässe bestehen – zu sehr volatilen und synchronisierten Nachfragespitzen führen können, die die Netzstabilität gefährden. Letztendlich hat das Projekt gezeigt, dass die standardmässigen, auf Erwartungen basierenden Risikomodelle für die Netzplanung recht robust sind; tatsächlich ist eine genaue Prognose der lokalen Nachfrage- und Ressourcenprofile für eine zuverlässige Planung entscheidender als die Verwendung sehr komplexer mathematischer Risikomodelle.

Résumé

Dans le cadre de ce projet, un outil complet de planification du réseau basé sur l'évaluation des risques a été développé, afin d'aider les gestionnaires de réseaux de distribution (GRD) à faire face aux incertitudes liées à la transition énergétique. Étant donné que l'on prévoit un déploiement massif de l'énergie photovoltaïque (PV), des véhicules électriques (VE) et des pompes à chaleur (PC) d'ici 2050, un cadre

d’optimisation à deux niveaux a été mis en place. Grâce à cette architecture, la planification à long terme de l’extension des capacités est mise en relation avec la flexibilité opérationnelle à court terme, ce qui permet de tester de manière rigoureuse le principe NOVA (qui donne la priorité à la flexibilité et à l’optimisation avant l’extension).

Des simulations à haute résolution ont été réalisées sur les réseaux réels du Groupe E et des Services Industriels de Lausanne, ce qui a permis d’obtenir plusieurs enseignements importants. Premièrement, bien que l’électrification du chauffage et de la mobilité modifie les profils de charge saisonniers, c’est la forte pénétration du photovoltaïque qui est la principale cause de la contrainte thermique subie par les transformateurs. De plus, notre analyse a montré que les tarifs en fonction de l’heure de consommation, en l’absence de contrainte de capacité, peuvent générer des pics de demande très volatils et synchronisés, qui constituent un danger pour la stabilité du réseau. En conclusion, le projet a démontré que les modèles de risque standard basés sur les prévisions sont tout à fait fiables pour la planification du réseau ; en effet, une prévision précise des profils locaux de la demande et des ressources est plus déterminante pour une planification fiable que l’utilisation de formulations mathématiques très complexes du risque.

Main findings (Take-Home Messages)

1) A comprehensive bottom-up modelling framework was developed to generate high-resolution hourly electricity demand and generation profiles for residential and non-residential sectors up to 2050, assuming high or even full diffusion of heat pumps, electric vehicles, photovoltaics, and appliances across different building archetypes and urban settings.
2) The results show that large-scale electrification of heating and mobility will substantially reshape seasonal and peak load patterns. While distributed rooftop photovoltaic (PV) deployment can partially offset electricity demand, high PV penetration particularly in 2050 scenarios may introduce operational challenges for distribution grids. These findings highlight the need for integrated, flexibility-oriented, and uncertainty aware distribution grid planning.
3) By integrating a multi-stage optimization framework, the Dig-A-Plan project delivers a robust grid asset planning tool that equips DSOs to handle the massive uncertain rollout of EVs, heat pumps, and targeted 35GW of PV capacity by 2050. The tool applies the NOVA principle by prioritizing flexibility and optimization before expansion and proving that dynamic switching and flexibility dispatch can reduce CAPEX in dense urban grids.
4) While advanced risk measures add significant mathematical complexity to grid planning, our findings show that standard expectation-based models are highly robust. Therefore, accurately generating future demand and resource profiles is ultimately more critical to reliable planning than employing highly complex mathematical risk formulations.

Contents

List of figures

List of abbreviations

SFOE	Swiss Federal Office of Energy
NOVA	Netzoptimierung vor Verstärkung vor Ausbau
DSO	Distribution System Operator
EV	Electric Vehicle
EVCS	Electric Vehicle Charging Stations
PV	Photovoltaic
HP	Heat Pump
ERA	Energy Reference Area
SH	Space Heating
HH	Household
IND	Industrial sector
SFH	Single Family House
MFH	Multi-family House
NR	non-residential
OCO	Office and Commercial Sector
ADMM	Alternating Direction Method of Multipliers
SDDP	Stochastic Dual Dynamic Programming
MILP	Mixed Integer Linear Programming
SOC	Second Order Cone
MISOCP	Mixed Integer Second Order Cone Programming
MDRO	Multi-stage Distributionally Robust Optimization

1. Introduction

1.1. Context and motivation

Due to the pressing need to address climate change and decarbonization, the deployment of electric vehicles (EVs), photovoltaics (PVs), and heat pumps (HPs) is quickly growing worldwide. However, this is challenging for electrical distribution grids, as increased supply or demand in low- and medium-voltage grids can lead to voltage violations, branch overloads, and transformer aging.

The Swiss federal office of energy (SFOE) foresees the installation of 35 GW of PV capacity and 34TWh of PV generation by the year 2050 [1]. To reach this very ambitious target, it is essential to ensure the required flexibility in the distribution grids, considering the impacts of EVs and HPs on the grid as well as the role of prosumers to provide flexibility. In this project, we developed a planning tool for reinforcing distribution grid assets while handling *known* and *unknown* uncertainties associated with load configuration, including the deployment of EVs, HPs, and PVs, as well as the available flexibility provided by the prosumers in the grid.

The project is in line with the “2021–2024 Energy Research Master Plan” [2], which prioritizes “the development of risk-based tools for planning resilient networks and systems that take into account the uncertainties”. It also meets the demands of the Energy Strategy Act [3], which mandates systems planners to optimize the cost of grid expansion by prioritizing flexibility choices over expensive alternatives (i.e., the NOVA[1] principle). The project addresses the second question of Topic 1 of the SFOE grid call by integrating the uncertainties of PV, EV, and HP deployments and the availability of flexibility in the model of distribution grid asset planning to minimize cost and uncertainties.

In numerous ways, the project contributes to safe, sustainable, and cost-effective energy provision as well as to lower and more rational energy consumption. First, the project leads to more rational energy consumption through improved links between sources of flexibility and grid expansion. Second, the project assures the reliability of the energy supply by accounting for the aging of transformers. This prevents system failures and guarantees that energy is available when needed.

1.2. Project objectives

The electrification of heat and transportation, as well as the rollout of renewable energy, notably distributed PVs, are causing significant changes in distribution grids in terms of load configuration and flexibility. As a result, distribution system operators (DSOs) need new and reliable grid planning tools to manage these changes and to ensure the secure and economically efficient operation of distribution grids.

Dealing with *unknown* uncertainties is one of the biggest challenges that DSOs face when planning grid assets during the energy transition [4]. An *unknown* uncertainty refers to a variable for which the DSO does not know the probability of distribution of its outcomes. For example, the spatial and temporal growths of PVs, EVs, and HPs in the grid are classified as *unknown* uncertainties as they depend on *unknown* exogenous variables that are difficult to predict precisely, like consumer behaviors, nationwide policy decisions, technological advancement, and so on. On the other hand, a *known* uncertainty refers to a variable for which the probability distribution of its outcomes is precisely specified with a small or negligible error, e.g., the PV power profile or load profile of representative days.

[1] Netzoptimierung vor Verstärkung vor Ausbau: Grid Optimization before Reinforcement before Expansion.

There are two main objectives for this project:

- The first objective is to quantify the *known* and *unknown* uncertainties during the energy transition that have impacts on the asset planning of DSOs. These uncertainties include changes in load configuration, daily load profile, PV power profile, and flexibility provided by prosumers until 2050.
- The second objective is to develop an asset-planning tool for DSOs that considers the technological risks of the energy transition, e.g., the impacts of EVs, PVs, and HPs on the grid, like voltage violations and branch overloads. The tool incorporates spatial and temporal uncertainties of the flexibility provided by prosumers. The tool's decision variables include reinforcement of the capacity of grid assets like transformers and branches. In addition, its decision variables include operational flexibility measures, including switching operations and transformer tap settings. The tool's overall purpose is to ensure that the distribution grid is operated securely and economically under uncertainty.

To achieve the above objectives, several statistical analyses have been executed along with the development of a multi-stage distributionally robust optimization (MDRO) model [5]. An asset-planning tool has been developed based on the MDRO model to support the decision-making of the DSOs.

1.3. Scientific methodology

In the Dig-A-Plan project, we developed an MDRO-based planning tool for grid assets like transformers and branches. The tool is developed based on a multistage decision-making framework, with each stage consisting of two sequential steps.

- In the first step of each stage, the decisions concerning reinforcement of grid assets like transformers and branches for the upcoming years of the planning time window are made (e.g., the next five years). Following the implementation of the decisions in the first step of each stage, the *unknown* uncertainties are revealed, including: (I) the load configuration, i.e., the installed capacity of PVs, EVs, and HPs at grid nodes; as well as (II) the available flexibility provided by the prosumers. The decisions in the first step of each stage must be robust against the probability of distribution of *unknown* uncertainties, or, in other words, distributionally robust.
- In the second step of each stage, the prosumers deployed flexibility in each hour of the days of the upcoming years of the planning time window is determined to keep the nodal voltage, branches, and transformers' currents within safe limits. In this step, the installed capacity of PVs, EVs, and HPs, as well as the prosumers' available flexibility in the first step, are *known*. On the other hand, the demand profile and PV power outputs are uncertain, while a few representative days over the year may be identified to plan flexibility exclusively for those days. The representative days are identified using a clustering technique in a way to properly represent load and generation availability within daily, weekly, and seasonal variations. In this case, the deployed flexibility for other days thereafter is the same as for the representative days, only with a small difference. In this formulation, the annual load profiles and PV generation are treated as *known* uncertainties.

Figure 1 depicts a simplified schematic of the proposed MDRO-based planning tool, which is based on a multistage decision-making framework and distributionally robust optimization. To obtain optimal grid asset planning, several iterations of finding optimal planning are needed over forward and backward passes.

The objective of the planning tool is to lower the required capital and operating expenses for the grid both at each stage and for the full period of planning, e.g., until the end of the 2050 horizon. The capital expenses (CAPEX) may include expenditure for transformer and branch expansion. On the other hand, the operational cost (OPEX) includes the cost of purchasing flexibility from prosumers, the cost of electrical loss, and the DSOs' balancing profit.

To guarantee the safe operation of distribution grids, the optimization problem is constrained by:

- Technical limitations of the distribution grid, such as voltage and power flow limits;
- The technical restrictions of prosumers, such as their available capacity; and
- Reliability and resilience metrics such as system average interruption frequency index (SAIFI) and system average interruption duration index (SAIDI).

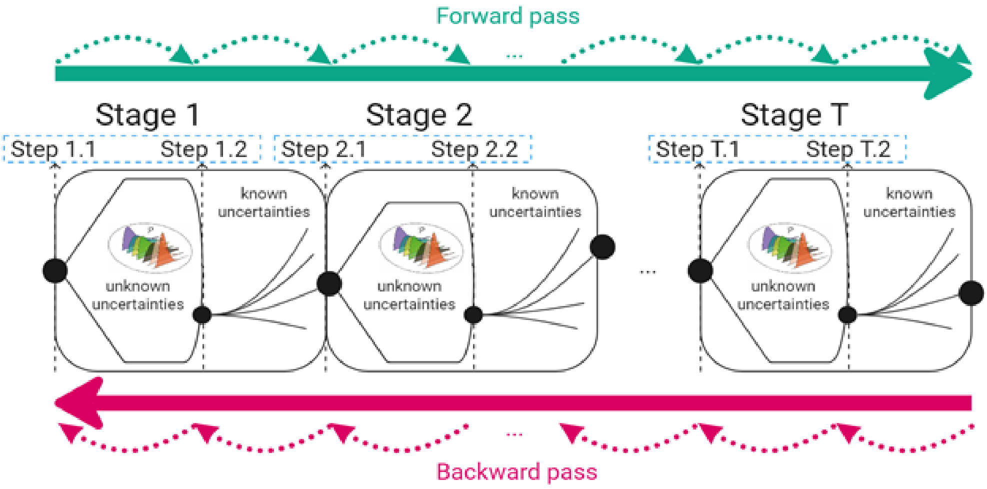

Figure 1: Multi-stage optimization framework.

To validate the planning tool based on MDRO, data collected from three DSOs is used. For the successful implementation of this project, we have further analyses in addition to the development of an optimization framework and its implementation in real-world case studies. Using system models and other types of analyses, e.g., statistical analyses, we generated the scenarios of energy transitions, and we analyzed their impacts on the day-to-day operation and management of DSOs. To this end, the project consists of the following steps with associated research methods:

- We estimated the future load configuration, i.e., the deployment of PVs, EVs, and HPs, at the national level. The distribution grid scope is added to the GRIMSEL-FLEX model as a nested unit.
- We extended the GRIMSEL-FLEX model by adding different designs of tariffs for prosumers. It requires an iterative approach to ensure comparable utility revenue across the tariffs. GRIMSEL-FLEX offers possibilities for tariff analysis that are complementary to approaches applied in earlier projects, particularly NETFLEX [6].
- We used a scenario-based approach to simulate the wholesale market across the 2050 horizon and determine plausible scenarios for the deployment of EVs, HPs, and PVs, as well as the flexibility provided by consumers.

Using the above analyses, we can solve the general formulation of asset planning optimization for the distribution grid based on MDRO. We validated the results of the selected mathematical formulation and in a numerical environment for the given case studies. We used existing open-source tools such as Pandapower and Pyomo to implement such mathematical formulation.

The solution to the optimization problem requires high-performance computing infrastructure or cloud computing resources. We used available research licenses for existing solvers such as HiGHS and GUROBI. We simulated the distribution grid for various pathways of deployment of PVs, EVs, and HPs to calculate the statistics of reliability and resilience metrics and costs. Finally, we revisited and improved the planning optimization tool based on the insights and advice of the industrial advisory board, including the experts of the DSOs in the domain of grid asset management and planning.

Our methodology for asset planning is based on MDRO since it is suitable for addressing problems with *known* and *unknown* uncertainties about the temporal and spatial evolution of load configuration and flexibility provision in distribution grids. In the MDRO-based planning framework, decisions are made in multiple instances, allowing us to account for all relevant implementation sequences. The decisions are robust against the probability density of *unknown* uncertainties. Furthermore, information related to *known* uncertainties has been exploited in the proposed framework. The curse of dimensionality in stochastic modelling is one of the main factors that might necessitate the use of decomposition and distributionally robust optimization for the proposed planning tool.

1.4. Project overview

To implement the above-mentioned scientific methodology, this project is organized in five work packages (WPs):

- WP1: Project management and steering.
- WP2: Data collection and characterization of case studies.
- WP3: Integrated modelling environment for the estimation of load configuration and flexibility.
- WP4: Mapping the results of the integrated modelling environment into the distribution grids.
- WP5: Development and validation of grid asset planning tools.

Figure 2 depicts a schematic representation of the relationships between WPs.

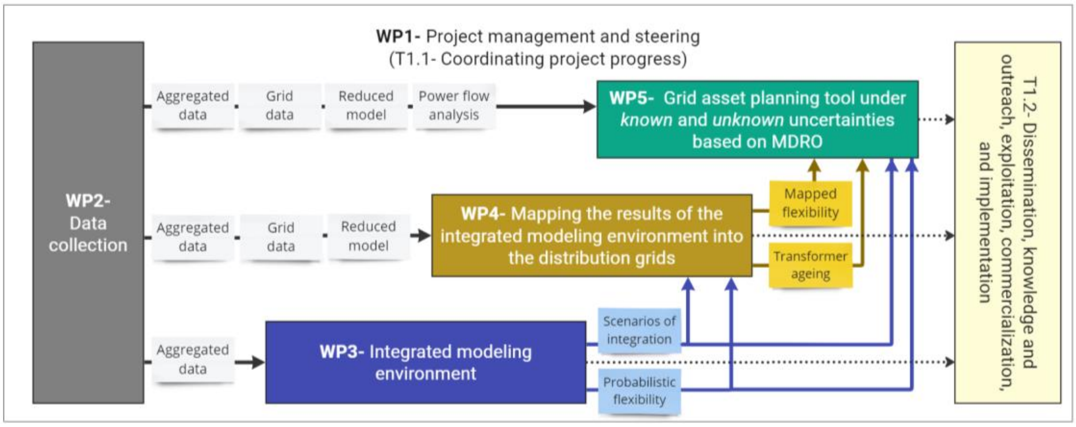

Figure 2: Schematic of the interaction between work packages.

WP2 is dedicated to the collection and pre-processing of the required data from the three DSO partners, namely Groupe E, Yverdon Energies, and SIL. WP3 uses aggregated data, whereas WPs 4 and 5 use aggregated data and topological models, as well as the reduced distribution grids. WP5 also uses power flow analysis to determine grid constraints. Regarding uncertainty modelling, WP3 generate scenarios of load configuration and the model of probabilistic flexibility provided by prosumers in the 2050 horizon using a techno-economic analysis based on the prediction of future load configuration and national deployment of PVs, EVs, and HPs. WP4 provides grid localization of load configuration and flexibility provision, as well as a transformer aging function. Technical developments in WP4 is based on generated scenarios and the probabilistic model of flexibility. WP5 can be considered as the project's theoretical core, developing the grid asset-planning tool with input from WPs 2, 3, and 4. WP5 deals with the overall design and execution of the model, utilizing existing planning tools. Overall, the WPs are interrelated and collaborate to achieve the project's goals.

1.5. Report structure

The following sections provide an overview of the project, including a summary of the methodology, key results, and main conclusions. More detailed descriptions of the work carried out under each work package are provided in the appendices. Appendix 1 presents the work related to deliverables 2.1 and 2.2, covering the data collection process and case studies. Appendix 2 describes the outcomes of deliverables 3.1 and 3.2, focusing on load growth scenarios and technology integration. Appendix 3 summarizes deliverables 4.1 and 4.2, presenting the expected asset distribution, flexibility potential, and projected transformer loss of life. Finally, Appendix 4 covers deliverables 5.1, 5.2, and 5.3, describing the distribution grid asset planning optimization, the validation of the proposed model, and the release of the planning tool.

2. Approach, method, results and discussion

2.1. Case studies

In this project, we used one benchmark (i.e., IEEE33 case) and two real distribution grids, i.e., the dense urban Boisy grid operated by SiL and the rural Estavayer-le-Lac grid operated by Groupe E. The Boisy grid contains two feeders (Feeder 1 and 2), while the Estavayer-le-Lac grid includes the Aumont, Autoroutes, Bel-Air, Centre-Ville, Tout-vent, Zone-Industrielle feeders. Detailed description of the case studies is provided in Deliverables 2.1 and 2.2.

2.2. Demand and resource scenarios

This section presents the methodology for estimating hourly electricity demand for HPs and EVs as well as for decentralized electricity generation profiles for PV systems in Estavayer-le-Lac and Boisy. The modelling framework covers the period from 2022 to 2050 in five-year steps and provides the basis for subsequent grid planning and optimization analysis. The approach integrates detailed building, mobility, and energy system data to generate consistent and spatially resolved load profiles for residential, service, and industrial sectors. The main results are graphically displayed in this section.

2.2.1. Procedure and method

This section explains the method applied for estimating hourly electricity consumption profiles pertaining to both current (2022) and prospective demand (2050) scenarios in 5-years steps. The hourly model represents the short-, medium- and long-term electricity consumption within the residential and non-residential sectors. It encompasses the demand associated with lighting and electric appliances, EVs, alongside the electricity requirements for space heating (SH) and the provision of domestic hot water (DHW) for households, including single (SFH) and multi-family houses (MFH), as well as services like offices and commercial sector (OCO), and industrial and agricultural (IND) sector operations. The methodology accounts for differences in building types, construction periods, and urban settings, as well as the share of buildings using HPs or electric resistance heating and their energy conversion efficiencies. Energy demand is determined by building archetype and aggregated to provide total electricity demand for a given area. The method is applied to two case studies and is validated using hourly feeder demand data from DSOs.

2.2.2. Modelling of space heating and domestic hot water

To model heat supply and demand, we used data based on national building and housing database of Switzerland, referred to as RegBL [7] , which categorizes and describes more than 2 million buildings. The classification of urban settings, i.e., urban, suburban, and rural, is based on [8]. The entire area Estavayer-le-Lac was found to be categorized as rural. Boisy is classified as urban area. RegBL datasets such as building type, building age, number of floors, and heating type are used to calculate the annual heat demand per building using the approach developed in the project “Future Energy Efficient Buildings & Districts (FEEBD)” [9]. Future decarbonized heating across residential building types is assumed to be ensured by HPs. Heat demand hourly profiles are estimated based on annual heat demand, the linearized heating curve and the heated floor area. Hourly heat demand is converted to electricity profiles by means of the coefficient of performance (COP), which is estimated based on Carnot efficiency and thermodynamic efficiency (see below for more details).

The energy reference area (ERA), representing the heated floor area used for energy calculations, is estimated using a regression function [10] based on building footprint, number of floors, and building type, i.e., SFH, MFH, OCO, IND, from the Swiss building registry or RegBL [7]. Annual heat demand per building (kWh/m²/year) is mapped according to archetype, construction period, and urban setting using the Future Energy Efficient Buildings & Districts (FEEBD) model [9]. Hourly thermal load curves for space heating (SH) are derived by multiplying normalized SH profiles from the FEEBD model (2022) [11] with the annual heat demand per square meter and the ERA. For domestic hot water (DHW), normalized DHW load curves from the FEEBD model (2022) [11] are multiplied by the annual DHW demand defined in the 2024 norm of the Swiss Society of Engineers and Architects (SIA) [12] and the corresponding ERA.

Hourly electricity demand for HPs is calculated by dividing the hourly thermal load curves by the hourly coefficient of performance (COP) for SH and DHW respectively. For electric resistance heating, a COP of one is assumed. The hourly COP of HPs is determined using Carnot efficiency and a thermodynamic efficiency of 44% [13], reflecting actual system performance. Heat supply temperatures are assumed to be 35°C for floor heating (post-1990 buildings), 55°C for radiators (pre-1990 buildings), and 60°C for hot water. According to the ZERO Basis scenario [14], average supply temperatures are expected to decrease to 30°C for new buildings and about 45°C for older buildings by 2050. Annual COP improvements are based on projections from the Energy Perspectives 2050+ (see Table A.2 in the appendix of deliverables 3.1 and 3.2). HPs for industrial processes have not been considered. For 2050, we assumed full electrification of all space heat and DHW heating systems, while retrofitting of the envelope of existing buildings and the construction of new highly efficient buildings are expected to result in a heating demand reduction rate of 1.35% per year between 2022 and 2050 (based on [14]).

2.2.3. Modelling of EVs

For EVs, today's electricity demand was estimated based on the stock of EVs per commune [15], travelled distance, and the electricity consumption per km (see appendix of deliverables 3.1 and 3.2, Table A.2). Syla et al. [16] developed load curves using data from the Swiss Micro census [17], [18], which allows to statistically tracking the mobility patterns of the Swiss population. This simulated data is based on surveys conducted every five years. This survey provides insights into the driving behavior for passenger cars, and it is used to model EV charging profiles. It is based on over 57'000 household interviews, where respondents were asked to describe each trip they made the previous day in detail, including the start and end points, trip purpose, and mode of transport [19], resulting in data on more than a quarter-million trips. In this study, both uncontrolled and controlled charging profiles were utilized, developed by Syla et al. as part of the open-source model GRIMSEL-EV [16], [20].

To calculate hourly energy demand [kWh] of EVs, we multiply the hourly charging profiles [kWh] on a typical day and per EV for uncontrolled with no flexibility and controlled charging by the driving frequency per day and number of EVs for 2022 and 2050 respectively.

The charging profiles for each EV are determined based on the energy required to fully charge it. This energy is calculated by multiplying the average distance travelled by each EV with a specific energy consumption rate of 0.2 kWh/km [16], which reflects the characteristics of EVs currently on the market. Charger efficiency is also considered, assuming a 90% efficiency rate [16] to convert nominal charging power into effective charging power for controlled and uncontrolled charging profiles representing a typical day.

The distribution of chargers, based on nominal charging power, is set at 68%, 30%, and 2% for 7kW, 11kW, and 22kW, respectively. The charging duration for each EV is then calculated by dividing the energy required for charging by the effective charging power. Finally, to generate the charging profiles, the energy demand for each EV is aggregated on an hourly basis throughout a week. This is done by multiplying the individual energy demands with the normalized load curves, as shown in Figure 9 of deliverables 3.1 and 3.2. The distribution of EV demand is determined by the number of cars per commune [15] and the number of households[2]. For 2050, we assumed full electrification of all passenger cars.

2.2.4. Modelling of appliances and processes

To model the appliance and processes profiles, we first developed their normalized profiles. Normalized electrical appliance load curves are derived by selecting representative feeders for each sector, including residential, service, and industrial, where PV generation is already included. For residential buildings, a feeder with 93% residential load is used, from which heating and EV demand are subtracted to isolate the appliance load; this is then divided by the number of households and normalized to obtain a

[2] The study area for the Estavayer-le-Lac region comprises the municipality of Estavayer together with fourteen neighboring communes. The Boisy study area comprises two communes.

standardized household profile. To model load curves for the service (OCO) and industrial (IND) sectors, feeders dominated by these sectors are selected, and EV demand, heating demand, and previously calculated household loads are removed to isolate sector-specific demand before normalization. Finally, the 2022 hourly energy demand (kWh) for appliances and processes in Estavayer-le-Lac and Boisy is calculated by multiplying annual energy consumption per building archetype from smart meters by the corresponding normalized load curve, after which PV production is added to convert feeder-level net curves into gross demand profiles.

The projections for electrical appliances and processes are based on the ZERO Basis scenario outlined in the Energy Perspective 2050+, as shown in Figure 9 of deliverables 3.1 and 3.2. By 2050, the annual energy demand is expected to decrease to 70.4GWh and 12.9GWh per annum in Estavayer-le-Lac and Boisy respectively, with an assumed yearly reduction rate of 0.67% (see Table A.1 in the appendix of deliverables 3.1 and 3.2). This decline is driven by a combination of technological advancements, regulatory changes, shifts in consumer behavior, and the integration of smart technologies, all aimed at enhancing energy efficiency and sustainability.

2.2.5. Deployment of PV

To estimate the future potential for PV deployment in Estavayer-le-Lac and Boisy, we use the open data developed by A. Walch [21], providing detailed information on the solar potential of each building rooftop in Switzerland. This information is based on the factors such as solar radiation exposure, rooftop area, orientation, inclination, and shading. A. Walch calculated these values based on data from SwissTopo [22]. Considering the current performance of PV systems (285W per 1.6m²), a percentage of 70% [23] is assumed as effectively available area resulting in a total estimated maximum PV electricity potential in Estavayer-le-Lac and Boisy of 212.3GWh (177MWp) and 21.6GWh (18MWp) per year, respectively.

2.2.6. Results and discussion

In this section, we present the results, detailing the hourly electrical demand for heating, EVs, and appliances and processes for both residential and non-residential customers in Estavayer-le-Lac and Boisy, as shown in Figure 3 (a) and (b), respectively. The electricity demand for heating in Figure 8 of deliverables 3.1 and 3.2 includes both the demand of HPs and of electric resistance heating. In 2022, the HP electricity demand for both space heating (SH) and domestic hot water (DHW) is dominated by single-family homes (SFH), followed by multi-family homes (MFH) and non-residential (NR) buildings.

In 2022, the shares of annual electricity demand in Estavayer-le-Lac were approximately 74% for appliances and processes, 24% for HP, and 3% for EVs, whereas in Boisy, the shares were approximately 90% for appliances and processes, 9% for HP, and 1% for EVs (see Figure 3).

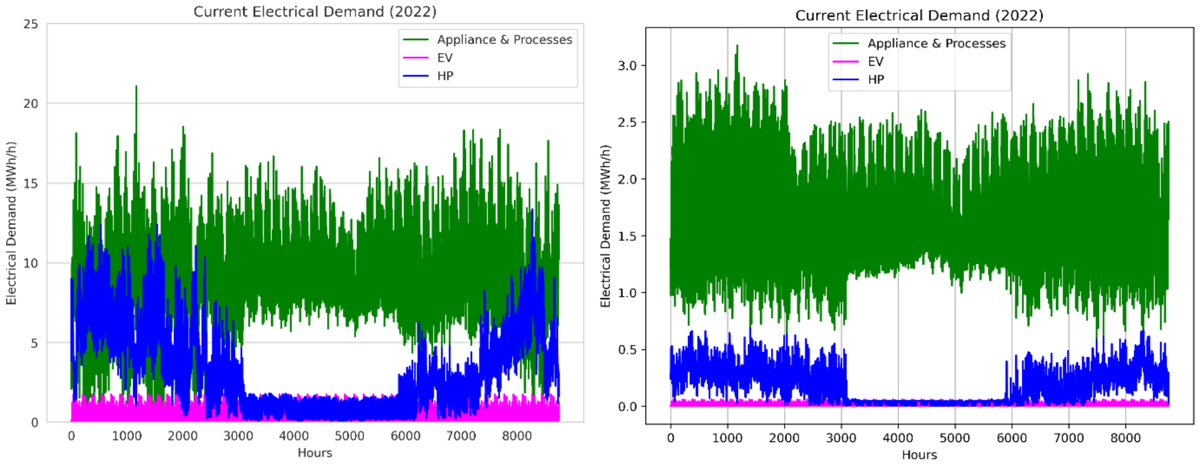

Figure 3: Hourly annual electricity demand for HP, EVs (uncontrolled charging), appliance and processes for both residential and non-residential customers in (a) Estavayer-le-Lac (left) and (b) Boisy in 2022 (right).

As shown in Figure 4 and Figure 5, the projected annual electricity demand of Estavayer-le-Lac and Boisy according to the default scenario is expected to evolve significantly from 2022 to 2050. In Estavayer-le-Lac, electricity demand is projected to increase by around 25GWh per year due to the adoption of HPs. In addition, electricity demand is projected to increase by around 38GWh per year through the electrification of mobility and EVs, while the electricity demand for appliances and processes is expected to decrease by 15GWh per year over the same period. This decrease is likewise based on the Energy Perspectives 2050+ [24]. In Boisy, electricity demand is projected to increase by around 13.9GWh per year for HPs and by 3.6GWh per year for EVs, while decreasing by 2.8GWh for appliances and processes.

The difference in electricity demand growth for EVs and HPs in the two locations is mainly explained by the local residential structure and mobility patterns. In Boisy, the building stock is dominated by MFH (~75%), where private car ownership is typically lower, resulting in a smaller increase in electricity demand from EV compared to HP. In contrast, Estavayer-le-Lac is largely dominated by SFH (~85%), where car ownership is much higher (by a factor of ~5.6), leading to a larger growth in electricity demand from EV relative to HP. In addition, the total number of cars in Boisy is considerably smaller than in Estavayer-le-Lac. In this default scenario, the net total electricity demand in Estavayer-le-Lac is projected to decrease from 108.8GWh per year in 2022 to -49GWh per year in 2050. Also, for Boisy, net demand is projected to decrease from 16.3GWh per year in 2022 to 9.6GWh per year in 2050. The reason for the difference in decrease in the two locations is much higher relative production of PV electricity in Estavayer-le-Lac compared to Boisy due to the larger roof area and much higher share of SFH in Estavayer-le-Lac compared to Boisy. The results show that at high PV deployment in 2050 scenarios may also introduce operational challenges due to the maximum feed in, i.e., load, from PV systems exceeding the maximum load of grid electricity demand by a factor of 3.

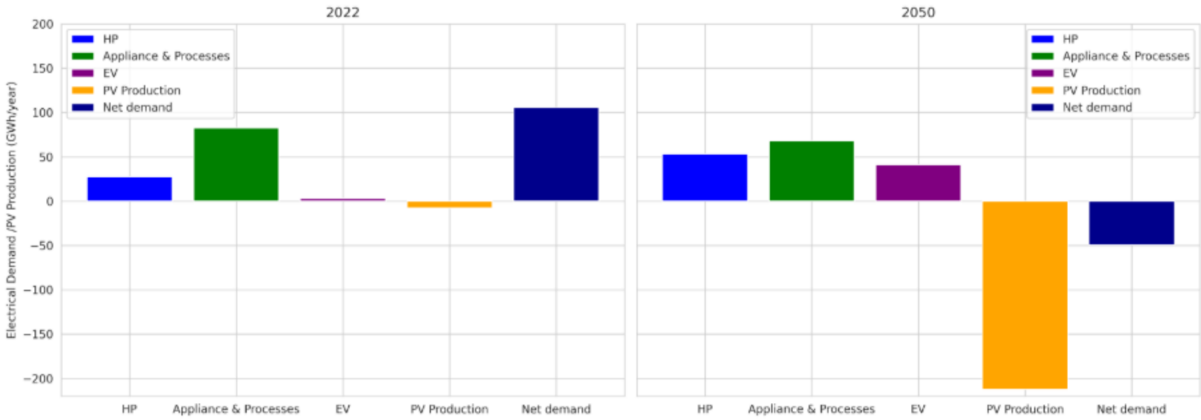

Figure 4: Annual Electrical demand with PV production for both 2022 (with uncontrolled EV charging) and 2050 (with con-trolled EV charging), Estavayer-le-Lac.

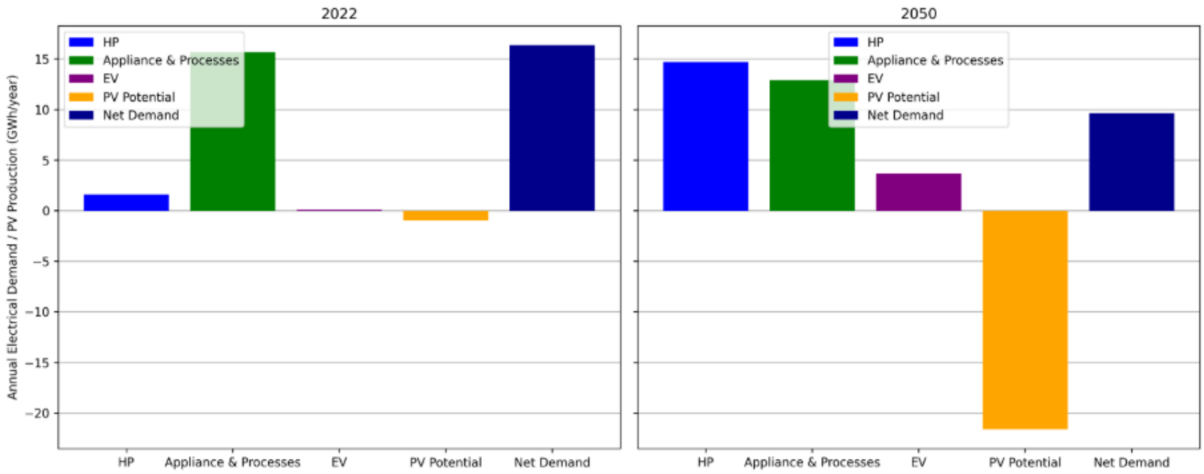

Figure 5: Annual Electrical demand with PV production for both 2022 (with uncontrolled EV charging) and 2050(with con-trolled EV charging), Boisy.

Figure 6 and Figure 7 show the total aggregated electricity demand in Estavayer-le-Lac and Boisy for 2022 and 2050 for heating, EV, and appliances and processes. The comparison of the electrical load curves in 2050 and 2022 shows that the seasonal difference becomes more pronounced in 2050. This is caused by electrical load curve for HP in 2050, which is displayed in Figure 8.

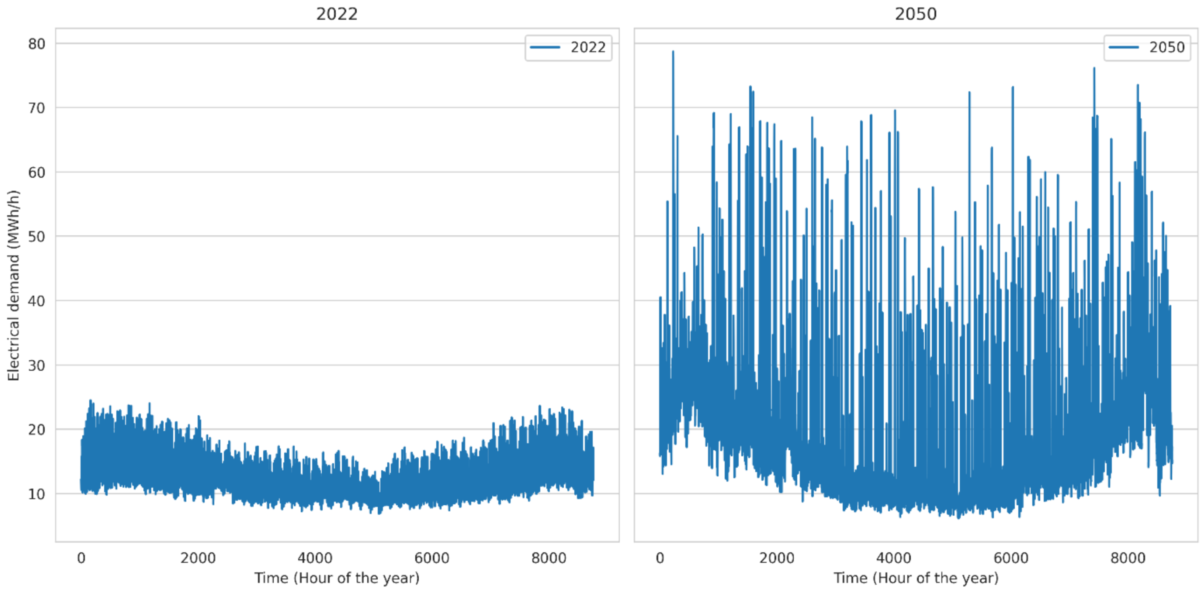

Figure 6: Total aggregated electricity demand [MWh] of HP, EV (uncontrolled charging for 2022 and controlled charging for 2050) and electrical appliances and processes in Estavayer-le-Lac for 2022 and 2050 without HPs for industrial processes.

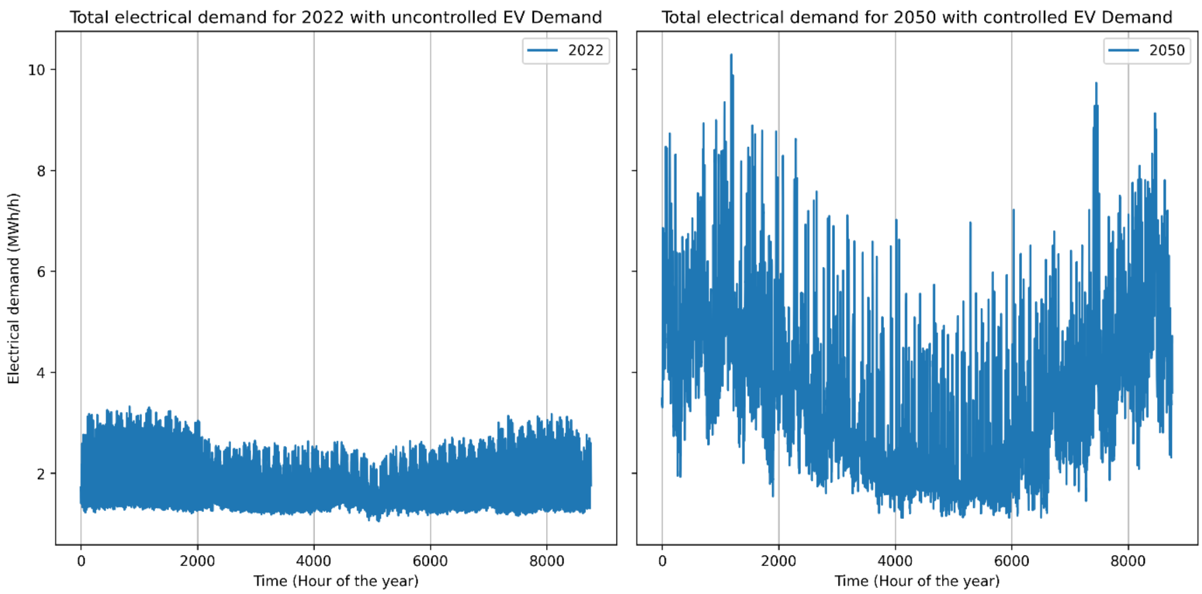

Figure 7: Total aggregated electricity demand [MWh] of HP, EV (uncontrolled charging for 2022 and controlled charging for 2050) and electrical appliances and processes Boisy for 2022 and 2050 without HPs for industrial processes.

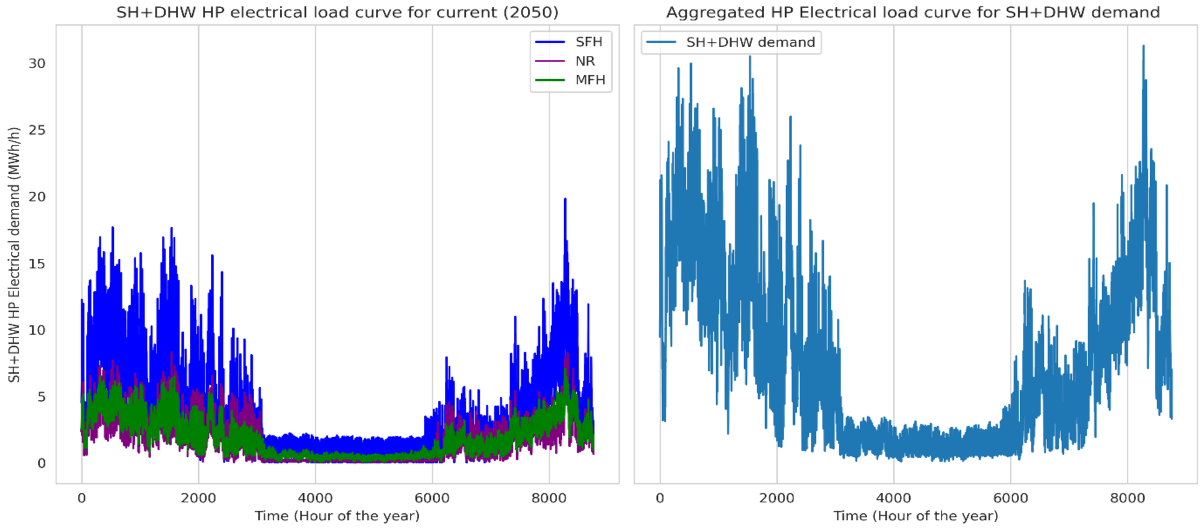

Figure 8: HP electrical load curves for both Space heating (SH) and Domestic hot water (DHW) for 2050 demand per archetype and the aggregated HP electrical load curve (based on assumption of 100% HP diffusion) for Estavayer-le-Lac without HPs for industrial processes.

2.3. Grid Mapping, Economic Optimization, and Transformer Aging

2.3.1. *Procedure and method*

Another simulation framework is developed that translate building-level energy behavior into a consistent representation of demand and flexibility across two Swiss low-voltage distribution networks: Estavayer-le-Lac and Boisy. The approach follows three successive stages, illustrated in Figure 9, and is applied from 2025 to 2050 in five-year increments across four technology scenarios and three tariff structures. Full details of the methodology are provided in the deliverables 4.1 and 4.2.

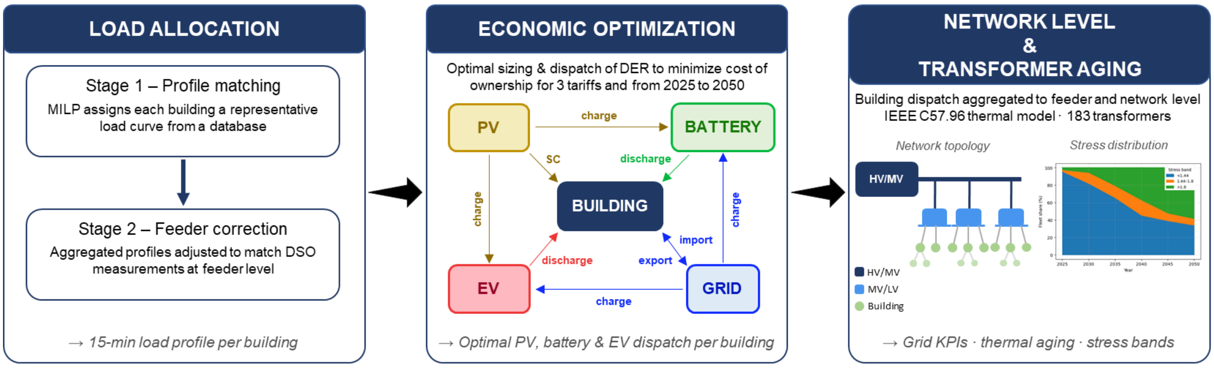

Figure 9: Overview of the simulation methodology, comprising three successive stages: load allocation, economic optimisation, and network-level aggregation with transformer thermal aging assessment.

Load allocation. The starting point is the reconstruction of 15-minute electricity demand profiles for each building in the network. Building locations are linked to grid connection points using the low-voltage network models from WP2, and annual consumption values are distributed across nodes. A two-stage optimization procedure then assigns representative virtual load curves: Stage 1 matches each building to a profile drawn from a database of representative virtual load curves using a MILP, constrained by building category. Stage 2 adjusts the aggregated profiles to match transformer-level measurements provided by the DSO, ensuring consistency at feeder level while conserving annual energy totals at each node. PV self-consumption, HP and DHW loads from WP3, and EV consumption are incorporated before the feeder correction is applied. EVs are distributed across the networks based on demographic statistics, mobility patterns, and building characteristics, producing charging availability curves that capture how electrification trends affect local demand and flexibility potential.

Economic optimization. Once building-level profiles are established, a MILP model determines the optimal sizing and dispatch of PV systems, battery storage, and EVs at each building node, minimising total cost of ownership over a 25-year horizon (Figure 9, centre). EV operation is modelled at the individual vehicle level, with charging and discharging schedules subject to availability constraints and V2H capabilities. The model is applied under three tariff structures – a flat Single Tariff (ST), a time-of-use Double Tariff (DT), and a Capacity Double Tariff (CDT) that adds a monthly peak power charge – and distinguishes between a 2025 baseline focused on operational dispatch and future scenarios from 2030 to 2050 incorporating investment decisions. Progressive deployment trajectories for PV, batteries, HPs, and EVs are aligned with the WP3 electrification targets.

Network level and transformer aging. Building-level dispatch results are then aggregated to feeder and network level to compute grid impact indicators such as peak demand, self-consumption and self-sufficiency rates, and load duration curves, among others; a full description is provided in the deliverables 4.1 and 4.2. Transformer thermal aging is assessed for all 183 MV/LV transformers in the studied networks using the IEEE C57.96 framework [25], which links hotspot temperature to insulation degradation and equivalent lifetime loss. This allows the progressive stress imposed by increasing DER penetration to be quantified across scenarios and years.

2.3.2. Results and discussion

PV deployment reshapes the energy balance of both networks decisively. By the early 2040s, total annual rooftop generation reaches and exceeds total network demand, shifting the primary challenge from reducing energy costs to controlling the timing and magnitude of power flows across the grid connection. Batteries and EVs address this effectively: in the full PV + Battery + EV scenario, the share of electricity drawn from the grid falls from 94% in 2025 to around 58% by 2050, with vehicle-to-home discharge alone covering approximately 10% of total demand by the end of the horizon. The two technologies complement rather than substitute each other, and stationary batteries remain worthwhile even as the EV fleet grows. Scenarios without stationary batteries, such as PV Only and PV + EV, are largely tariff-independent, with grid import shares and transformer loading remaining close across all three tariffs throughout the horizon. In scenarios that include batteries, grid import shares converge within 4 to 5 percentage points across tariffs by 2050. Both DT and CDT result in smaller battery installations than ST, as off-peak grid charging allows each unit of capacity to be used more intensively, making smaller batteries economically sufficient. Despite this, overall grid independence remains comparable across all three tariffs.

Peak demand tells a very different story. PV penetration is the primary driver of transformer stress, progressively pushing a larger share of the fleet toward operational limits regardless of tariff or technology combination, with the After Diversity Maximum Demand (ADMD) and the share of transformers in the high-stress band rising consistently across all tariffs over the horizon. No tariff reduces stress below this PV-driven baseline; tariff design can only moderate or worsen the trend by influencing the synchronisation of flexible assets. Under DT, coincident battery charging just before peak price windows generates feeder import peaks 5 to 7 times larger than under ST. The Normalised Load Ramp Steepness Index (NLRSI), which measures the volatility of grid import ramps, reaches approximately 11 under DT by 2050 – an order of magnitude above the ST baseline – reflecting infrastructure requirements far beyond what annual energy metrics would suggest. CDT largely contains this effect, limiting peak demand to 2.5 to 3 times the ST baseline while achieving comparable grid import shares, and emerges as the more grid-compatible instrument for networks with high battery penetration. EV flexibility introduces temporal diversity in charging demand, partially smoothing the coincident peaks that battery-only scenarios produce under DT; batteries and EVs should therefore be assessed jointly when evaluating tariff policies.

An ex-ante and ex-post analysis further shows that DT and CDT activate comparable volumes of off-peak grid charging, exceeding 20GWh annually by 2050, but differ in how that energy is subsequently discharged. Under DT, concentrated peak-hour discharge largely offsets the additional off-peak charging, keeping net new grid consumption at around 2GWh per year. Under CDT, the smoother discharge profile results in higher net new consumption of around 4.7GWh by 2050. This illustrates that smoothing peak demand and reducing total grid consumption are not the same objective, and a tariff can achieve one without necessarily achieving the other.

These results highlight a fundamental tension in tariff-driven flexibility: the same price signal that activates flexible assets can, if it contains sharp price transitions, generate coincident demand peaks that undermine the very grid stability the flexibility was meant to support. Moving toward continuously varying dynamic price signals, rather than discrete peak and off-peak boundaries, would reduce the incentive for all assets to respond simultaneously. Future network planning should assess peak loading conditions and transformer thermal aging jointly alongside annual energy metrics, rather than relying on energy balances alone when evaluating reinforcement needs under increasing DER penetration. Full results, scenario breakdowns, and indicator time series are provided in the deliverables 4.1 and 4.2.

2.4. The Integrated planning framework

The integrated planning framework structured across three connected time horizons that represent the natural evolution of grid planning and operation:

- **Short-term (Flexibility Dispatch):** This horizon focuses on the daily operation and scheduling of flexible assets, such as PVs, EVs, and HPs.
- **Mid-term (Operational Configuration):** This horizon optimizes network reconfiguration and control settings, such as switch states and transformer tap positions, to guarantee reliable operation.
- **Long-term (Expansion Planning):** This horizon handles strategic investment decisions regarding the expansion of transformer and line capacities.

The optimization problems of these three horizons are interdependent. The outcome of the short-term flexibility dispatch informs the mid-term configuration layer, identifying effective switching strategies. In turn, the mid-term configuration defines the operational constraints that strictly guide long-term planning and investment decisions.

A foundational aspect of this integrated framework is the explicit distinction between *known* uncertainties (daily and seasonal variations in load and PV generation) and *unknown* uncertainties (long-term DER deployment, EV/HP connection requests). The lack of accurate probabilistic models in *unknown* uncertainties is handled in the long-term planning layer to ensure expansion decisions remain robust against ambiguous future developments.

2.4.1. Proposed methodology

To bridge the gap between long-term planning and short-term feasibility, the proposed framework utilizes a coordinated two-layer numerical environment. The *upper* layer manages long-term investment decisions under *unknown* uncertainties. It is implemented in Julia and formulated as a stochastic dual dynamic programming (SDDP) model [24]. This layer determines the optimal reinforcement of grid assets across multi-year planning stages. It leverages a risk measure to produce optimal decisions that are robust against future *unknown* uncertainties. The *lower* layer optimizes grid flexibility to handle voltage and current limitations under variable demand and generation profiles, addressing *known* uncertainties. It is formulated as a Mixed Integer Second-Order Cone Program (MISOCP). To maintain computational tractability for large-scale grids, this layer implemented in Python using Pyomo and solved via a consensus Alternating Direction Method of Multipliers (ADMM) decomposition [26]. The ADMM allows individual operating scenarios and each section of the grid to be solved independently while enforcing global consistency on shared decisions like switch statuses and tap positions.

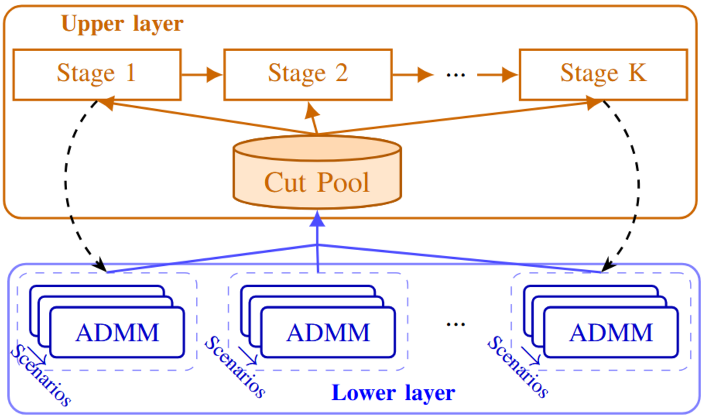

Figure 10: Proposed Two-Layer Framework.

To handle *unknown* uncertainties, the *upper* layer can utilize different risk operators to model the DSO's risk attitude: *Expectation*, *Worst-Case*, and *Wasserstein*. The risk neutral baseline approach focuses on minimizing the average expansion expenditure. On the other hand, the highly conservative policy is to optimize for the extreme scenario. The *Wasserstein* strikes a balance between the expectation and worst-case strategies. By evaluating the worst-case expected cost over all plausible probability distributions that are close to the nominal distribution (within a *Wasserstein* ball [27]), it achieves near risk-neutral cost efficiency while still protecting the grid against costly, adverse scenarios.

2.4.2. Software-level architecture

The software-level architecture and the closed-loop interaction of the proposed two layers are illustrated in Figure 11. The left side features the Julia-based SDDP expansion model, which executes investment iterations using the HiGHS solver. Conversely, the right side presents the Python-based ADMM operational model, which handles operational feasibility using `Gurobi` optimization solver within Pyomo. These two layers are linked through an API-based interface that coordinates the bidirectional data transfer, managing the exchange of grid expansion updates and operational cuts between the models.

The bifurcated architecture, combining the SDDP framework in Julia with a Python environment, was adopted due to practical implementation constraints. Developing a custom multistage stochastic optimization tool from scratch is technically demanding, particularly because solving the dual problem backward introduces substantial mathematical complexity and a high risk of implementation errors. Instead, the approach leverages established open-source tools, notably the SDDP.jl package, which provides a mature implementation of multistage stochastic and distributionally robust optimization. Although linking the two environments through an API introduces some communication overhead, this trade-off enables the framework to use specialized solvers for each layer while maintaining modularity and improving the reliability of the overall asset-planning system.

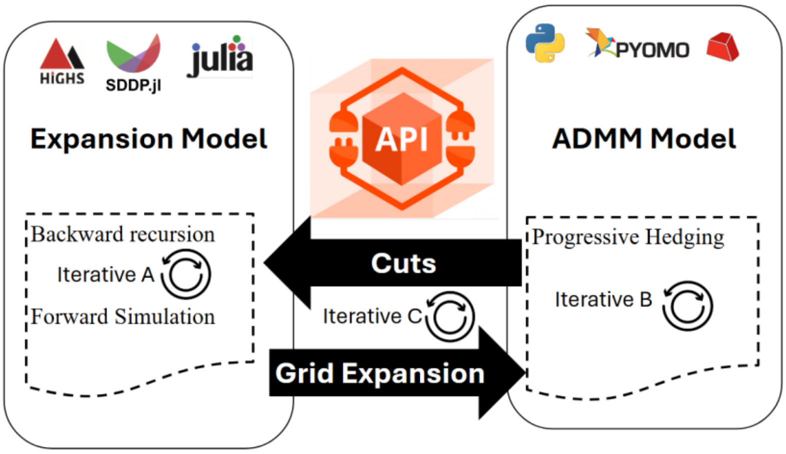

Figure 11: Software-level architecture of the integrated framework, showing the interaction between the Julia-based SDDP expansion model and the Python-based ADMM operational model.

The proposed optimization framework operates on three distinct iteration loops: Iteration (A) includes the backward recursion and forward simulation passes within the SDDP expansion model; Iteration (B) governs the progressive hedging and distributed operational analysis of the ADMM model; and Iteration (C) acts as the outer loop, managing the iterative cut exchange and interaction between the two models. Ultimately, the cuts generated by the lower layer are aggregated in a central cut pool and passed back to the SDDP expansion model. It updates the value function representation to ensure that all long-term investments remain physically and operationally feasible.

A full and comprehensive description of this integrated asset-planning framework including its mathematical optimization methodology, software implementation, numerical validation results, and public release details is detailed across Deliverables 5.1, 5.2, and 5.3.

2.5. Case studies and tool validation

The proposed integrated framework is technically validated on one benchmark (i.e., IEEE33 case) and two real distribution grids. The expansion planning analysis is performed under three energy transition scenarios (i.e., Baseline, Sustainable, and Full) representing different levels of electrification and DER deployment. Detailed description of the case studies is provided in Deliverables 2.1 and 2.2. The full description of energy transition scenarios is given in Deliverable 5.2.

For the IEEE33 benchmark grid, the CAPEX distribution under different risk attitudes is given in Figure 12. The expectation policy minimizes average costs but exposes the grid to higher risks, while the worst-case policy is too conservative and expensive. The *Wasserstein* risk metric provides a balance between cost-efficiency and protection against extreme uncertainty.

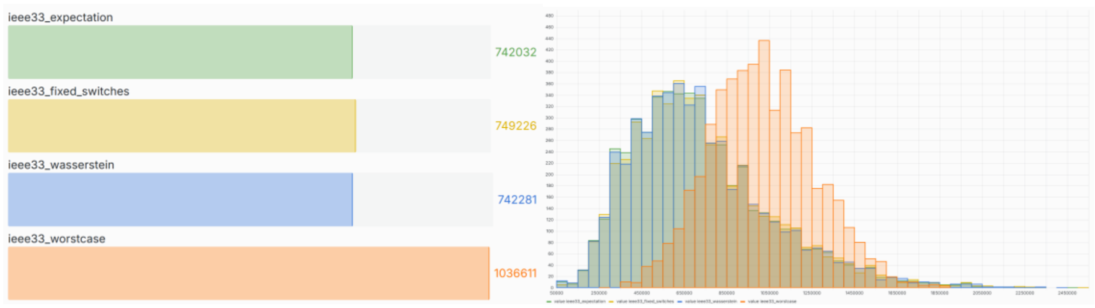

Figure 12: CAPEX distribution under different risk measure and fixed switches configuration.

For the Boisy grid, the CAPEX distribution is shown in Figure 13. Results indicate that ADMM-based dynamic switching significantly reduces expansion costs in highly interconnected networks (Feeder 1). However, for more linear and constrained feeders (Feeder 2), switching flexibility gain no economic benefit over a fixed-switch configuration. Considering both feeders together, which supply roughly 1500 customers, and assuming a 25-year planning horizon with interest rate 5%, the average annual expansion cost per customer is approximately 260CHF.

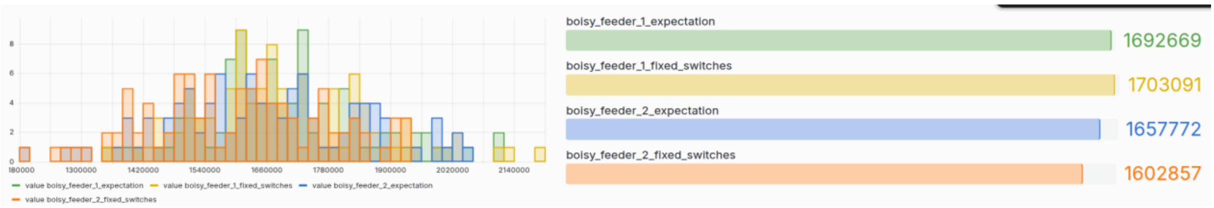

Figure 13: The comparison of results for feeders 1, 2, and fixed switches versus the expectation risk measure.

For the Estavayer Centre-Ville feeder, the results are displayed in Figure 14, indicating that this grid is relatively overdesigned for the modelled demand levels, with the total expansion of about 87kCHF. Because the grid is largely radial with few switching points, dynamic reconfiguration yields limited economic benefits.

A detailed presentation of the integrated framework results is provided in Deliverable 5.2.

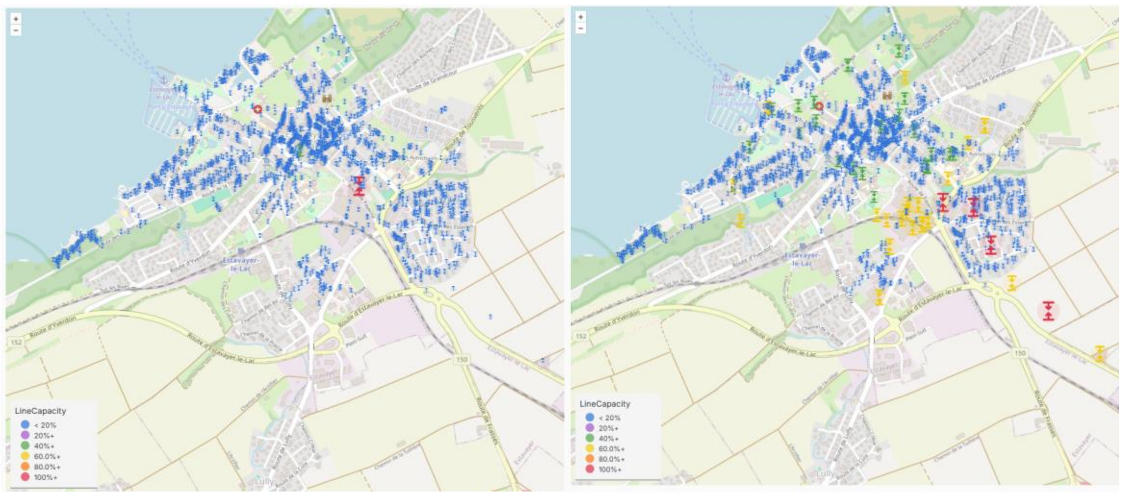

Figure 14: The expansion trajectory for Estavayer centre-ville. The left panel shows the network at the initial stage, while the right panel illustrates the configuration at Stage 5.

Another validation approach involved probabilistic load flow analysis using three generated power profiles over a 25-year horizon. A benchmark expansion strategy was defined in which lines and transformers are reinforced solely based on their loading percentages, without any optimization or forward-looking planning.

The comparison shows that, for the Boisy case, the proposed methodology achieves approximately a twofold CAPEX deferral relative to the benchmark. Specifically, the benchmark expansion results in an investment of about 23 MCHF, whereas the worst-case planning scenario under the proposed methodology requires around 10 MCHF. Additional results on the benchmark expansion are provided in Deliverable 5.2.

3. Conclusions and outlook

The developed modelling framework provides a robust and spatially detailed basis for analyzing future electricity demand under large-scale electrification of heating and transport. High electrification and decentralized PV electricity generation will substantially increase stress on distribution grids. Within this context, the results highlight that without coordinated deployment of PVs and flexibility measures; electrification will lead to substantial seasonal and peak load challenges in distribution networks.

A key driver behind these dynamics is the rapid expansion of PV gentian. PV deployment is the central driver of the energy transition in distribution networks, reducing grid import shares from 94% in 2025 to around 58% by 2050 when combined with batteries and EVs, as observed across the Estavayer network. As penetration grows, however, managing the timing and magnitude of power flows becomes the central planning challenge, and network reinforcement strategies must account for thermal stress on transformers alongside annual energy metrics.

This shift naturally leads to the role of tariff design in shaping system behaviour. While tariff structure does not significantly alter the level of grid independence achieved, but it has a decisive effect on peak power flows. Under time-of-use tariffs, coincident battery charging generates demand peaks an order of magnitude more volatile than under a flat tariff, requiring infrastructure dimensioned far beyond what annual energy metrics would suggest. If a time-of-use structure is to remain in place, adding a capacity charge component, as in the capacity double tariff (CDT), largely contains this effect and should be considered as a preferred instrument in markets with high battery penetration.

The same price signal that activates flexible assets can, if it contains sharp price transitions, generate the very demand peaks it was meant to suppress. Transitioning toward continuously varying dynamic tariffs, and assessing batteries and EVs jointly rather than independently, are necessary conditions for tariff-driven flexibility to remain compatible with grid stability as distributed generation and storage continues to expand.

From the planning perspective, incorporating risk measures into the planning process introduces significant mathematical complexity; however, our results indicate that relying on the expectation risk measure is generally robust and sufficient. The stability of these decisions is evidenced by the narrow gap between in-sample and out-of-sample performance.

Another finding from the planning perspective is that the effectiveness of two-layer optimization framework depends on network topology. The two-layer optimization framework proves highly valuable in dense, interconnected urban areas where operational flexibility and dynamic switching can efficiently manage congestion and reduce expansion costs. Conversely, in rural networks characterized by largely radial topologies and limited switching capabilities, dynamic reconfiguration offers less economic benefit. In such rural systems, factors like reliability often take precedence over pure cost-efficiency, a constraint that was not explicitly modelled in this study.

A final observation is that, when comparing the expansion results obtained using a worst-case risk measure with a benchmark expansion approach without optimization, the CAPEX deferral is on the order of a factor of two for the case of Boisy grid. This highlights the economic value of incorporating both optimization and flexibility into long-term distribution grid planning.

These findings point directly to several directions for future work:

First, a more advanced decomposition strategy could improve scalability and computational efficiency. An ADMM-based formulation could enable a geographical decomposition of the network into separate feeders, allowing each feeder to be optimized independently while maintaining consensus on shared variables such as boundary flows and switching states.

Second, further progress in generating grid-aware load profiles is important. If smart meter datasets are enriched with features such as building archetype, construction period, floor area, and related attributes, it becomes possible to generate power profiles that explicitly account for grid constraints. This would support the development of a more accurate digital twin of LV grids, while the proposed methodology remains well suited for MV grid applications.

Third, the current study does not provide an integrated long-term asset planning framework that jointly considers the role of energy storage in providing short-term operational flexibility, which can defer reinforcement investment (CAPEX), and the impact of transformer aging, which may necessitate transformer replacement over the medium term. While the effects of the energy transition on transformer aging are analysed separately for the case studies, these aspects are not integrated within a unified planning model. Incorporating transformer aging into the planning framework would enable the assessment of cumulative thermal stress alongside investment and operational decisions. Such an integrated approach would also reveal how inadequate tariff design and resulting operational strategies, particularly those driving synchronized EV charging, can significantly accelerate asset degradation and become a critical planning constraint in long-term.

Finally, reliability considerations should be integrated explicitly into the optimization model. Reliability is a critical planning criterion in many real distribution systems, as illustrated by the Estavayer network, where operational reliability strongly influences infrastructure design. Incorporating reliability constraints or reliability-based cost metrics would provide a more comprehensive representation of real-world planning objectives.

4. National and international cooperation

At national level, there is a good synergy and cooperation between this project and “Smart Energy District” project funded by HES-SO. The project unites many DSOs, technology providers, and four HES schools in which HEIG-VD is one of the main academic partners responsible for technical developments and Groupe E and Yverdon Energies are also strongly engaged. In particular, the cooperation is on data models and pre-processing procedures as well as scenarios for changes in load and generation configuration at regional and district level.

At international level, Mokhtar Bozorg is participating in IEEE working group on revision of “Guide for Conducting Impact Studies for Distributed Energy Resource Interconnection” and is in contact with another IEEE working group on “Modern and Future Distribution System Planning”.

The project was carried out in close collaboration between HEIG-VD, UNIGE, and EPFL. The partnership facilitated the exchange of expertise in grid analysis and optimization, allowing each institution to contribute its specialized knowledge. Regular coordination meetings and workshops were organized throughout the project, ensuring continuous communication, alignment of objectives, and effective joint progress. This collaborative framework strengthened the overall quality of the research outcomes and promoted knowledge sharing.

Throughout the project, HEIG-VD, UNIGE, and EPFL maintained active collaboration with DSOs. This included regular data sharing, progress meetings, and ongoing discussions, which ensured alignment between the research team and the operators’ practical needs. The collaboration also fostered continuous knowledge exchange, allowing both the academic institutions and DSOs to benefit from shared expertise in grid analysis, optimization, and operational practices. This joint effort strengthened the relevance and applicability of the project outcomes for real-world distribution networks.

5. Publications and other communications

- The source code, including instructions for local deployment, is available at the following repository: https://github.com/heig-vd-ie/dig-a-plan-optimization.
- The full technical documentation is accessible at https://heig-vd-ie.github.io/dig-a-plan-optimization/.
- Mokhles Gerami, L. Tomasini, M. Rayati, M. Bozorg, "Flexible Distribution Network Reconfiguration via Scalable Alternating Direction Method of Multipliers", published in SEGAN, 2026.
- Mohammad Rayati, Adeleh Mokhles Gerami, Mokhtar Bozorg, "Distribution Expansion Planning under Renewable and Electrification Uncertainty considering Grid Operational Flexibility", under progress.
- The open-source model developed for integrated modelling is available at the following repository: GitHub Repository – Unige-Dig_a_plan-Integrated_modeling
- Nyandwi, Arbogast, et al. "Estimating the Effect of Heating and Transport Electrification on Self-Sufficiency and Self-Consumption for residential buildings in rural settings." Journal of Physics: Conference Series. Vol. 3140. No. 6. IOP Publishing, 2025.
- Selected results from WP4 will be presented at the PV-Tagung conference (31 March – 1 April).
- A paper based on the WP4 findings is being prepared for submission this summer.
- One publication integrating the different components of the project is planned for 2026.
- Mokhtar Bozorg et al. « Méthodologie pour la planification des réseaux de distribution à long terme, de la modélisation des consommateurs à l'optimisation des investissements », Bulletin.ch, 5/2026, Smart energy.
- One workshop with other DSOs and other research institute is envisaged for June-August 2026.

6. References

[1] V. Umwelt, «Energie und Kommunikation UVEK, Eidgenössisches Departement für. “Energieperspektiven 2050+,» Dec. 2021. [Online]. Available: https://www.bfe.admin.ch/bfe/en/home/policy/energy-perspectives-2050-plus.html.

[2] K. Maus, «2021-2024 Energy Research Master Plan. pubdb.bfe.admin.ch. ern, Switzerland: Federal Energy Research Commission CORE.,» May 2023. [Online]. Available: https://pubdb.bfe.admin.ch/en/publication/download/10328. .

[3] V. Umwelt, «Energie und Kommunikation UVEK, Eidgenössisches Departement für Energy Strategy 2050.” Energy Strategy 2050 - UVEK,,» July 2017. [Online]. Available: https://www.uvek.admin.ch/uvek/en/home/energy/energy-strategy-2050.html.

[4] C. Chow, Clare und R. K. Sarin, «Known, unknown, and unknowable uncertainties,» *Theory and Decision,* Bd. 52, Nr. 2, pp. 127-138, 2002.

[5] R. Huang, S. Qu, X. Yang und Zhang, «Huang, Ripeng, Shaojian Qu, Xiaoguang Yang, and Zhimin Liuc,» *Huang, Ripeng, Shaojian Qu, Xiaoguang Yang, and Zhimin Liu,* Bd. 17, Nr. 1, 2021.

[6] Verbraucher, « NETFLEX – Effiziente Netzentgelte für flexible, NETFLEX – Effiziente Netzentgelte für flexible Verbraucher,» 2023. [Online]. Available: https://www.aramis.admin.ch/Texte/?ProjectID=44252.

[7] «Federal Statistical office, Registre fèdèral des batiments et des logements (RegBL). [Online]. Available: https://www.housing-stat.ch/fr/index.html,» [Online].

[8] «Federal Statistical, “Office federal de la statistique, ‘Urbain-rural Typologie 2012’.,” Accessed: April 2024. [Online]. Available: https://www.atlas.bfs.admin.ch/maps/13/fr/17223_12361_3191_227/26733.html,» [Online].

[9] P. H. P. L. S. J. K. M. P. a. B. L. S. Schneider, «Spatial–Temporal analysis of the heat and electricity demand of the Swiss building stock,» *Front. Built Environ.,* Bd. 3, Nr. doi: 10.3389/fbuil.2017.00053, pp. 1-17, 2017.

[10] T. Shluck, K. N. Streicher und S. Mennel, «Statistical modelling of the energy reference area based on the Swiss building stock,» *J. Phys. Conf. Ser.,* Bd. 1343, Nr. doi: 10.1088/1742-6596/1343/1/012031, 2019.

[11] S. Schneider, P. Hollmuller, J. Chambers und M. Patel, «Heat Demand Load Curve Model of the Swiss National Territory,» *IOP Conf. Ser. Earth Environ. Sci.,* Bd. 290, Nr. doi: 10.1088/1755-1315/290/1/012107, 2019.

[12] «“Schweizerischer Ingenieur- und Archtiktenverein. SIA 380 – Grundlagen f¨ur energetische Berechnungen von Geb¨auden, 2015”.,» [Online].

[13] S. Callegari, «Energy conversions and Energy systemsc,» M.Sc. thesis (MUSE), 2018.

[14] «Swiss Federal Office of Energy, “Energy perspectives 2050+.” [Online]. Available: https://www.bfe.admin.ch/bfe/en/home/policy/energy-perspectives-2050-plus.html/».

[15] «Federal Roads office, “Vehicle data,” https://www.astra.admin.ch/astra/en/home/dokumentation/daten-informationsprodukte/informationsprodukte.html. 2024.».

[16] A. Syla, A. Rinaldi, D. Parra und M. K. Patel, «Optimal capacity planning for the electrification of personal transport: The interplay between flexible charging and energy system infrastructure,» *Renewable and Sustainable Energy Reviews,* Bd. 192, Nr. doi: 10.1016/j.rser.2023.114214, p. 114214, 2023.

[17] «Federal Statistical office, “Microcensus Mobility and Transport(MZMV).” [Online]. Available: https://www.bfs.admin.ch/bfs/de/home/statistiken/mobilitaet-verkehr/erhebungen/mzmv.html».

[18] «Bundesamt für Statistik, Verkehrsverhalten der Bevölkerung - Ergebnisse des Mikrozensus Mobilität und Verkehr 2015 (Transport behavior of the population - results of the microcensus mobility and transport 2015), no. 1840477. 2017.,» [Online]. Available: https://www.bfs.admin.ch/hub/api/dam/assets/1840477/master.

[19] «'NETFLEX – Effiziente Netzentgelte für flexible Verbraucher,' SFOE, 2023," https://www.aramis.admin.ch/Texte/?ProjectID=44252.».

[20] A. Syla, D. Parra und M. K. Patel, «Assessing flexibility from electric vehicles using an open-source energy system model: trade-offs between smart charging, vehicle-to-grid and an extensive charging infrastructure,» *Energy,* Bd. 326, Nr. doi: 10.1016/J.ENERGY.2025.136236, p. 136236, 2025.

[21] A. Walch, R. Castello, N. Mohajeri und J. L. Scar, «ig data mining for the estimation of hourly rooftop photovoltaic potential and its uncertainty,» *Applied Energy,* Bd. 262, Nr. doi: 10.1016/j.apenergy.2019.114404, p. 114404, 2019.

[22] «Swiss Federal Office of Energy, "'Federal Office of Topography swisstopo.' ," [Online]. Available: https://www.uvek-gis.admin.ch/BFE/sonnendach/.,» [Online].

[23] A. Rinaldi, D. Parra und M. K. Patel, «Optimized allocation of PV and storage capacity among different consumer types and urban settings: A prospective analysis for Switzerland,» *Journal of cleaner production,* Bd. 259, p. 120762, 2020.

[24] O. Dowson und L. Kapelevich, «SDDP. jl: a Julia package for stochastic dual dynamic programmingc,» *INFORMS Journal on Computing,* Bd. 33, Nr. 1, pp. 27-33, 2021.

[25] *IEEE Std C57.96-2013. IEEE Guide for Loading Dry-Type Distribution and Power Transformers..*

[26] Y. Mokhtari, P. Coirault und E. Moula, «Distributed ADMM Approach for the Power Distribution Network Reconfiguration,» *Sustainable Energy, Grids and Networks,* Bd. 101890, 2025.

[27] M.-C. Yue, D. Kuhn und W. Wiesemann, «On linear optimization over Wasserstein balls,» *Mathematical Programming,* Bd. 195, Nr. 1, pp. 1107-1122, 2022.

7. Data management plan and open access/data/ model strategy

All data related to DSOs and end customers are stored on servers located in Switzerland and treated as confidential. These data are used exclusively for the objectives defined within each project and are not reused for any other purpose after project completion. Confidentiality is ensured through non-disclosure agreements (NDAs) established between the DSO partners and the participating universities.

The source code developed in WP5 is made publicly available, but it does not include any operational grid data. This separation ensures that sensitive information remains protected while allowing the research methods and algorithms to remain transparent and reproducible. Users who have authorized access to the relevant grid data can execute the optimal reconfiguration experiments directly from the project repository by providing the appropriate input data. For the IEEE 33-bus grid test case, no special data access is required because this benchmark network is publicly available.

The scripts used to reproduce the reconfiguration experiments for the different study cases are available at the following locations:

- https://github.com/heig-vd-ie/dig-a-plan-optimization/blob/main/experiments/boisy/01-reconfiguration.py,
- https://github.com/heig-vd-ie/dig-a-plan-optimization/blob/main/experiments/estavayer/01-reconfiguration.py,
- https://github.com/heig-vd-ie/dig-a-plan-optimization/blob/main/experiments/ieee_33/01-reconfiguration.py,
- https://github.com/heig-vd-ie/dig-a-plan-optimization/blob/main/scripts/run-all.sh.

To run a specific study case, the input payload must be adapted to the targeted feeder and to the selected power profile.

The full source code, together with instructions for local deployment, is available at

- https://github.com/heig-vd-ie/dig-a-plan-optimization.

The technical documentation describing the architecture, configuration, and usage of the software is available at

- https://heig-vd-ie.github.io/dig-a-plan-optimization/.

Appendices

- *Appendix 1 (Deliverables 2.1 and 2.2): Data collection and case studies*
- *Appendix 2 (Deliverables 3.1 and 3.2): Scenarios of load growth and technology integration*
- *Appendix 3 (Deliverables 4.1 and 4.2): Expected asset distribution, flexibility amount, and expected transformer loss of life*
- *Appendix 4 (Deliverables 5.1, 5.2, and 5.3): Distribution grid asset planning optimization, validation of the model, and release of the planning tool*

Schweizerische Eidgenossenschaft
Confédération suisse
Confederazione Svizzera
Confederaziun svizra

Federal Department of the Environment,
Transport, Energy and Communications DETEC

Swiss Federal Office of Energy
Energy Research and Cleantech

Final report 30 April 2026

Dig-A-Plan

Appendix 1: Data collection and case studies

D2.1 Multiple representative grids as case studies in addition to a synthesized grid

D2.2 Reduced topological models of representative distribution grids

---

Publisher:
Swiss Federal Office of Energy SFOE
Energy Research and Cleantech
CH-3003 Berne
www.energy-research.ch

Co-financing: In-kind contributions provided by
Groupe e, 1763 Granges-Paccot

Services Industriels Lausanne (SiL), 1003 Lausanne

Yverdon Energies, 1400 Yverdon

Subsidy recipients:
Haute École d'Ingénierie et de Gestion du Canton de Vaud (HEIG-VD), Institute of Energies (IE)
1400 Yverdon-les-Bains
https://heig-vd.ch/recherche/instituts/ie/

Université de Genève (UNIGE), Institute for Environnemental Sciences (ISE)
1205 Genève
https://www.unige.ch/energy/

EPFL, photovoltaic research laboratory (PV-LAB)
2002 Neuchâtel
https://www.epfl.ch/labs/pvlab/

Authors:

Mokhtar Bozorg, HEIG-VD, mokhtar.bozorg@heig-vd.ch
Mohammad Rayati, HEIG-VD, mohammad.rayiati@heig-vd.ch
Adeleh Mokhles-Gerami, HEIG-VD, adeleh.mokhles-gerami@heig-vd.ch
Luca Tomasini, HEIG-VD, luca.tomasini@heig-vd.ch

SFOE project coordinator:
Dr Michael Moser, Michael.moser@bfe.ch

SFOE contract number: SI/502666-01

Table of contents

List of figures

List of tables

1 Introduction

The Dig-A-Plan project aims to develop and validate a risk-based tool for planning the reinforcement, replacement, and expansion of distribution grid assets under uncertainty, with particular attention to transformers and branches affected by the accelerating deployment of PV, EV charging, and heat pumps, as well as prosumer flexibility. Achieving this objective requires not only advanced planning and optimization methods, but also a reliable data foundation that reflects real network structures and operating conditions. Therefore, WP2 establishes the practical basis for the project by selecting representative case studies and preparing consistent grid datasets that can be used for scenario generation, operational feasibility checks, and long-term planning validation in subsequent work packages.

In this report, two deliverables of the Dig-A-Plan project are presented:

- D2.1: Multiple representative grids as case studies in addition to a synthesized grid
- D2.2: Reduced topological models of representative distribution grids

They together constitute the core process of WP2, data collection and characterization of case studies. D2.1 addresses the identification and characterization of multiple representative real-world distribution grids provided by the DSO partners, the grid of Estavayer-le-Lac of Groupe E and the grid of Boisy of Services Industriels de Lausanne (SiL). In addition, this deliverable addresses the specification of required datasets and the data acquisition, including network topology and equipment parameters, operating configurations and switching states, and available SCADA and/or smart-meter measurements. D2.2 describes the federation workflow used to harmonize heterogeneous DSO inputs into consistent, simulation- and optimization-ready grid models through a standardized CGMES-inspired data schema, dedicated data connectors, and data quality/completeness checks. In addition to the DSO case studies, controlled benchmarking and reproducibility are supported by including the IEEE 33-bus benchmark feeder as a standardized reference network. To ensure computational tractability for scenario-based simulations and iterative planning optimization in later work packages, reduced surrogate topological models are produced where required; notably, the Boisy grid is reduced from 1,004 nodes to 234 nodes while preserving key electrical and topological characteristics, enabling efficient power-flow studies and scalable validation of the Dig-A-Plan planning tool.

2 WP2 tasks

2.1 WP2 description

WP2 “Data collection and characterization of case studies” establishes the data backbone of Dig-A-Plan and ensures that subsequent work packages can be executed on consistent, simulation- and optimization-ready grid models. WP2 covers the full process from selecting representative DSO networks to transforming heterogeneous raw datasets into a unified and quality-checked grid representation suitable for stationary power-flow analysis, time-series scenario handling, and planning optimization.

WP2 consists of two tasks:

- Task 2.1: Specifying and collecting data for the targeted case studies.
- Task 2.2: Federating and aggregating the grid topological model, including network aggregation and model reduction to generate tractable surrogate topologies where required (e.g., Boisy).

WP2 provides the validated data foundation required for WPs 3-5. It includes the selection and characterization of two representative DSO case-study grids, i.e., Estavayer-le-Lac in Groupe E and Boisy in Services Industriels de Lausanne (SiL). In addition, the IEEE 33-bus benchmark feeder has been selected to support controlled benchmarking and reproducibility.

2.2 Tasks definition

This report summarizes the activities performed under Task 2.1 and Task 2.2. The corresponding sub-tasks and technical actions are detailed below.

Task 2.1: Specifying and collecting data for the targeted case studies

I. Selection of one representative distribution grid per DSO based on project requirements (urban/rural coverage, residential/commercial/industrial mix) and practical data availability.
II. Definition of the minimum dataset needed for downstream modelling and validation, including topology/connectivity, asset parameters (lines, transformers, switches), normal operating configurations (e.g., feeder structure and switching status), and available measurements (SCADA and/or smart meters).
III. Data acquisition under the corresponding NDAs and consolidation of the received inputs into a structured and documented dataset per case study.
IV. Initial screening of data readiness by documenting completeness, identifying missing elements, and recording assumptions required for later scenario generation and validation activities.
V. Preparation of a standardized reference dataset based on the IEEE 33-bus benchmark feeder to enable controlled testing and reproducibility alongside the DSO case studies.

Task 2.2: Federating and aggregating the grid topological model

I. Definition and implementation of a unified data representation to harmonize heterogeneous DSO inputs into a consistent grid model suitable for stationary power-flow studies and planning optimization.
II. Development of dedicated connectors to translate DSO-specific formats and populate the unified model with connectivity, equipment parameters, and measurement/time-series inputs where available.
III. Execution of consistency and quality checks (e.g., connectivity validation, parameter completeness) to ensure that the federated models are technically usable for simulation and optimization.
IV. Aggregation and export of simulation-ready grid representations to analysis tools (e.g., power-flow environments) and preparation of supporting visualization outputs where relevant.
V. Reduction of network complexity where required for computational tractability, by generating surrogate (reduced) topologies that preserve the key electrical and structural characteristics needed for WPs 3-5 studies (e.g., reduction applied for Boisy).

The next sections present the detailed contents of each task and their mapping to the deliverables 2.1 and D2.2.

3 Deliverable 2.1 - Multiple representative grids as case studies in addition to a synthesized grid

3.1. Objective and scope

Deliverable 2.1 documents the selection of representative distribution grids provided by the DSO partners and reports the status of data acquisition under NDA. For each case study, the grid is characterized according to project requirements (urban/rural coverage, consumer mix) and data readiness (availability of topology, asset registries, and measurements), providing the data baseline required for downstream analyses in WPs 3-5.

3.2. Case study 1 - Groupe E (Estavayer-le-Lac region)

The Estavayer-le-Lac case study represents a rural distribution grid supplied by a single HV transformation substation feeding eight feeders in a tree-based radial configuration under normal operating conditions with no redundancy/meshing enabled. One of the feeders supplies an industrial district, while the others cover an area of approximately 86 km² with about 688 km of power lines (140 km MV and 548 km LV). It supplies electricity to around 12'000 customers, who collectively own approximately 1'200 PV installations, 100 distributed storage units, 1'500 heat pumps, and 280 EV chargers. This sub-grid has a higher PV penetration compared to the national average.

The NDA with Groupe E was signed by the end of 2023. Data collection concluded by June 2024, and data pre-processing/federation has been completed; aggregated datasets are available for further work in WPs 3-5. The analysis results are reported in deliverables 3.1 and 3.2 regarding load and generation scenarios. The analysis results regarding the use of flexibility and transformer aging are reported in deliverables 4.1 and 4.2. Finally, the results regarding the expansion planning are reported in deliverables 5.1 and 5.2.

3.3. Case study 2 - Services Industriels de Lausanne (Boisy)

The Boisy case study represents a dense urban area located in the northwest neighborhood of Lausanne. The grid is supplied by two main MV feeders and it includes more than 20 MV/LV substations, serving a mixture of residential and commercial consumers. The smart-meter deployment is ongoing, and some metering data are available from 2023.

The NDA with SiL was signed by the end of April 2024, and data were collected in September 2024. HEIG-VD concluded data pre-processing and federation in July 2025. The resulting datasets are used in WPs 3-5 for scenario analysis and validation of the grid optimization tool.

3.4. Standardized benchmark - IEEE 33-bus feeder (reference dataset)

In addition to the real DSO case studies, the project includes the IEEE 33-node benchmark feeder [1] as a standardized reference network to support controlled testing, reproducibility, and regression checks of scenario generation and optimization workflows.

4 Deliverable 2.2 - Reduced topological models of representative distribution grids

4.1. Objective and scope

Deliverable 2.2 describes the federation workflow used to transform heterogeneous DSO datasets, including topology files, SCADA, smart meters, and other sources, into consistent, simulation- and optimization-ready grid models. Because each DSO provides data in a different format, a standardized data schema is implemented as a common foundation for harmonizing inputs and enabling consistent integration across case studies.

4.2. Unified data schema (CGMES-based) and project-specific extensions

The federation framework is built upon the Common Grid Model Exchange Specification (CGMES) developed by ENTSO-E [2], which supports the exchange of operational and planning data between transmission and distribution system operators and provides a comprehensive structure to represent grid equipment. Since CGMES includes features beyond the needs of Dig-A-Plan, the implemented schema focuses on the tables required for stationary power-flow analysis, capturing:

- Equipment and parameters (e.g., lines, transformers, switches),
- Electrical connections and network configurations,
- Both measured and estimated time-series data.

To satisfy the specific requirements of the Dig-A-Plan optimization model, the schema is extended beyond CGMES to support:

- Recording equipment installations and topology changes: By tracking these modifications, the schema can accurately reflect the evolving state of the electrical grid.
- Tracking discrepancies between planned and actual installations: This feature helps identify and address differences between the planned and realized grid configurations, ensuring that the grid model remains accurate and up to date.
- Recording evolution and time-series scenarios: This enables the modeling and analysis of various grid scenarios over time, allowing for more effective planning, forecasting, and decision-making based on evolving grid conditions.

For each case study, a dedicated connector is developed to interpret the DSO-specific data structure and populate the schema tables. A thorough understanding of each DSO's source data is required for reliable mapping. Where relevant, publicly available datasets (e.g., RegBL and rooftop solar data) can be used to verify assumptions and fill data gaps. A list of requested input data and public datasets used for pre-processing and enrichment of the dataset is available in the section of available datasets.

3.3 Federation results by case study

3.3.1 Estavayer region (Groupe E)

The Estavayer topological data are in good condition. Most of the grid's equipment is successfully connected with minimal data pre-processing (less than 2% of equipment remains disconnected from the main grid). The dataset includes parameterized line and transformer data as well as normal-operation switch statuses. Groupe E also provided a customer list including grid connection information and yearly consumption values (with an unspecified reference year). In addition, a list of special equipment and their electrical connections is available; however, because this information is based on owner-submitted forms, it may not be exhaustive.

A key limitation is the missing link between customers/equipment and buildings represented by EGID numbers[1]. Since building data is essential for accurately estimating and predicting power consumption profiles, cross validating our assumptions has been challenging. Additionally, many large consumers connected to the industrial feeder, which are part of the open energy market; do not appear in the customer list provided.

Although smart-meter time-series data are not yet available, one year of power profiles is available for each MV feeder connected to the HV post. Consequently, we focus on MV- and LV-level power disaggregation to generate the required scenarios.

Yearly aggregated consumption per feeder is computed from SCADA time-series data and conventional customer metering. Discrepancies are observed; in some cases, the mismatch exceeds **50%**, likely due to differences in measurement dates and missing data in the conventional metering system (Table 1). To handle this case, we correct the conventional customer metering data with data coming from SCADA system and the rated power of the respected customer.

The processed data populates the schema successfully. A connector exporting the federated data to `Pandapower` for power-flow analysis is implemented, and a QGIS-based geo-visualization is developed to display processed data and preliminary power-flow results (Figure 1).

[1] https://www.bfs.admin.ch/bfs/fr/home/registres/registre-personnes/harmonisation-registres/egid-ewid.html.

Table 1: Load data of Estavayer Region

feeder name	Conventional meter [GWh]	SCADA measurement [GWh]	Error [%]
Name 1	2.78	1.69	64
Name 2	19.54	14.8	32
Name 3	4.99	3.07	63
Name 4	-		
Name 5	12.23	13.81	11
Name 6	16.19	16.44	2
Name 7	11.13	10.29	8
Name 8	18.37	16.67	10
Total	85.23	110.73	23

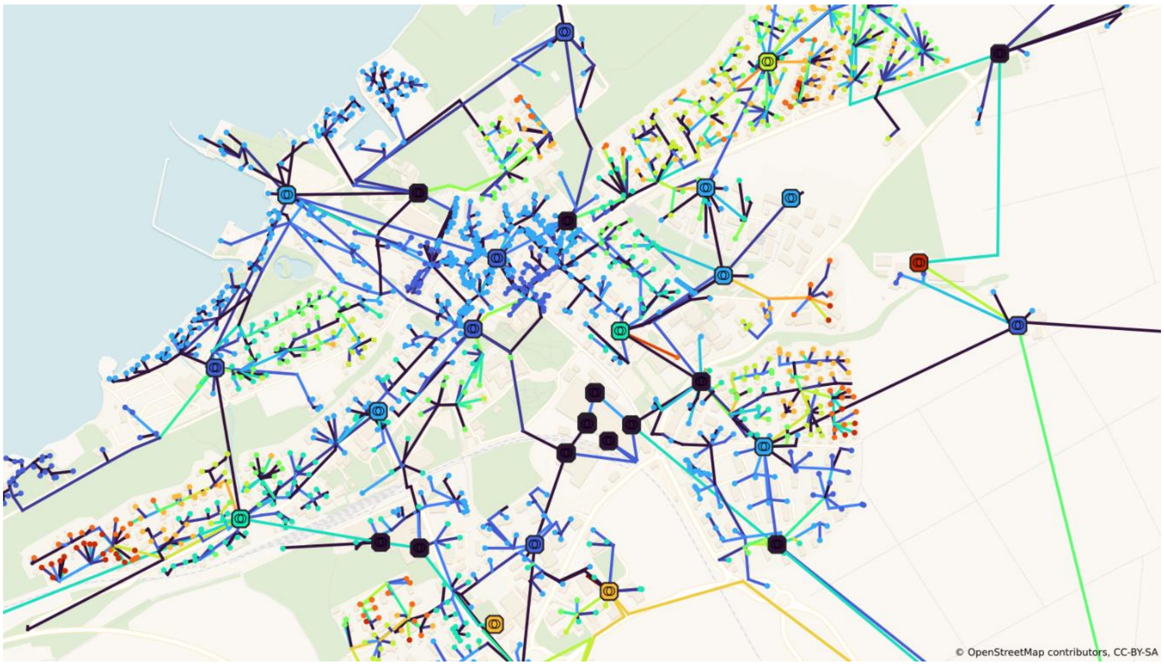

Figure 1: Visualization platform demonstrating power flow analysis in part of Estavayer region

3.3.2 Boisy region (SiL)

The Boisy distribution grid, provided by SiL, represents a dense urban area in the northwest neighborhood of Lausanne. The grid is supplied by two main MV feeders and it includes multiple MV/LV substations serving a mixture of residential and commercial consumers.

The network consists of 1’004 nodes, 740 lines, 281 switches, 31 transformers, and 447 loads. The grid includes 17 PV installations with total nominal PV capacity of 0.716 MW, while the total nominal load reaches 4.746 MW. Due to its compact urban topology and the ongoing smart-meter deployment, Boisy grid is a suitable case study for testing grid reconfiguration and flexibility management under realistic operating conditions. The collected data includes network topology, equipment parameters, and aggregated load information from SCADA and metering systems. A representative overview is shown in Figure 2, illustrating the dense LV network, transformer distribution, and the geographical layout of connected PV installations.

The detailed time-series data, the topological and static datasets have been successfully integrated into the unified data schema developed in WP2, enabling power-flow simulations and preliminary scenario analyses in WPs 3-5.

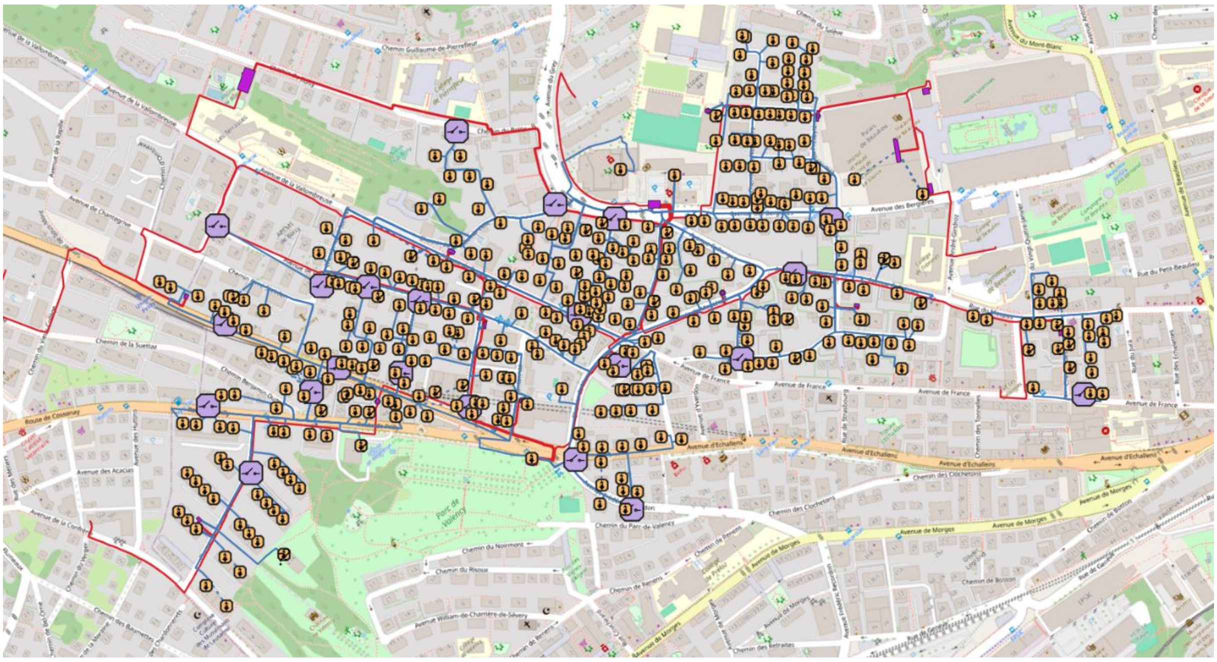

Figure 2: Overview of the Boisy distribution grid (SiL)

3.3.3 Reducing the Boisy grid topological model

Because the original Boisy network model is highly detailed, it can lead to excessive computational complexity for optimization and time-series simulations. Therefore, a network simplification procedure is implemented to reduce model size while preserving key electrical and topological characteristics required for mid- and long-term planning.

The simplification process (Figure 3) includes:

- Aggregation of series/parallel switches,
- Substation simplification (replacing multi-bus/ring secondary substations by equivalent single-node representations),
- LV grid clustering behind MV/LV substations into aggregated nodes, and
- Aggregation of homogeneous series line segments into equivalent lines.

After simplification, the Boisy model is reduced to 234 nodes, 160 lines, 90 switches, 19 transformers, and 158 loads, while maintaining the total nominal load (4.746 MW) and PV capacity (0.716 MW). The simplified surrogate preserves main feeders, substation locations, and load centers, enabling computationally efficient power-flow analysis, reconfiguration studies, and expansion planning.

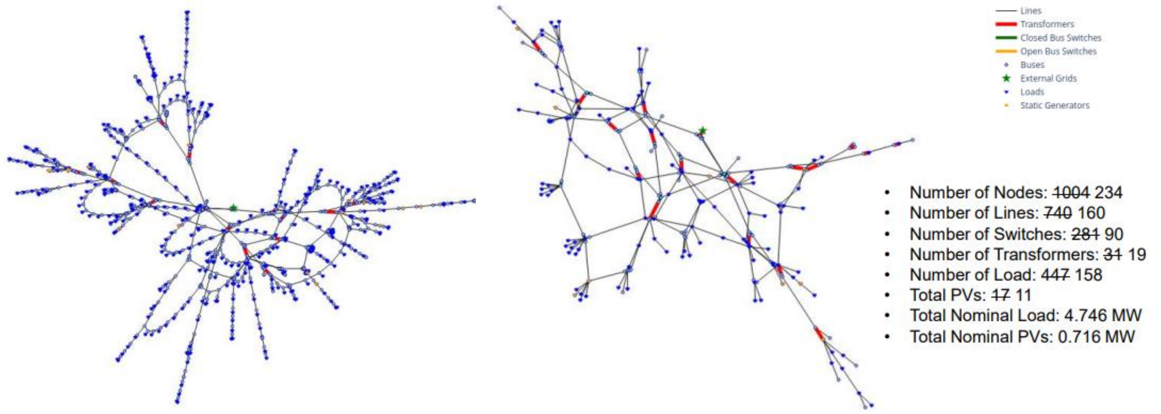

Figure 3: Real MV/LV network from Boisy (left: 1004 nodes) and its simplified surrogate (right: 234 nodes)

5 Available Datasets

7.1 Input Data Format

The following tables describe all the data required for the modelling energy demands, grid model, and measurement data (if available).

7.1.1 Energy Demand Model

Name of input data	List of required parameters	Extracted data formats	Notes
Buildings	. Option 1: Address . Option 2: EGID (better)		EGID (identification number for each building in CH)
PVs	. PV name . Node name . Installed capacity (kW)	. Export from GIS or Simulation software . CSV transformed from the previous export (example pvParameters.csv)	Otherwise we need to go via Pronovo which will hopefully not take too much time
EV charging stations	. Installed power (kW) - charging profiles (smart, uncontrolled and/or realistic) . Installed capacity (kWh)		If known to DSO
Stationary battery	. Installed power (kW) . Installed capacity (kWh)		If known to DSO
Heating	. Type: heat pump, district, oil, gas, electric resistance heating . Size of installed heat pump (kW)		These info are included in the Federal Building Register but they are not always reliable; it would be better to receive them from the utility
Typical load profile (as total and if possible, additionally for * residential sector * services * industry (the latter two may also be combined)	. Category (summer, winter, weekday, weekend) . Timestamp . Active power (kW) . Reactive power		

7.1.2. Grid Model

Following information are available in GIS or power system simulation software (cyme, Digsilent, Neplan).

Name of input data	List of required parameters	Extracted data formats	Notes
node geographical location	. Node name . Latitude . longitude	i. GIS export ii. CSV transformed from GIS export (example nodeGeo.csv)	
line parameters	. Line name . Node from name . Node to name <u>option 1</u> . Length (km) . Cross section (mm2) . Type <u>option 2</u> . Length (km) . Nominal current (A) . R (ohm/km) . X (ohm/km) . B (Siemens/km) . G (Siemens /km) <u>Optional</u> . branch geo path (latitude and longitude)	i. export from GIS or Simulation software ii. CSV transformed from the previous export (example lineParameters.csv)	
transformer parameters	. Transformer name . Node from name . Node to name . Nominal power (kVA) . Vector group . Impedance voltage (%) . short circuit losses (kW) . no load losses (kW) . no load current (A) . r (ohm) . x (ohm) . b (ohm) . g (ohm) . MV tap ranges (5 values of Line-Line voltages) . LV tap ranges (1 value of Line-Line voltage)	i. export from GIS or Simulation software ii. CSV transformed from the previous export (example transformerParameters.csv)	The data can be collected from the nameplates or typical data based on transformers rated power.
Switch parameters	. Switch name . Node name . Line/transformer name . Switch type (breaker, sectionalizer, manual switch, and fuse) . normally open (True/False)	. Export from GIS or SCADA . CSV transformed from the previous export (example switchParameters.csv)	

7.1.3. Measurement Data

Name of input data	List of required parameters	Extracted data formats	Notes
Position of grid monitoring devices	. Monitoring device name . Node name . feeder name	. Export from GIS or Platform of monitoring device . CSV transformed from the previous export (example locationGridMonitoring.csv)	
Time-series of grid measurement data	. Timestamp . Voltage (V) . Current (A) . Active power (kW) . Reactive power (kVAR)	CSV files exported from monitoring platform . PMU platform . PQ analyzers (example timeseriesGridMonitoring.csv)	
Transformers	. Timestamp . Temperature		Historical data related to transformers

7.2. Open Source Datasets

Avichal Malhotra, Julian Bischof, James Allan, James O'Donnell, Thomas Schweiger, Joachim Benner, Gerald Schweiger (2020). A Review of country specific data availability and acquisition techniques

For city quarter information modelling for building energy analysis. In proceedings of the eighth German Austrian IBPSA Conference BauSIM 2020: September 23 - September 25th / Publisher TU Graz.

https://ibpsa.github.io/project1-wp-2-1-cim-gis/Switzerland.html.

CATEGORY	SOURCE	WEB-SOURCE	AVAILABILITY	COVERAGE	RESOLUTION	INCLUDES NON-RESIDENTIAL	COMMENT (RESOLUTION, QUALITY...)
	Open Street Map (OSM)	Ht tp://download.geofabrik.de/europe/switzerland.html	Open	National	Building level	Yes	NaN
BUILDING FOOTPRINTS	swissBUILDINGS3D 1.0	https://shop.swisstopo.admin.ch/en/products/landscape/build3D	Commercial/Academic	National	Building level	Yes	Multiple formats available
BUILDING HEIGHT	swissBUILDINGS3D 1.0	https://shop.swisstopo.admin.ch/en/products/landscape/build3D	Commercial/Academic	National	Building level	Yes	Multiple formats available
3D BUILDING MODEL	swissBUILDINGS3D 2.0	https://shop.swisstopo.admin.ch/en/products/landscape/build3D2	Commercial/Academic	National	Building level (LoD 2)	Yes	Multiple formats available
DIGITAL ELEVATION MODEL	SwissSurface3D	https://shop.swisstopo.admin.ch/en/products/height_models/surface3d	Commercial/Academic	National	15/20 pts/m2	NaN	
BUILT FORM	GEAK	https://www.geak.ch/Pages/GEAK/System/InformationPage.aspx	Commercial	~60,000 dwellings	Building level	No	Survey data for energy certification of residential buildings
THERMAL ENVELOPE	GEAK	https://www.geak.ch/Pages/GEAK/System/InformationPage.aspx	Commercial	~60,000 dwellings	Building level	No	Survey data for energy certification of residential buildings
BUILDING AGE	Federal Register of Buildings and Housing (GWR) – Gebaude	https://www.bfs.admin.ch/bfs/de/home/register/gebaeude-wohnungsregister.html	Governmental/Academic restrictions apply	National	Building level	No	Buildings records are listed by their unique identification EGID. 13 Age categories between 1919 and 2015. 10

							of which are after 1960.
BUILDING USE	Federal Register of Buildings and Housing (GWR) – Gebaude	https://www.bfs.admin.ch/bfs/de/home/register/gebaeude-wohnungsregister.html	Governmental/Academic restrictions apply	National	Building level	No	Residential buildings are categorized as Single Family Home, Multi Family Home, and Residential Building with Side Usage and Building with partially residential usage.
BUILDING USE	STATENT	https://www.bfs.admin.ch/bfs/de/home/statistiken/industrie-dienstleistungen/erhebungen/statent.html	Governmental/Academic restrictions apply	National	Building level	Yes	Provides information on the structure of the Swiss Economy. Provides information on the number of people working, full time and total. Contains the coordinates of the building location and the business sector associated with the building
OCCUPANT COMPOSITION	Federal Register of Buildings and Housing (GWR) – Wohnung	https://www.bfs.admin.ch/bfs/de/home/statistiken/bau-wohnungswesen/erhebungen/gws2009.html https://www.housing-stat.ch	Governmental/Academic restrictions apply	National	Building level	No	This data can be linked to the Gebaude (Building) data through the EGID identified. The dataset contains a household composition variable.
TENURE	No source identified	No source identified	No source identified	No source identified	No source identified	No source identified	No source identified
BUILDING ENERGY SYSTEM	GEAK	https://www.geak.ch/Pages/GEAK/System/InformationPage.aspx	Commercial	~60,000 dwellings	Building level	No	Survey data for energy certification of residential buildings
BUILDING ENERGY SYSTEM	Federal Register of Buildings and Housing (GWR) – Gebaude	https://www.bfs.admin.ch/bfs/de/home/register/gebaeude-wohnungsregister.html	Governmental/Academic restrictions apply	National	Building level	No	Information is provided on the heating system, with 7 categories including space heating. The presence of hot water is also recorded, but there are no details on the system. The energy carrier/fuel for heating is also specified.
ADDRESS DATA	Register of Buildings and Dwellings	https://map.geo.admin.ch	Open – usage restrictions apply	National	Building level	Yes	Register of Buildings and Dwellings can be downloaded as a .csv for each canton individually. It contains records for each building in the canton, providing the unique EGID number and the address. Easting and Northing coords are provided using CH1903+/LV95 projection

BUILDING TYPOLOGY	Community typology ARE	https://opendata.swiss/de/dataset/gemeindetypologie-are	Open	NaN	NaN	No	A shape file which contains the urban typology of the buildings contained within. e.g. Large Urban, Secondary Urban Centers, Rural, Tourist etc.
STOCK DEVELOPMENT	No source identified	No source identified	No source identified	No source identified	No source identified	No source identified	No source identified
ENERGY GENERATION AND DISTRIBUTION	No source identified	No source identified	No source identified	No source identified	No source identified	No source identified	No source identified
WEATHER DATA	Climate One Building	http://climate.onebuilding.org/WMO_Region_6_Europe/CHE_Switzerland/	Open	National	NaN	NaN	Contains weather files in formats specifically for building energy simulation.

6 Conclusion

In this report, WP2 activities of the Dig-A-Plan project are presented through Deliverables 2.1 and 2.2, which together establish the data foundation required for scenario generation, simulation, and optimization in subsequent work packages. In D2.1, two representative real-world distribution grids provided by the DSO partners, Groupe E (Estavayer-le-Lac) and Services Industriels de Lausanne (Boisy), are identified and characterized. In addition, the specification of required datasets and the status of data acquisition under NDAs are documented. Finally, the IEEE 33-node benchmark feeder is included as a standardized reference network to support controlled benchmarking and reproducibility alongside the real DSO case studies.

In D2.2, a federation workflow is developed to harmonize heterogeneous DSO inputs (topology, asset registries, SCADA, and smart-meter data) into consistent, simulation- and optimization-ready grid models. This workflow relies on a CGMES-based data schema tailored to stationary power-flow analysis and extended to support optimization-oriented requirements such as tracking topology evolution, recording installation changes, and handling time-series scenarios. Dedicated connectors are implemented for each case study to populate the schema tables, while quality and completeness checks are performed to identify practical limitations affecting load attribution and profile estimation, e.g., missing customer-to-building linkage, incomplete visibility of large consumers, and limited metering availability.

To ensure computational tractability for scenario-based simulations and iterative planning optimization, reduced surrogate topological models are generated where required while preserving key electrical and topological characteristics. In particular, the Boisy network is reduced from 1’004 nodes to 234 nodes while maintaining the nominal load and installed PV capacity, enabling efficient power-flow studies and scalable validation of the Dig-A-Plan planning tool. Overall, the outcomes of D2.1 and D2.2 provide a validated and harmonized data backbone that supports the analyses and tool validation activities planned in WPs 3-5.

7 References

[1] S. Dolatabadi, et al. "An enhanced IEEE 33 bus benchmark test system for distribution system studies." IEEE Transactions on Power Systems 36, no. 3 (2020): 2565-2572.

[2] Common Grid Model Exchange Standard (CGMES) Library. (n.d.). https://www.entsoe.eu/data/cim/cim-for-grid-models-exchange/.

Schweizerische Eidgenossenschaft
Confédération suisse
Confederazione Svizzera
Confederaziun svizra

Federal Department of the Environment,
Transport, Energy and Communications DETEC

Swiss Federal Office of Energy
Energy Research and Cleantech

Final report 30 April 2026

Dig-A-Plan

Appendix 3: Expected asset distribution, flexibility amount, and expected transformer loss of life

D3.1 A set of possible scenarios for load growth and possible technology integration

D3.2 Results of the extended GRIMSEL-FLEX model (including the differences in implementation levels for storage and PV systems) for all scenarios

---

Publisher:
Swiss Federal Office of Energy SFOE
Energy Research and Cleantech
CH-3003 Berne
www.energy-research.ch

Co-financing: In-kind contributions provided by
Groupe e, 1763 Granges-Paccot

Services Industriels Lausanne (SiL), 1003 Lausanne

Yverdon Energies, 1400 Yverdon

Subsidy recipients:
Haute École d'Ingénierie et de Gestion du Canton de Vaud (HEIG-VD), Institute of Energies (IE)
1400 Yverdon-les-Bains
https://heig-vd.ch/recherche/instituts/ie/

Université de Genève (UNIGE), Institute for Environnemental Sciences (ISE)
1205 Genève
https://www.unige.ch/energy/

EPFL, photovoltaic research laboratory (PV-LAB)
2002 Neuchâtel
https://www.epfl.ch/labs/pvlab/

Authors:

Arbogast Nyandwi, UNIGE, Arbogast.Nyandwi@unige.ch
Martin Patel, UNIGE, Martin.Patel@unige.ch

SFOE project coordinator:
Dr Michael Moser, Michael.moser@bfe.ch

SFOE contract number: SI/502666-01

Table of contents

List of figures

List of tables

1 Introduction

The deliverables D3.1 and D.3.2 consist of a high-resolution bottom-up modelling framework to represent electricity consumption and production in the distribution grid of Estavayer-le-Lac and Boisy, based on hourly electricity demand and PV production profiles from 2022 to 2050 in five-year steps. The methodology differentiates residential (SFH, MFH) and non-residential (service and industrial) building archetypes across rural and urban contexts, integrating space heating, domestic hot water, electric vehicles, and appliances and processes using detailed building registry data, archetype-based heat demand models, mobility survey-based EV charging profiles, and feeder-level measurements. Heat demand is converted into electricity through temperature-dependent load curves and performance-based COP modelling, while EV demand reflects both uncontrolled and controlled charging strategies. Rooftop PV production is estimated from installed capacity and geospatial solar potential datasets, enabling assessment of both current generation and maximum deployment scenarios. Results show that electrification of heating and transport significantly increases seasonal and peak loads particularly in winter while appliance demand declines due to efficiency gains; high PV penetration partly offsets demand growth, especially in rural areas with greater rooftop availability. Scenario analyses further highlight the substantial uncertainty associated with EV diffusion, charging behavior, building retrofits, and future consumption patterns, underscoring the importance of flexibility measures and uncertainty-aware planning for resilient distribution grid development.

Work Package 3 builds upon the foundations established in previous work packages by developing detailed demand and generation modelling for selected case study areas. WP3 provides the methodological framework and datasets required to represent electricity consumption and production at high spatial and temporal resolution. The core outputs of this work package include the development of bottom-up electricity demand models for residential and non-residential buildings, electrified heating systems, and electric vehicles, as well as rooftop photovoltaic (PV) generation modelling. These components are integrated into a unified hourly simulation framework covering the period 2022–2050. The modelling approach relies on established building archetype methods, mobility data, and geospatial PV potential assessments, enabling consistent scenario analysis and supporting distribution grid planning at the local (municipal and feeder) scale.

2 WP3 tasks

2.1 WP3 description

WP3 develops an ‘integrated modeling environment for the estimation of load configuration scenarios and provided flexibility’. The modelling environment enables the estimation of hourly electricity demand and production profiles for the period 2022–2050, considering the progressive electrification of heating, mobility, and distributed renewable generation. The distribution grids of Estavayer-le-Lac and Boisy are analyzed, which serve as representative case studies for rural and urban grid configurations respectively.

The modelling framework integrates several key components:

- Consumer and producer characterization within the distribution grid.
- Hourly electricity demands modelling for residential and non-residential sectors.
- Technology diffusion scenarios, including electric vehicles (EVs), heat pumps (HPs), and photovoltaic (PV) systems.
- Future electricity demands up to 2050 with a five-year temporal resolution.
- Flexibility considerations, particularly related to EV charging behavior and tariff design.

The outputs of this work contribute to the development of the extended modelling environment used for evaluating grid flexibility and tariff configurations. Deliverable 3.1 presents the scenario framework for load growth and technology integration, while D3.2 provides the results obtained from the extended modelling framework.

3 Combined Deliverable 3.1 and 3.2 Scenario analysis for electricity load growth as input for assessing grid impacts

3.1 Deliverable content

This document combines the results of Deliverables D3.1 and D3.2 into a single comprehensive report describing the development of load growth scenarios and the modelling results derived from these scenarios.

The deliverable provides:

- a description of the modelling used to estimate electricity demand profiles,
- the data sources and modelling assumptions used to characterize consumer and producer behavior,
- the scenario design for future electricity demand evolution, and
- the results obtained for the case study distribution grids.

The modelling framework integrates several sectoral models for estimating electricity demand associated with space heating, domestic hot water (DHW), electrical appliances and processes, electric vehicles, and photovoltaic generation. These modules are documented in the following sections.

3.2 Consumer and Producer types in the distribution grid

The work outlines a methodology for the estimation of hourly electricity consumption profiles pertaining to both current (2022) and prospective demand (2050) scenarios in 5-years steps. The hourly model represents the short, medium and long-term electricity consumption within the residential and non-residential sectors, encompassing the demand associated with electric appliances and processes (including lighting), Electrical vehicles (EV), alongside the electricity requirements for space heating (SH) and the provision of domestic hot water (DHW) for households (single and multi-family houses, i.e. SFH, MFH), as well as services (Offices and Commercial sector, OCO), and industrial and agricultural (IND) sector operations. The methodology is articulated in a generalized manner; however, it is grounded in the available datasets specific to Estavayer-le-Lac and Boisy considering the following elements:

- Differences between residential (i.e. SFH, MFH) and non-residential (NR) building typologies, rural, urban and sub-urban settings, building construction periods and building type per each service sub-sectors.
- Shares of buildings using electricity for space heating and domestic hot water (heat pumps and electric resistance heating) and energy conversion efficiencies.

The distribution of energy demand is determined per building archetypes (SFH, MFH, OCO and IND), allowing to map it to statistical data at any spatial resolution. By aggregating the energy demand of various users in each geographical scope, the aggregated total energy demand is established. The method is applied to estimate the current electricity demand of DSO case studies and is validated against hourly feeder demand data from DSOs.

3.3 Climate Data

The model's climate data consists of hourly outdoor temperature and solar irradiation data used to derive temperature-dependent heat demand and photovoltaic (PV) generation profiles for Estavayer-le-Lac and Boisy. For the reference year 2022, observed hourly weather data were applied to construct heating load curves and to distribute PV production over the year. For future projections, climate assumptions follow the MeteoSwiss design reference years in line with the Swiss CH2018 climate scenarios. These datasets provide hourly meteorological variables and are commonly used for building energy simulations in accordance with SIA 2028 [1], which are also consistent with the Energy Perspectives 2050+ framework [2]. Specifically, for 2035–2040, hourly data based on the RCP 8.5-2035 scenario were used, and for

2045–2050, the RCP 8.5-2060 reference year was applied [1]. These datasets ensure methodological consistency in assessing the evolution of space heating demand and seasonal PV generation under future climatic conditions within WP3. The RCP 8.5 scenario was selected to capture a high-emission, upper-bound climate pathway, allowing the analysis to account for stronger temperature increases and extreme conditions that could affect heat demand and PV generation. This approach aligns with European studies and projects, such as the EU JRC PESETA on climate impact assessments [3] and EURO-CORDEX regional climate projections, which recommend RCP 8.5 for stress-testing energy [1], [2].

3.4 Building Data

Building characteristics constitute a key input for estimating both heat demand and electricity consumption associated with heating systems. The primary source of building data used in this study is the Swiss Federal Register of Buildings and Dwellings (FRBD) [4]. This national database categorizes and describes more than two million buildings across Switzerland and provides detailed information on building characteristics relevant for energy demand modelling. The FRBD datasets include variables such as building type, construction period, number of floors, and heating system type. These attributes are used to characterize building archetypes and to estimate the Energy Reference Area (ERA) as well as the associated annual heat demand for each building.

Using these datasets, the annual heat demand per building is calculated following the methodology developed within the project Future Energy Efficient Buildings & Districts (FEEBD) [5]. This approach maps building characteristics such as building typology, age, and urban context to archetype-based heat demand values expressed in kWh/m² per year. Within the modelling framework, residential and non-residential buildings are categorized into several archetypes, including single-family houses (SFH), multi-family houses (MFH), offices and commercial buildings (OCO), and industrial buildings (IND). These archetypes allow the aggregation of heat demand and electricity consumption at different spatial scales within the studied distribution grids.

For future scenarios, the decarbonization of heating systems in the residential building sector is assumed to occur primarily through the deployment of heat pumps (HPs), which progressively replace conventional heating technologies. This assumption aligns with national decarbonization pathways and enables the estimation of future electricity demand associated with building heating.

3.4.1 Building and space heating demand modeling

To model heat supply and demand, we use data based on national building and housing database of Switzerland, FRBD [4]. The classification of urban settings (urban, suburban, and rural) is based on [8], the entire area of Estavayer-le-Lac was found to be categorized as rural; Boisy is classified as urban area. FRBD datasets such as building type, building age, number of floors, heating type etc. are used to calculate the annual heat demand per building using the approach developed in the project 'Future Energy Efficient Buildings & Districts (FEEBD) [5]. Future decarbonized heating across residential building types is assumed to be ensured by heat-pumps (HPs). Heat demand profiles (hourly) are estimated based on annual heat demand, the heating curve (linearized) and the heated floor area (Energy Reference Area (ERA) which is estimated using a regression function [6] based on building footprint, number of floors, and building type (SFH, MFH, OCO, IND) from the Swiss building registry (RegBL) [4].). Hourly heat demand is converted to electricity profiles by means of the Coefficient of Performance (COP), which is estimated based on Carnot efficiency and a thermodynamic efficiency of 44% [7], reflecting actual system performance. (see below for more details).

3.4.2 Electrical Vehicle modelling

To calculate hourly energy demand [kWh] of electrical vehicles, we multiply a typical-day charging profiles for uncontrolled and controlled charging by the daily driving frequency to account for the fact that not all cars are driven daily and the number of EVs for 2022 and 2050. The charging energy per EV is derived from the average travel distance and a consumption rate of 0.2 kWh/km, adjusted for 90% charger efficiency, with charger shares of 68% (7 kW), 30% (11 kW), and 2% (22 kW) used to determine charging duration. Weekly hourly demand profiles are then produced by combining individual energy needs with normalized load curves and distributing the demand across communes[1] [8], [9], based on the number of cars and households.

3.4.3 Electrical appliances and processes Modelling

To model the appliance and processes profiles, we first developed their normalized profiles. Normalized electrical appliance load curves are derived by selecting representative feeders for each sector (residential, service, and industrial) where PV generation is already included. For residential buildings, a feeder with 93% residential load is used, from which heating and EV demand are subtracted to isolate the appliance load; this is then divided by the number of households and normalized to obtain a standardized household profile. To model load curves for the service (OCO) and industrial (IND) sectors, feeders dominated by these sectors are selected, and EV demand, heating demand, and previously calculated household loads are removed to isolate sector-specific demand before normalization. Finally, the 2022 hourly energy demand (kWh) for appliances and processes in Estavayer-le-Lac and Boisy is calculated by multiplying annual energy consumption per building archetype (from smart meters) by the corresponding normalized load curve, after which PV production is added to convert feeder-level net curves into gross demand profiles.

3.5 Possible Scenarios for Load Growth and Technology Integration

The scenarios are based on the ZERO Basis projections published in the Energy Perspectives 2050+ [2]. It is hence assumed that the future development in Estavayer-le-Lac and Boisy will be aligned to the expected evolution of population, households and residential floor area (ERA/HH) at the national level see Table A.2. As an exception, we assume the full electrification of all passenger cars in 2050 while the Energy Perspectives 2050+ assume a share of 69.1% in 2050. We made this assumption to avoid underestimation of electricity demand. To calculate the electricity demand of EVs, we assume 16,060 km/year based on Swiss National household travel survey (NHTS) [10].

3.5.1 Heating Scenario

The heating demand scenario is projected based on national data using [4]. The final energy in Estavayer-le-Lac, as shown in Figure 8, is calculated based on the shares of the various energy carriers according to Energy Perspectives 2050+ [2]. Driven by population growth and socio-economic change, the number of apartments and living space will continue to rise throughout the scenario period (see Table A.2). While this would increase the demand for space heating, improved thermal performance (insulation) and of the diffusion of heat pumps (which are much more efficient than other heating systems) results in a decrease of final energy demand.For 2050, we assumed full electrification of all space heat and DHW heating systems, while retrofitting of the envelope of existing buildings and the construction of new highly efficient buildings are expected to result in a heating demand reduction rate of 1.35% per year between 2022 and 2050 (based on [2]). Heat supply temperatures are assumed to be 35°C for floor heating (post-1990 buildings), 55°C for radiators (pre-1990 buildings), and 60°C for hot water. According to the ZERO Basis scenario [2], average supply temperatures are expected to decrease to 30°C for new buildings and about 45°C for older buildings by 2050. Annual COP improvements are based on projections from the Energy Perspectives 2050+ (see Table 2) (heat pumps for industrial processes have not been considered).

3.5.2 The Electrical appliances and processes Scenario

The projections for electrical appliances and processes are based on the ZERO Basis scenario outlined in the Energy Perspective 2050+, as shown in Figure 9. By 2050, the annual energy demand is expected to decrease to 70.4 and 12.9 GWh per annum in Estavayer-le-Lac and Boisy respectively, with an assumed yearly reduction rate of 0.67% (see Table 1). This decline is driven by a combination of

[1] The study area for the Estavayer-le-Lac region comprises the municipality of Estavayer together with fourteen neighbouring communes. The Boisy study area comprises two communes.

technological advancements, regulatory changes, shifts in consumer behaviour, and the integration of smart technologies, all aimed at enhancing energy efficiency and sustainability.

3.5.3 Transport Outlook of Switzerland: Basis, SuS and Full Electrification Scenario

Figure 6 shows three scenarios considered, two of which (Basis and SuS) are based on the Transport Outlook of Switzerland [11]. The Basis scenario foresees that the development of transport sector will be business-as-usual, while for SuS, sustainable policies are assumed to be promoted (i.e., promoting EVs and other modes of transportation such as local transportation or bikes). For the third scenario named Full electrification, we assume that all passenger cars are electric by 2050. According to the Basis, SuS and full electrification scenarios, 38% (5800 cars), 74% (9900 cars) and 100% (15000 cars) of all passenger cars in Estavayer-le-Lac will be electric by 2050 respectively. For Boisy, the corresponding shares are 38% (510 cars), 74% (870 cars) and 100% (1300 cars) of all passenger cars. The numbers of EVs in intermediate years are determined by linear interpolation between the current and future number of cars by 2050.

3.5.4 Baseline Scenario (ZERO Basis): High PV Penetration Scenario: Maximum rooftop PV utilization

In Switzerland, PV installations are so far limited to rooftops, and this is expected to remain the case in the future [12]. The assessment of rooftop suitability and solar potential is based on the SwissTopo geospatial dataset, which provide detailed information on roof orientation, inclination, shading, and available surface area for all buildings in Switzerland. Using this dataset, hourly PV generation profiles are derived by distributing annual PV potential over the irradiance patterns observed in 2022. To estimate the future potential for PV deployment in Estavayer-le-Lac and Boisy, we use the open data developed by A. Walch[12], providing detailed information on the solar potential of each building rooftop in Switzerland. This includes parameters such as solar radiation exposure, rooftop area, orientation, inclination, and shading. A. Walch calculated these values based on data from SwissTopo [13]. Considering the current performance of PV systems (285W per 1.6 m²), a percentage of 70% [14] is assumed as effectively available roof area resulting in a total estimated maximum PV electricity potential in Estavayer-le-Lac and Boisy of 212.3 and 21.6 GWh per year respectively. This allows the modelling of temporal generation patterns at the building level, which can be aggregated to the feeder or network level. The scenario evaluates the impact of maximum PV deployment on net electricity demand, and the temporal alignment of generation with residential, commercial, and industrial loads. The results highlight the significant contribution of rooftop PV to local energy supply, particularly in areas with high single-family housing density, and its potential to partially offset future electricity demand growth driven by electrification of heating and transport.

3.5.6 Flexibility-Oriented Scenarios

1) High Flexibility Scenario: High adoption of controlled EV charging for 2050

In the flexibility-oriented scenario, controlled electric vehicle (EV) charging is implemented for the year 2050 to evaluate the impact of demand-side flexibility under high electrification conditions. Unlike the baseline case, which assumes uncontrolled and user-driven charging behaviour, the 2050 scenario assumes that charging is actively managed through smart charging strategies. The controlled load profiles are based on the methodology developed by Syla et al. [15], [16], which uses Swiss mobility survey data from the Swiss Micro census [17], [18], which allows to statistically track the mobility patterns of the Swiss population to ensure realistic driving behaviour while shifting charging demand within available time windows. Controlled charging does not reduce total electricity consumption but redistributes it to reduce simultaneity and peak demand. The results show a significant smoothing of daily load curves and a marked reduction in evening peak loads, leading to lower transformer loading and improved utilization of existing grid infrastructure. This demonstrates that flexibility measures will be essential for integrating large-scale EV adoption in a cost-effective and grid-friendly manner by 2050.

2) Low Flexibility Scenario: Predominantly uncontrolled charging (across scenarios until 2045)

In the low flexibility scenario, electric vehicle (EV) charging is assumed to remain predominantly uncontrolled across all projection years up to 2045. Charging behavior follows user-driven patterns, with vehicles typically being charged immediately upon arrival at home, resulting in high simultaneity during evening hours. The uncontrolled charging profiles applied in this analysis are based on the modelling framework developed by Syla et al. [15], [16], which uses Swiss mobility survey data from the Swiss Micro census [17], [18] to generate statistically representative charging patterns without temporal optimization. Under this configuration, increasing EV diffusion leads to a pronounced amplification of evening peak loads and higher transformer loading levels. Because no active load shifting is implemented, simultaneity effects become more significant as electrification progresses, particularly in residential areas with high EV penetration. This scenario therefore provides a conservative reference case, illustrating the potential grid stress and reinforcement needs associated with delayed adoption of flexibility measures.

4 Tariffs Configurations

The modelling framework developed in WP3 provides the basis for evaluating tariff configurations that can encourage demand flexibility and efficient grid operation.

We made inventory of different tariffs structures from literature; these structures may influence consumer behavior by incentivizing:

- load shifting
- controlled EV charging
- self-consumption of photovoltaic generation
- participation in demand response mechanisms

The load scenarios and demand profiles and tariffs structures generated in this deliverable serve as input datasets for WP4. See Table A.3 for selected Electricity Tariffs (proposal).

5 Results for the Case studies

5.1 Hourly electrical profiles

In 2022, the shares of annual electricity demand in Estavayer-le-Lac were approximately 74% for appliances and processes, 24% for heat pumps (HP), and 3% for electric vehicles (EVs), whereas in Boisy the shares were approximately 90% for appliances and processes, 9% for HP, and 1% for EVs (see Figure 1).

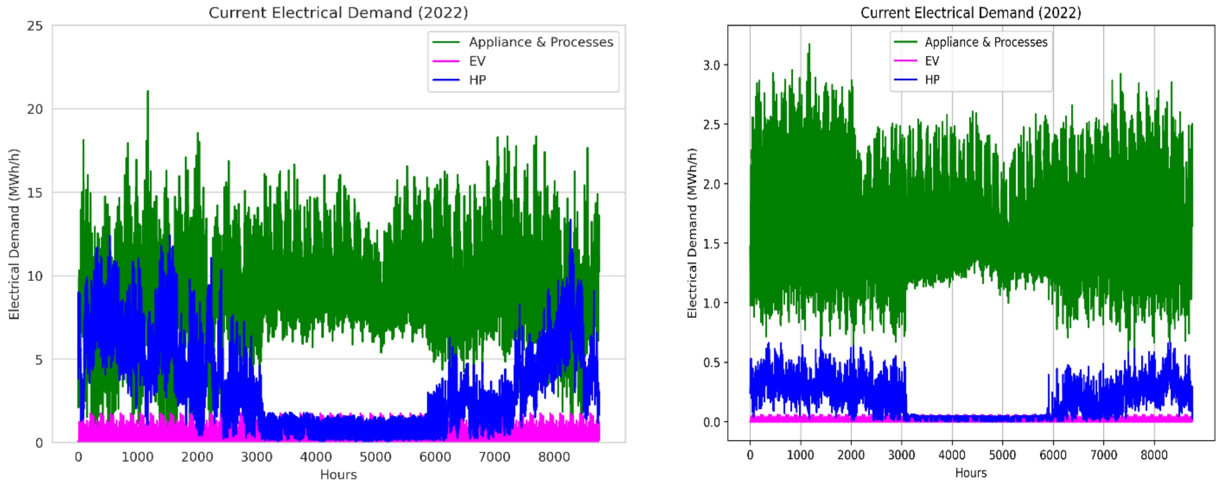

Figure 1: Hourly annual electricity demand for HP, EVs (uncontrolled charging) and Appliance and processes for both residential and non-residential customers in (a) Estavayer-le-Lac (left) and (b) Boisy (right) in 2022.

Figure 2 shows the total aggregated electricity demand in Estavayer-le-Lac and Boisy for 2022 and 2050 for heating, EV, and appliances and processes. The comparison with base demand (2022) shows that the seasonal difference becomes more pronounced in 2050. The seasonal pattern of Figure 2 is caused by electrical load curve for HP in 2050, which is displayed in Figure 3.

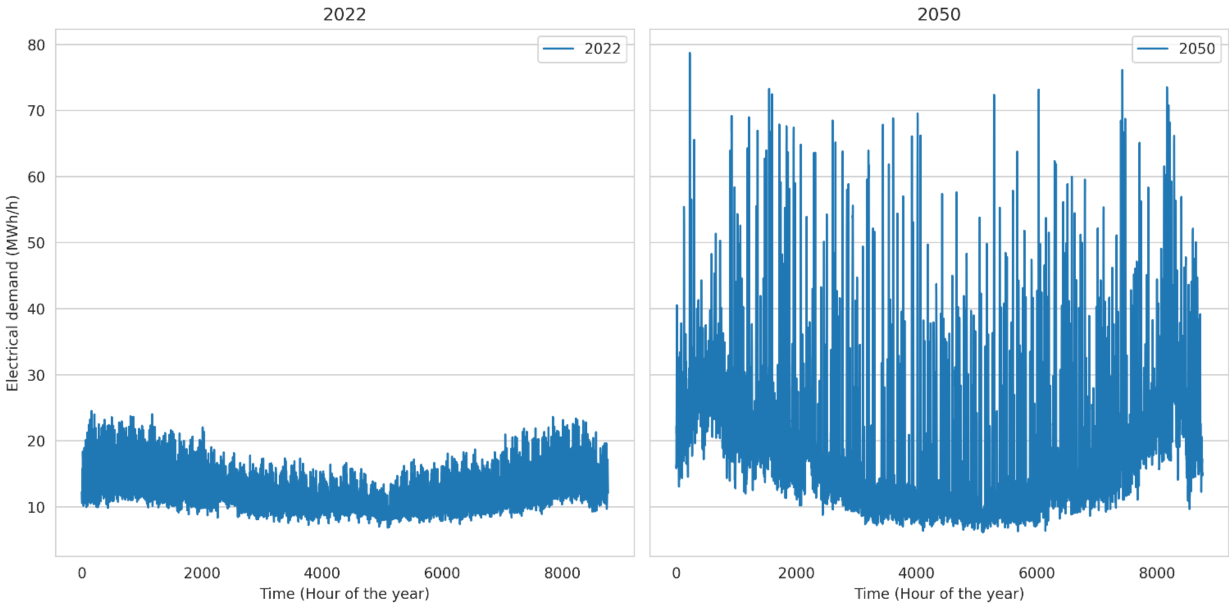

(a)

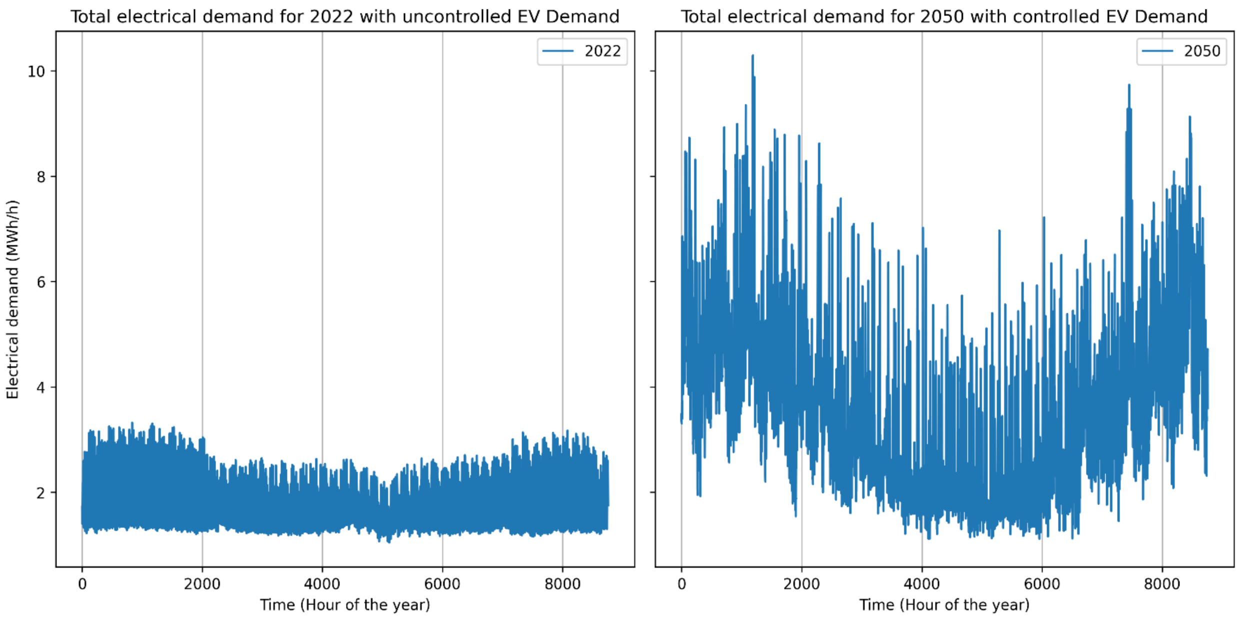

(b)

Figure 2: Total aggregated electricity demand [MWh] of HP, EV and electrical appliances and processes in (a) Estavayer-le-Lac (b) Boisy for 2022 and 2050 (without heat pumps for industrial processes).

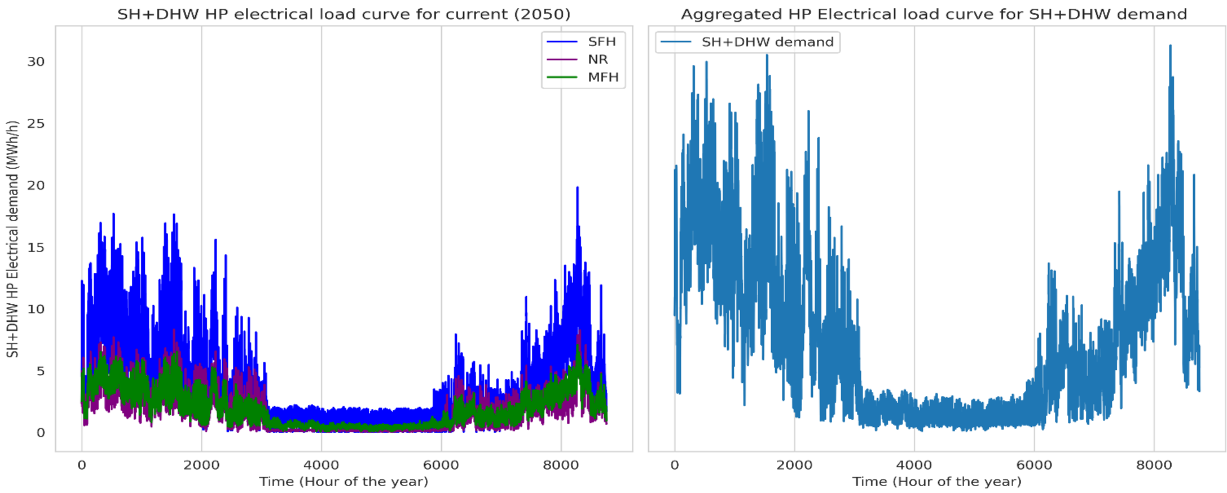

Figure 3: HP electrical load curves for both Space heating (SH) and Domestic hot water (DHW) for 2050 demand per archetype (left) and the aggregated HP electrical load curve (right) (based on assumption of 100% HP diffusion) for Estavayer-le-Lac.

5.2 Annual Electrical demand

As shown in Figure 4, the projected annual electricity demand of Estavayer-le-Lac and Boisy according to the default scenario is expected to evolve significantly from 2022 to 2050. In Estavayer-le-Lac, electricity demand is projected to increase by around 25 GWh p.a. due to the adoption of heat pumps and by around 38 GWh p.a. through the electrification of mobility (EVs), while the electricity demand for appliances and process is expected to decrease by 15 GWh p.a. over the same period (this decrease is likewise based on the Energy Perspectives 2050+ [3]). In Boisy, electricity demand is projected to increase by around 13.9 GWh p.a. for heat pumps and by 3.6 GWh p.a. for EVs, while decreasing by 2.8 GWh for appliances and processes. The difference in electricity demand growth between EV and HP is mainly explained by the local residential structure and mobility patterns. In Boisy, the building stock is dominated by MFH (~75%), where private car ownership is typically lower, resulting in a smaller increase in electricity demand from EV compared to HP. In contrast, Estavayer-le-Lac is largely dominated by SFH (~85%), where car ownership is much higher (by a factor of ~5.6), leading to a larger growth in electricity demand from EV relative to HP. Also, the total number of cars in Boisy is considerably smaller than in Estavayer-le-Lac In this default scenario, the net total electricity demand in Estavayer-le-Lac is projected to decrease from 108.8 GWh/a in 2022 to -49 GWh/a in 2050.Also for Boisy, net demand is projected to decrease from 16.3 GWh/a in 2022 to 9.6 GWh/ain 2050. The reason for this decreases difference is much higher relative production of PV electricity in Estavayer-le-Lac compared to Boisy due to the difference in roof area (much higher share of SFH in Estavayer-le-Lac compared to Boisy). The results show that at high PV deployment in 2050 scenarios may also introduce operational challenges due to the maximum feed in (load) from PV systems exceeding the maximum load of grid electricity demand by a factor of ~3.

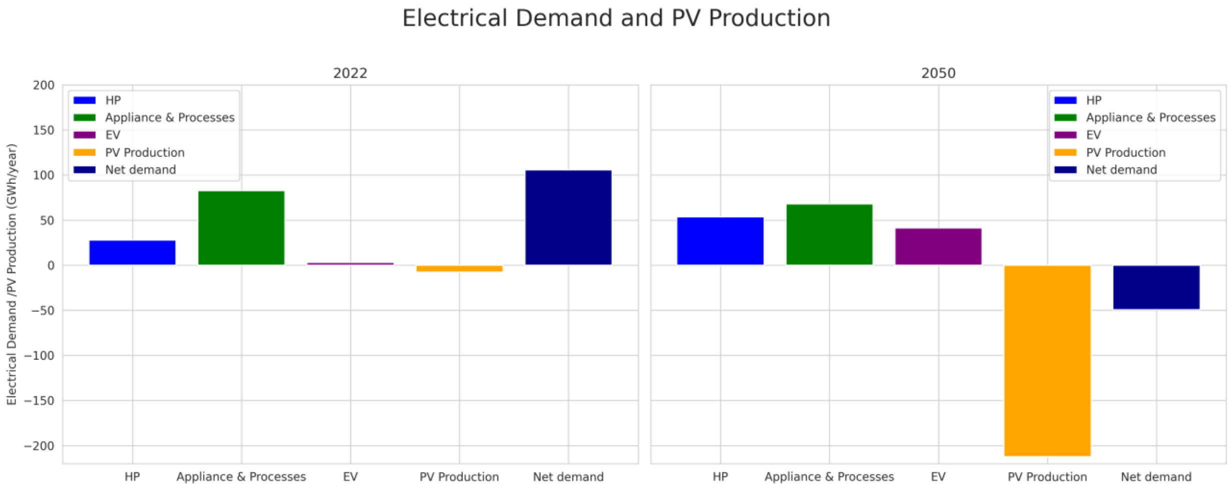

(a)

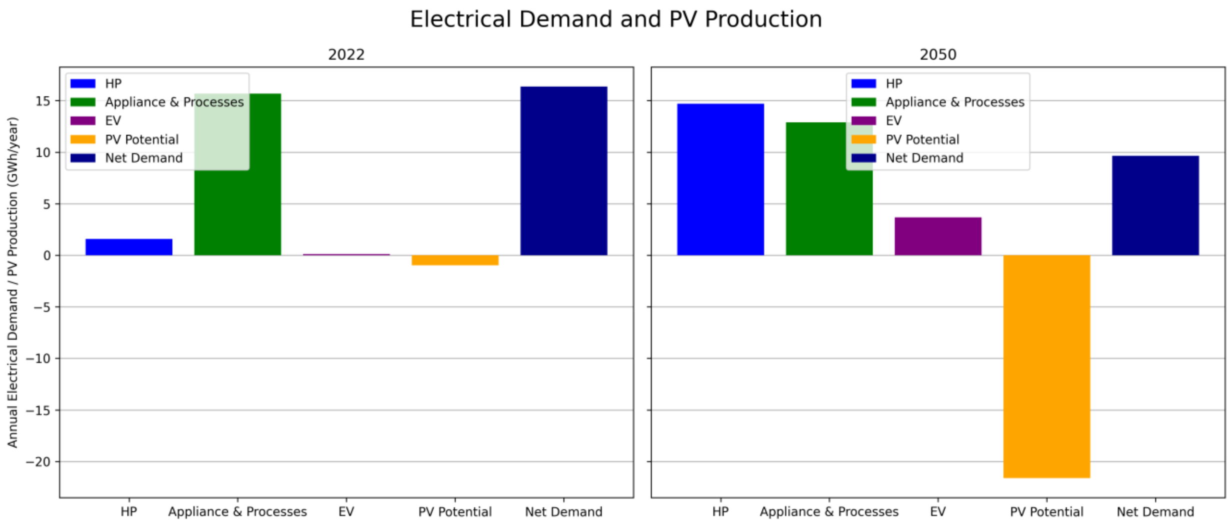

(b)

Figure 4: Annual Electrical demand with PV production for both 2022 (with uncontrolled EV charging) and 2050 (with controlled EV charging) (a) Estavayer-le-Lac (b) Boisy.

5.3 Seasonal Pattern

To provide a more detailed analysis of the seasonal electrical load demand, Figure 5 presents the electrical loads for both winter and summer weeks. The results indicate that the electricity demand for heat pumps (HP) is higher in winter compared to summer season, both for the current period (2022) and in the future (2050). Electric vehicle (EV) demand remains relatively low for both seasons today but is projected to increase significantly in the future for both winter and summer. The pattern also shows a reduction in electrical demand for appliances and processes in the future, during both summer and winter seasons.

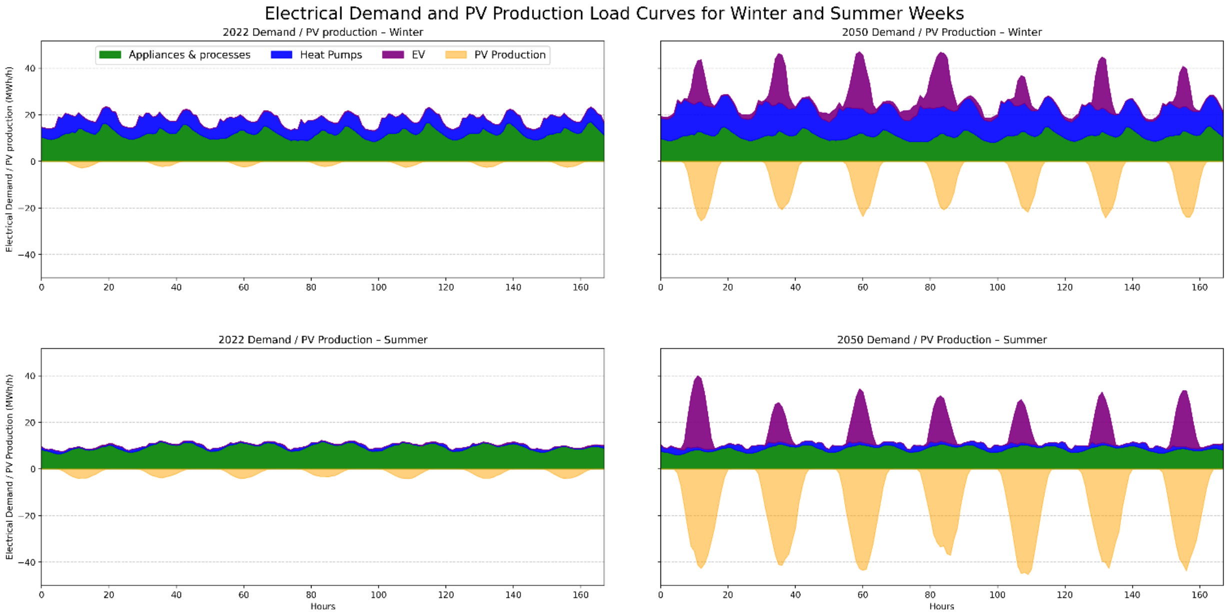

Figure 5: Electrical demand for winter and summer weeks both for current demand (2022) (left) and future demand (2050) (right) for Estavayer-le-Lac, in 2050, controlled EV charging is used.

6 Overview of Scenario Features and Electricity Growth up to 2050

To address more detailed evolution of EVs, HP and Electrical appliances and processes, various scenarios were created, with Table 1 showing the scenario features. The diffusion rates of EVs, charging strategies, energy demand of HPs and energy efficiency are given exogenously.

Table 1: Overview of the scenario features, including the levels and description by component.

Scenario features	Variants	Description
EV diffusion	3	Three scenarios with different EV diffusion rates: Basis, SuS, and full electrification
Charging strategy	2	Two charging strategies, i.e. i) uncontrolled charging and ii) controlled charging
Heating	1	Full electrification of residential heating using heat pumps (HP), while retrofitting of the envelopes of existing buildings and the construction of new highly efficient buildings are expected to result in a heating demand rate of 1.35% per year between 2022 and 2050 (based on [2]).
Energy efficiency	1	Assumed rate of electrical consumption per household reduction: 0.67% per year (based on [2])

6.1 Electrical Vehicle (EVs) Scenario

The numbers of EVs in intermediate years are determined by linear interpolation between the current and future number of cars by 2050.

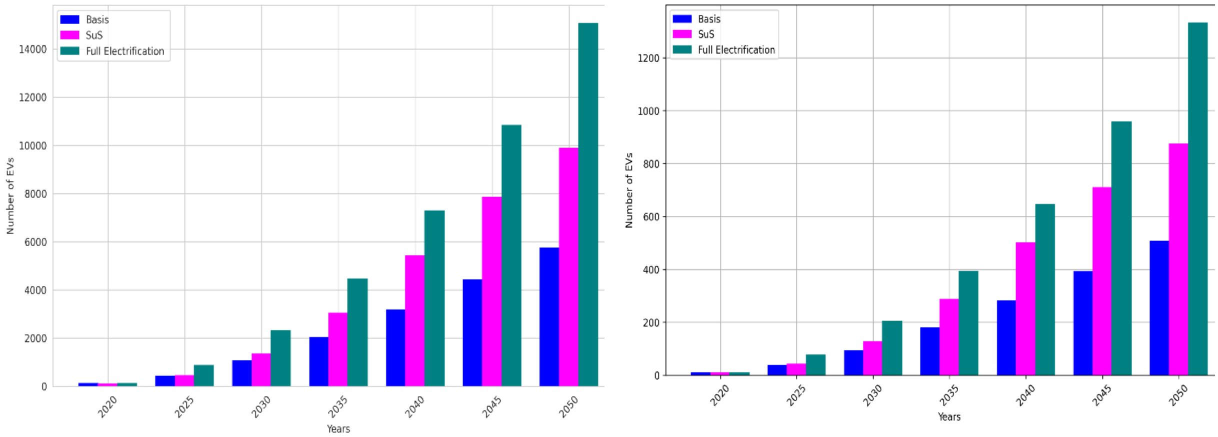

Figure 6: Number of EVs in (a) Estavayer-le-Lac (left) (b) Boisy (right) according to the three scenarios Basis, SuS and Full.

Figure 7 shows the annual electricity demand for the three scenarios.

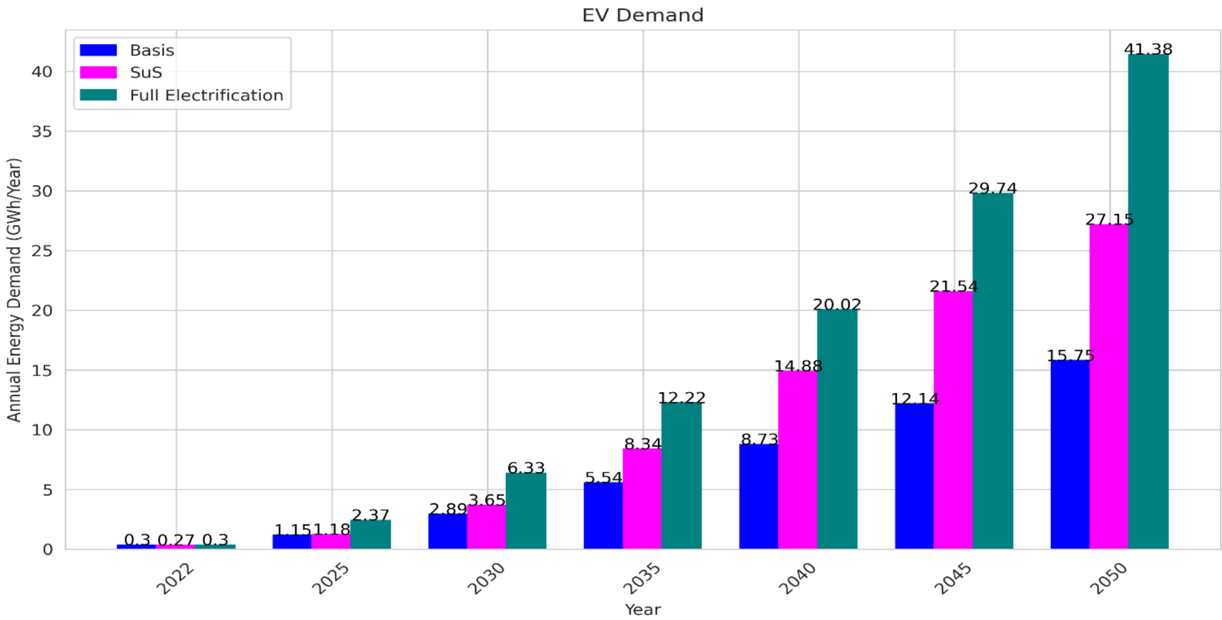

Figure 7: Annual electricity demand in Estavayer-le-Lac (in GWh/year) for EVs calculated under three EV scenarios from 2020 to 2050.

6.2 The heating Scenario

The final energy in Estavayer-le-Lac, as shown in Figure 8, is calculated based on the shares of the various energy carriers according to Energy Perspectives 2050+ [3]. The results show that by 2050, heating demand will be largely dominated by heat pumps (29.54 GWh/year), with only minor contributions from wood (1.47 GWh/year) and fuel-based systems (0.59 GWh/year). Beyond 2050, fuel-based heating is assumed to be fully phased out, resulting in the complete elimination of fuel consumption for heating.

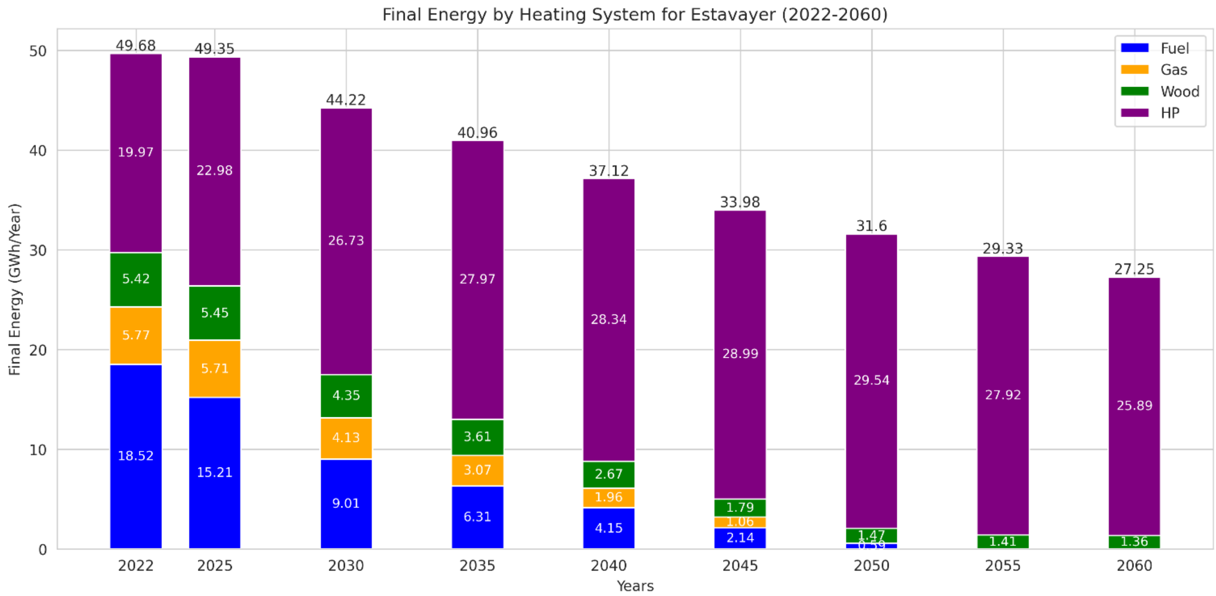

Figure 8: Annual final energy demand in Estavayer-le-Lac (in GWh/year) for space heating (SH) projected based on the Energy Perspectives 2050+.

6.3 Electrical appliances and processes Scenario

The projections for electrical appliances and processes are based on the ZERO Basis scenario outlined in the Energy Perspective 2050+, as shown in Figure 9.

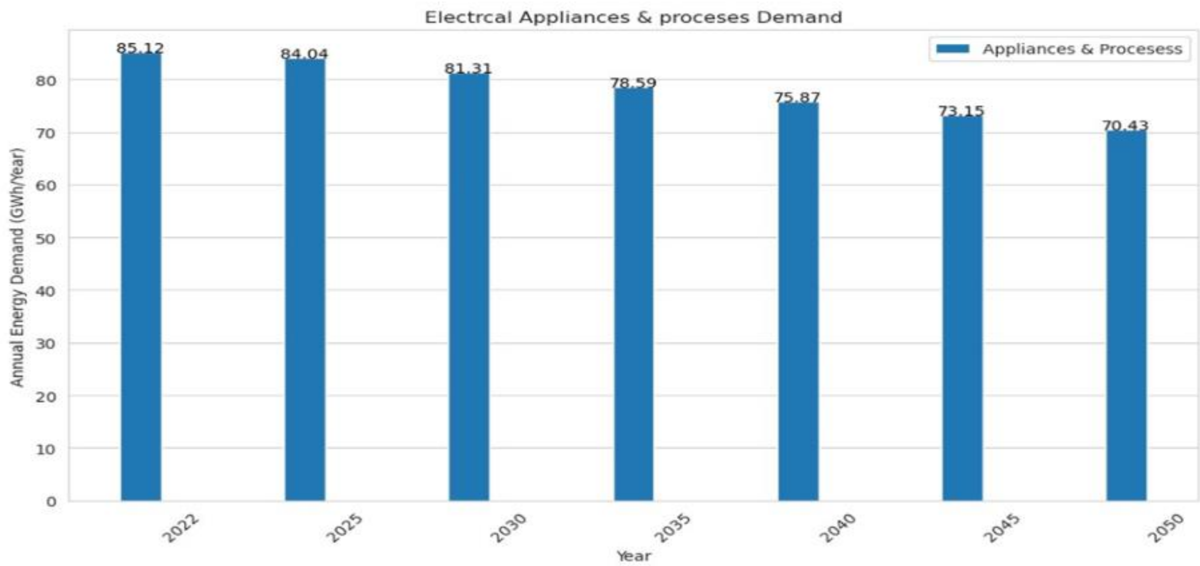

Figure 9: Annual Energy demand for Appliances and processes for both residential and non-residential customers in Estavayer-le-Lac based on Energy perspective 2050+.

7 Additional Data

Table 2: Annual COP for Space heating based on WP 3.

System	Year	COP
Modelled SH	2022	3.38
Energy Perspectives 2050+	2020	3.19
Modelled SH	2050	4.17*)
Energy Perspectives 2050+	2050	4.12

* Calculated from COP 2022 based on COP ratio from Energy Perspectives 2050+

Table 3: Scenario assumption based on WP 3.

Parameters	2022	2050
Population	22,970	26,709*
Number of Households (HH)	10,077	12,081*
People/HH	2.28	2.21*
ERA/HH	137	142
Total ERA of HH	1,380,536	1,711,288*
Total ERA of OCO	121,994	151,221*
Total ERA of IND ***	445,720	552,507*
Electric resistance heating in HH	7.7%	0%
HP diffusion in HH	37.4%	100%
HP diffusion in OCO	21.8%	100%
HP diffusion in IND***	3.6%	100%
Vehicle-km per car [km/car/a]	16,060	16,060
Number of cars/HH	1.44	1.25
Total number of cars	14,545	15,052
Number of EVs/HH	0.11	1.25
Total number of EVs	1,118	15,052
EV diffusion (private passenger cars)	7.43%	100%
Electricity Demand (appliances) per HH [kWh/HH/a]	3055	2750 (-10%)
Heat Demand (SH) per HH [kWh/m2/a]	87.5	57.5
Heat Demand (DHW) per HH [kWh/m2/a]	21.8	21.8
Cooling demand per HH	n/a	n/a
Heat demand OCO [kWh/m^2. a]	75.2	37.5*
Electricity demand OCO [GWh]	4.9	3.5
Cooling demand OCO	n/a	n/a
Heat demand industry, building [kWh/m^2. a]	67.3	39.1*

Heat demand industry, process	n/a	n/a
Electricity demand industry [GWh]	50.1	36.02*
Cooling demand industry	n/a	n/a
PV electricity generation [GWh] in Estavayer	7.71	212.3
PV electricity generation [GWh] in Boisy	0.9	21.6

Note:

* Based on Energy Perspectives 2050+

** Buildings with district heating are not included in the ERA and HP values above

*** This includes industry and agriculture

Table 4: Selected Electricity Tariffs (Proposal).

DSOs			**Energy tariffs (ct/kWh)**	**Distribution tariffs (ct/kWh)**	**Transmission Grid Tariffs (ct/kWh)**	**Reactive energy (ct/kVArh)**	**Hydraulic reserve (ct/kWh)**	**Total Tariffs/HH (Ct/kWh)**	
								Out VAT	VAT incl.
Single Tariff	Yverdon Energies	Full hours	20.84	12.92	0.75	-	1.20	35.71	38.60
		Off-peak hours							
		Max Power (CHF/kW/month)	-	-	-	-	-	-	-
		Increment for 100% PV						+2.60	+2.81
		Increment for 80% Hydro + 20% PV						+0.60	+0.65
		Subscription (by meter) (CHF/month)	5.95					5.95	6.43
Double Tariff	Yverdon Energies	Full hours	21.00	13.11	0.75	-	1.20	36.06	38.98
		Off-peak hours	18.75	7.56				28.26	30.55
		Max Power (CHF/KW/month)	-	-	-	-	-	-	-
		Increment for 100% PV						+2.60	+2.81
		Increment for 80% Hydro + 20% PV						+0.60	+0.65
		Subscription (by meter) (CHF/month)	7.85					7.85	8.49
Combined Double and Capacity Tariff (nativa plus)	Services Industriels de Lausanne (SIL) Double Tariff Normal	Peak Hours[1]	12.27	A : 6.53	0.75	4.00	1.20	20.75	22.43
		Off-Peak Hours[2]	9.44	A : 4.08				15.47	16.72
		Max Power (CHF/kW)	4.55	A : 17.16	-	-	-	21.71	23.47
		Peak Hours[1]	15.09	A : 6.53	0.75	4.00	1.20	23.57	25.48
		Off-Peak Hours[2]	12.26	A :4.08	0.75	4.00	1.20	18.29	19.77
		Max Power (fr/kW)	4.55	A :17.16	-	-	-	21.71	23.47
		Subscription (by meter) (CHF/month)	7.85					7.85	8.49

8 Model Repository

The open-source model used in this work is available at the following repository: GitHub Repository – https://github.com/Arbogast12/Unige-Dig_a_plan-Integrated_modeling.

9 Conclusion

In this report, WP3 activities of the Dig-A-Plan project are presented through Deliverables D3.1 and D3.2, which together establish the hourly electrical demand profile scenarios required for simulation and optimization in subsequent work packages. In combined D3.1 and D3.2, two representative real-world distribution grids provided by the DSO partners, Groupe E (Estavayer-le-Lac) and Services Industriels de Lausanne (Boisy), are characterized as the case-study networks for scenario development. Across the combined work of D3.1 and D3.2, a structured workflow is developed to generate future demand scenarios and harmonize heterogeneous DSO inputs into consistent, simulation- and optimization-ready datasets. This workflow relies on the classification of buildings and consumers into representative archetypes, including single-family houses (SFH), multi-family houses (MFH), service-sector buildings (OCO), and industrial consumers (IND), enabling the construction of sector-specific demand profiles.

Overall, the outputs of WP3 provide harmonized hourly electricity demand scenarios and load profiles up to 2050, developed in 5-year intervals, which serve as key input datasets for the mapping and modelling environment used to analyses tariff impacts, grid flexibility, and distribution network performance in the subsequent Dig-A-Plan work packages. The outcomes of D3.1 and D3.2 therefore provide a validated and harmonized data backbone supporting the analysis and tool validation activities carried out in WPs 4 and 5.

10 References

[1] “Schweizerischer Ingenieur- und Archtiktenverein. SIA 380 – Grundlagen f¨ur energetische Berechnungen von Geb¨auden, 2015”.

[2] Swiss Federal Office of Energy, “Energy perspectives 2050+.” [Online]. Available: https://www.bfe.admin.ch/bfe/en/home/policy/energy-perspectives-2050-plus.html/

[3] J. C. . Ciscar, L. . Feyen, D. . Ibarreta, and A. . Soria, Climate impacts in Europe : : final report of the JRC PESETA III project. Publications Office of the European Union, 2018.

[4] Federal Statistical office, “Registre fèdèral des batiments et des logements (RegBL).” [Online]. Available: https://www.housing-stat.ch/fr/index.html

[5] S. Schneider, P. Hollmuller, P. Le Strat, J. Khoury, M. Patel, and B. Lachal, “Spatial–Temporal analysis of the heat and electricity demand of the Swiss building stock,” Front. Built Environ., vol. 3, no. August, pp. 1–17, 2017, doi: 10.3389/fbuil.2017.00053.

[6] T. Schluck, K. N. Streicher, and S. Mennel, “Statistical modelling of the energy reference area based on the Swiss building stock,” J. Phys. Conf. Ser., vol. 1343, no. 1, 2019, doi: 10.1088/1742-6596/1343/1/012031.

[7] S. Callegari, “Energy conversions and Energy systems,” M.Sc. thesis (MUSE), 2018.

[8] Federal Roads office, “Vehicle data,” https://www.astra.admin.ch/astra/en/home/dokumentation/daten-informationsprodukte/informationsprodukte.html. 2024.

[9] Federal Roads ofice, “Vehicle data.” [Online]. Available: https://www.astra.admin.ch/astra/en/home/dokumentation/daten-informationsprodukte/informationsprodukte.html

[10] “Verkehrsverhalten der Bevölkerung.” [Online]. Available: www.statistik.ch

[11] Federal Department of the Environment. Transport. Energy and.Communications, “Transport Outlook 2050,” Federal Office for Spatial Development, 2024.

[12] A. Walch, R. Castello, N. Mohajeri, and J. L. Scartezzini, “Big data mining for the estimation of hourly rooftop photovoltaic potential and its uncertainty,” Appl. Energy, vol. 262, no. December 2019, p. 114404, 2020, doi: 10.1016/j.apenergy.2019.114404.

[13] Swiss Federal Office of Energy, “‘Federal Office of Topography swisstopo.’ ,” [Online]. Available: https://www.uvek-gis.admin.ch/BFE/sonnendach/.

[14] A. M. C. S. M. K. P. and D. Parra. Rinaldi, “Optimized allocation of PV and storage capacity among different consumer types and urban settings: A prospective analysis for Switzerland.,” Journal of cleaner production 259 (2020): 120762. .

[15] A. Syla, A. Rinaldi, D. Parra, and M. K. Patel, “Optimal capacity planning for the electrification of personal transport: The interplay between flexible charging and energy system infrastructure,” Renewable and Sustainable Energy Reviews, vol. 192, no. June 2023, p. 114214, 2024, doi: 10.1016/j.rser.2023.114214.

[16] A. Syla, D. Parra, and M. K. Patel, “Assessing flexibility from electric vehicles using an open-source energy system model: trade-offs between smart charging, vehicle-to-grid and an extensive charging infrastructure,” Energy, vol. 326, p. 136236, Jul. 2025, doi: 10.1016/J.ENERGY.2025.136236.

[17] Federal Statistical office, “Microcensus Mobility and Transport(MZMV).” [Online]. Available: https://www.bfs.admin.ch/bfs/de/home/statistiken/mobilitaet-verkehr/erhebungen/mzmv.html

[18] Bundesamt für Statistik, Verkehrsverhalten der Bevölkerung - Ergebnisse des Mikrozensus Mobilität und Verkehr 2015 (Transport behavior of the population - results of the microcensus mobility and transport 2015), no. 1840477. 2017. [Online]. Available: https://www.bfs.admin.ch/hub/api/dam/assets/1840477/master

Schweizerische Eidgenossenschaft
Confédération suisse
Confederazione Svizzera
Confederaziun svizra

Federal Department of the Environment,
Transport, Energy and Communications DETEC

Swiss Federal Office of Energy
Energy Research and Cleantech

Final report from 30 April 2026

Dig-A-Plan

Appendix 3: Expected asset distribution, flexibility amount, and expected transformer loss of life

D4.1 Document of expected asset distribution and flexibility amount within the distribution grids of the
case studies

D4.2 Document of expected transformer loss of life across the scenarios of the Swiss energy transition

---

Publisher:
Swiss Federal Office of Energy SFOE
Energy Research and Cleantech
CH-3003 Berne
www.energy-research.ch

Co-financing: In-kind contributions provided by
Groupe e, 1763 Granges-Paccot

Services Industriels Lausanne (SiL), 1003 Lausanne

Yverdon Energies, 1400 Yverdon

Subsidy recipients:
Haute École d'Ingénierie et de Gestion du Canton de Vaud (HEIG-VD), Institute of Energies (IE)
1400 Yverdon-les-Bains
https://heig-vd.ch/recherche/instituts/ie/

Université de Genève (UNIGE), Institute for Environnemental Sciences (ISE)
1205 Genève
https://www.unige.ch/energy/

EPFL, photovoltaic research laboratory (PV-LAB)
2002 Neuchâtel
https://www.epfl.ch/labs/pvlab/

Authors:

Alejandro Pena-Bello, EPFL, alejandro.penabello@epfl.ch
Gerard Marias Gonzalez, EPFL, gerard.mariasgonzalez@epfl.ch
Nicolas Wyrsch, EPFL, nicolas.wyrsch@epfl.ch

SFOE project coordinators:

Dr Michael Moser, Michael.moser@bfe.ch

SFOE contract number: SI/502666-01

Table of contents

List of figures

List of tables

1 Methodology

The methodological developments carried out in this phase aim to translate building-level energy behavior into a consistent representation of demand and flexibility within the studied low-voltage distribution grids. The focus is on generating realistic temporal load profiles, allocating emerging flexible assets, and constructing future deployment trajectories.

The foundation of the approach is a load allocation process that derives 15-minute electricity demand profiles for each household by linking building locations to grid connection points, distributing annual consumption values, and assigning representative virtual load curves through an optimization procedure. Different assets and PV self-consumption are then incorporated, and a second optimization ensures that aggregated behavior matches the transformer-level measured power. Complementing this, dedicated methodologies distribute electric vehicles across the networks based on demographic statistics, mobility patterns, and building characteristics, producing charging curves that capture how electrification trends affect local demand and flexibility potential.

Once building-level profiles are established, an economic optimization model based on Pyomo evaluates operational behavior under different tariff structures and explores future investment scenarios, minimizing total cost of ownership over a 25-year horizon. EV operation is modelled at the individual vehicle level, incorporating charging and discharging constraints, availability profiles, and V2H capabilities. Baseline and future scenarios distinguish between present-day operational optimization and long-term investment planning from 2030 to 2050 in five-year increments, with progressive deployment strategies for PV, batteries, heat pumps, and EVs aligned with the WP3 electrification targets.

Finally, a set of key performance indicators is defined to quantify grid impact, flexibility utilization, and building-level energy autonomy across scenarios and tariff structures. A transformer thermal aging model based on the IEEE C57.96 framework [1] is also introduced to assess the progressive loss of insulation life under increasing distributed energy resources (DER) penetration.

Together, these steps provide the necessary inputs to map present and future load configurations into the distribution grids of the case studies, enabling subsequent assessment of flexibility provision and the effects of tariff structures.

1.1. Load allocation

Due to the lack of publicly available building-level demand measurements in low-voltage networks, each building's 15-minute load curve is inferred by combining three datasets [2]: (i) static building attributes from the Registre fédéral des bâtiments et des logements (RegBL) [3], including year of construction/renovation, use category, conditioned floor area, and number of storeys; (ii) Swiss SIA electricity-intensity benchmarks by building type and vintage; and (iii) anonymized 15-minute smart-meter load curves from the Flexi projects [4,5], providing representative profiles for residential and non-residential buildings.

The methodology follows a two-stage optimization procedure, illustrated in Figure 1, preceded by a preliminary step that links each building to its electrical connection node using the low-voltage network models from WP2 and establishes annual energy targets. For buildings without measured yearly consumption, values are estimated and assigned. Where multiple buildings share a connection point, aggregated demand is redistributed proportionally based on floor area as reported in the RegBL.

Stage 1 – Base load allocation. The total annual energy at each node is partitioned by subtracting the known load components from the total annual consumption to obtain the remaining building base load. These known components include heat pumps and domestic hot water demand, derived from WP3 projections, electric vehicle consumption, and self-consumed PV generation, where a fixed self-consumption rate of 30% of total PV generation is assumed. Each building's base load is then defined as:

$$E_{base} = E_{annual,tot} - E_{HP} - E_{DHW} + 0.3 \cdot E_{PV} - E_{EV}$$

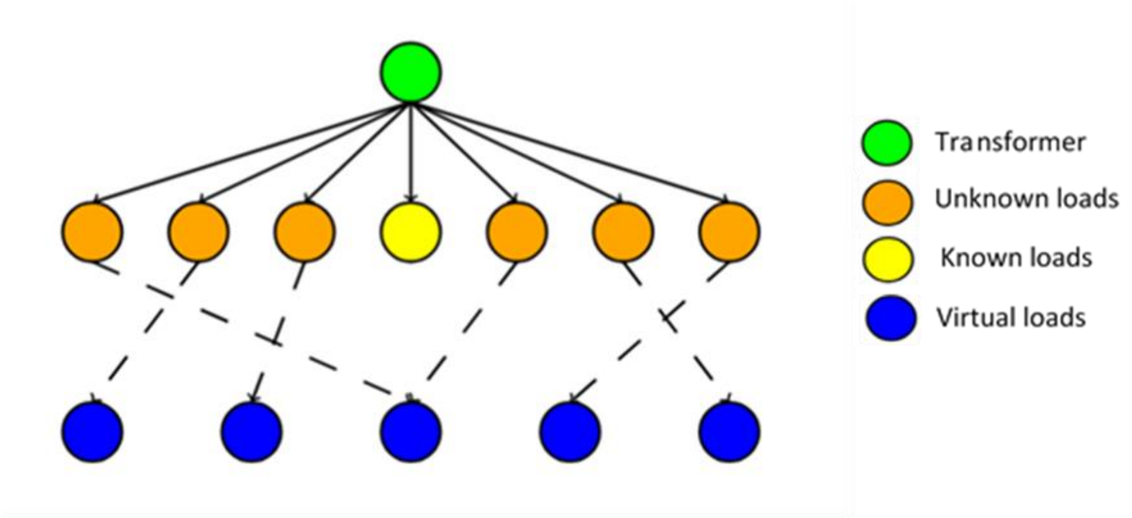

Figure 1. Load allocation scheme

This base load is assigned to each building using a Mixed-Integer Linear Programming (MILP) optimization, which matches each building to a representative profile from a database of 3,089 virtual loads (shown in blue in Figure 1), constrained by building and dwelling category (Residential, Public, Commercial, and Industrial) to minimize error with the E_{base} target. Known loads such as HP, DHW, EV, and PV self-consumption are then added to produce the initial household load profile P_{init}.

Stage 2 – Feeder matching correction. A final optimization adjusts P_{init} so that aggregated demand at the feeder transformer matches the measured profile provided by the Distribution System Operator (DSO), while conserving annual energy totals at each node. This ensures consistency between individual household behavior and transformer-level observations.

It is worth noting that the transformer shown above refers to the feeder-level connection point, as the measured load curves available from the DSO correspond to this level. Load curves at the individual low-voltage transformer level are not available, meaning the Stage 2 correction ensures consistency at the feeder level but cannot correct discrepancies at individual downstream transformers. This limitation is discussed further in the context of the transformer stress results in subsection 2.4.

1.2. EV Allocation on Low-Voltage Networks

The methodology to distribute EVs on low-voltage networks integrates several data sources, as illustrated in Figure 2. Grid topology and building data are provided by WP2, while population data comes from the Federal Statistical Office [6] and mobility patterns from the Swiss Microcensus on Mobility and Transport [7]. Population distribution per household determines the number of EVs at each connection node, combined with car ownership data. Trips from the Microcensus are filtered by transport mode and classified by day type (weekday, Saturday, Sunday), focusing on regions representative of the studied networks in the canton of Vaud. Car occupancy rates and arrival time data are combined to derive the car arrival time schedule, which together with commuting distances determines the mobility need for each vehicle. Vehicle technical specifications, including energy consumption per kilometer by car category, are incorporated to translate mobility needs into charging load curves. Battery Electric Vehicles (BEVs) are modelled with a 62 kWh battery capacity, consistent with representative market specifications, and their energy consumption per trip is calculated as a function of vehicle weight, drag coefficient, rolling resistance, trip distance, and duration. Where local data is available, it is used to refine the model, as is the case for Estavayer-le-Lac.

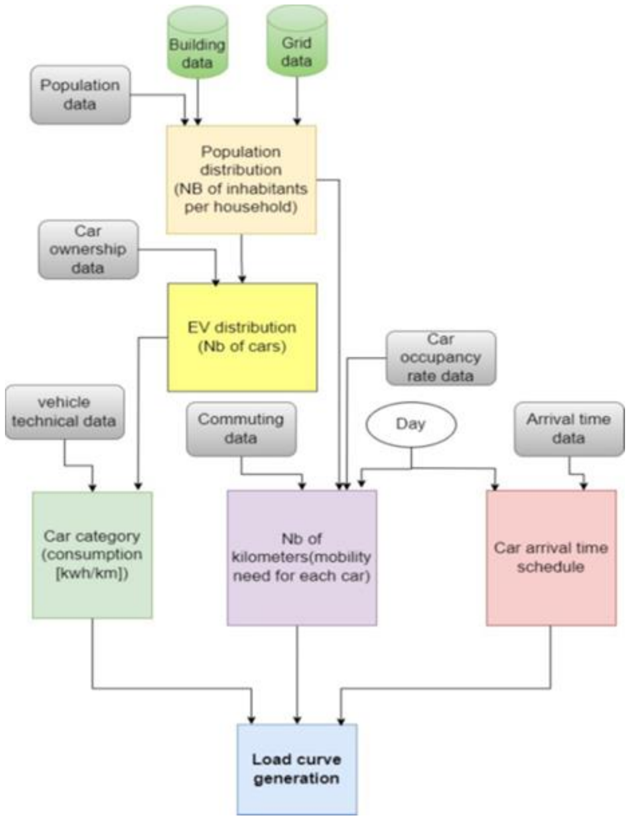

Figure 2: Schematic representation of the methodology to distribute EVs on low-voltage networks.

The population distribution per household determines the number of EVs in each household, and based on daily travel distances, mobility needs are assigned accordingly. Each household is allocated a number of EVs based on conditional probabilities derived from federal statistics, and the corresponding energy consumption is calculated by distributing daily mobility needs across the EVs. For each simulated vehicle, charging events are modelled at three location types: home (11 kW), workplace, and public infrastructure (up to 250 kW). At each stop, a charging event is initiated if three conditions are met: the location type allows charging (with probability 1 at home and 0.2 at workplace and public infrastructure), the stop duration exceeds approximately 60 minutes, and the vehicle's current State of Charge (SOC), adjusted by a price influence term, falls below a randomly drawn SOC target threshold, normally distributed around 0.6. This last condition captures the tendency of drivers to charge when the battery is sufficiently depleted relative to a desired level. The simulation alternates between weekday and weekend trip distributions and reassigns trip profiles stochastically each day to capture inter-day variability. Following the simulation, the battery state of each BEV is reconstructed at 15-minute resolution over a full year (35,040 timesteps), from which both the load curves and a binary home-presence indicator are derived. The resulting dataset comprises 750 empirical EV profiles, each containing a full-year battery state time series, load curve, and home-availability indicator, which are assigned deterministically to each building node (EGID) based on its identifier, ensuring reproducibility of results across all future simulation years from 2030 to 2050.

In contrast, the model used in WP3 estimates the aggregate hourly energy demand of EVs by applying typical daily charging profiles, offering a broad view of energy requirements. While the WP3 model provides an overview of overall demand, the model described above focuses on a more localized and detailed analysis by considering household distribution, daily travel needs, and grid connection points. This comparison helps assess both macro-level demand trends and more granular spatial variations in energy consumption. Understanding these differences is crucial for infrastructure planning and flexibility strategies, ensuring energy systems can accommodate both general and region-specific demands effectively. Figure 3 was prepared using data that refer specifically to Estavayer-le-Lac.

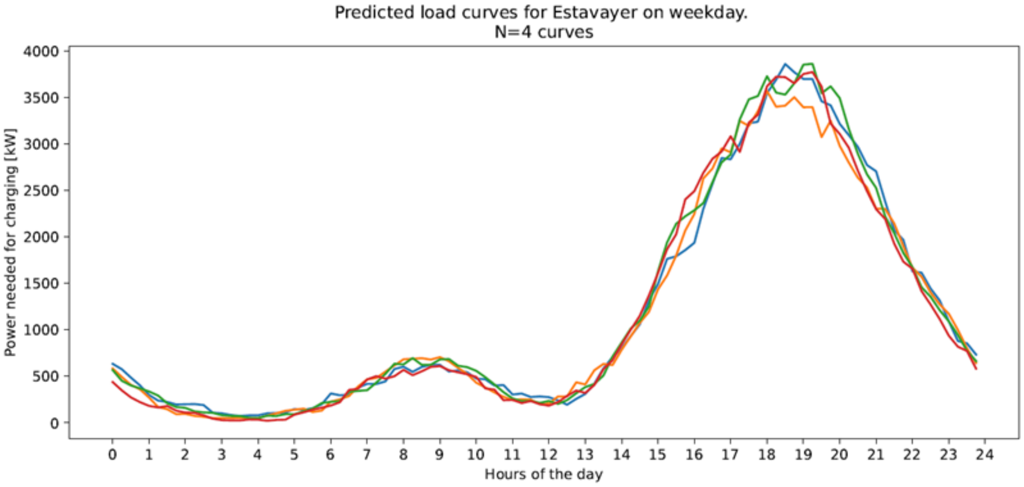

Figure 3: Predicted load curves for EV charging in Estavayer on a weekday. The curves represent the total charging demand for 6284 electric vehicles, with individual charger capacities varying between 3.7 kW and 11 kW, depending on the vehicle type.

1.3. Economic Optimization

A Pyomo-based Mixed-Integer Linear Programming (MILP) model is developed to assess the techno-economic performance of DER under current and future grid scenarios. The model is applied at the building level, once the 15-minute load profiles for each building have been established, and determines the optimal configuration and operation of PV systems, battery storage, and electric vehicles. The objective is to minimize the total cost of ownership (TOTEX) over a 25-year lifetime, which accounts for two main components: operating expenditures (OPEX), covering grid exchange costs, battery, EV operation, and PV maintenance, and annualized capital expenditures (CAPEX), corresponding to investments in PV and battery systems. EVs are included as flexible assets within the operational dispatch but are assumed to carry no investment cost, as the vehicle purchase is considered outside the scope of the energy system optimization. Their participation in flexibility provision is constrained by home plug-in availability, derived from the presence indicators described in the previous section.

Formally, the optimization problem is expressed as:

$$TOTEX = OPEX + R \cdot CAPEX$$

where R is the annuity factor that accounts for the system lifetime L and discount rate r:

$$R = \frac{r \cdot (1+r)^L}{(1+r)^L - 1}$$

OPEX includes four components: grid exchanges, battery, EV operation, and PV maintenance:

$$OPEX = OX_{ge} + OX_{bo} + OX_{pm}$$

Grid exchanges $$OX_{ge} = OX_{ge}^{vol} + OX_{ge}^{pow}$$

Battery operation $$OX_{bo} = \sum_{t=1}^{T} \left(P_t^{DIS,bat} \cdot C_d^{BAT} + P_t^{CH,bat} \cdot C_c^{BAT} \right) \cdot TS_t$$

EV operation $$OX_{evo} = \sum_{t=1}^{T} \left(P_t^{DIS,ev} \cdot C_d^{EV} + P_t^{CH,ev} \cdot C_c^{EV} \right) \cdot TS_t$$

PV maintenance $OX_{pm} = \gamma^M \cdot CX_{pv}$

Where P_t^{DIS}, and P_t^{CH} denote the discharging and charging power at time step *t* for the battery and EV, C_d and C_c are the levelized cost of storage (LCOS) associated with discharge and charge operations, reflecting cycling degradation costs, for both the battery and the EV. TS_t is the simulation time-step.

Depending on the tariff, there are two components of the grid exchange costs (OX_{ge}): the volumetric and the capacity based. They are calculated as:

Volumetric tariff $OX_{ge}^{vol} = \sum_{t=1}^{T} |P_t^{IMP} \cdot t_t^{IMP} - P_t^{EXP} \cdot t_t^{EXP}| \cdot TS_t$

Capacity-based tariff $OX_{ge}^{pow} = \sum_{k=1}^{K} P_k^{MAX} \cdot T_k^{MAX}$

where P^{IMP} and P^{EXP} denote the imported and exported power at time step t. t_t^{IMP} and $t_t^{EXP}$are the volumetric import and export tariffs, respectively, in CHF/kWh, and TS_t is the simulation time-step.

For the capacity-based tariff, P_k^{MAX} is the maximum (peak) imported power during the k-th billing period (e.g., month), and T_k^{MAX} is the corresponding capacity tariff (e.g., in CHF/kW) for that period.

CAPEX captures the investment costs of PV and battery systems:

$$CAPEX = CX_{pv} + \frac{L}{L^{BAT}} \cdot CX_{bat}$$

PV $CX_{pv} = \sum_{i=1}^{N} \mu_i^{MOD} \cdot P_{nom,i}^{MOD} \cdot C^{MOD} + \beta^W \cdot C^{FW}$

Battery $CX_{bat} = \sum_{j=1}^{B} E_{cap,j}^{BAT} \cdot C_{sp}^{BAT} + \beta^{BAT} \cdot C_{fix}^{BAT}$

Where μ_i^{MOD} is the number of installed PV modules of configuration *i*, $P_{nom,i}^{MOD}$ is the nominal power of a single module of configuration *i*, and C^{MOD} is the specific cost per installed watt (CHF/W). β^W is a binary variable indicating the presence of any PV installation and C^{FW} is the associated fixed installation cost (CHF). For the battery, $E_{cap,j}^{BAT}$ is the installed capacity of the battery *j* (kWh), C_{sp}^{BAT} is the specific cost per installed kWh (CHF/kWh), β^{BAT} is a binary variable indicating the presence of a battery system and C_{fix}^{BAT} is the corresponding fixed installation cost (CHF).

The PV and battery price levels are determined from data in the IRENA report [8], calibrated to Swiss price levels in a market study [9] using the empirical model proposed by Bloch et al. [10]. The resulting PV and battery cost functions are separated into fixed and linear components. For PV, the fixed component covers administrative procedures and installation costs, while the linear component is proportional to the installed capacity. For batteries, fixed costs are incorporated into the specific cost per installed kWh and are therefore not listed separately. The main techno-economic parameters used for present and future scenarios are summarised in Table 1.

Table 1. Present and future techno-economic parameters used in this study.

Parameter	2025	2030	2035	2040	2045	2050	Reference
System lifetime [year]	25						[9,10]
Discount rate [%]	3						Own assumption
PV fixed cost [CHF]	10049						[9,10]
PV specific costs [CHF/W]	1.05	0.83	0.69	0.59	0.52	0.46	[9,10]
Battery specific costs [CHF/kWh]	229.0	182.4	151.5	129.5	113.1	100.4	[9,10]

The following Table 2 details the electricity tariffs used in this analysis, based on data from two Swiss providers: Yverdon Energies and Services Industriels de Lausanne (SIL).

Table 2. Breakdown of electricity tariff components for the Single, Double, and Combined Capacity models from Yverdon Energies and SIL.

		Energy tariffs (ct/kWh)	Distribution tariffs (ct/kWh)	Transmission Grid Tariffs (ct/kWh)	Reactive energy (ct/kVArh)	Hydraulic reserve (ct/kWh)	Total Tariff/HH (Ct/kWh)	
							Out VAT	VAT incl.
Single tariff	Full hours	20.84	12.92	0.75	-	1.20	35.71	38.60
	Off-peak hours							
	Max Power (CHF/kW/month)	-	-	-	-	-	-	-
	Increment for 100% PV						+2.60	+2.81
	Increment for 80% Hydro + 20% PV						+0.60	+0.65
	Subscription (by meter) (CHF/month)	5.95					5.95	6.43
Double tariff	Full hours	21.00	13.11	0.75	-	1.20	36.06	38.98
	Off-peak hours	18.75	7.56				28.26	30.55
	Max Power (CHF/KW/month)	-	-	-	-	-	-	-
	Increment for 100% PV						+2.60	+2.81
	Increment for 80% Hydro + 20% PV						+0.60	+0.65
	Subscription (by meter) (CHF/month)	7.85					7.85	8.49
Combined Double and Capacity Tariff	Peak Hours	12.27	6.53	0.75	4.00	1.20	20.75	22.43
	Off-Peak Hours	9.44	4.08				15.47	16.72
	Max Power (CHF/kW)	4.55	17.16	-	-	-	21.71	23.47
	Subscription (by meter) (CHF/month)	7.85					7.85	8.49

The tariffs are broken down into their core components, including:

- Volumetric charges (ct/kWh): Costs for energy, distribution, transmission, and hydraulic reserves.
- Capacity charges (CHF/kW/month): Costs based on the maximum power consumed, where applicable.
- Fixed Charges (CHF/month): A standard subscription fee per meter.

To ensure comparability between the Double Tariff and the Combined Double and Capacity Tariff, a standardized time-of-use schedule is applied: peak hours are defined as Monday to Friday from 07:00 to 10:00 and from 17:00 to 22:00, while all other times, including weekends, are considered off-peak. As a result, the Combined Double and Capacity Tariff does not exactly reflect its real-world implementation, but rather a modified version adapted for analytical consistency. Furthermore, for the Combined Double and Capacity Tariff (nativa plus), the capacity charge is subject to a minimum billed demand of 30 kW; therefore, even if the measured peak power is below 30 kW, the customer is charged as if 30 kW were consumed.

1.4. EV operation

The controlled charging of EVs is modeled at the individual vehicle level. Each EV assigned to a building node is characterized by its battery capacity (62 kWh), a maximum charger of 11 kW for residential connections, charging and discharging efficiencies of 95% [11] and a self-discharge rate of 0.01% per day [12]. The optimization determines the optimal charging schedule for each EV at every 15-minute timestep, subject to a set of operational constraints derived from the empirical availability profiles described in the previous section.

The SOC dynamics of each EV follow different rules depending on the vehicle's presence at the residential node. Four distinct cases are handled:

- Home to home: When the vehicle is at home at both the current and previous timestep, the SOC evolves according to the charge/discharge dynamics:

  $$e_{ev}[t] = \alpha \cdot e_{ev}[t-1] + p_{ev,cha}[t-1] \cdot \eta_{ch} \cdot TS - p_{ev,dis}[t-1] \cdot (1/\eta_{dis}) \cdot TS\text{t}$$

  Where α is the self-discharge factor $(1 - 0.01 \cdot TS/86400)$, η_{ch} and η_dis are the charging and discharging efficiencies, and TS is the timestep duration in seconds.

- Away to away: When the vehicle is away at both timesteps, the SOC follows the baseline mobility profile derived from the empirical dataset, ensuring that the energy consumed during trips is consistently represented.

- Departure: When the vehicle leaves home, a minimum SOC constraint is enforced to guarantee that the vehicle has sufficient energy to complete the trip. Specifically, the SOC at departure must cover the maximum energy drop expected during the entire trip, derived from the baseline SOC trajectory plus a minimum reserve of 10% of the battery capacity. This constraint is formulated as:

  $$SOC\_departure \geq min(1.0, 0.10 + max\_trip\_energy\_drop \,/\, 62\, kWh)$$

  This ensures that the optimization does not exploit charging flexibility at the expense of the vehicle's mobility needs.

During home presence, a physical minimum SOC of 4% is always maintained to protect battery health and enable Vehicle-to-Home (V2H) operation.

The model supports Vehicle-to-Home (V2H) operation, whereby the EV battery can discharge to supply the building load, reducing grid imports. Vehicle-to-Grid (V2G) operation, i.e., export of EV energy to the distribution network, is disabled by default in the present study. Simultaneous charging and discharging are prevented through binary exclusion constraints. The EV charging and discharging power flows are further decomposed into their origin and destination, distinguishing between charging from the grid and from PV generation, and discharging to cover building load (V2H), consistent with the power flow accounting used for stationary batteries:

Charging decomposition: $p_{ev,cha}[t] = p_{ev,cha_{imp}}[t] + p_{ev,cha_{pv}}[t]$

Discharging decomposition: $p_{ev,dis}[t] = p_{ev,dis_{sc}}[t] + p_{ev,dis\_exp}[t]$ (where $p_{ev,dis\_exp} = 0$ if V2G disabled)

1.5. Baseline and future scenarios

The optimization framework is applied in two distinct phases: first as a baseline operational model for the present day, and then as a comprehensive investment and dispatch model for long-term planning.

Present Scenario (2025 Baseline)

Optimization focuses exclusively on minimizing OPEX. The model considers only existing, deployed assets. No new investments are allowed. The optimization decision variables are the battery and EV dispatch schedules. The battery capacity is fixed at its existing installed size and is not a decision variable. The goal is to determine the optimal battery and EV operation strategy to reduce costs through time-of-use load shifting and to maximize PV self-consumption, given the existing installed capacities.

Future Scenarios (2030-2050)

For future scenarios, the objective function is modified to minimize the TOTEX, incorporating both investment and operational costs. This analysis is run in 5-year increments (2030, 2035, 2040, 2045, and 2050) to model the progressive evolution of the grid. The optimization decision variables are:

- PV capacity per building
- Battery capacity per building
- Battery dispatch schedule
- EV dispatch schedule

1.6. Future deployment strategies

For the long-term scenarios, the optimization model incorporates the following progressive deployment strategies:

- **PV Generation and Deployment Strategy:**
- Simulation Model. Roof geometry (usable area, azimuth, tilt) for each building is extracted from the RegBL. Photovoltaic generation is simulated using monitored irradiance and temperature from the MeteoSwiss station in Payerne (close to the studied network). Module electrical parameters (SunPower SPR-315E-WHT) are taken from the Sandia PV database to compute the building-level power output. The maximum feasible capacity per building corresponds to 70% of the available roof area.
- Deployment Strategy. The maximum feasible PV potential for 2050 is estimated following an approach consistent with WP3: building rooftops in the studied areas are assessed using the SFOE dataset [13], which rates every rooftop in Switzerland according to its solar suitability. The least favorable surfaces (unfavorable orientation, shading, or low irradiance) are excluded, retaining only the suitable area as the upper bound. To reach full deployment of this potential by 2050, a linear rollout is assumed, making an additional 20% of the suitable rooftop area available at each 5-year time step. This staged deployment reflects the observed tendency for PV installations to prioritize the most favorable rooftops first, with progressively less optimal surfaces being adopted over time. The optimization model then determines the optimal PV sizing on this newly available area, reaching 100% penetration by 2050.
- **Battery Deployment Strategy**: The model's battery optimization logic is enabled for any building that meets one of two conditions:
    - New PV. Any building that has newly installed a PV system (as per the deployment logic above) will also have its battery system optimized.
    - Existing PV. Buildings that already have PV in 2025 but do not yet have a battery are progressively equipped with one. A gradual battery rollout logic is applied, prioritizing buildings by their PV production size and enabling battery optimization for the top 20% in 2030, the top 40% in 2035, and so on, until all existing PV systems are paired with a battery by 2050.
- **Progressive Electrification (HP)**: The impact of HPs adoption is modelled as an exogenous input. The HP load profiles provided by UniGe (WP3) for each year are added directly to the building's baseline demand. This simulates the increased electrical load from the electrification of heating before the optimization is run. The HP operation is not optimized.
- **Progressive Electrification (EV):** The adoption of EVs follows the Full Electrification scenario defined in WP3, which estimates that 100% of private cars will be electrified by 2050. The corresponding EV penetration targets are translated into absolute numbers of vehicles per feeder, distributed proportionally to the number of connection nodes in each area. EVs are assigned

exclusively to residential buildings, identified by building categories (single-family and multi-family dwellings). The assignment follows a two-phase process:

- **Phase 1: Existing EVs.** Buildings with existing EV chargers in the baseline year (2025) are identified from the network data based on their rated charger capacity. The number of EVs per building is inferred from this capacity: 11 kW corresponds to 1 EV, 22 kW to 2 EVs, and so on. These buildings retain their EVs across all scenario years to ensure continuity. Each building is assigned a fixed EV usage profile (charging availability and state-of-charge patterns) derived deterministically from its unique identifier, so that the same building always receives the same profile regardless of the simulation year. For future scenarios (2030–2050), EV deployment is restricted to residential buildings only; chargers located in industrial, commercial, or public buildings are not considered in the rollout.
- **Phase 2: New EVs to reach rollout target.** After Phase 1, if the total number of assigned EVs is below the yearly electrification target, additional EVs are distributed among candidate residential buildings. Buildings are ranked by total annual PV production, prioritizing EV adoption at sites with existing solar installations. Households with solar panels have been found to be 30% more likely to own an EV across ten European countries [14]. EVs are added iteratively, with a maximum number of EVs per building determined by their annual electricity consumption, used as a proxy for the household size and occupancy. Buildings consuming less than 3,000 kWh are assigned a maximum of 2 EVs (studio or single-person households), those between 3,000 and 10,000 kWh, a maximum of 3 EVs (typical family households), and larger buildings receive one additional EV per 5,000 kWh of annual consumption. This threshold approximates the number of dwellings within a building, noting that the Swiss Federal Office of Energy reports a typical household consumption of 2,200-3,900 kWh/year for apartment units excluding heat pumps and electric water heating [15]. Since the consumption in the studied networks for future scenarios already incorporates these additional loads, 5,000 kWh remains a plausible reference value per dwelling in this context.

Each building is assigned a fixed sequence of EV charging profiles drawn from an empirical set of profiles derived from the mobility simulation described in the EV Allocation section. The sequence is based on each building's unique identifier, so a building receiving 1 EV in 2030 and 2 EVs in 2035 always gets the same first profile in both years, with a second profile added in 2035.

1.7. Key Performance Indicators

To assess the impact of PV, battery, and EV deployment across scenarios and tariff structures, a set of key performance indicators is defined below. These indicators are computed at the feeder or network level from the 15-minute resolution simulation output and cover three complementary dimensions: building-level energy autonomy, flexibility utilization, and grid impact.

After Diversity Maximum Demand (ADMD). The ADMD is the highest import power recorded at the feeder connection point over the simulation year, normalized by the number of connected buildings:

$$ADMD = \frac{1}{N} \cdot \max\left(\sum_{i=1}^{N} p_i\right)$$

Where N is the number of buildings and p_i is the demand profile of building i over the simulation year. It reflects the worst-case demand placed on the upstream network per building and is the primary indicator for grid infrastructure dimensioning.

After Diversity Maximum Export (ADME). The ADME captures the peak reverse power flow at the feeder connection point, normalized by the number of connected buildings:

$$ADME = \frac{1}{N} \cdot \max\left(0, \max\left(\sum_{i=1}^{N} -p_i\right)\right)$$

Where negative values of p_i correspond to net generation exceeding local consumption. It characterizes the worst-case export condition that the network must accommodate as PV deployment grows.

Self-Consumption Rate (SC)

The self-consumption rate measures the fraction of total PV generation that is consumed locally rather than exported to the grid:

$$SC = \frac{E_{PV,load}}{E_{PV,total}} \cdot 100$$

Where $E_{PV,local}$ is the annual PV energy consumed on-site (directly, via battery, or via EV) and $E_{PV,total}$ is the total annual PV generation. A high SC indicates that the building makes effective use of its own solar production.

Self-Sufficiency Rate (SS)

The self-sufficiency rate measures the fraction of annual electricity demand that is met by local PV generation:

$$SS = \frac{E_{PV,local}}{E_{total}} \cdot 100$$

A value above 50% indicates that more than half of the building's demand is covered locally. Buildings above the diagonal in SC–SS scatter plots are net producers, meaning annual PV generation exceeds annual consumption.

Flexibility Factor (FF)

The flexibility factor captures the share of total electricity demand met by dispatchable flexible assets, namely stationary battery discharge and vehicle-to-home (V2H) discharge combined:

$$FF = \frac{E_{bat,dis} + E_{V2H}}{E_{total}} \cdot 100$$

Where $E_{bat,dis}$ is the annual energy discharged by the stationary battery and E_{V2H} is the annual energy discharged from EVs to the building. FF grows as battery and EV penetration increases and is sensitive to the tariff structure, which influences the number of battery cycles per year.

EV Load Shift Ratio (EV-LSR)

The EV load shift ratio quantifies the extent to which smart charging increases total EV energy consumption relative to an uncontrolled baseline:

$$EV - LSR = \frac{E_{EV,opt}}{E_{EV,base}}$$

Where $E_{EV,opt}$ is the total annual EV energy consumption under optimized charging and $E_{EV,base}$ is the energy, the fleet would have consumed under uncontrolled charging. Values above 1 indicate that the price signal induces additional grid charging beyond the baseline vehicle energy need. The indicator is computed only for scenarios including EVs.

Net Load Ramp Smoothing Index (NLRSI)

The NLRSI quantifies the effect of a given tariff structure on the volatility of grid import ramps relative to the ST baseline:

$$NLRSI = \frac{\sigma \cdot (\Delta p_{imp,tariff})}{\sigma \cdot (\Delta p_{imp,ST})}$$

Where $\Delta p_{imp}(t) = p_{imp}(t) - p_{imp}(t-1)$ is the 15-minute ramp in feeder import power and σ denotes the standard deviation computed over the full simulation year. The ST denominator is held fixed for each year, providing a consistent baseline across tariffs. A value below 1 indicates that the tariff smooths grid import volatility relative to ST, while values above 1 indicate that the price signal worsens it. The NLRSI is the most relevant indicator from a distribution system operator's perspective, as large ramps impose stress on network assets regardless of the absolute power level.

1.8. Transformer Thermal Aging Model

The equivalent lifetime of a distribution transformer was computed following the thermal aging framework defined in the *IEEE Guide for Loading Dry-Type Distribution and Power Transformers* [1] and applied by Powell et al. [16] for the evaluation of transformer aging under electric-vehicle charging. The model quantifies the progressive loss of insulation life as a function of the transformer's thermal stress, where the hottest-spot temperature is the key determinant of insulation aging.

The analysis combines transformer load and temperature data to calculate (i) the hottest-spot temperature rise, (ii) the instantaneous insulation lifetime, (iii) the accelerated aging factor, and (iv) the equivalent lifetime of the transformer for the observed operating period.

Hottest-Spot Temperature Calculation

The winding hottest-spot temperature $\theta_H(t)$ represents the point of maximum thermal stress within the transformer insulation. It is calculated as the sum of the ambient temperature $\theta_a(t)$ and the load-dependent temperature rise in the winding:

$$\theta_H(t) = \theta_a(t) + \Delta\theta_H(t)$$

$$\Delta\theta_H(t) = C_1 \cdot L(t-1)^{2m} + C_2 \cdot \Delta\theta_H(t-1)$$

Where $\theta_H(t)$ (in °C) is the hottest-spot temperature at the time t, $\theta_a(t)$ is the ambient temperature (°C), $L(t)$ is the transformer load expressed in per-unit of rated kVA, C_1 and C_2 are thermal coefficients related to the transformer's thermal capacity and winding losses, and m is an empirical exponent representing the nonlinear relationship between load and temperature rise (typically $m = 0.8$ for self-cooled dry-type transformers).

Lifetime at Constant Temperature

The thermal degradation of transformer insulation is governed by the Arrhenius law, which links the rate of chemical deterioration to the absolute temperature. The expected lifetime of the insulation under a constant hot-spot temperature T (in °C) is given by:

$$LT = a \cdot \exp\left(\frac{b}{\theta_H + 273.15}\right)$$

Where LT (in hours) is the insulation lifetime at temperature θ_H.a and b are empirical constants specific to the insulation class and material composition.

Table 3. Key values from IEEE C57.96 used in the simulations.

Description	Typical value	Unit	Source / Note
Time step	15	min	
Reference for the hottest-spot temperature	220	°C	IEEE C57.96 (typical for dry-type)
ln(a) - Arrhenius' equation constant at 10 °C	-22.082	-	IEEE C57.96
b - Arrhenius' equation constant at 10 °C	16515	-	IEEE C57.96
Empirical thermal exponent	0.8	–	IEEE C57.96

The constants a and b are determined experimentally from accelerated aging tests. For a class-220 insulation system (corresponding to a 210 °C rated hottest-spot temperature), the IEEE standard recommends a value for $ln(a)$ of -22.082 and for b of 16515 (see Table 3 of the standard shown above). These values correspond to a nominal life expectancy of approximately 180,000 hours (20 years) when operating at the rated temperature of 210 °C. This relationship captures the exponential sensitivity of insulation life to temperature, meaning that even modest overloads or ambient temperature increases can drastically reduce the expected service life.

Accelerated Aging Factor

This factor quantifies how much faster the insulation of a transformer ages under the actual hottest-spot temperature. The accelerated aging factor $F_{AA}(t)$ is computed as:

$$F_{AA}(t) = \frac{LT(\theta_{H,R})}{LT\big(\theta_H(t)\big)}$$

Where $LT(\theta_{H,R})$ is the lifetime at the reference (rated) temperature, and $LT\big(\theta_H(t)\big)$ is the lifetime at the instantaneous hottest-spot temperature. The accelerated aging factor for each interval of time compares life at a reference hottest-spot temperature to life at the realized temperature. It is derived from the Arrhenius law for chemical reaction rates, which captures the exponential dependence of insulation degradation on temperature. The underlying principle is that insulation aging is dominated by thermally activated reactions, mainly oxidation and depolymerization of the cellulose in the paper-oil system, or thermal degradation in dry-type materials.

When the reference and the operation temperature are the same, the accelerated aging factor ($F_{AA}(t)$) has a value of 1, meaning the insulation ages at its nominal rate. If the hottest-spot temperature increases, even slightly, the factor grows exponentially, implying a rapid acceleration of aging.

In a time-varying load profile, $F_{AA}(t)$ is computed at each timestep based on the instantaneous $\theta_{H,R}$. The cumulative effect over a time horizon T is then captured through the equivalent aging factor, which represents the average rate of aging relative to nominal conditions:

$$\overline{F_{AA}} = \frac{1}{T}\sum_{t=1}^{T} F_{AA}(t)$$

Equivalent Lifetime Estimation

The equivalent lifetime estimation translates a varying thermal operating profile into an equivalent duration of life consumed under standard (reference) conditions. In other words, it expresses how much of the transformer's insulation life has been used up, accounting for the fact that aging occurs at different rates depending on the hottest-spot temperature.

The equivalent aging factor $\overline{F_{AA}}$ (i.e., the average of the instantaneous accelerated aging factors) allows estimating the remaining transformer lifetime as:

$$LT_{eq} = \frac{LT(\theta_{H,R})}{\overline{F_{AA}}}$$

Where LT_{normal} is the nominal lifetime (e.g., 180,000 hours or 20 years at the reference hottest-spot temperature defined in IEEE C57.96 or IEC 60076-7).

If $\overline{F_{AA}} = 1.5$, the insulation ages 1.5 times faster than normal, meaning one year of operation consumes 1.5 years of expected life. Tracking the equivalent aging factor over time helps estimate the fraction of life consumed and predict maintenance or replacement needs.

The model requires two primary input datasets. The first is a time series of transformer loading, $L(t)$, derived either from measured power flow or simulated network data and expressed in kVA or as a per-unit value relative to the rated power. The second is a corresponding ambient temperature profile, $\theta_a(t)$, obtained from local weather stations or on-site measurements. Both datasets must share the same temporal resolution; in this study, a 15-minute interval ($\Delta t = 15\ min$) was adopted.

For each time step, the algorithm calculates the hottest-spot temperature $\theta_H(t)$ from the load and ambient temperature, determines the instantaneous lifetime $LT(t)$ through the Arrhenius relation, computes the accelerated aging factor $F_{AA}(t)$, and integrates these values over time to estimate the equivalent lifetime LT_{eq}. The resulting LT_{eq} is expressed in hours and is then converted into years for practical interpretation.

2 Results

This section presents the simulation results for the Estavayer network. Results for Boisy are reported in Appendix A following the same structure. In both cases, the network is organized around medium-voltage lines, referred to here as feeders, each grouping a set of downstream medium-voltage/low-voltage (MV/LV) transformer stations and their low-voltage connections within its supply area. Boisy comprises two feeders, both of which are included in the analysis. Estavayer consists of eight feeders, of which seven are retained: Aumont, Autoroutes, Bel-Air, St-Aubin, Tout-Vent, Zone Industrielle, and Centre-Ville. The eighth feeder, Elsa, was excluded as no load data was available for any of its connections. The results are structured at four levels of analysis. The first level provides a network-level overview, examining how energy demand, asset deployment, and grid flows evolve from 2025 to 2050 across all scenarios and tariff structures. The second level focuses on the Bel-Air feeder, where the full 15-minute resolution of the simulation output allows for a detailed examination of flexibility behavior, self-consumption dynamics, and grid impact. The third level quantifies the flexibility activated by the price signal itself, using energy-based and statistical indicators to characterize how each tariff structure reshapes grid exchanges relative to the flat tariff baseline. The fourth level assesses transformer stress across both networks, examining how increasing DER penetration and tariff-driven flexibility affect transformer loading and thermal aging from 2025 to 2050.

Three tariff structures are considered throughout: the Simple Tariff (ST), which applies a flat electricity price at all hours; the Double Tariff (DT), which distinguishes between peak and off-peak prices; and the Capacity Double Tariff (CDT), which adds a peak power charge on top of the DT structure, penalizing high-power import events. Four deployment scenarios are also considered. The PV Only scenario serves as the baseline, where buildings are equipped with photovoltaic systems following the progressive rollout described in subsection 1.5. The PV + EV scenario adds the full electrification of the private vehicle fleet, as defined by the WP3 targets, without any stationary battery storage. The PV + Battery scenario introduces stationary batteries optimized to maximize self-consumption from PV, without EV integration. Finally, the PV + Battery + EV scenario combines all three technologies, where the battery capacity is optimized to complement the flexibility already provided by the EV fleet.

2.1. Network-Level Overview

2.1.1. Asset Deployment

The results presented in this section cover the full simulation horizon from 2025 to 2050. Figure 4 shows the evolution of installed PV, battery, and EV capacity for the Estavayer network under ST. PV capacity grows from 23.4 MWp in 2025 to approximately 191 MWp by 2050. While small differences in PV capacity exist across scenarios due to the continuous optimization of system sizing, these are negligible in practice and cannot be distinguished in the figure. Battery capacity, by contrast, varies significantly across scenarios and tariff structures. In the PV + Battery case it reaches 236 MWh by 2050 under ST, while the addition of EVs reduces this to around 98 MWh, as the EV fleet partially substitutes the role of stationary storage. Nevertheless, stationary batteries remain a worthwhile addition even in scenarios with a large EV fleet. This is because EVs are not permanently available at the residential connection point: during working hours and trips, the vehicle is absent and cannot contribute to load shifting or self-consumption. Stationary batteries fill this gap, absorbing PV surplus and supplying load during periods when the EV is away, so that the two technologies serve complementary rather than competing roles.

To examine the effect of the tariff structure on battery sizing, Table 4 reports the optimal stationary battery capacity across all scenarios, tariffs, and years. Battery capacity varies considerably across tariff structures and is also strongly influenced by the presence of EVs in the system. An interesting pattern emerges in the PV + Battery + EV scenario under ST and DT: battery capacity grows until around 2040 and then gradually decreases. In the early years, EVs are still scarce, and the stationary battery is the primary source of flexibility, so it grows alongside PV deployment. As EV penetration increases beyond 2040, the fleet provides sufficient flexibility on its own, and this results in reduced stationary battery capacity. Under CDT, this pattern does not appear because the slower battery growth never reaches the point at which EV penetration becomes sufficient to start displacing it.

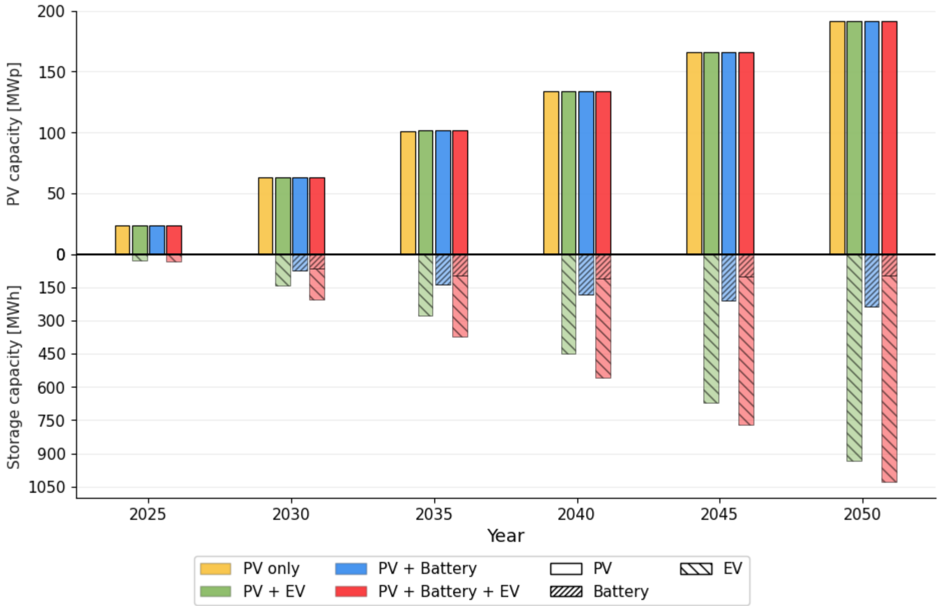

Figure 4. Installed PV capacity (above) and storage capacity (below) for the Estavayer network under ST, from 2025 to 2050. Storage capacity is shown separately for stationary batteries and EV fleet across all four scenarios.

The relatively low battery capacities observed under the DT and the CDT compared to the ST may seem counterintuitive, particularly considering findings from Pena-Bello et al. [17], who showed that capacity-based tariffs tend to result in larger battery installations. In our case, however, two key differences explain this apparent contradiction. Grid charging is enabled, and the CDT retains a double tariff energy component rather than a flat price. These two features fundamentally change the sizing and operation of the battery under each tariff.

Table 4. Optimal stationary battery capacity (MWh) for the Estavayer network across scenarios, tariff structures, and simulation years.

Scenario	Tariff	2025	2030	2035	2040	2045	2050
PV + Battery	ST	1.40	72.6	137.4	181.8	209.4	236.0
	DT		68.0	132.6	175.6	200.3	226.5
	CDT		38.0	85.7	122.6	147.5	171.7
PV + Battery + EV	ST	1.40	64.3	96.3	108.0	100.6	97.6
	DT		60.9	96.9	112.5	108.3	108.9
	CDT		34.7	63.6	75.8	82.0	89.1

To understand why, it helps to consider each tariff separately. Under ST, a flat price applies at all hours, so there is no incentive to charge the battery from the grid. The battery is mainly used to store excess PV generation and discharge it later, and its size is determined purely by the amount of PV surplus available. Under DT, the price difference between peak (38.98 cts/kWh) and off-peak (30.55 cts/kWh) hours creates an energy arbitrage opportunity. The battery charges from the grid during cheap hours and discharges during expensive ones, generating additional cycles beyond those driven by PV alone. This increased cycling means each unit of battery capacity is used more intensively, so the same economic performance can be achieved with a smaller installation. Under CDT, the same arbitrage logic applies and grid charging volumes remain comparable to DT. However, the narrower price spread between peak (22.43 cts/kWh) and off-peak (16.72 cts/kWh) hours reduces the marginal benefit of adding extra capacity, resulting in even smaller installations than under DT.

2.1.2. Energy Demand and PV Generation

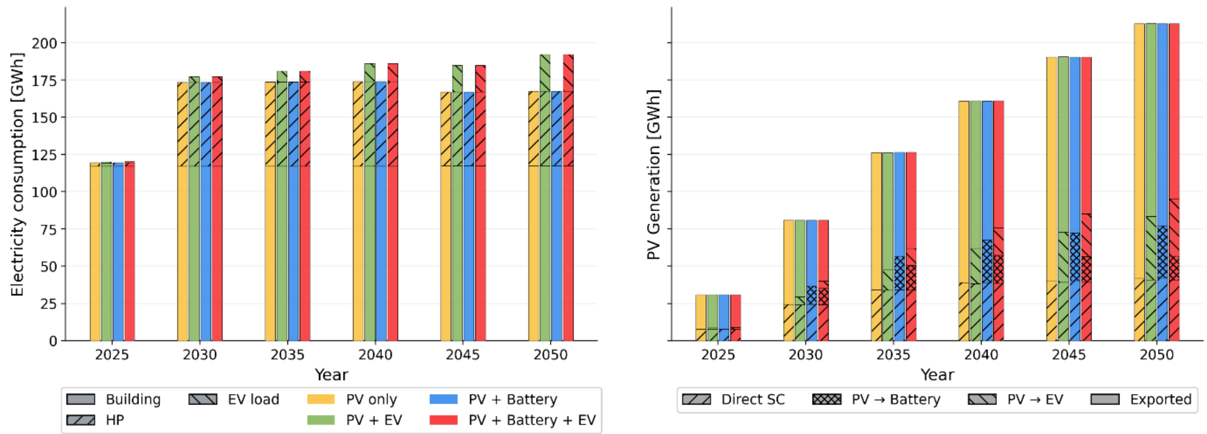

Figure 5. Annual electricity consumption by load type (left) and PV generation distribution by use (right) for the Estavayer network under ST, from 2025 to 2050.

Figure 5 presents the evolution of annual electricity consumption and PV generation distribution for the Estavayer network under ST. Since electricity consumption is independent of the tariff structure and differences in PV generation distribution across tariffs are small, ST is shown as the reference case. The left plot shows total electricity demand decomposed by load type across all scenarios. Base building consumption remains stable at approximately 117 GWh throughout the entire horizon. The most notable feature is the sharp demand increase between 2025 and 2030, driven by the large-scale deployment of heat pumps as defined by the WP3 electrification targets, which adds around 56 GWh to annual consumption. Once heat pumps are fully deployed, their contribution gradually decreases from 56 GWh in 2030 to 50 GWh by 2050, reflecting progressive improvements in building thermal performance, as projected in the Energy Perspectives 2050+ used in WP3. EV charging load, present only in the PV + EV and PV + Battery + EV scenarios, grows steadily from under 1 GWh in 2025 to approximately 25 GWh by 2050 as fleet electrification increases. The combination of these effects results in total annual demand growing from 120 GWh in 2025 to approximately 167 GWh by 2050 in scenarios without EVs, and up to 192 GWh in scenarios including EV charging.

Turning to PV generation, the right plot shows how it is distributed across uses: direct self-consumption, charging to batteries, charging to EVs, and grid exports. As PV deployment grows, total generation increases from around 31 GWh in 2025 to over 210 GWh by 2050. Notably, total PV generation reaches and exceeds total network demand somewhere between 2040 and 2045, highlighting the scale of the solar deployment achieved under the modeled rollout scenarios. In the PV Only scenario, the absence of batteries and EVs means most generation beyond immediate self-consumption is exported to the grid. As batteries and EVs are added, an increasing share is absorbed locally. The distribution of PV generation is largely consistent across tariffs, with two notable exceptions. Under CDT, the share directed to battery charging is considerably lower, consistent with the smaller battery capacities installed under this tariff. Conversely, the share directed to EV charging is slightly higher under CDT in the PV + Battery + EV scenario, as the reduced battery capacity leaves a greater portion of PV surplus available for direct EV charging. These differences are small in absolute terms and are not shown separately, as the tariff comparison follows the same structure as the consumption analysis discussed above.

2.1.3. Grid Exchanges

Figure 6 presents the evolution of annual electricity imports and exports across all feeders, scenarios, and tariff structures. To better assess the effect of local technologies, imports are interpreted relative to total electricity demand. Grid imports gradually decline as local generation and flexibility increase, while exports rise substantially as PV deployment expands.

Figure 6. Annual grid import (solid bars) and export (hatched bars) for the Estavayer network under ST, from 2025 to 2050. Diamond markers indicate total electricity demand for each scenario.

At first glance, the PV + Battery scenario appears to achieve the largest reduction in grid imports, as it consistently shows the lowest import values in absolute terms. This comparison is not straightforward, however, since total electricity demand differs across scenarios: those including EVs have higher consumption due to charging loads, which mechanically raises the amount of electricity drawn from the grid. Figure 7 decomposes electricity consumption by supply source and expresses imports as a share of total demand, whereas the relative performance of each scenario becomes clearer.

Grid exports increase substantially as PV capacity expands. In the PV Only scenario, exports rise from around 23 GWh in 2025 to nearly 170 GWh by 2050. The introduction of local flexibility absorbs part of this surplus: in the PV + Battery + EV scenario, exports reach approximately 118 GWh by 2050, a reduction of roughly 30% compared to the PV Only case. Even so, exports remain significant given the scale of PV deployment. It is worth noting, however, that total electricity demand in scenarios with high PV penetration remains lower than, or at most equal to, what it would be without PV, since local self-consumption directly offsets grid imports. This holds even in 2050 under the highest-penetration scenarios: the network remains a net consumer of grid electricity, and the large export volumes reflect surplus generation rather than a reversal of the overall energy balance.

Differences between tariff structures are relatively modest in absolute terms. In the PV + Battery scenario in 2050, imports increase from about 92 GWh under ST to 94 GWh under DT and 100 GWh under CDT, while exports rise from roughly 136 GWh to 137 GWh and 143 GWh respectively. Although CDT leads to smaller battery capacities, its effect on total yearly exchanges remains limited. When imports are expressed relative to total demand, however, the picture shifts considerably, as discussed below.

Figure 7 decomposes annual electricity consumption by supply source for all feeders combined under ST. In the PV Only scenario, grid import dominates throughout the entire horizon, supplying 93.6% of total demand in 2025 and still 74.8% by 2050, as the absence of any storage or flexible load means most PV generation occurs at times that do not coincide with local consumption.

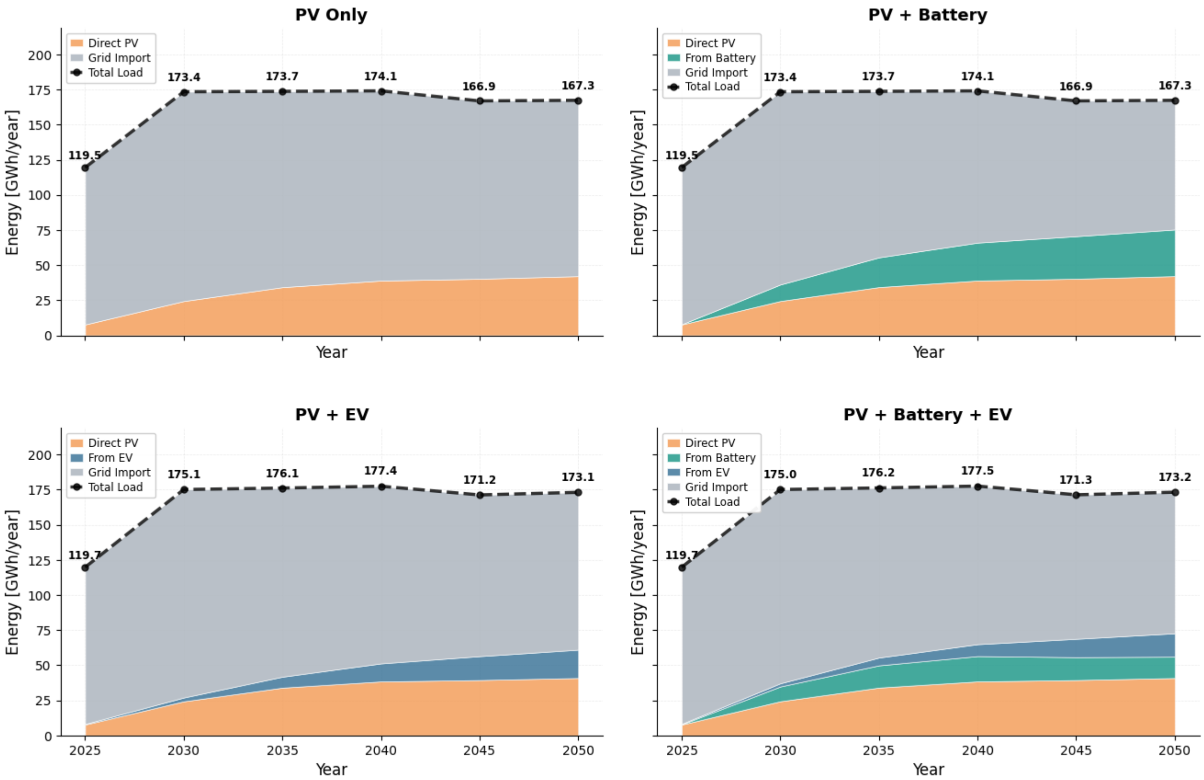

Figure 7. Annual electricity consumption decomposed by supply source for the Estavayer network under ST, from 2025 to 2050. Each panel shows one scenario, with total load indicated by the dashed line.

The introduction of stationary batteries in the PV + Battery scenario substantially increases the locally consumed fraction. Battery discharge grows from a negligible contribution in 2025 to 19.8% of total demand by 2050 under ST, reducing grid import to 55.0%. In the PV + EV scenario, V2H discharge plays a complementary role, contributing 11.7% of total supply by 2050 under ST and reducing grid import to 64.8%. The PV + Battery + EV scenario achieves the lowest grid dependency, with grid import falling to 58.0% by 2050 under ST. The remaining demand is met by direct PV self-consumption (23.6%), battery discharge (8.8%), and V2H (9.6%). The battery share peaks around 2040 at 10.2% and gradually declines thereafter, consistent with the battery sizing pattern discussed earlier: as V2H discharge grows with fleet electrification, stationary battery capacity is reduced accordingly.

Table 5. Grid import as a share of total electricity demand (%) for the PV + Battery and PV + Battery + EV scenarios across all three tariff structures, at selected years.

Scenario	Tariff	2030	2040	2050
PV + battery	ST	79.2	62.1	55.0
	DT	77.2	58.7	51.9
	CDT	81.6	63.4	55.8
PV + battery + EV	ST	78.8	63.4	58.0
	DT	75.6	58.6	53.5
	CDT	79.2	61.3	55.0

Table 5 reports the grid import share for the two battery scenarios across all three tariffs at three points in the simulation horizon. Only the PV + Battery and PV + Battery + EV scenarios are shown, as these are the cases where the tariff structure meaningfully affects the supply mix through battery operation. The PV Only and PV + EV scenarios are largely tariff-independent and are discussed in the text. Years 2030, 2040, and 2050 are selected to represent the early deployment phase, the mid-horizon period where battery and EV penetration are both substantial, and the end of the simulation horizon, respectively.

Two differences stand out across tariff structures. First, under DT and CDT, total demand in scenarios with batteries is higher than under ST, reaching approximately 181 GWh in the PV + Battery case by 2050 compared to 167 GWh under ST. This reflects increased grid charging during off-peak hours incentivized by the time-of-use price structure, which raises total network consumption while also enabling additional battery cycling. As a result, despite the higher absolute demand, the grid import share under DT falls to 51.9% in the PV + Battery scenario, lower than the 55.0% observed under ST. Second, in the PV + Battery + EV scenario, the DT grid import share (53.5%) is again lower than ST (58.0%), while CDT falls in between at 55.0%. The additional cycling enabled by off-peak arbitrage under DT compensates for the higher total demand. Notably, despite CDT producing the smallest battery capacities of the three tariffs, the resulting grid imports remain close to those under ST and DT throughout the horizon. In the PV + Battery scenario, the difference across tariffs never exceeds 5 percentage points at any year, and by 2050 all three converge within a narrow range of 51.9% to 55.8%. This indicates that a smaller battery operated under a capacity tariff, where the peak power charge naturally encourages distributed and frequent cycling, can achieve a level of grid independence comparable to the larger installations sized under ST and DT.

2.1.4. Peak Demand and Export

Figure 8 presents the evolution of peak import and peak export power per building for a representative feeder across all scenarios and tariff structures. Peak import, referred to here as the After Diversity Maximum Demand (ADMD), corresponds to the highest import power recorded at the feeder connection point over the simulation year, normalized by the number of connected buildings to give a per-building average. It reflects the maximum instantaneous demand placed on the upstream network at the level of a typical building in the feeder. Peak export, referred to as the After Diversity Maximum Export (ADME), is its counterpart, capturing the peak power injected back into the grid per building during periods of high PV generation and low local consumption. Together they characterize the worst-case loading conditions that network operators must plan for, and their evolution over time reflects how the deployment of PV, batteries, and EVs reshapes the demand profile seen at the feeder level.

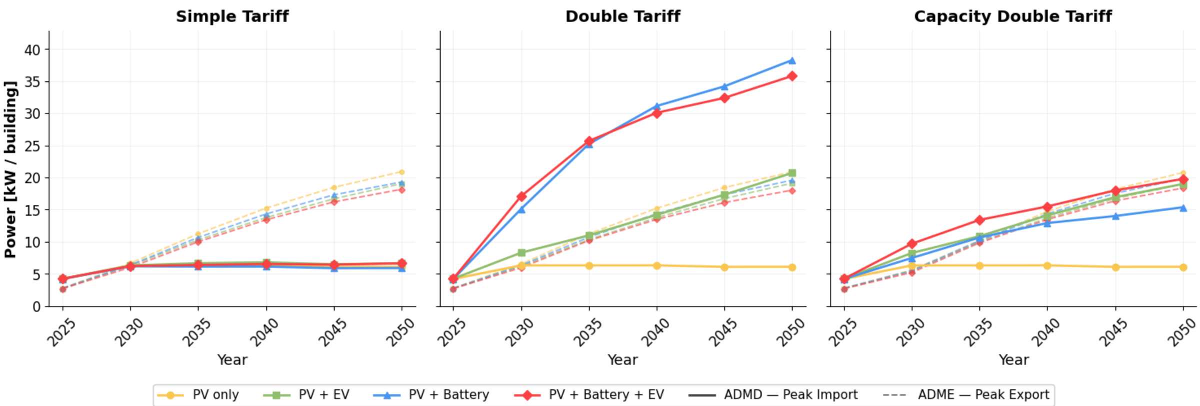

Figure 8. After Diversity Maximum Demand (ADMD, solid lines) and After Diversity Maximum Export (ADME, dashed lines) per building for the Bel-Air feeder across all scenarios and tariff structures, from 2025 to 2050.

Despite differences in feeder size, the patterns are consistent across all seven feeders. Under ST, ADMD remains nearly flat throughout the horizon across all scenarios, staying in the range of 5–8 kW/building for most feeders. Adding batteries or EVs does not significantly increase peak import, since under a flat tariff the battery charges from PV surplus and overnight (EVs) without concentrating demand at any hour. ADME grows steadily as PV capacity expands, but batteries and EVs moderate this growth by absorbing part of the surplus locally.

Under DT, the picture changes dramatically. ADMD in the PV + Battery scenario grows sharply, reaching values between 5 and 7 times higher than under ST by 2050, with per-building peak imports rising from around 5–8 kW under ST to 30–45 kW under DT across most feeders. This is a direct consequence of the sharp price difference in the peak and off-peak hours, which drives all batteries to concentrate their demand within the same narrow time window, creating large coincident peaks at the feeder level. The PV + Battery + EV scenario follows a similar trajectory, though slightly lower in most feeders, suggesting that EV flexibility introduces some temporal diversity in charging and partially smooths the coincidence peak.

CDT largely contains this effect. ADMD under CDT rises to approximately 15–22 kW/building by 2050, roughly 2.5 to 3 times the ST baseline and substantially below the DT values. The capacity charge penalizes high-power import events directly, so battery charging is spread over time rather than concentrated during off-peak windows. This confirms that CDT achieves its intended effect at the feeder level, limiting peak demand growth despite the large battery capacity installed.

The patterns described above are consistent across all seven feeders. **Bel-Air is selected as the representative case for the remainder of the analysis**, with 1088 connected buildings placing it near the middle of the range across the network, which spans from 246 to 1884, making it a reasonable proxy for the network.

2.2. Feeder-Scale Analysis

The network-level results establish how energy demand, asset deployment, and grid exchanges evolve over the simulation horizon, and identify peak demand under DT as the primary concern for grid planning. They do not, however, reveal the temporal dynamics that produce these outcomes. The analysis that follows draws on the full 15-minute resolution of the simulation output to examine how flexibility is dispatched in time, how self-consumption and self-sufficiency evolve at the building level, and how the resulting power flows shape the grid loading profile across seasons and hours of the day. Four complementary perspectives are presented, covering EV and battery dispatch patterns, self-consumption and self-sufficiency distributions across buildings, load duration curves, and seasonal load profiles.

2.2.1. EV and Battery Dispatch Patterns

Figure 9 presents the mean hourly EV charging load aggregated across the Bel-Air feeder for the PV + Battery + EV scenario, comparing the unoptimized initial demand profile against the optimized profiles under each tariff structure for 2030 and 2050. The initial EV load, shown in the left panel, reflects a typical evening-dominated charging pattern, broadly distributed between approximately 15h and 22h and uniform across all months, consistent with vehicles being plugged in upon return from work. Overnight charging is also present, including on weekends, though at low intensity. In the heatmaps, white cells indicate strictly zero mean charging, while light-colored cells indicate positive but low values. The absence of deep color outside the main evening band should therefore not be read as an absence of charging.

Under ST, optimization shifts charging almost entirely to midday hours, concentrated between roughly 9h and 15h. Comparing 2030 and 2050, the highest charging intensity migrates from summer towards spring and autumn months, roughly February to April and September to November. This reflects a gradual shift in the underlying generation profile as PV deployment progresses. South-facing installations dominate the early deployment years and produce generation concentrated around solar noon with a strong summer peak, while as rooftop coverage approaches saturation, an increasing share of new capacity is installed in east-west orientations, which produce a broader daily profile with relatively higher contributions in spring and autumn. By 2050, this shift is sufficient to concentrate flexible charging in these months, as the marginal PV surplus available for flexible loads is greatest during this period. Under DT and CDT, the midday self-consumption pattern is partially preserved but combined with a sharp charging band at the start of the peak hours, visible around 6h in winter and shifting to around 5h in summer. This one-hour shift is an artefact of the simulation data being stored in UTC rather than local time, which places the peak hour boundary one hour earlier during the summer period. The EV charging profiles under DT and CDT are nearly identical, confirming that the capacity charge has little additional effect on EV scheduling beyond what the energy price signal already achieves.

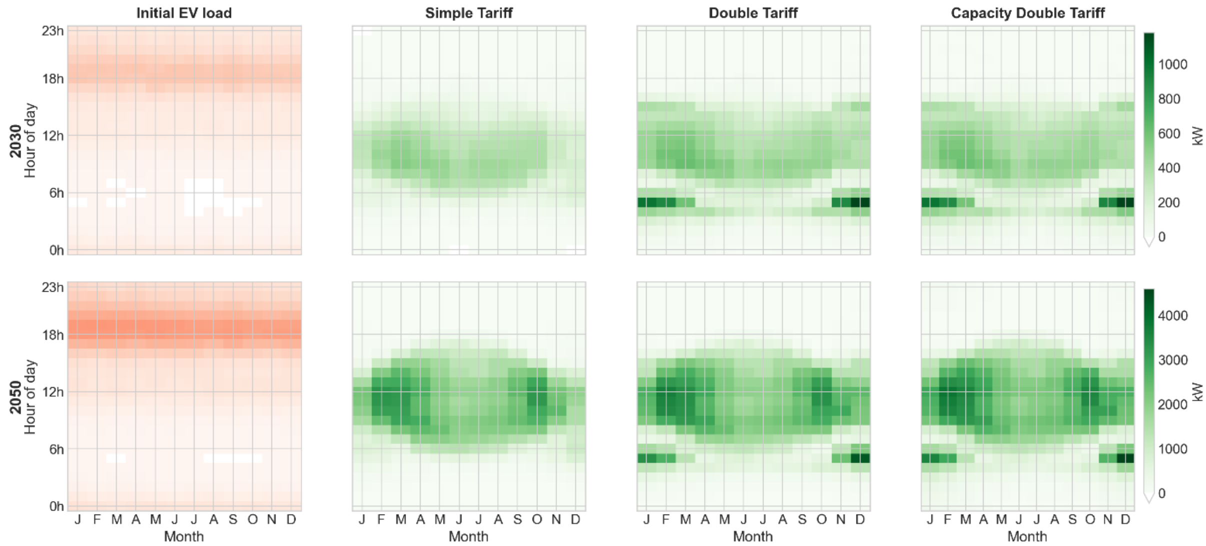

Figure 9. Mean hourly EV charging load (kW) for the Bel-Air feeder, PV + Battery + EV scenario, 2030 (top) and 2050 (bottom). Left: unoptimized baseline. Right: optimized profiles under ST, DT, and CDT.

Figure 10 shows the mean net battery power for the same scenario and year, where positive values indicate charging, and negative values indicate discharging. Under ST, the battery follows a clean PV-driven cycle. Charging during midday hours when solar surplus is available, with intensity peaking in spring and autumn for the same reasons discussed above and discharging in the late afternoon and evening to cover building loads. The pattern is smooth and seasonally coherent, with no abrupt transitions.

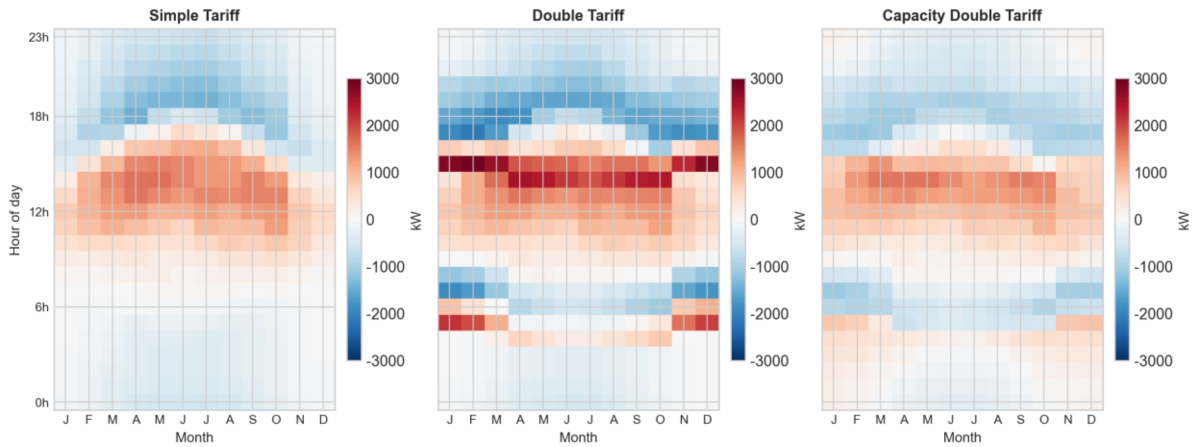

Figure 10. Mean net battery power (kW) for the Bel-Air feeder, PV + Battery + EV scenario, 2050. Positive values indicate charging, negative values indicate discharging.

Under DT, the picture changes distinctly. Two concentrated charging bands appear just before the peak hours, at approximately 6h and 16h, where the battery charges at maximum power in the final off-peak window before prices rise. Peak hours run from 7h to 10h and from 17h to 22h, so charging is systematically concentrated in the hour immediately preceding each price transition to exploit the full price differential. Discharging occurs intensely during peak price hours in the morning and again in the evening. The result is a highly structured, block-like pattern driven by price signals rather than solar availability, which explains the large coincidence peaks observed in the ADMD analysis. Under CDT, the discharge pattern is broadly similar to DT, but the charging bands are considerably less concentrated. The capacity charge penalizes high-power import events, so charging is spread more gradually across the off-peak period rather than ramping to maximum power at the window boundaries. This produces a smoother heatmap and directly explains the substantially lower ADMD values observed under CDT compared to DT.

2.2.2. Self-Consumption and Self-Sufficiency

Self-consumption (SC) and self-sufficiency (SS) rates for all PV-equipped buildings in the Bel-Air feeder are shown in Figure 11 across three years, all scenarios, and all tariff structures. SC measures the fraction of total PV generation that is consumed locally rather than exported to the grid, indicating how effectively a building makes use of its own solar production. SS measures the fraction of annual electricity demand that is met by local PV generation and reflects the degree to which a building is independent from the grid.

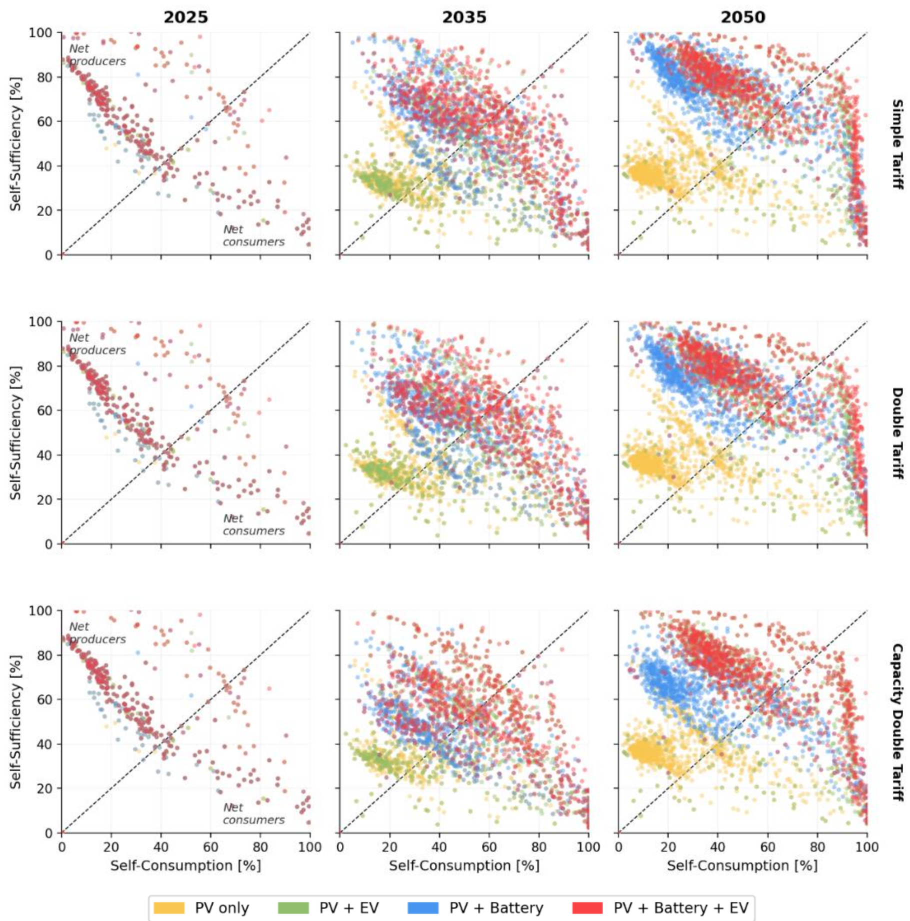

Figure 11. Self-consumption (SC) and self-sufficiency (SS) rates for all PV-equipped buildings in the Bel-Air feeder, shown for 2025, 2035, and 2050 across all scenarios and tariff structures.

Each point represents one building, with the dashed diagonal separating net producers, where SS exceeds SC indicating that annual PV generation exceeds annual consumption, from net consumers, where consumption exceeds generation.

In 2025, PV penetration is still limited, and all scenarios produce nearly identical distributions, with most buildings clustered around moderate SC and low SS values. The spread along the diagonal reflects the diversity of building sizes and PV system capacities already present in the feeder at this stage.

By 2035, the scenarios begin to separate visibly. The PV Only cluster shifts toward higher SC but remains constrained in SS, as buildings consume a growing share of their generation, but total PV output is still modest relative to annual demand. Battery scenarios push buildings upward and to the right, simultaneously increasing both SC and SS as stored energy fills demand gaps that would otherwise require grid import.

By 2050, the separation is pronounced. PV Only buildings form a dispersed horizontal band at relatively low SS values, reflecting the large PV systems installed by this point. Generation exceeds local demand, so self-sufficiency saturates while a significant fraction of production is still exported. The PV + Battery cluster concentrates in the upper right corner, achieving high SC and high SS simultaneously, as batteries capture the surplus that would otherwise be exported and shift it to cover evening and morning demand. The PV + Battery + EV cluster overlaps substantially with the battery-only case but sits slightly lower in SC, consistent with the higher total demand introduced by EV charging, which absorbs more grid electricity and leaves less room for full self-consumption of PV output.

Across tariff structures the distributions are broadly similar, with one consistent difference: under CDT the PV + Battery cluster is slightly more dispersed and shifted toward lower SC compared to ST, reflecting the smaller battery capacities installed under this tariff and their reduced ability to capture all available PV surplus. The difference between DT and ST is less pronounced, consistent with the finding that DT produces battery capacities close to those under ST despite enabling grid charging.

2.2.3. Load Duration Curves

From a network operator's perspective, annual energy balances are of limited relevance. What matters is the magnitude and frequency of peak power flows, as these determine the loading conditions that the grid infrastructure must withstand. The load duration curve in Figure 12 addresses this by sorting all 15-minute net power measurements at the feeder connection point over the full simulation year in descending order, from the highest export event to the highest import event. The resulting curve does not represent the chronological sequence of power flows but rather their statistical distribution. The x-axis indicates how many hours per year the feeder operates at or above a given power level, and the y-axis gives the corresponding power value. Positive values correspond to net export to the grid, negative values to net import. The curve is shown here for 2025, 2035, and 2050 under all scenarios and tariff structures, aggregated across the Bel-Air and Centre-Ville feeders, which are supplied by the same medium-voltage/high-voltage (MV/HV) transformer.

In 2025, PV penetration is still limited, and all curves are nearly indistinguishable, with no meaningful export and a modest peak demand of around 7 MW. By 2035, PV injections begin to appear in the upper portion of the curve, and scenarios start to separate slightly at both extremes. By 2050, the divergence is pronounced. Peak export reaches around 35–40 MW, and peak demand approaches 80 MW in the most extreme cases, while for most of the year, the feeders still operate close to zero net exchange. The transformer rating of 25 MW is already exceeded on the injection side across all scenarios by 2050, and on the demand side, most severely under DT, where coincident battery charging pushes peak import to nearly three times the transformer rating. However, the overlap between curves in the main panels makes it difficult to distinguish the effect of individual tariff structures, particularly at the extremes where the differences are most consequential.

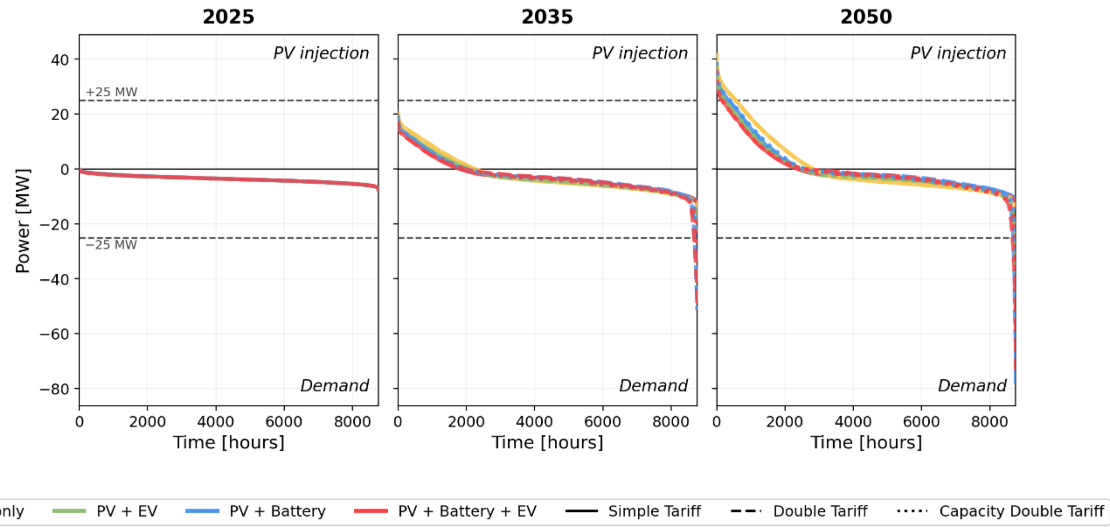

Figure 12. Load duration curves for the Bel-Air and Centre-Ville feeders combined, in 2025, 2035, and 2050 across all scenarios and tariff structures. Positive values indicate net exports, and negative values net imports. The dashed grey lines mark the nominal rating of the shared MV/HV transformer (±25 MVA)

Figure 13 isolates the 2050 curves and zooms into both extremes. In the peak injection range, PV Only produces the highest export power throughout, while scenarios with batteries and EVs reduce peak injection noticeably as surplus generation is absorbed locally. Differences between tariff structures in this region are modest, with CDT and DT running slightly above ST in battery scenarios, consistent with their smaller installed capacities leaving more surplus to be exported.

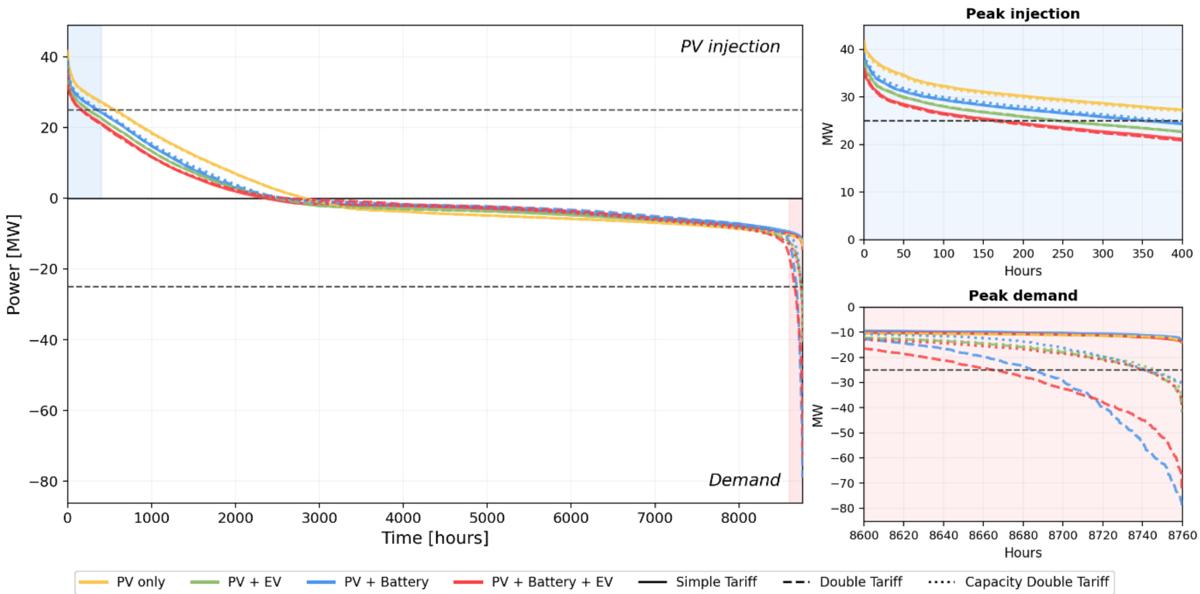

Figure 13. Load duration curve for the Bel-Air and Centre-Ville feeders combined in 2050 across all scenarios and tariff structures, with insects zooming into the peak injection range (top right) and peak demand range (bottom right). Positive values indicate net exports, and negative values net imports. The dashed grey lines mark the nominal rating of the shared MV/HV transformer (±25 MVA)

In the peak demand range, the picture reverses sharply. PV Only and PV + EV produce the lowest peak demand, while battery scenarios under DT reach import peaks approaching 80 MW at the annual maximum. This is the direct expression of the coincident charging behavior identified in the heatmaps.

Under DT, all batteries ramp simultaneously just before peak hours, creating extreme demand spikes that occur only a few hours per year but far exceed the transformer rating. Under DT, PV + Battery reaches a slightly higher peak than PV + Battery + EV, as EV flexibility introduces some temporal diversity in charging that partially smooths the coincidence peak. Under CDT, peak demand is considerably lower and remains much closer to the ST baseline, confirming that the capacity charge is effective at limiting worst-case grid loading.

2.2.4. Seasonal Load Profiles

Seasonal load profiles are shown in Figure 14 for the Bel-Air feeder in 2050, where the reference day for each season is selected as the day with the highest peak import grid under DT and applied consistently across all tariffs to allow direct comparison. The winter profile corresponds to 19 December and the summer profile to 31 August. Each panel shows the net feeder power over 24 hours, with positive values indicating import from the grid and negative values indicating export.

In winter, the ST column reveals the baseline daily demand shape in the absence of price signals. A broad morning and evening demand peak of around 5 to 7 MW, a midday dip where PV generation partially offsets load, and a smooth profile throughout the day. Adding EVs and batteries under ST shifts some demand away from the evening but does not significantly alter the overall shape or magnitude. Under DT, the picture changes dramatically. Two sharp spikes appear at approximately 6h and 16h, reaching 40 MW and 32 MW, respectively, for the battery scenarios, corresponding to the simultaneous ramp-up of all batteries just before the peak price windows begin. Outside these spikes, the demand profile is lower than under ST, as batteries discharge aggressively during peak hours to exploit the price differential. Under CDT, the spikes are still visible but reduced to around 20 MW, confirming that the capacity charge discourages the most extreme coincidence charging events while preserving the underlying price-driven charging logic.

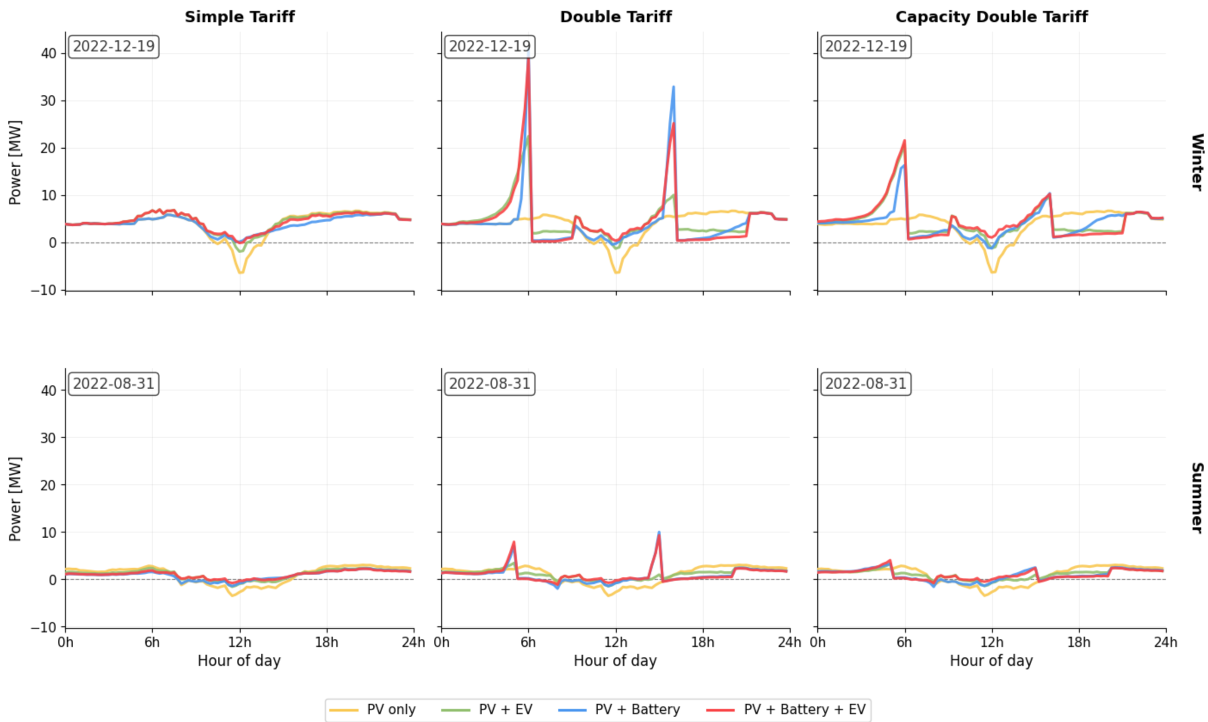

Figure 14. Net feeder power (MW) for the Bel-Air feeder on the worst demand day of winter (top) and summer (bottom) in 2050, across all scenarios and tariff structures. Positive values indicate grid imports, negative values export.

In summer, the profiles look fundamentally different. PV generation is large enough to push net feeder power below zero for most of the central hours of the day across all scenarios, with export reaching around 5 MW under PV Only and battery scenarios. Under ST, batteries and EVs absorb much of this surplus, reducing the midday export and the evening import peak. Under DT, the characteristic spikes reappear at the price transition hours, though they are smaller in magnitude than in winter because some of the battery charging energy comes from local PV surplus rather than grid import. Under CDT the summer profile is smooth and closely tracks the ST case, with only modest differences between scenarios, reflecting the fact that in summer, the capacity charge is less binding since PV generation naturally limits the peak import power.

2.3. Flexibility Quantification

The preceding sections show the consequences of price-driven dispatch on grid loading and building-level energy balances, but do not distinguish between flexibility that would have occurred anyway under cost minimization and flexibility that the price signal itself induced. What remains to be quantified is the degree to which the observed changes represent genuinely activated flexibility, and how efficiently that flexibility is deployed from a grid perspective. This section addresses these questions through two complementary analyses. The first is a direct comparison of grid import energy under each tariff against the ST baseline, and the second is a set of indicators that summarize the flexibility contribution of each technology and tariff combination.

2.3.1. Ex-ante and Ex-post Flexibility

The ST serves as the ex-ante reference in this analysis, representing the flexibility that the system activates in the absence of any price signal beyond flat cost minimization. Under ST, batteries and EVs still shift demand in time to maximize self-consumption of local PV generation, with no incentive to respond to grid conditions or exploit price differentials. The DT and CDT profiles represent the ex-post state, where explicit price signals activate additional flexibility. The difference in feeder import power between each tariff and ST therefore quantifies the flexibility that the price signal itself induces, independently of the technology deployment.

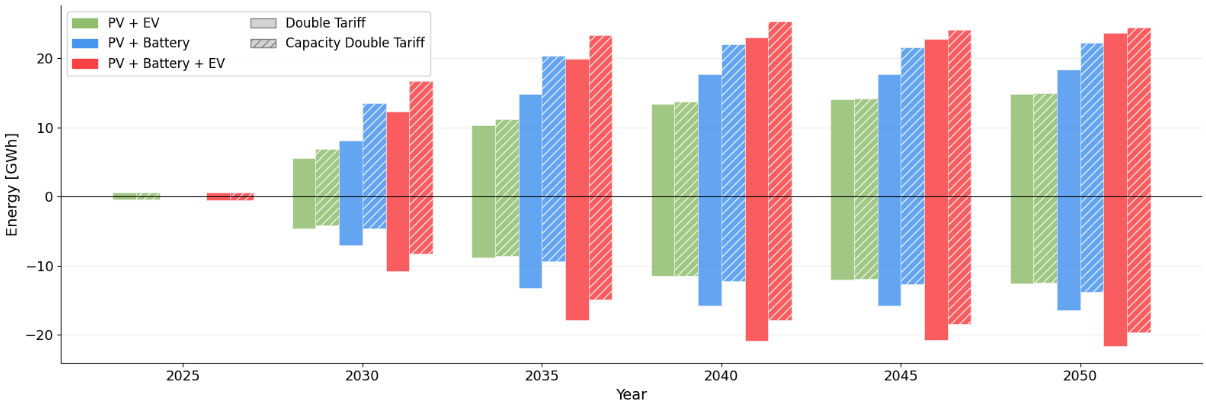

Figure 15. Annual volume of activated flexibility for the Estavayer network, expressed as additional off-peak grid import (positive) and reduced peak-hour import (negative) relative to ST, across all scenarios and years under DT (solid) and CDT (hatched).

Figure 15 shows this activated flexibility for the Estavayer network across all scenarios and years, expressed as the annual volume of additional grid import during off-peak hours and reduced grid import during peak hours, both relative to ST. Positive values, therefore, represent additional grid energy drawn under DT or CDT that was not drawn under ST, while negative values represent grid energy that was avoided relative to the ST baseline. Together, they quantify the positive and negative flexibility activated by the price signal itself. In scenarios without stationary batteries, activated flexibility remains modest throughout the horizon. The PV-only scenario is excluded from the figure as it contains no flexible assets, and the price signal has nothing to act on, since we do not consider smart inverters in this study. PV + EV contributes a growing volume from 2030 onward, driven by smart EV charging and V2H discharge responding to price transitions, reaching approximately 15 GWh of additional off-peak import and 12 GWh of reduced peak import by 2050. The bulk of activated flexibility comes from stationary batteries. Under both DT and CDT, battery scenarios draw over 20 GWh of additional off-peak energy from the grid annually by 2050, while simultaneously reducing peak-hour import by a comparable amount.

A consistent asymmetry is visible across all battery scenarios and years. The positive bars are systematically larger than the negative ones. This reflects the fact that DT and CDT do not merely redistribute existing demand in time but also induce new net consumption. Under ST, batteries charge exclusively from PV surplus, keeping total grid import relatively low. Under DT and CDT, the off-peak price discount creates an incentive to draw additional energy from the grid, generating charging volumes that have no corresponding reduction elsewhere in the day. The positive bars, therefore, capture two distinct effects. Load shifting away from peak hours, and net additional grid charging that did not occur under ST. The negative bars capture only the first of these effects, and their difference defines the net additional energy drawn from the grid purely because of the price signal.

Comparing the two tariffs on this metric reveals a counterintuitive result: despite its explicit aim of limiting peak power events, CDT induces more net new grid consumption relative to ST than DT does. Under DT, concentrated discharge during peak price windows largely offsets the additional off-peak charging, with net additional grid consumption growing from 1.4 GWh in 2030 to approximately 2.0 GWh by 2050. Under CDT, the picture is different. The capacity charge discourages high-power discharge events, so rather than concentrating discharge during peak hours, the battery releases energy gradually across a wider time window. Additionally, CDT incentivizes the installation of smaller battery capacities than DT, meaning the total energy available for discharge is lower, which further limits the peak reduction that can be achieved relative to the off-peak charging volumes. Together, these two effects mean that a greater share of the additional energy drawn from the grid during off-peak hours is discharged outside the peak import periods, leaving a larger net surplus without a corresponding peak offset. Net additional grid consumption under CDT consequently reaches 8.4 GWh in 2035 before declining to 4.7 GWh by 2050, considerably higher than the 2 GWh observed under DT. This means that total network demand is higher under CDT than under DT, despite CDT activating a lower absolute volume of flexibility overall.

2.3.2. Flexibility indicators

Three indicators are computed and presented in Figure 16 for the Estavayer network across all scenarios, tariff structures, and years, as previously defined in subsection 1.7: the Flexibility Factor (FF), the EV Load Shift Ratio (EV-LSR), and the Net Load Ramp Smoothing Index (NLRSI).

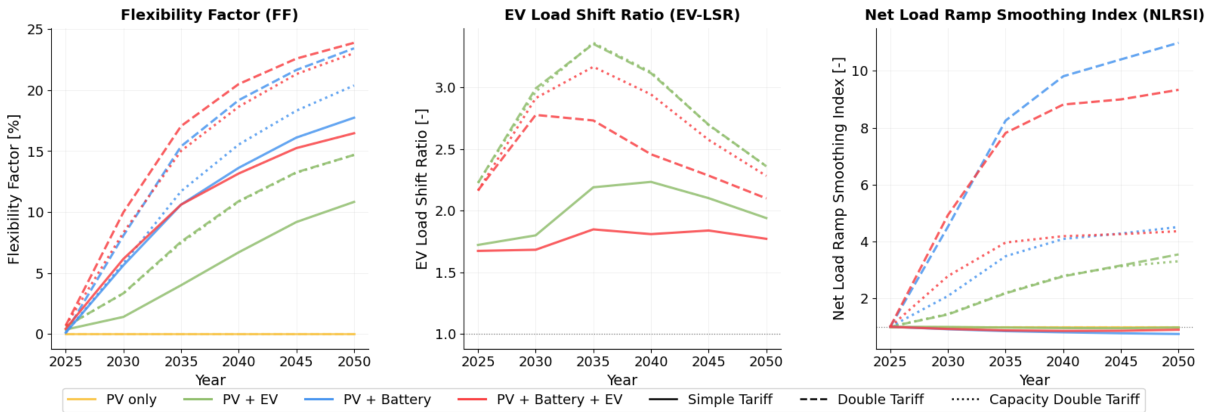

Figure 16. Flexibility Factor (FF, left), EV Load Shift Ratio (EV-LSR, center), and Net Load Ramp Smoothing Index (NLRSI, right) for the Estavayer network across all scenarios, tariff structures, and years.

The FF grows steadily across all battery and EV scenarios, reaching approximately 16% under ST and 24% under DT for the PV + Battery + EV scenario by 2050. PV Only remains at zero throughout, as without flexible assets, no local supply shifting occurs. Under ST, PV + Battery and PV + Battery + EV converge to nearly identical FF values by 2050, suggesting that at full deployment the stationary battery contributes a similar share of local supply regardless of whether EVs are present. The gap between tariffs widens over time, with DT producing the highest FF due to the additional battery cycling driven by off-peak grid charging, followed by CDT and then ST. The PV + EV scenario reaches around 11% under DT by 2050, reflecting the growing contribution of V2H discharge as fleet electrification progresses.

The EV-LSR confirms that all tariff structures induce substantially more EV energy consumption than the uncontrolled baseline, with values ranging from approximately 1.7 in 2025 to between 1.9 and 3.2 by 2050, where the lower end corresponds to the PV + Battery + EV scenario under ST and the upper end to PV + EV under DT. The PV + EV scenario consistently shows higher ratios than PV + Battery + EV, as the stationary battery competes with EVs for PV surplus and off-peak charging opportunities, reducing the additional grid charging attributable to the EV fleet alone. The ratio peaks around 2035 before declining slightly, as growing PV availability reduces the incentive for grid charging once more surplus is available for direct self-consumption. All values remain well above 1 throughout, confirming that no tariff structure preserves uncontrolled EV consumption patterns.

The NLRSI tells the most consequential story from a grid operator's perspective. Under ST, all scenarios remain close to or below 1 throughout the horizon, indicating that flexibility deployed under a flat tariff modestly smooths grid import ramps. Under DT, the index rises sharply from 2030 onward as battery penetration grows, reaching approximately 11 for PV + Battery and 9 for PV + Battery + EV by 2050, meaning import ramps are an order of magnitude more volatile than under ST. CDT sits between the two, reaching values of around 4 to 5 by 2050, substantially lower than DT but still well above 1. The PV + EV scenario remains near 1 under ST throughout the horizon but reaches values of around 3 under DT and CDT by 2050, suggesting that EV flexibility alone can still worsen ramp behavior when a time-of-use or capacity price signal is applied, though to a much lesser degree than battery scenarios.

These results highlight a tension in tariff-driven flexibility. The same price signal that activates flexible assets can, if it contains sharp price transitions, generate coincident demand peaks that undermine the very grid stability the flexibility was meant to support. Under DT, all batteries respond simultaneously to the same price boundary, concentrating imports in a narrow window and producing the severe ramp events captured by the NLRSI. CDT partially mitigates this through the capacity charge, but the volumetric DT component it retains still enables simultaneous asset activation and grid-to-battery charging, which limits how far the capacity charge alone can smooth coincident behavior. This distinction is important when comparing it with previous work. Studies report that capacity-based tariffs lead to larger batteries and better grid outcomes, such as Pena-Bello et al. [17], typically assumed a flat energy price combined with the capacity charge and did not allow grid charging. In that configuration, batteries respond only to PV surplus and local demand rather than to a shared price boundary, making simultaneous activation across buildings far less likely. Once grid charging is enabled and the energy component retains a time-of-use structure, the dynamics change fundamentally. A more grid-compatible alternative would be to move toward fully dynamic tariffs with smoother, continuously varying price signals rather than discrete peak and off-peak boundaries, which would reduce the incentive for all assets to respond at the same moment. This points to tariff design as a critical lever that must be considered jointly with flexibility deployment, rather than as an independent policy instrument.

2.4. Transformer Stress Analysis

2.4.1. Estavayer

The results for 159 MV/LV transformers in the zone of Estavayer were analyzed for four scenarios (PV, PV + Battery, PV + EV, and PV + Battery + EV) and for six years (2025-2050 in 5-year increments). The results are presented in different figures displaying the stress distribution of all the transformers over time. We divided stress into three stress bands, representing different levels of loading on the distribution infrastructure, and presented them as a share of the total amount of transformers (in %). The low-stress band (<1.44) corresponds to operating conditions where network components are within their limits, and the system has sufficient flexibility to accommodate additional load or generation for the short term. This limit is given by the maximum charge from the transformer divided by the nominal capacity of the transformer, as reported by the DSO (Groupe E in this case). The moderate-stress band (1.44–1.8) indicates increasing utilization of network capacity, where the grid begins to approach operational constraints, and the risk of congestion or voltage issues becomes more likely. The high-stress band (>1.8) reflects conditions where the network is heavily loaded and technical limits are frequently approached or exceeded, signaling a high probability of congestion and potential need for mitigation measures such as curtailment, storage, or grid reinforcement. The duration of the overload capacity significantly accelerates thermal aging of transformers and increases the risk of voltage violations. For planning, within this analysis, we use the threshold of 1.8 p.u. as an indicative reinforcement trigger, meaning that transformers exceeding this loading level are considered to operate under high stress and would typically be flagged for operational mitigation or potential grid reinforcement from a DSO planning perspective. In addition, a thermal threshold of Θ_H = 160°C is used to identify conditions where hotspot temperatures reach levels associated with accelerated insulation aging. Transformers exceeding this temperature are considered to operate under severe thermal stress, which would also prompt operational intervention or infrastructure reinforcement in practical distribution system operation.

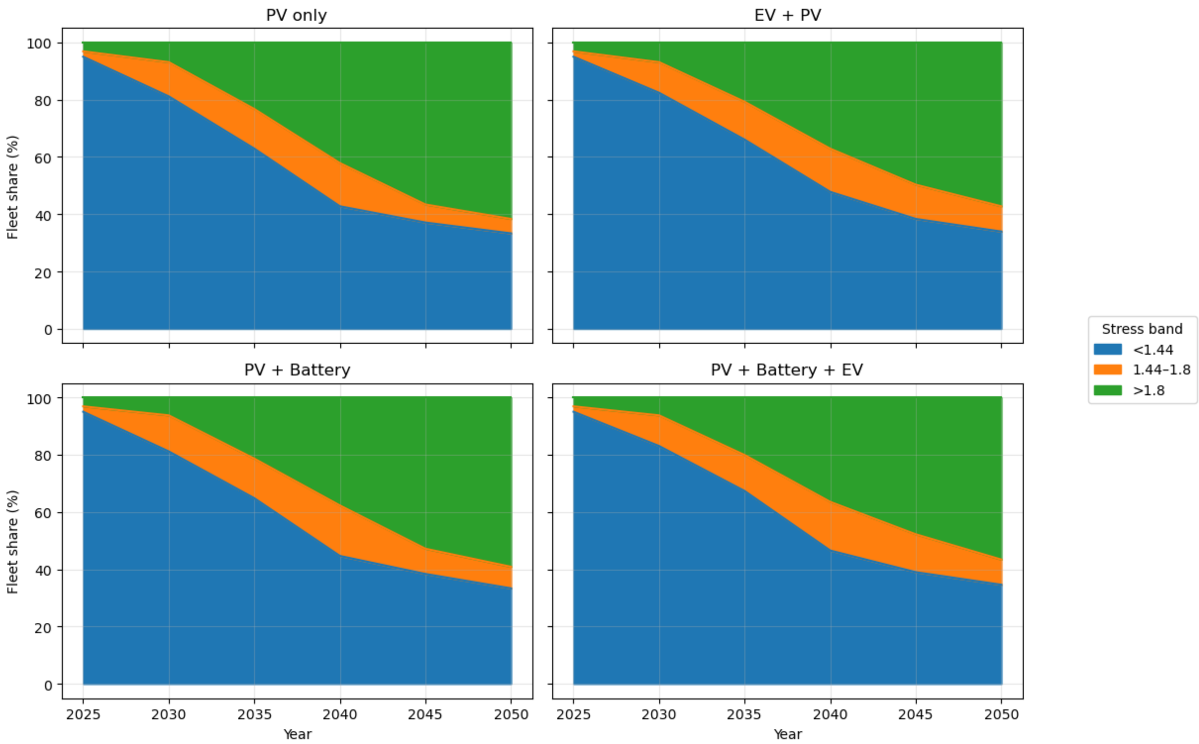

Figure 17. Evolution of Estavayer’s transformer fleet stress distribution from 2025 to 2050 under a single tariff (ST) across four configurations: PV only, EV + PV, PV + Battery, and PV + Battery + EV. The stacked areas show the share of the fleet operating in three loading bands (<1.44, 1.44–1.8, >1.8).

Figure 17 displays the stress distribution over time for the ST. The ST produces the most gradual transition overall from the transformer perspective. Because there is no time differentiation or explicit capacity signal, the system evolves mostly according to the physical penetration of PV. As a result, the growth of the high-stress band is slower than under DT and like CDT. However, the absence of incentives for load shifting means that EV integration does not significantly mitigate stress unless batteries are present.

Under DT (see Figure 18), the transition toward higher stress occurs fastest when only PV is present. By 2050, roughly two-thirds of the fleet lies in the high-stress band in the PV-only case. Adding EVs slightly worsens the situation, suggesting that EV charging aligns poorly with PV production when only price differentiation between peak/off-peak exists. Batteries significantly reduce low-stress shares early but stabilize the system later because they absorb PV surplus; however, even with batteries and EVs, the high-stress share still exceeds ~70% by 2050.

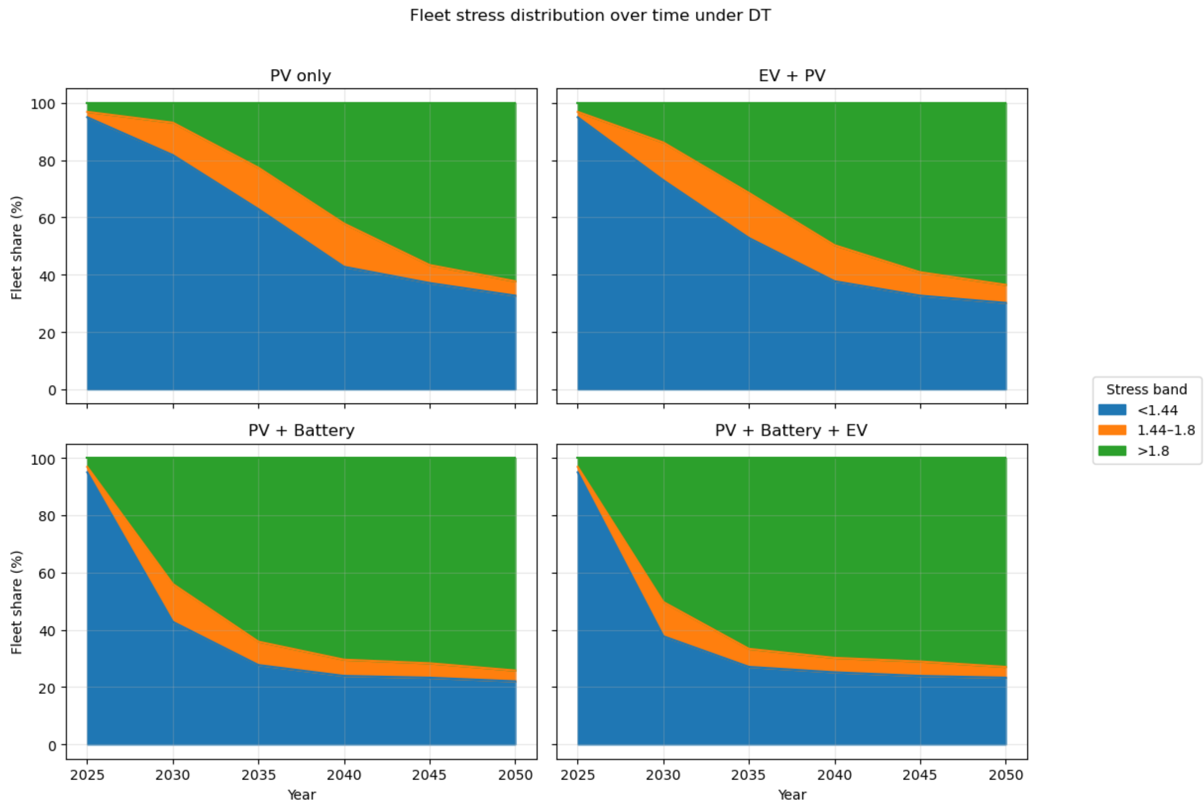

Figure 18. Evolution of Estavayer's transformer fleet stress distribution from 2025 to 2050 under a double tariff (DT) across four configurations: PV only, EV + PV, PV + Battery, and PV + Battery + EV. The stacked areas show the share of the fleet operating in three loading bands (<1.44, 1.44–1.8, >1.8).

With CDT the system behaves more smoothly than under DT. The decline of the low-stress band is slower and the moderate stress band (1.44–1.8 p.u.) remains slightly larger for longer. The effect of the capacity component is visible especially in the PV + Battery case where high stress grows more gradually than under DT. When EVs are included, CDT still leads to high stress by 2050 but less abruptly than with DT.

Across all three tariffs, the results are consistent with the different combinations of technologies (see Figure 36). The results indicate that a growing portion of the fleet operates close to infrastructure limits by 2050. Average transformer loading rises from approximately 0.64 p.u. in 2025 to around 2.2–2.5 p.u. by 2050 under most scenarios. At the same time, the upper tail of the distribution increases strongly, with the 90th percentile rising from about 1.18 p.u. in 2025 to 4.2–4.6 p.u. by 2050, which indicates that a growing fraction of the fleet operates close to or above critical loading levels. The transition is primarily driven by the physical growth of PV capacity, which increases power flows and pushes more transformers toward their operational limits despite the presence of batteries and EV flexibility. Adding EVs without storage generally does not relieve stress and can even slightly increase it if charging patterns coincide with existing peaks. Batteries systematically delay the shift toward the high-stress band because they buffer PV output and reshape the load curve. In this sense, technology adoption seems to be more important than tariff structure, although tariff structure do influence the speed and severity of stress growth.

Differences across tariffs mainly appear in the upper tail of the distribution. Under the DT tariff, the concentration of power flows is significantly stronger when batteries respond to price signals. In the PV + Battery scenario, mean loading reaches 4.03 p.u. by 2050, compared with 2.37 p.u. under ST and 2.40 p.u. under CDT. The 90th percentile reaches 7.27 p.u. under DT, while remaining around 4.5 p.u. under the other tariffs.

The high stress share of transformers in 2025 across the three tariffs corresponds to five transformers (i.e. 3.14%). This reflects the limitation of the load allocation method. The feeder level matching correction in Stage 2 (explained in subsection 1.1) ensures that aggregated demand at the feeder matches the DSO measured profile, but individual transformer loadings are derived from the building level allocation and are not corrected against measured data at that level. As a result, the allocation is accurate at the feeder level but introduces local discrepancies at individual low-voltage transformers, which explains why these five transformers already appear overloaded in 2025.

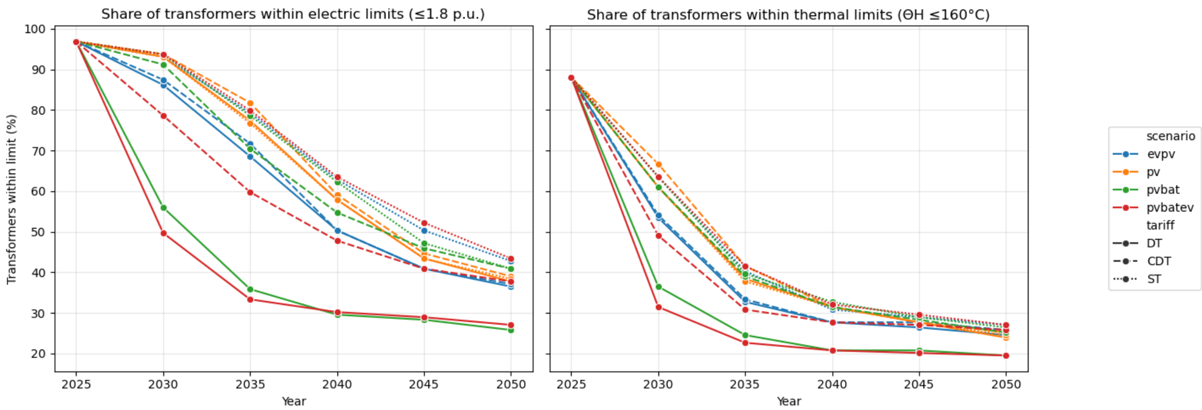

Figure 19. Share of Estavayer transformers operating within electrical limits (≤1.8 p.u., left) and thermal limits (hot-spot temperature Θ_H ≤160 °C, right) from 2025 to 2050 under three tariff schemes (ST, DT, CDT) and four technology scenarios (PV, EV + PV, PV + Battery, PV + Battery + EV).

Figure 19 compares the share of transformers that remain within electrical limits (≤1.8 p.u.) and thermal limits (Θ_H ≤160°C) in Estavayer across the three tariffs and four scenarios. In 2025 almost the entire fleet operates within electrical limits (around 97%), while about 88% remains within the thermal threshold. As DER penetration increases, the acceptable share decreases steadily in all scenarios. By 2050, the share of transformers remaining within electrical limits falls to roughly 26–44% across scenarios, meaning that more than half of the fleet would exceed the planning loading threshold under different technology combinations. The decline is even stronger for the thermal criterion with only about 19–27% of transformers remaining within acceptable hotspot temperatures by the end of the period. Differences across tariffs are relatively moderate, with the capacity-based tariff (CDT) and single tariff (ST) generally maintaining slightly higher shares of acceptable transformers compared with the dynamic tariff (DT). Across scenarios, configurations including batteries and EVs tend to accelerate the decline in acceptable transformers, particularly in the early transition years. Other thermal results are presented in Appendix B.

2.4.2. Boisy

Like the results of Estavayer, in this section we present the results for Boisy, with significantly less transformers (only 24), for the same scenarios and years. Figure 20 displays the stress distribution over time for the ST tariff. Under this tariff the transition is relatively gradual and largely driven by the physical growth of PV generation. The share of transformers in the high-stress band increases steadily over time in the PV-only configuration, reaching roughly half of the fleet by 2050. When EVs are added without storage, the evolution becomes slightly more stable with the share of transformers in the low-stress band remaining around 42% toward the end of the period, which indicates that EV demand does not strongly amplify transformer loading under a single tariff structure. The presence of batteries moderates the evolution further. In the PV + Battery and PV + Battery + EV scenarios the high-stress share still grows over time but remains somewhat lower than in the PV-only case because batteries absorb part of the PV surplus and smooth power injections into the grid. Overall, under ST the system evolves progressively without abrupt changes in the stress distribution.

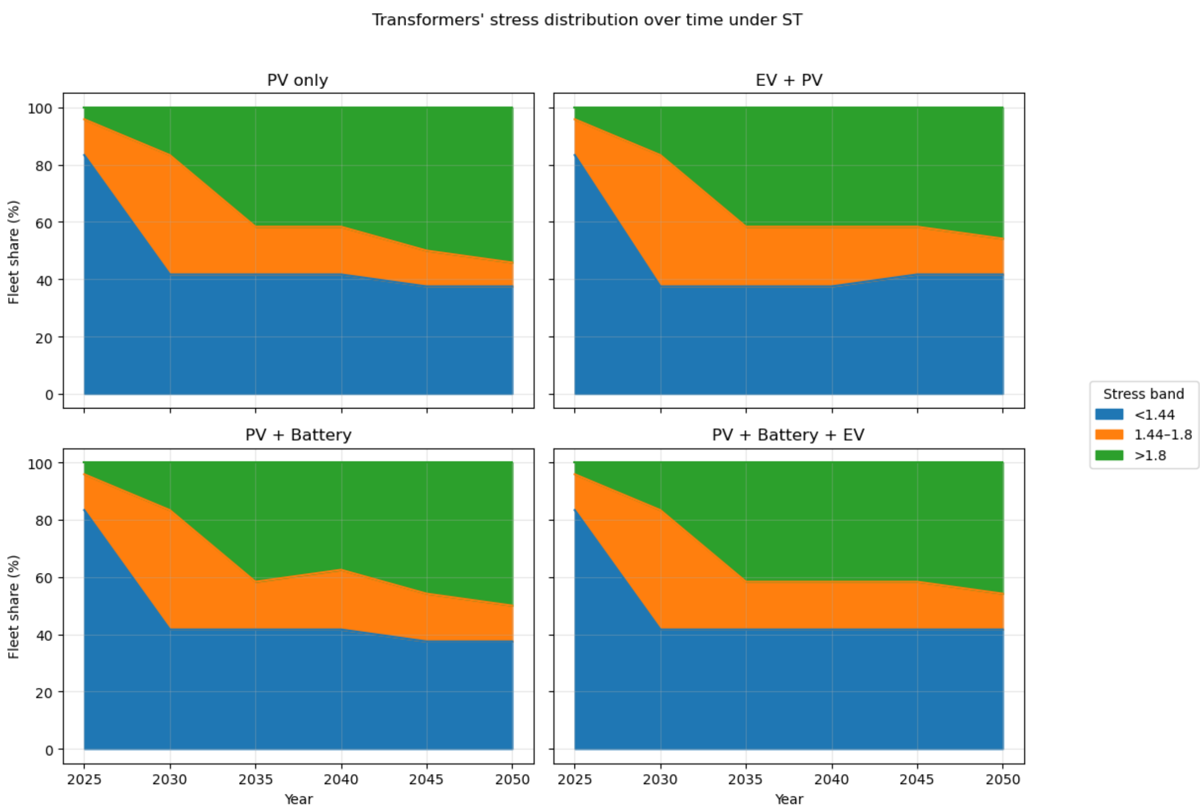

Figure 20. Evolution of Boisy's transformer fleet stress distribution from 2025 to 2050 under a simple tariff (ST) across four configurations: PV only, EV + PV, PV + Battery, and PV + Battery + EV. The stacked areas show the share of the fleet operating in three loading bands (<1.44, 1.44–1.8, >1.8).

Under the DT tariff (see Figure 21) the transition toward higher stress is noticeably faster in scenarios including batteries. When only PV is present, the evolution remains similar to the ST case, with the high-stress share increasing gradually over time reaching more than half of the total transformers by 2050 (54.2%). In the EV + PV scenario there is an increase in stress (66.6%). In the PV + Battery and PV + Battery + EV scenarios the share of transformers operating in the high-stress band rises rapidly and dominates the fleet by 2050 (reaching 75%). This reflects a similar contribution from battery arbitrage and EV charging to transformer stress.

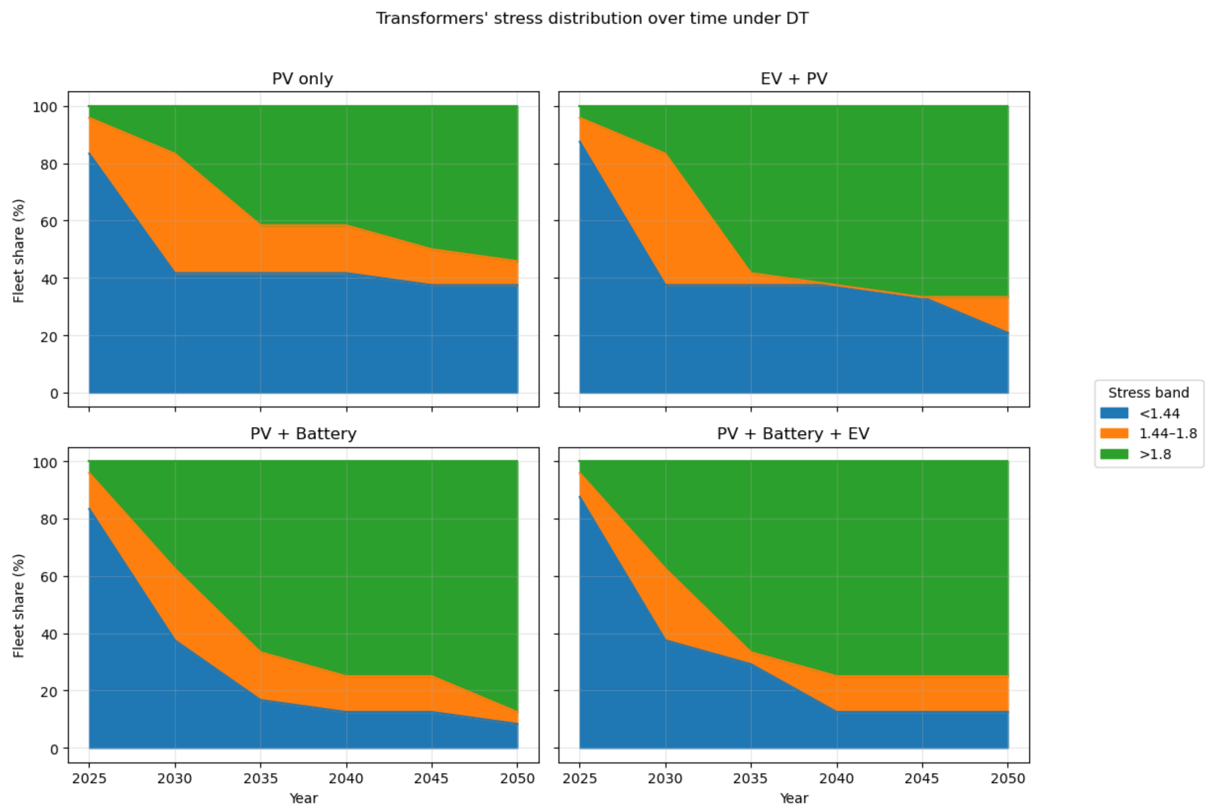

Figure 21. Evolution of Boisy's transformer fleet stress distribution from 2025 to 2050 under a double tariff (DT) across four configurations: PV only, EV + PV, PV + Battery, and PV + Battery + EV. The stacked areas show the share of the fleet operating in three loading bands (<1.44, 1.44–1.8, >1.8).

With a capacity-based tariff (CDT), the evolution of the system is smoother than under DT. The decline of the low-stress band occurs more gradually, and the moderate-stress band persists for a longer period. Batteries under CDT contribute to stabilizing transformer loading because the capacity component discourages strong peak power injections, with only 33.3% of the transformers reaching the high-stress band. As a result, the PV + Battery and PV + Battery + EV scenarios exhibit a more balanced distribution across stress bands compared with DT, with the same share reaching the high-stress band. Although the high-stress share still grows by 2050, the transition is less abrupt, and a larger portion of the fleet remains in the low-stress band.

Across all three tariffs, the general trend remains consistent with PV penetration being the main driver pushing transformers toward higher loading levels. Average transformer loading increases from approximately 0.69 p.u. in 2025 to around 1.6–1.9 p.u. by 2050, depending on the scenario and tariff. The upper tail of the distribution also grows significantly, with the 90th percentile increasing from about 1.54 p.u. in 2025 to values between roughly 2.0 and 3.7 p.u. in 2050, depending on the configuration. This indicates that an increasing fraction of the fleet operates near or above critical loading levels over time.

Differences across tariffs mainly appear in the upper tail of the distribution. Under DT, price-driven battery operation leads to the strongest concentration of flows. In the PV + Battery scenario, the mean loading reaches about 4.34 p.u. by 2050, and the 90th percentile reaches approximately 7.18 p.u., with extreme values exceeding 14 p.u. In comparison, under ST and CDT the mean loading remains around 1.6–1.8 p.u. by 2050, and the 90th percentile remains near 2.0–2.6 p.u. These results indicate that technology adoption, particularly batteries, strongly shapes the evolution of transformer stress, while tariff design influences the synchronization of power flows and therefore the severity of peak loading conditions.

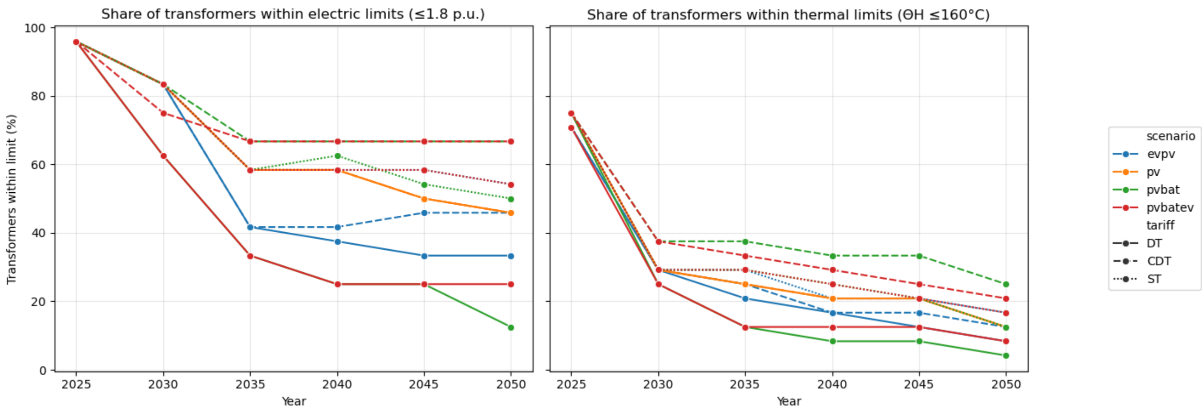

Figure 22. Share of Boisy transformers operating within electrical limits (≤1.8 p.u., left) and thermal limits (hot-spot temperature Θ_H ≤160 °C, right) from 2025 to 2050 under three tariff schemes (ST, DT, CDT) and four technology scenarios (PV, EV + PV, PV + Battery, PV + Battery + EV).

Figure 22 compares the share of transformers that remain within electrical limits (≤1.8 p.u.) and thermal limits (Θ_H ≤160°C) across scenarios and tariffs from 2025 to 2050. In both panels, the acceptable share declines steadily over time, reflecting the increasing stress caused by the growth of DER. The decline is stronger for the thermal criterion, which highlights that temperature limits become restrictive earlier than electrical loading limits. By 2050, only a small fraction of transformers will remain within thermal limits in most scenarios (4%-25%), while a larger share will still satisfy the electrical threshold (33%-66%). Other thermal results are presented in Appendix.

The results show how thermal constraints appear earlier and affect a larger portion of the fleet, meaning that transformer aging becomes a limiting factor before purely electrical overload conditions are reached. Equally important, the scenarios including batteries tend to produce the strongest stress, particularly under double tariffs (DT), where coordinated battery operation amplifies peak flows.

The share of transformers with an effective lifetime below 10 years (i.e. 50% of the nominal lifetime) when the simulated behavior is maintained, reinforces this picture by quantifying how thermal stress translates into accelerated asset degradation. Starting from low levels in 2025 (~4% across all scenarios), this share increases rapidly with DER penetration, reaching around 15–20% by 2030 and 30–40% by 2035 in most cases. By 2040, roughly half of the fleet falls below the 10-year lifetime threshold, and by 2050 this rises to about 63–74% depending on the scenario and tariff. Scenarios including batteries consistently show higher shares earlier in the transition, particularly under DT, where up to 50% of transformers already fall below half of the expected lifetime by 2030. Differences across tariffs remain visible but secondary compared to technology effects, with DT generally leading to slightly higher shares and earlier degradation. Overall, these results indicate that a substantial portion of the transformer fleet would face very short effective lifetimes under sustained future operating conditions, confirming that thermal aging, becomes a central constraint for network planning.

From the results, there are four main insights. First, the primary driver of transformer stress is the growth of PV penetration. Across all tariffs, the share of transformers in the high-stress band increases over time, and average loading rises, indicating that PV deployment progressively pushes a larger portion of the fleet toward operational limits. Second, tariff design strongly affects the concentration of extreme loading events. In particular, the double tariff (DT) leads to the strongest clustering of power flows when batteries respond to price signals. In sum, technology adoption, and PV in particular, drives the overall trend in transformer stress, while tariff structures can amplify or moderate peak loading (but according to our results, they cannot reduce the peak) by influencing the synchronization of flexible resources. Third, the effective lifetime of the transformers is considerably reduced with the increase of DER penetration and is mainly due to thermal aging. Finally, overall, the results suggest that future planning of distribution networks should consider thermal aging alongside electrical loading when assessing reinforcement needs under increasing DER penetration.

3 Boisy Flexibility Results

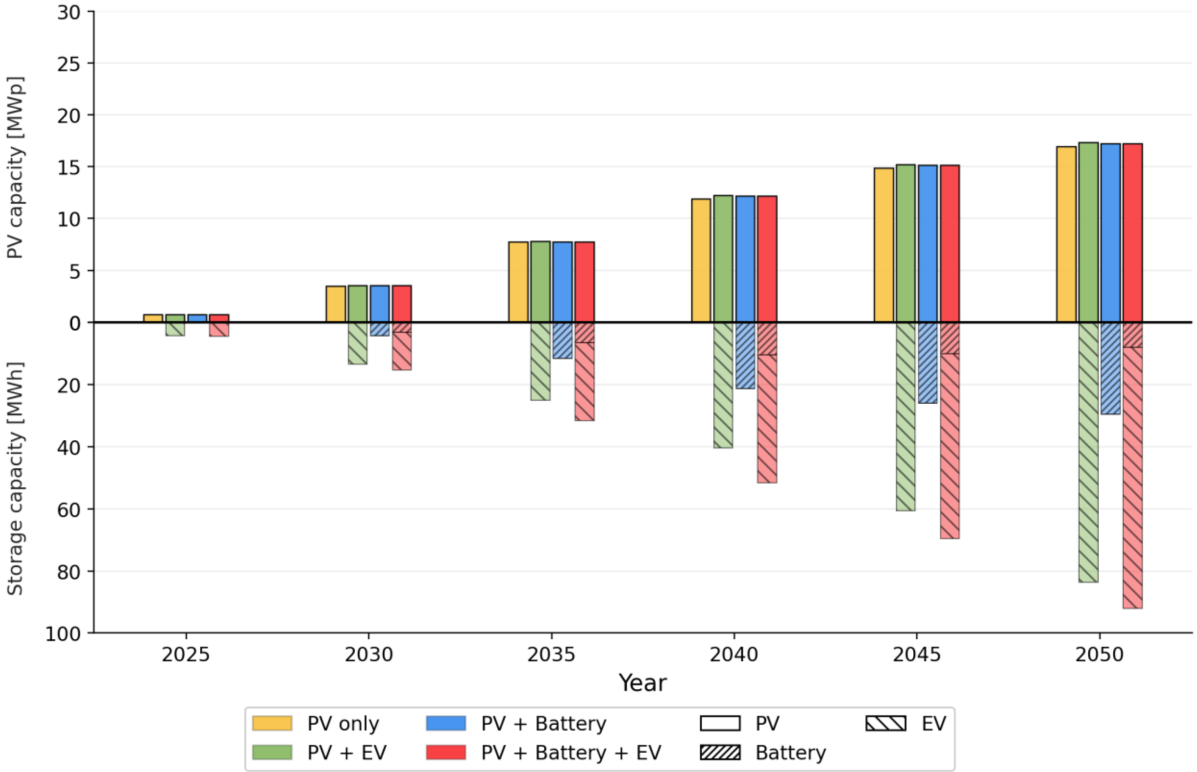

Figure 23. Installed PV capacity (above) and storage capacity (below) for the Boisy network under ST, from 2025 to 2050. Storage capacity is shown separately for the stationary batteries and EV fleet across all four scenarios.

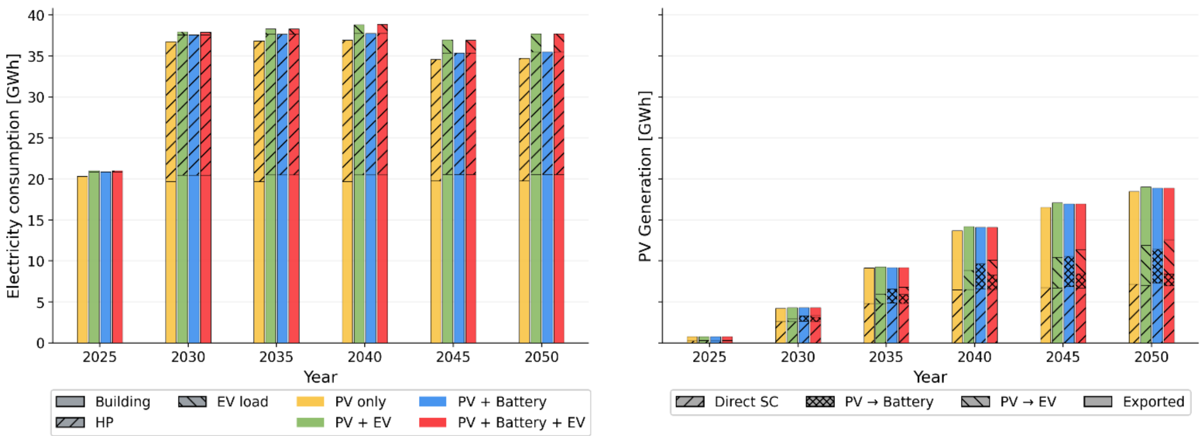

Figure 24. Annual electricity consumption by load type (left) and PV generation distribution by use (right) for the Boisy network under ST, from 2025 to 2050.

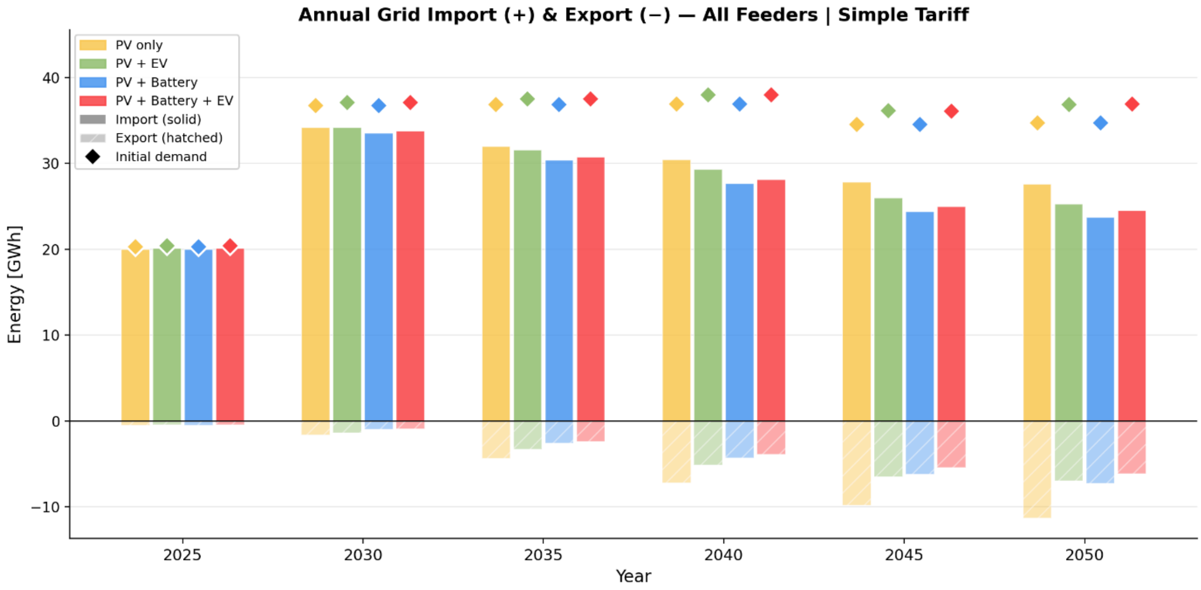

Figure 25. Annual grid import (solid bars) and export (hatched bars) for the Boisy network under ST, from 2025 to 2050.

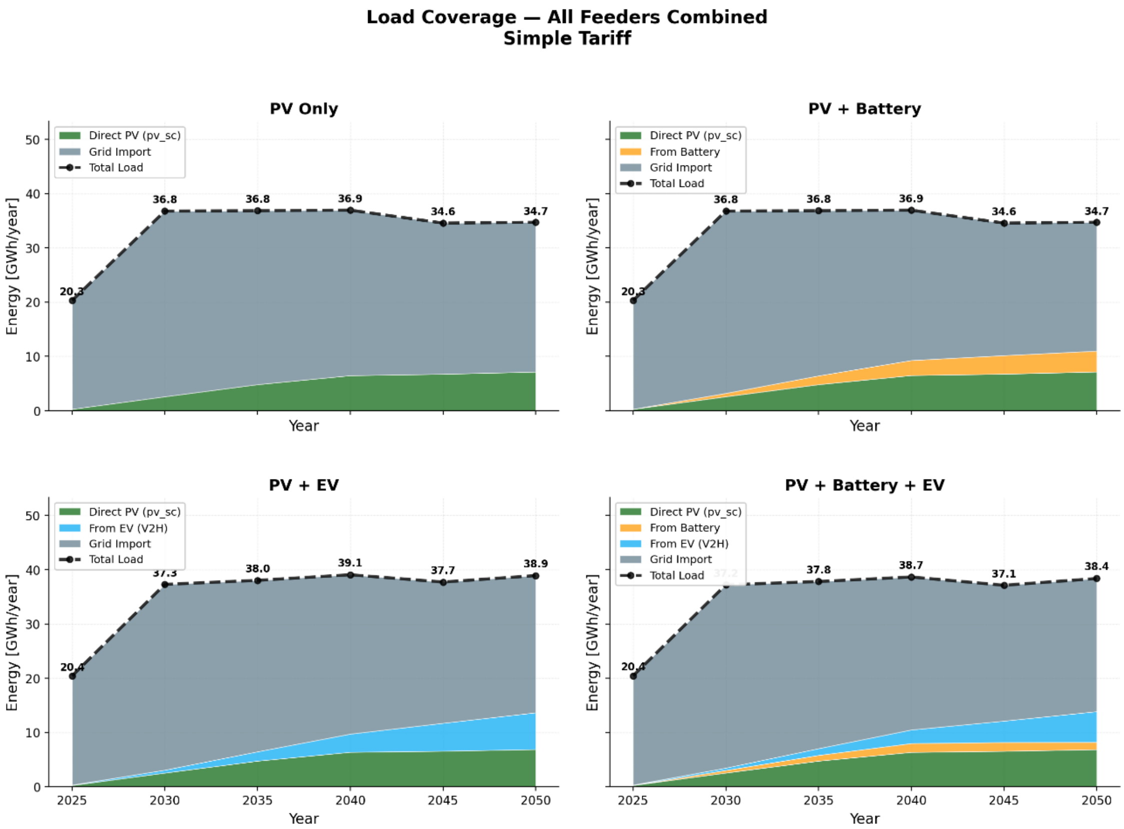

Figure 26. Annual electricity consumption decomposed by supply source for the Boisy network under ST, from 2025 to 2050.

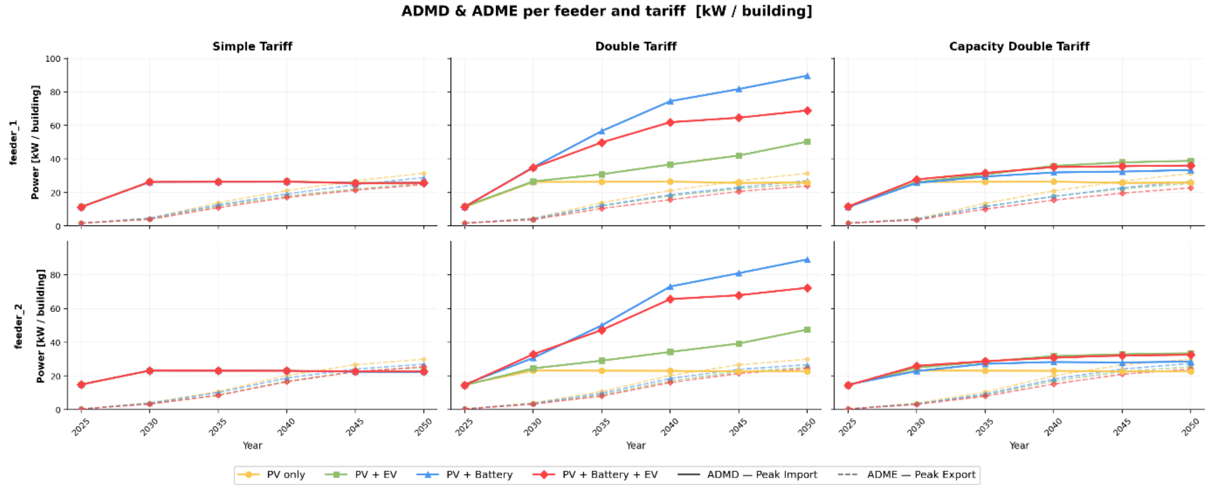

Figure 27. After Diversity Maximum Demand (ADMD, solid lines) and After Diversity Maximum Export (ADME, dashed lines) per building for Boisy feeders, across all scenarios and tariff structures, from 2025 to 2050.

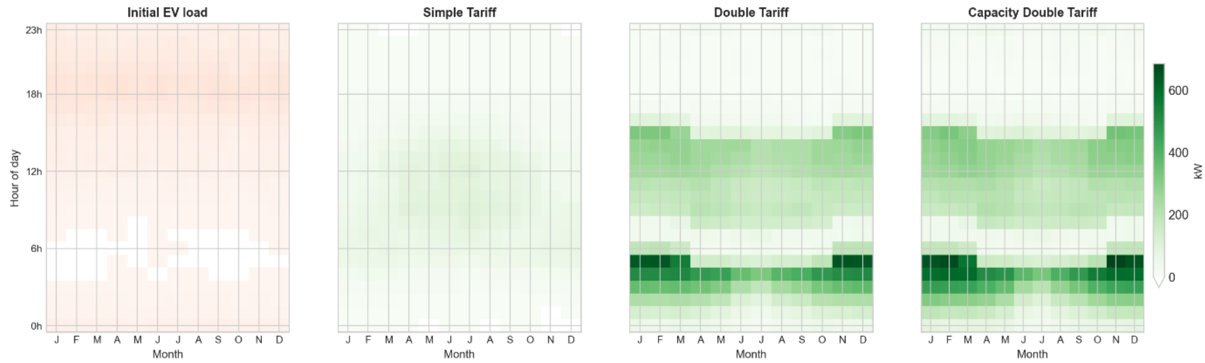

Figure 28. Mean hourly EV charging load (kW) for feeder 1 from Boisy, PV + Battery + EV scenario, 2030.

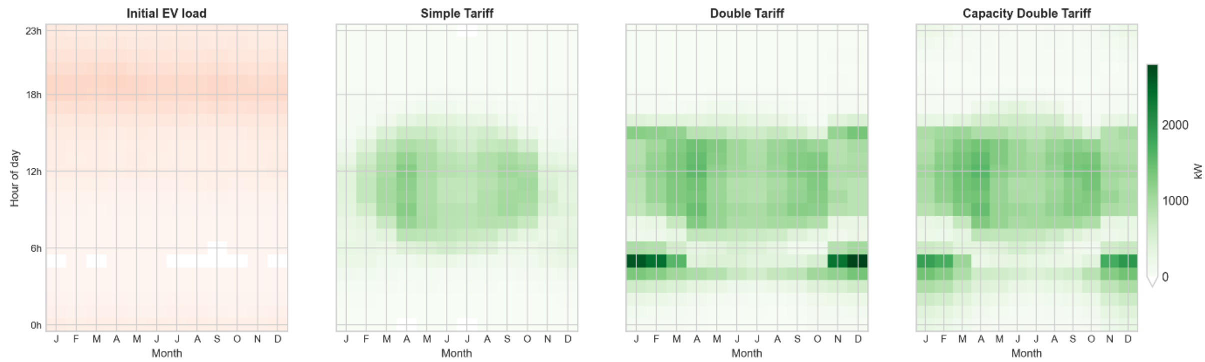

Figure 29. Mean hourly EV charging load (kW) for feeder 1 from Boisy, PV + Battery + EV scenario, 2050.

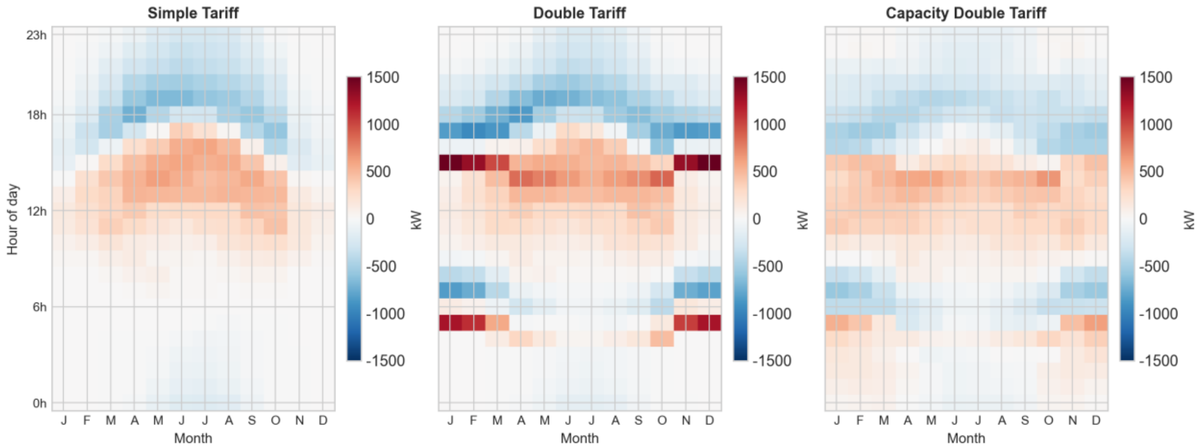

Figure 30. Mean net battery power (kW) for feeder 1 from Boisy, PV + Battery + EV scenario, 2050.

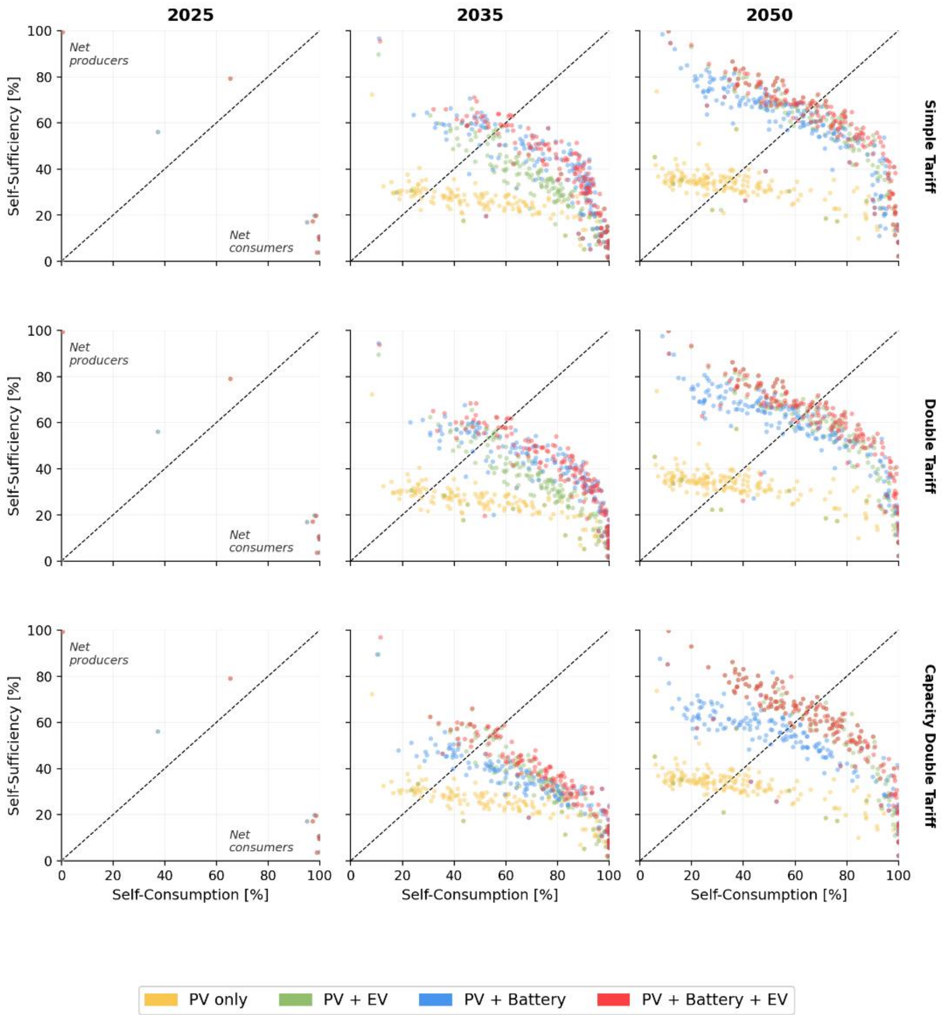

Figure 31. Self-consumption (SC) and self-sufficiency (SS) rates for all PV-equipped buildings in the feeder 1 from Boisy, shown for 2025, 2035, and 2050 across all scenarios and tariff structures.

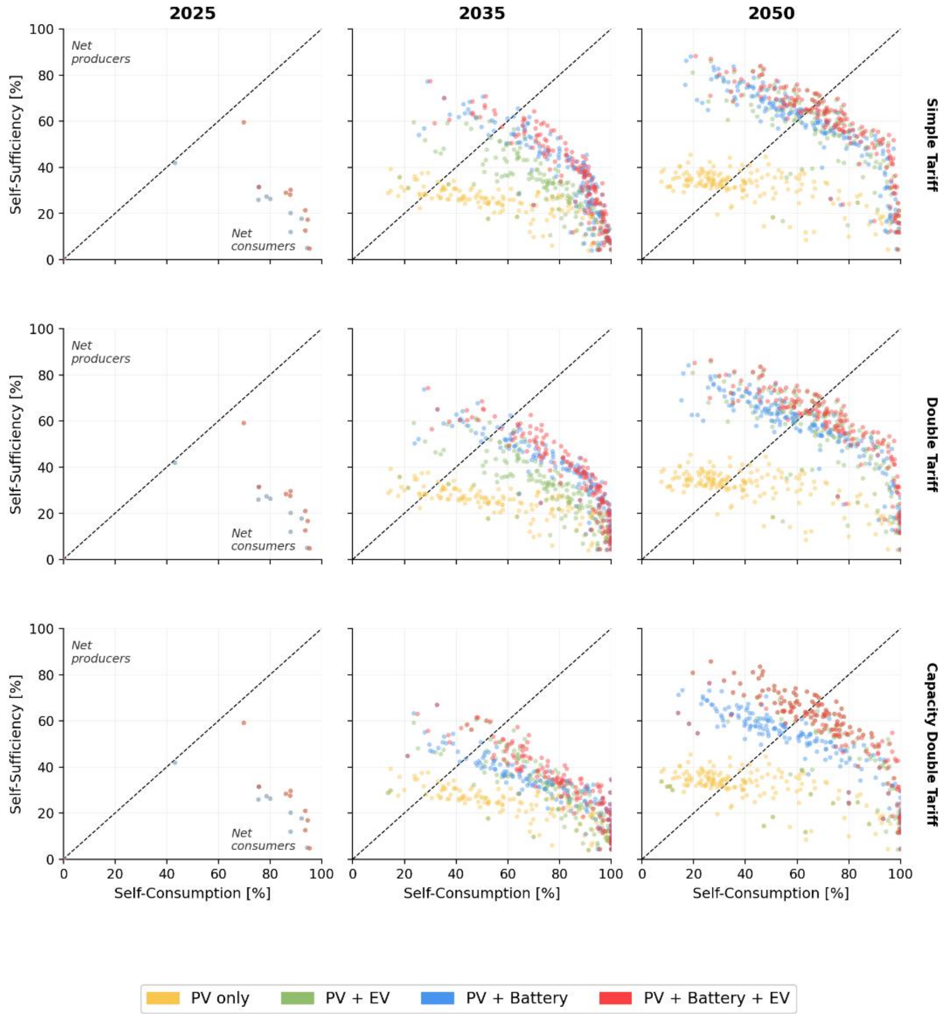

Figure 32. Self-consumption (SC) and self-sufficiency (SS) rates for all PV-equipped buildings in the feeder 2 from Boisy, shown for 2025, 2035, and 2050 across all scenarios and tariff structures.

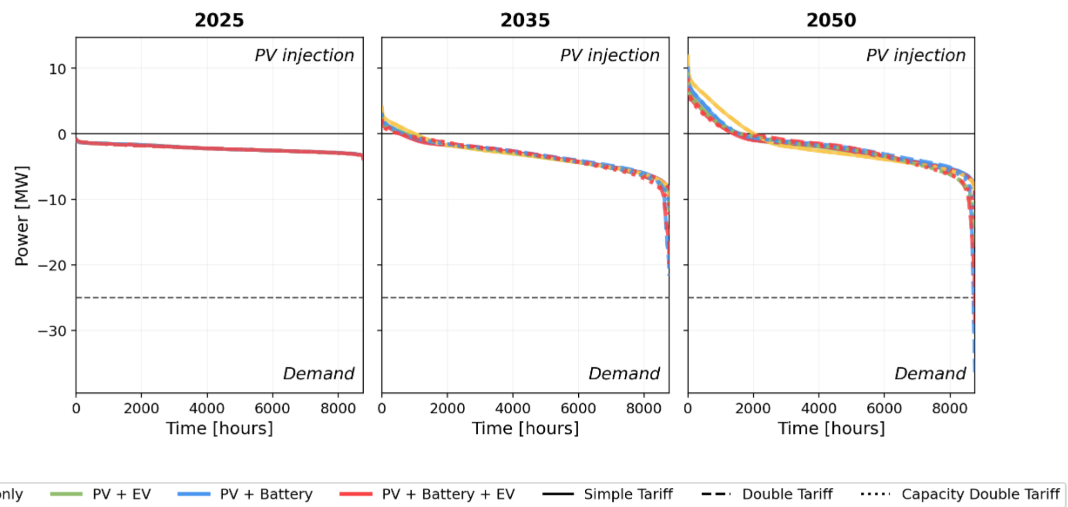

Figure 33. Load duration curves for the Boisy feeders combined, in 2025, 2035, and 2050 across all scenarios and tariff structures.

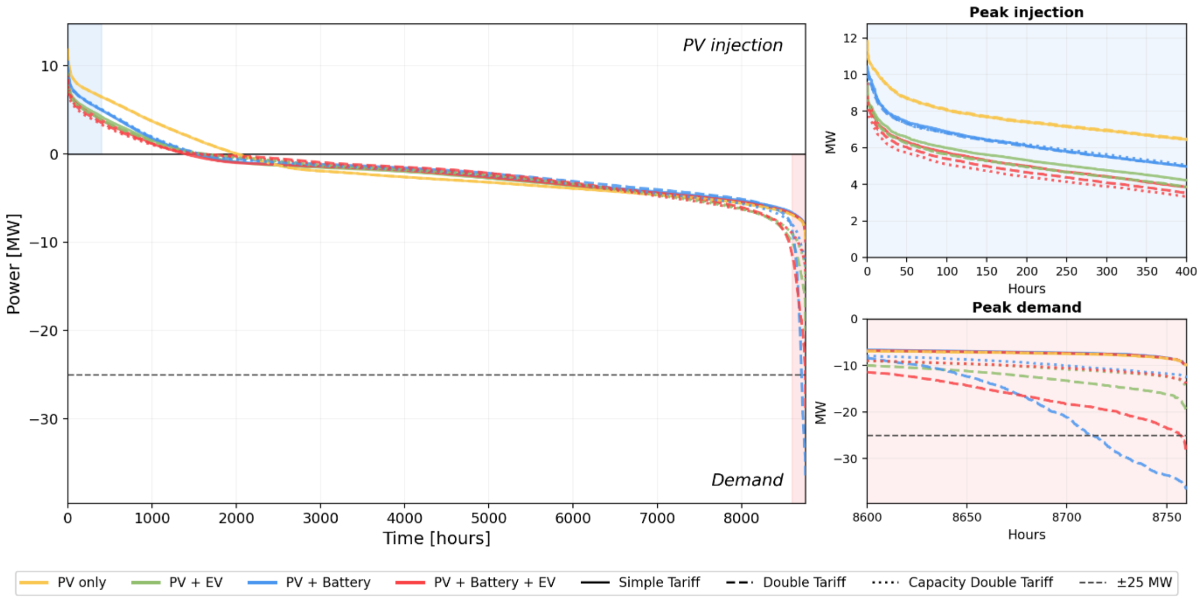

Figure 34. Load duration curve for the Boisy feeders combined in 2050 across all scenarios and tariff structures, with insets zooming into the peak injection range (top right) and peak demand range (bottom right).

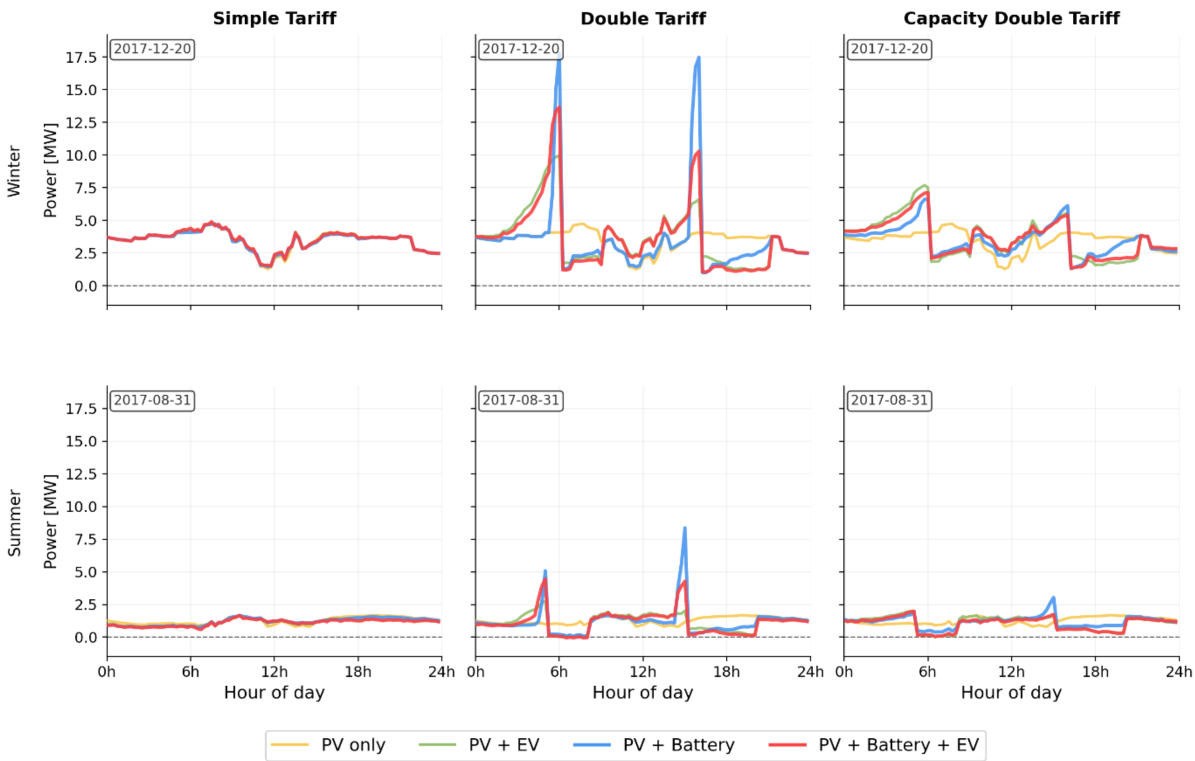

Figure 35. Net feeder power (MW) for the feeder 1 on the worst demand day of winter (top) and summer (bottom) in 2050, across all scenarios and tariff structures.

4 Transformer aging

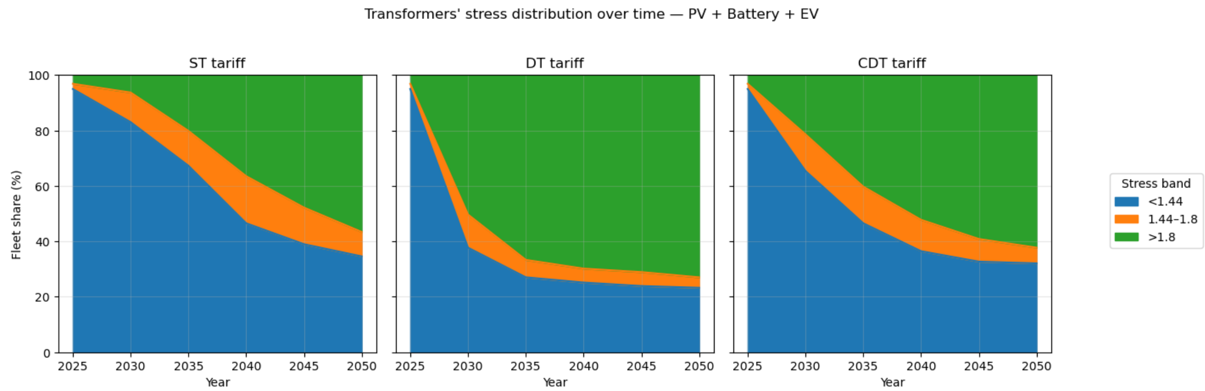

Figure 36. Evolution of Estavayer's transformer fleet stress distribution from 2025 to 2050 configurations. Comparing the 3 different tariffs for the PV+Battery+EV scenario.

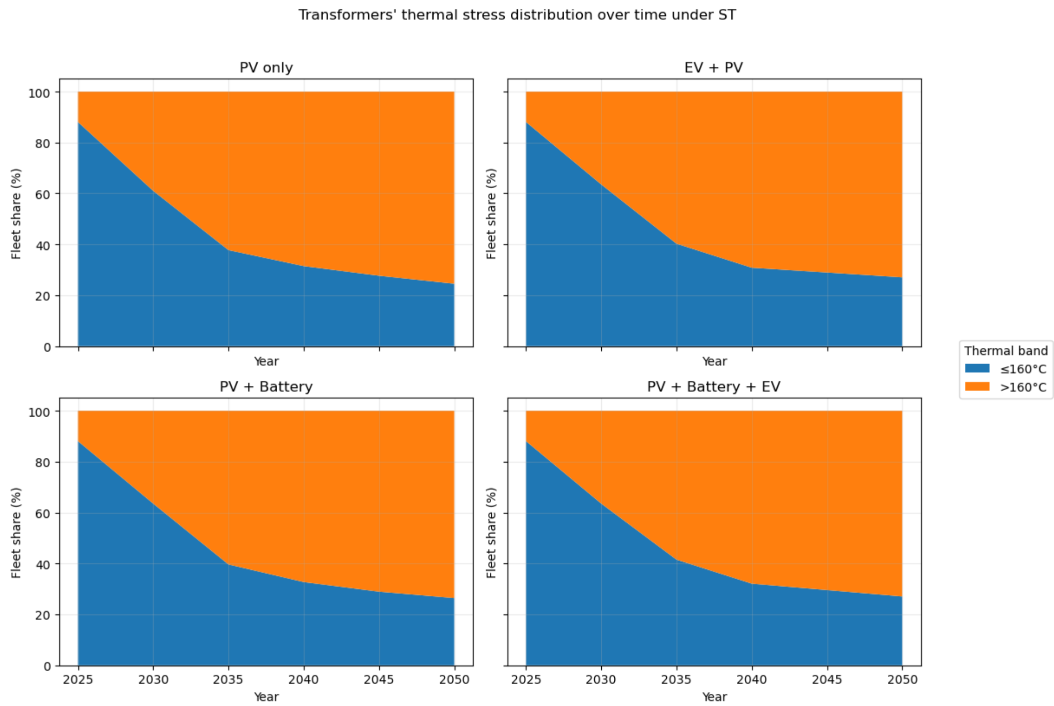

Figure 37.Evolution of Estavayer's transformer fleet thermal stress distribution from 2025 to 2050 under a single tariff (ST) across four configurations: PV only, EV + PV, PV + Battery, and PV + Battery + EV. The stacked areas show the share of the fleet operating at temperatures higher or lower than 160 ºC

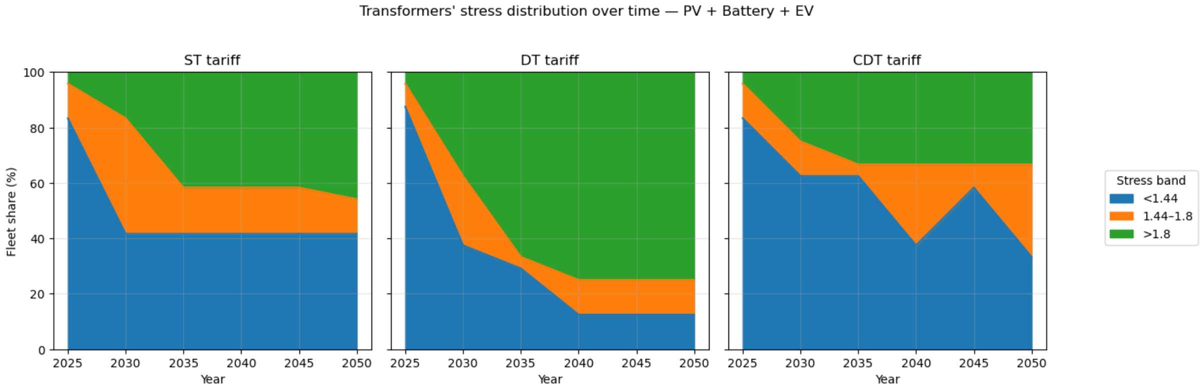

Figure 38. Evolution of Boisy's transformer fleet stress distribution from 2025 to 2050 configurations. Comparing the 3 different tariffs for the PV+Battery+EV scenario.

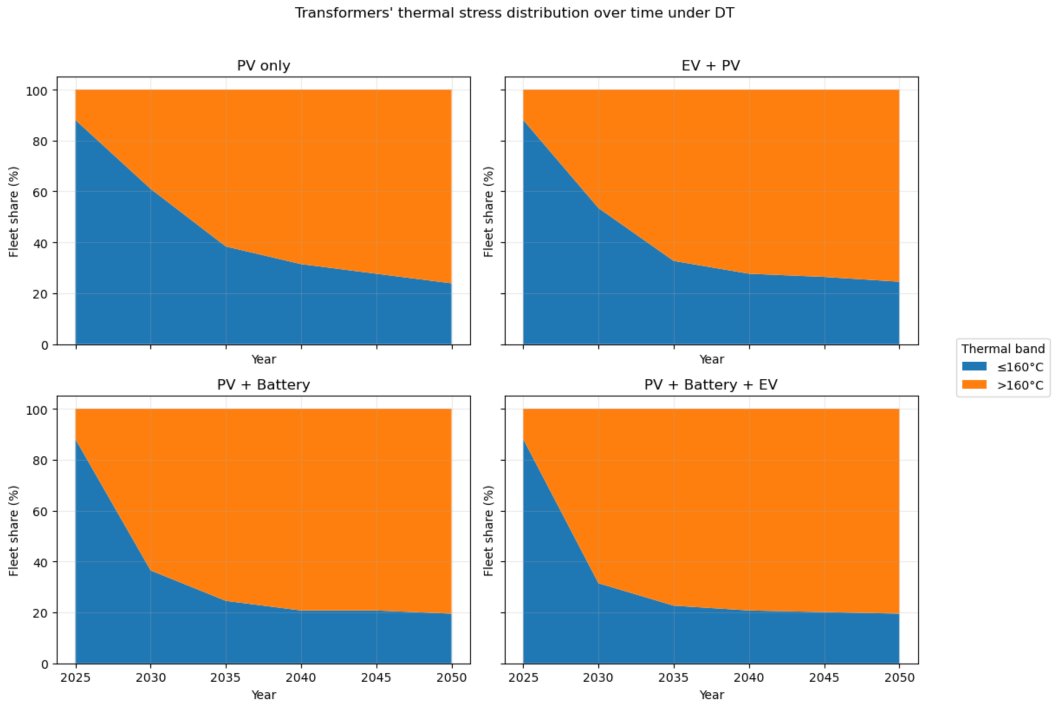

Figure 39. Evolution of Estavayer's transformer fleet thermal stress distribution from 2025 to 2050 under a double tariff (DT) across four configurations.

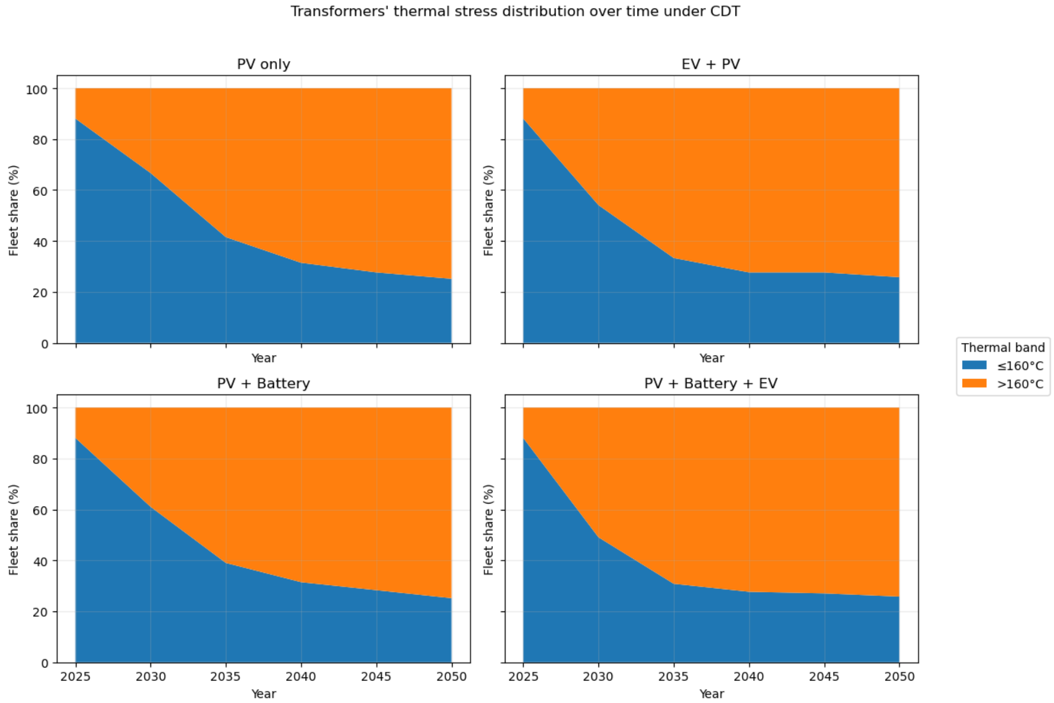

Figure 40. Evolution of Estavayer's transformer fleet thermal stress distribution from 2025 to 2050 under a capacity double tariff (CDT) across four configurations.

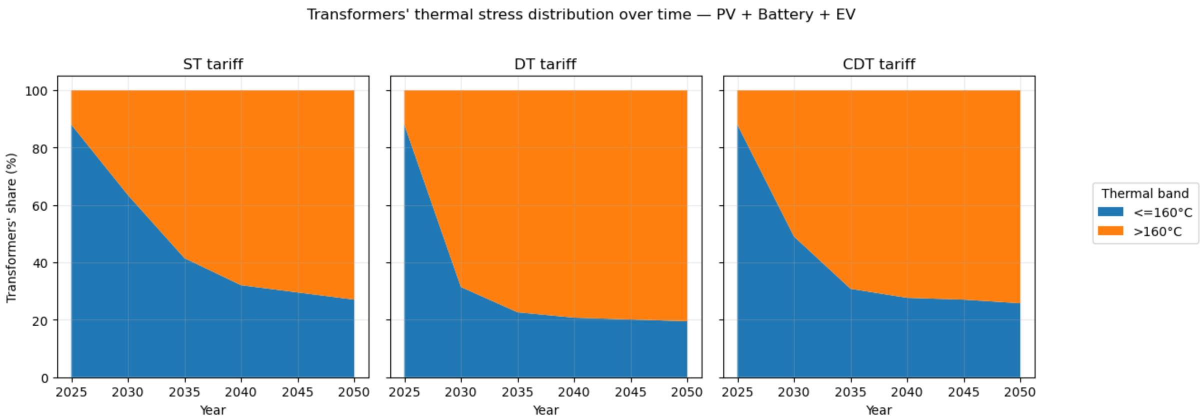

Figure 41. Evolution of Estavayer's transformer fleet thermal stress distribution from 2025 to 2050 configurations. Comparing the 3 different tariffs for the PV+Battery+EV scenario.

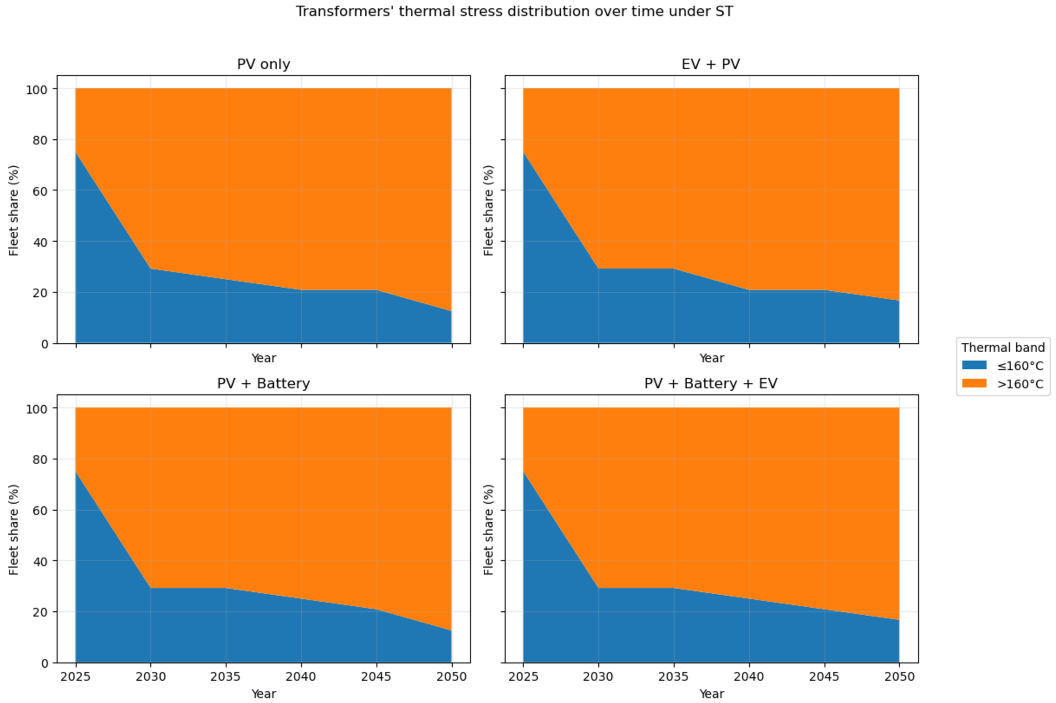

Figure 42. Evolution of Boisy's transformer fleet thermal stress distribution from 2025 to 2050 under a single tariff (ST) across four configurations: PV only, EV + PV, PV + Battery, and PV + Battery + EV.

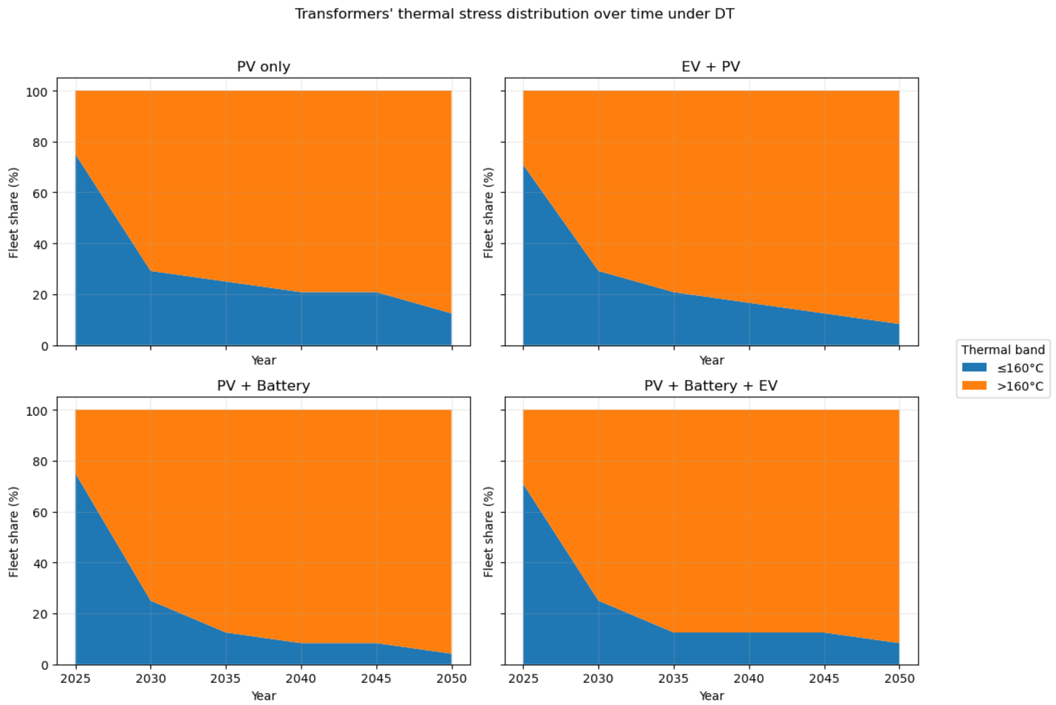

Figure 43. Evolution of Boisy's transformer fleet thermal stress distribution from 2025 to 2050 under a double tariff (DT) across four configurations: PV only, EV + PV, PV + Battery, and PV + Battery + EV

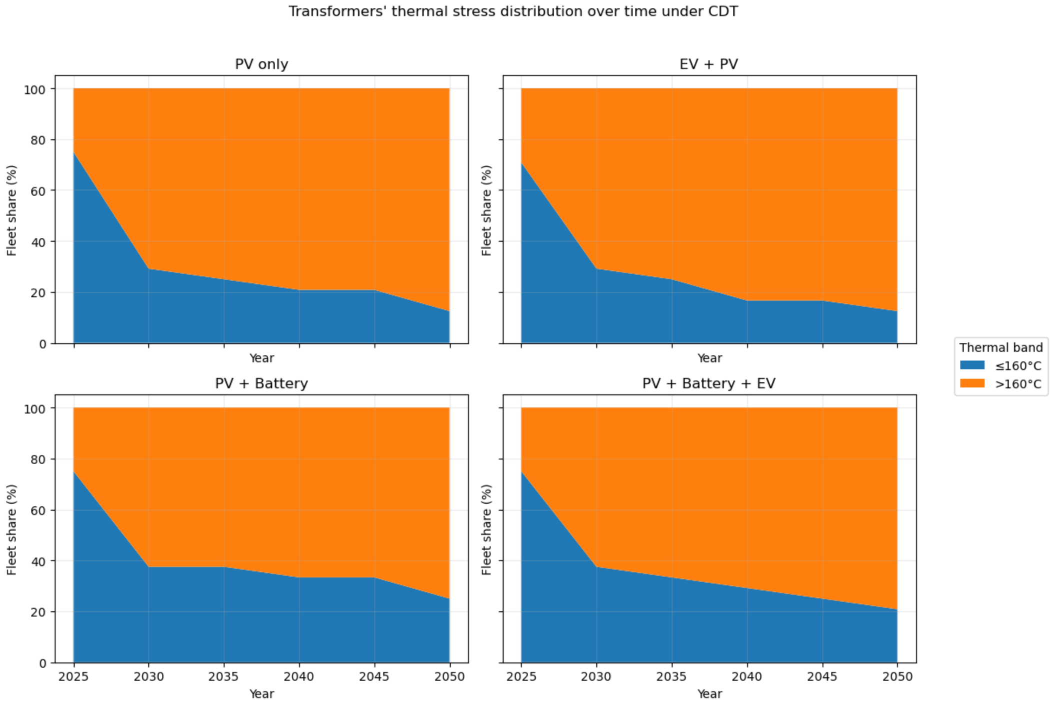

Figure 44. Evolution of Boisy's transformer fleet thermal stress distribution from 2025 to 2050 under a capacity double tariff (CDT) across four configurations: PV only, EV + PV, PV + Battery, and PV + Battery + EV

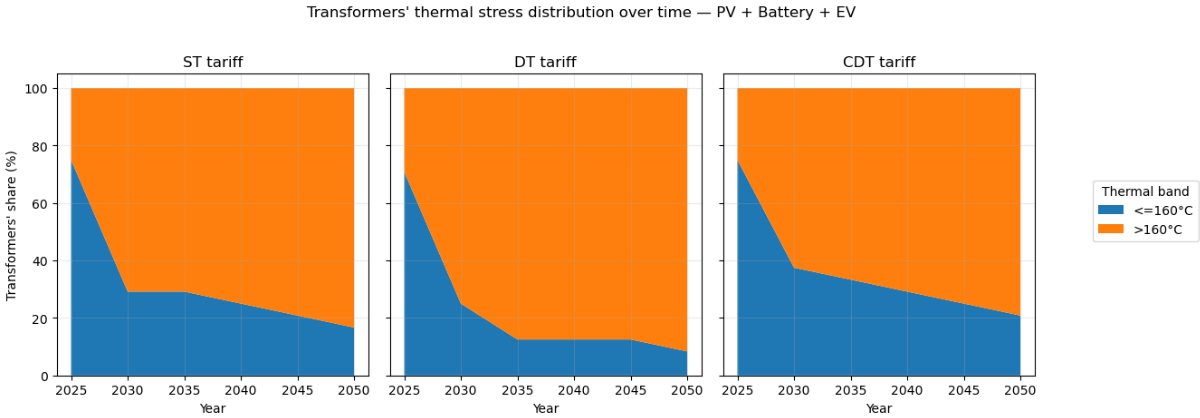

Figure 45. Evolution of Boisy's transformer fleet thermal stress distribution from 2025 to 2050 configurations. Comparing the 3 different tariffs for the PV+Battery+EV scenario.

5 Conclusions

The rapid deployment of PV, stationary batteries, and electric vehicles in distribution networks raises a set of interconnected questions for planners and regulators alike. How quickly does local generation displace grid imports? Do batteries and EVs complement or substitute each other as the fleet grows? And how sensitive are the answers to the tariff structure under which these assets are operated? This study addressed all three dimensions across two Swiss low-voltage networks over the period 2025 to 2050, under four technology scenarios and three tariff structures. The results show that the same assets that reduce grid dependency and enable local energy autonomy can, under the wrong tariff structure, generate demand peaks that exceed what the network was initially designed to handle.

PV deployment reshapes the energy balance of both networks. By the early 2040s, total annual generation from rooftop solar reaches and exceeds total network demand, shifting the primary challenge from reducing energy costs to controlling when and how much power flows across the grid connection. Batteries and EVs address this effectively: in the PV + Battery + EV scenario, the share of electricity drawn from the grid falls from 94% in 2025 to 58% by 2050 under ST, with vehicle-to-home discharge alone covering around 10% of total demand by the end of the horizon. Stationary batteries remain worthwhile even as the EV fleet grows, since the two technologies complement rather than substitute each other.

The tariff structure has a limited influence on annual energy balances while having a decisive influence on peak power flows. Scenarios without stationary batteries, such as PV Only and PV + EV, are largely tariff-independent, with grid import shares and transformer loading remaining close across all three tariffs throughout the horizon. In scenarios that include stationary batteries, grid import shares converge within 4 to 5 percent across tariffs by 2050, indicating that the choice of tariff does not substantially alter the overall level of independence achieved. Both DT and CDT result in smaller battery installations than ST, as off-peak grid charging means each unit of capacity is used more intensively, making smaller batteries economically sufficient. Under CDT, the narrower price spread between peak and off-peak hours reduces the marginal benefit of additional capacity further. Despite this, grid independence remains comparable across all three tariffs.

Peak demand tells a very different story. The primary driver of transformer stress is PV penetration itself, which progressively pushes a larger share of the transformer fleet toward operational limits regardless of tariff structure, with average loading and the share of transformers in the high-stress band rising consistently across all tariffs over the horizon. Crucially, no tariff structure reduces transformer stress below the PV-driven baseline. Tariff design can only worsen or moderate the trend by influencing the synchronization of flexible resources. Under DT, coincident battery charging just before the peak price windows creates feeder import peaks 5 to 7 times larger than under ST, large enough to require grid infrastructure dimensioned far beyond what the annual energy balance would suggest. The NLRSI reaches approximately 11 under DT by 2050, meaning grid import ramps are an order of magnitude more volatile than under ST. CDT largely contains this effect, limiting peak demand to 2.5 to 3 times the ST baseline while achieving comparable grid import shares. Future network planning should therefore consider peak loading conditions and thermal aging of assets jointly, rather than relying on annual energy metrics alone when assessing reinforcement needs under increasing DER penetration.

The ex-ante and ex-post analysis show that DT and CDT activate comparable volumes of off-peak grid charging, exceeding 20 GWh annually by 2050, but differ in how that energy is discharged. Under DT, concentrated peak-hour discharge largely offsets the additional off-peak charging, keeping net new grid consumption at around 2 GWh per year. Under CDT, the smoother discharge profile leaves a larger share without a corresponding peak reduction, resulting in higher net new consumption of around 4.7 GWh by 2050. Smoothing peak demand and reducing total grid consumption are not the same objective, and a tariff can achieve one but not necessarily the other.

EV flexibility introduces temporal diversity in charging demand, partially smoothing the coincidence peaks that battery-only scenarios generate under DT. Batteries and EVs should therefore be assessed jointly when evaluating tariff policies. More broadly, these results highlight an important tension in tariff-driven flexibility: the same price signal that activates flexible assets can, if it contains sharp price transitions, generate coincident demand peaks that undermine the very grid stability the flexibility was meant to support. The CDT examined here retains a volumetric time-of-use component alongside the capacity charge, which continues to enable simultaneous asset activation and grid-to-battery charging. This differs from capacity tariffs combined with flat energy prices studied in previous work, where grid charging was absent, and simultaneous activation was far less likely. Moving toward fully dynamic tariffs with continuously varying price signals, rather than discrete peak and off-peak boundaries, would reduce the incentive for all assets to respond at exactly the same moment. Tariff design must therefore be considered jointly with flexibility deployment as distributed generation and storage continue to expand across Swiss residential networks.

6 References

[1] IEEE Std C57.96-2013. IEEE Guide for Loading Dry-Type Distribution and Power Transformers. IEEE Power and Energy Society, 2014.

[2] A. Pena-Bello, G. M. Gonzalez, N. Wyrsch, and C. Ballif, "Assessing strategies to manage distributed photovoltaics in Swiss low-voltage networks: An analysis of curtailment, export tariffs, and resource sharing," arXiv preprint, 2024. arXiv:2409.16078.

[3] Swiss Federal Statistical Office (FSO), "Registre fédéral des bâtiments et des logements (RegBL) / Federal Register of Buildings and Dwellings," 2024. Accessed on 20/06/2025. https://www.housing-stat.ch/fr/index.html

[4] L. Perret, J. Fahrni, N. Wyrsch, Y. Riesen, S. Puddu, S. Weber, and D. Pacheco-Barzallo, "Flexi: Determining the flexibilization potential of the electricity demand," tech. rep., BFE Bundesamt für Energie, 2015. Accessed on 20/03/2023. https://www.aramis.admin.ch/Default?DocumentID=61177&Load=true

[5] J. Holweger, L. Bloch, C. Ballif, and N. Wyrsch, "Privacy compliant methods for low-voltage grid simulations using smart meter data," arXiv preprint, 2024. Accessed on 30/10/2024. http://dx.doi.org/10.2139/ssrn.4998882

[6] Federal Statistical Office, "Urban-Rural Typology 2012," Accessed: April 2024. https://www.atlas.bfs.admin.ch/maps/13/fr/17223_12361_3191_227/26733.html

[7] Federal Statistical Office, "Microcensus Mobility and Transport (Mikrozensus Mobilität und Verkehr)." https://www.bfs.admin.ch/bfs/de/home/statistiken/mobilitaet-verkehr/erhebungen/mzmv.html

[8] IRENA. Electricity Storage and Renewables: Costs and Markets to 2030. International Renewable Energy Agency, Abu Dhabi, 2017. Accessed on 20/03/2023. https://www.irena.org/-/media/Files/IRENA/Agency/Publication/2017/Oct/IRENA_Electricity_Storage_Costs_2017.pdf

[9] G. Leguay, Y. Sauter, and F. Jacqmin, "Observation des prix du marché photovoltaïque 2020," tech. rep., Suisse Energie, 2021. Accessed on 20/03/2023. https://pubdb.bfe.admin.ch/fr/publication/download/10552

[10] L. Bloch, J. Holweger, C. Ballif, and N. Wyrsch, "Impact of advanced electricity tariff structures on the optimal design, operation and profitability of a grid-connected PV system with energy storage," Energy Informatics, vol. 2, no. 1, pp. 1–19, 2019. https://doi.org/10.1186/s42162-019-0085-z

[11] A. Thingvad, M. Marinelli, and P. B. Andersen, "Experimental validation of onboard electric vehicle chargers to improve the efficiency of smart charging operation," Applied Energy, vol. 330, p. 120210, 2023. https://doi.org/10.1016/j.apenergy.2022.120210

[12] E. Redondo-Iglesias and S. Pelissier, "On the Efficiency of LFP Lithium-ion Batteries," in 2022 Second International Conference on Sustainable Mobility Applications, Renewables and Technology (SMART), IEEE, 2022. DOI: 10.1109/SMART55236.2022.9990093

[13] Swiss Federal Office of Energy, "Toitsolaire.ch — Sonnendach," 2023. https://www.uvek-gis.admin.ch/BFE/sonnendach/?lang=fr

[14] M. Gezelius and R. Mortazavi, "Effect of having solar panels on the probability of owning a battery electric vehicle," World Electric Vehicle Journal, vol. 13, no. 7, p. 125, 2022.

[15] J. Nipkow, "Typischer Haushalt-Stromverbrauch," Swiss Federal Office of Energy (SFOE), 2021. https://pubdb.bfe.admin.ch/fr/publication/download/10559

[16] S. Powell, E. C. Kara, G. V. Cezar, S. Kiliccote, and R. Rajagopal, "Controlled workplace charging of electric vehicles: The impact of rate schedules on transformer aging," Applied Energy, vol. 276, p. 115352, 2020.

[17] A. Pena-Bello, R. Junod, C. Ballif, and N. Wyrsch, "Balancing DSO interests and PV system economics with alternative tariffs," Energy Policy, vol. 183, p. 113828, 2023. https://doi.org/10.1016/j.enpol.2023.113828

Schweizerische Eidgenossenschaft
Confédération suisse
Confederazione Svizzera
Confederaziun svizra

Federal Department of the Environment,
Transport, Energy and Communications DETEC

Swiss Federal Office of Energy
Energy Research and Cleantech

Final report 30 April 2026

Dig-A-Plan

Appendix 4: Distribution grid asset planning optimization, validation of the model, and release of the planning tool

D5.1 Document of distribution grid asset planning optimization

D5.2 Technical report containing the validation of the proposed model utilizing appropriate test benches and scenarios in a numerical environment

D5.3 Release of the asset-planning tool

Publisher:
Swiss Federal Office of Energy SFOE
Energy Research and Cleantech
CH-3003 Berne
www.energy-research.ch

Co-financing: In-kind contributions provided by
Groupe e, 1763 Granges-Paccot

Services Industriels Lausanne (SiL), 1003 Lausanne

Yverdon Energies, 1400 Yverdon

Subsidy recipients:
Haute École d'Ingénierie et de Gestion du Canton de Vaud (HEIG-VD), Institute of Energies (IE)
1400 Yverdon-les-Bains
https://heig-vd.ch/recherche/instituts/ie/

Université de Genève (UNIGE), Institute for Environnemental Sciences (ISE)
1205 Genève
https://www.unige.ch/energy/

EPFL, photovoltaic research laboratory (PV-LAB)
2002 Neuchâtel
https://www.epfl.ch/labs/pvlab/

Authors:

Mokhtar Bozorg, HEIG-VD, mokhtar.bozorg@heig-vd.ch
Mohammad Rayati, HEIG-VD, mohammad.rayiati@heig-vd.ch
Adeleh Mokhles-Gerami, HEIG-VD, adeleh.mokhles-gerami@heig-vd.ch
Luca Tomasini, HEIG-VD, luca.tomasini@heig-vd.ch

SFOE project coordinator:
Dr Michael Moser, Michael.moser@bfe.ch

SFOE contract number: SI/502666-01

Table of contents

List of figures

1 Introduction

The energy transition is creating major challenges for distribution system operators (DSOs) in both operation and planning of the distribution grids. The increasing penetration of distributed energy resources and flexible loads, particularly photovoltaic (PV) systems, electric vehicles (EVs), and heat pumps (HPs), changes load and generation patterns and may lead to voltage deviations, line and transformer congestion, and earlier reinforcement needs. As a result, distribution grid asset planning increasingly requires methods that can account for uncertainty while preserving operational feasibility under realistic grid conditions.

A key methodological aspect of this problem is the distinction between *known* and *unknown* uncertainties. *Known* uncertainties include daily and seasonal variations of load and PV production; they can be represented through operational scenarios. *Unknown* uncertainties include future distributed energy resource (DER) deployment rates, demand growth, and connection requests; they affect long-term investment decisions and are more difficult to characterize directly. This distinction motivates a multi-layer planning framework in which long-term asset decisions are coordinated with operational validation and reconfiguration analyses.

Within the Dig-A-Plan project, this approach is implemented in WP5, which develops and validates the optimization-based planning tool. The WP5 framework links long-term expansion planning decisions like reinforcement of grid assets with operational flexibility dispatch and network reconfiguration to ensure that planning decisions remain technically feasible under representative operating scenarios. The work reported in WP5 builds on the project's data and grid model preparation in WP2 and on the scenario and flexibility-related inputs developed in WPs 3-4.

This document presents Deliverables 5.1, 5.2 and 5.3 of the Dig-A-Plan under WP5 entitled "Development and validation of grid asset planning tool". It describes the optimization methodology of the planning framework, its software implementation, the numerical validation results, and the public release details of the open-source tool.

Deliverable 5.1 defines the optimization formulation for distribution grid asset planning under both deterministic conditions and *known* versus *unknown* uncertainties. The proposed framework is structured in three decision layers: short-term flexibility dispatch, mid-term operational reconfiguration, and long-term expansion planning. In the short-term layer, the methodology for producing load and generation power profiles is detailed. The mid-term layer is formulated as a convex DistFlow-based mixed-integer second-order cone program (MISOCP), incorporating operational and radiality constraints; Bender decomposition and consensus alternating direction method of multipliers (ADMM) are considered to improve computational scalability. The long-term expansion problem is formulated as a multi-stage stochastic dynamic programming model, solved using backward induction and forward simulation.

Deliverable 5.2 describes the implementation and technical validation within an integrated computational environment that combines a Julia-based long-term expansion module using stochastic dual dynamic programming (SDDP) and a Python with Pyomo-based operational validation module implemented with ADMM. Validation is conducted on the IEEE 33-bus feeder, the Boisy distribution grid, and the Estavayer case study under three transition scenarios: Baseline, Moderate, and Full. The section concludes with the results of the ADMM-based reconfiguration model and the SDDP-based planning analyses.

Deliverable 5.3 provides the public release information of the asset-planning tool, including the access link to the Dig-A-Plan optimization documentation and repository. Confidential and DSO-specific data are excluded from the public version.

1.1. Dig-A-Plan project description

Dig-A-Plan addresses distribution grid asset planning under *known* and *unknown* uncertainties during the energy transition. The project develops a series of methods to support decisions related to expansion of distribution grid assets, while accounting for the operational impacts of DER integration and flexibility management. In particular, the project considers the interaction between operational flexibility management, network reconfiguration, and long-term planning decisions to improve the robustness and practicality of grid planning results.

Within this framework, WP5 constitutes the methodological and computational core of the project. It covers the development of optimization formulation, the software implementation of the asset-planning tool in a numerical environment, the simulation of targeted distribution grids under different energy-transition scenarios, and the public release of the proposed asset-planning tool. More specifically, WP5 includes:

(i) The development of the optimization formulation under *known* and *unknown* uncertainties.

(ii) The software implementation of the proposed asset-planning tool in a numerical environment.

(iii) The simulation of targeted distribution grids under different energy-transition scenarios.

(iv) The release of the proposed asset-planning tool, its documentation, and its repository.

In the Dig-A-Plan project, we developed a planning tool for grid assets like transformers and branches. The tool is developed based on a multistage decision-making framework, with each stage consisting of two sequential steps.

In the first step of each stage, the decisions concerning expansion of grid assets like transformers and branches for the upcoming years of the planning time window, e.g., the next five years, are made. Following the implementation of the decisions in the first step of each stage, the *unknown* uncertainties will be revealed, including:

(I) The load configuration, i.e., the installed capacity of PVs, EVs, and HPs at grid nodes.

(II) The available flexibility provided by the prosumers.

The decisions in the first step of each stage must be robust against the probability of distribution of *unknown* uncertainties, or, in other words, distributionally robust.

In the second step of each stage, the prosumers deployed flexibility in each hour of the days of the planning time window will be determined to keep the nodal voltage, branches, and transformers' currents within the safe limits. In this step, the installed capacity of PVs, EVs, and HPs, as well as the prosumers' available flexibility in the first step, are *known*. On the other hand, the demand profile and PV power outputs are uncertain, while a few representative days over the year may be identified to plan flexibility exclusively for those days. The representative days will be identified using a clustering technique in a way to represent load and generation availability within daily, weekly, and seasonal variations. In this case, the deployed flexibility for other days will thereafter be the same as for the representative days, only with a small difference. As a result, the load profile and PV power output over a year can be regarded as *known* uncertainties.

Figure 1 depicts a simplified schematic of the proposed planning tool, which is based on a multistage decision-making framework and distributionally robust optimization. To obtain optimal grid asset planning, several iterations of finding optimal planning will be needed over forward and backward passes.

The objective of the planning tool is to lower the required capital and operating expenses for the grid both at each stage and for the full period of planning, e.g., until the end of the 2050 horizon. The capital may include expenditure for transformers and branch expansion. On the other hand, the operational cost includes the expenses for maintaining the transformers under pressure, the cost of purchasing flexibility from prosumers, and the DSOs' balancing profit.

To guarantee the safe operation of distribution grids, the optimization problem will be constrained by:

(i) Reliability and resilience metrics such as system average interruption frequency index (SAIFI) and system average interruption duration index (SAIDI);
(ii) Technical limitations of the distribution grid, such as voltage and power flow limits; and
(iii) The technical restrictions of prosumers, such as their available capacity.

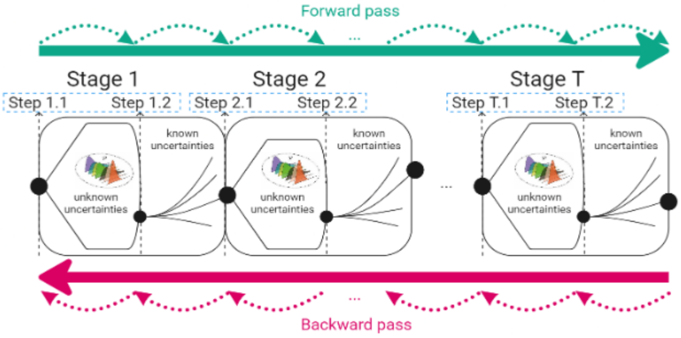

Figure 1: Multi-stage optimization framework

To validate the proposed planning tool, data collected from three DSOs will be used. We will compare the outcomes of the proposed planning tool with the original long-term plan without considering uncertainties to identify the benefits of the inclusion of uncertainty modelling in long-term planning.

A multistage distributionally robust optimization (MDRO) is used for asset planning since it is suitable for addressing problems with *known* and *unknown* uncertainties about the temporal and spatial evolution of load configuration and flexibility provision in distribution grids. In the MDRO-based planning framework, decisions are made in multiple instances, allowing us to account for all relevant implementation sequences. The decisions are robust against the probability density of *unknown* uncertainties. Furthermore, information related to known uncertainties will be exploited in the proposed framework. The curse of dimensionality in stochastic modelling is one of the main factors that necessitates the use of distributionally robust optimization for the proposed planning tool.

1.2. WP5 description

WP5, entitled *"Development and validation of grid asset planning tool",* addresses the formulation, software implementation, numerical validation, and the release of an optimization-based planning tool for distribution grids under uncertainty. This work package integrates short-term operational flexibility dispatch, mid-term network reconfiguration, and long-term asset planning decisions in a coordinated structure designed for scalable and realistic numerical studies.

The scientific developments in WP5 include:

- A multi-horizon optimization formulation for distribution grid asset planning under *known* and *unknown* uncertainties.
- A numerical implementation combining a long-term planning layer and an operational reconfiguration layer for validating the results of upper layer.
- Scenario-based simulations on benchmark and representative distribution grids to assess operational feasibility, flexibility use, and reinforcement needs under different energy-transition pathways.

In the developed framework, long-term planning decisions are coordinated with operational validation so that reinforcement decisions remain feasible under representative operating scenarios. This is reflected in the numerical implementation through a long-term planning layer (*SDDP-based*) and an operational validation/reconfiguration layer (*ADMM-based*), which are used to evaluate grid behavior under different transition scenarios.

WP5 consists of the following tasks:

- **T.1:** Developing the optimization formulation of grid asset planning tool under *known* and *unknown* uncertainties.
- **T.2:** Building the grid asset-planning tool based on the developed formulation in a numerical environment.

- **T.3:** Simulating the targeted distribution grid for different scenarios of energy transition.
- **T.4:** Public release information of the planning tool, its documentation, and repository access.

1.3. Tasks definition

This report summarizes the activities performed under T.1, T.2, T.3, and T.4. The corresponding sub-tasks and technical actions are detailed below.

T.1: Developing the optimization formulation of grid asset planning tool under *known* and *unknown* uncertainties.

I. Definition of a multi-horizon planning framework linking short-term flexibility dispatch, mid-term operational reconfiguration, and long-term asset planning decisions for distribution grids under uncertainty.
II. Formulation of the optimization problem under *known* and *unknown* uncertainties, distinguishing scenario-based operational variability from long-term uncertainty in demand growth and DER integration.
III. Development of the mid-term operational reconfiguration model using a convex DistFlow-based formulation with operational and topological constraints, including nodal power balance, voltage limits, current limits, and radiality requirements.
IV. Investigation of scalable solution strategies for large-scale systems, including decomposition approaches such as Bender's decomposition and distributed consensus ADMM.
V. Definition of methodological links between operational feasibility analysis and long-term reinforcement planning to support the integrated planning framework.

T.2: Building the grid asset-planning tool based on the developed formulation in a numerical environment.

I. Implementation of the long-term planning layer in a numerical environment for multistage expansion planning under uncertainty (SDDP-based framework in Julia).
II. Implementation of the operational validation and reconfiguration layer in a numerical environment for scenario-based feasibility analysis and network reconfiguration with ADMM-based formulation in Pyomo.
III. Development of the interface and iterative coordination mechanism between the long-term planning and operational layers, including the exchange of decisions and feasibility/optimality information.
IV. Integration of benchmark and representative grid models into the numerical workflow and preparation of simulation-ready inputs for validation studies.
V. Execution of technical validation tests in the numerical environment to assess feasibility, scalability, and consistency of the implemented planning framework.

T.3: Simulating the targeted distribution grid for different scenarios of energy transition.

I. Definition and application of energy-transition scenarios, e.g., Baseline, Moderate, and Full transition, for the assessment of future grid operation and planning needs.
II. Simulation of benchmark and representative distribution grids, including IEEE 33-bus, Boisy, and Estavayer cases, under the defined scenarios and representative operating profiles.
III. Evaluation of operational reconfiguration results, including flexibility use, switching decisions, tap decisions, and compliance with network operational constraints.
IV. Evaluation of long-term planning results, including reinforcement decisions obtained from the SDDP-based planning layer.
V. Comparative analysis of the impact of scenarios on grid feasibility, operational performance, and reinforcement requirements to support the validation of the planning tool.

T.4: Public release information of the planning tool, its documentation, and repository access.

I. Preparation of the public release package of the proposed asset planning tool, including the optimization codebase and supporting documentation suitable for external use.

II. Publication of the Dig-A-Plan planning tool documentation and repository through the public access page[1].
III. Exclusion of confidential or DSO-specific data from the public release in accordance with project confidentiality constraints.

The next sections present the detailed contents of each task and their mapping to Deliverables 5.1, 5.2, and 5.3.

2 Deliverable 5.1: Document of distribution grid asset planning optimization

2.1. Objective and scope

Deliverable 5.1 documents the optimization formulation developed for the Dig-A-Plan grid asset-planning tool under *known* and *unknown* uncertainties. The objective of this deliverable is to define the methodological basis of the planning framework and to describe how operational and planning decisions are linked across different time horizons. The formulation is intended to support realistic distribution grid planning by combining short-term flexibility management, mid-term network reconfiguration, and long-term reinforcement decisions in a unified optimization structure.

The scope of deliverable 5.1 is limited to the formulation of the asset-planning problem and the associated methodological developments. Therefore, it focuses on the mathematical structure of the optimization framework, the treatment of uncertainty, and the scalable solution approaches considered for large-scale systems. The numerical implementation and validation results are reported separately in deliverable 5.2, while the public release information of the tool is reported in deliverable 5.3.

2.2. Deliverable 5.1 definition

Deliverable 5.1 addresses the development of the optimization formulation of the grid asset-planning tool under *known* and *unknown* uncertainties. It establishes the main optimization core of the Dig-A-Plan project by linking operational reconfiguration, grid reinforcement, and long-term expansion planning into a unified multi-stage formulation. The work carried out in this task includes the definition of a multi-horizon planning structure, the formulation of the operational reconfiguration problem, and the development and assessment of scalable decomposition approaches for large-scale systems.

2.3. Existing open-source tools

The overarching objective of the project is to devise a strategic plan for expanding distribution grid lines and transformers over time. At any given moment, the decision lies between immediate construction, incurring the full cost of new infrastructure, or deferring construction to a later time, thereby reducing the net cost (factoring in interest rates). Alternatively, we may opt for utilizing the flexibility offered by new loads and generation sources, albeit at a higher cost, especially when adding numerous lines or transformers simultaneously is not feasible.

Initially inspired by [1], we envisaged the concept of developing a stochastic optimization tool tailored for distribution grids. An overview of the proposed multi-stage robust optimization is presented in Figure 1. However, deploying the proposed optimization methods with corresponding solution algorithm outlined poses several challenges. Notably, it necessitates solving the dual problem in backward direction, a task that may be challenging with current toolsets. Moreover, the algorithm’s complexity escalates substantially when faced with a vast array of constraints and variables of power flow equations. Implementation errors is possible, particularly concerning the intricate power flow equations and their various formulations. Furthermore, the mentioned paper treats all uncertain parameters as

[1] https://heig-vd-ie.github.io/dig-a-plan-optimization/.

unknown, raising questions about integrating *known* uncertainties. Perhaps constructing a deterministic equivalent for *known* uncertainties within the stochastic framework could offer a solution.

Drawing insights from [2], we explore methodologies that sidestep the requirement for calculating the dual problem. Some approaches detailed therein rely on data-driven implementations. Ultimately, our strategy is in leveraging Julia-based tools such as `SDDP.jl` and `JuMP`, as presented in Figure 2. The tool `SDDP.jl` facilitates the implementation of multistage distributionally robust optimization techniques. The tool `JuMP` is indispensable for utilizing the models developed with `PowerModels.jl` and seamlessly integrating them into `SDDP.jl`. A summary and references to the above-mentioned open-access tools are presented in Figure 2 below.

pandapower	POWER MODELS	PandaModel	JuMP	SDDP.jl
An easy to use open source tool for power system modeling, analysis and optimization with a high degree of automation.	A Julia package for Steady-State Power Network Optimization. It decouples Problem Specifications (e.g. Power Flow, Optimal Power Flow, ...) from the Formulation Details (e.g. AC, DC approximation, SOC relaxation, ...).	A Julia package which containing supplementary data and codes to prepare pandapower networks in a compatible format for Julia packages which are based on InfrastructureModels, such as PowerModels.jl	A domain-specific modeling language for mathematical optimization embedded in Julia. It can uses different LP, NLP, MILP, MINLP solvers like Ipopt, HiGHS, Gurobi, etc.	A package for solving large convex multistage stochastic programming problems using stochastic dual dynamic programming. - infinite horizon problems - convex risk measures - mixed-integer state and control variables - partially observable stochastic processes.

Figure 2: Existing open-source tools that might be useful for the project.

2.4. Multi-horizon planning framework

As illustrated in Figure 3, the optimization structure is organized across three connected time horizons representing the natural evolution of grid planning and operation:

- **Short-term (flexibility dispatch):** operation and scheduling of flexible assets such as PVs, EVs, and heat pumps.
- **Mid-term (operational configuration):** optimization of network reconfiguration and control settings to ensure reliable operation.
- **Long-term (expansion planning):** strategic investment decisions regarding transformers and line capacity expansion.

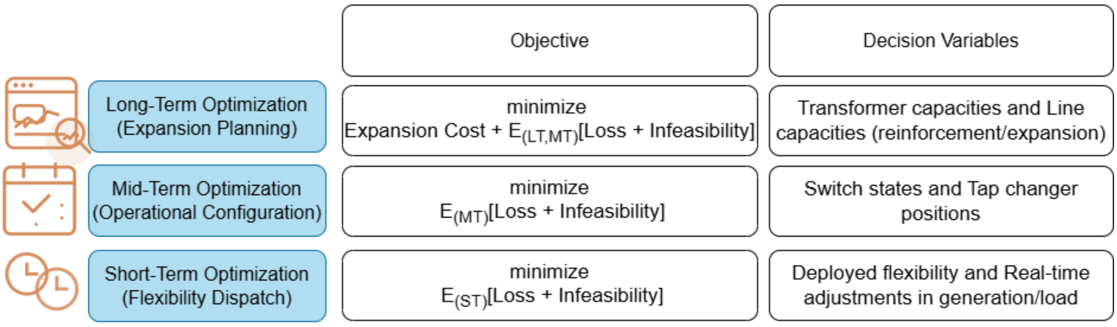

Figure 3: Structure of the optimization framework linking short-, mid-, and long-term decision horizons.

The outcomes of the short-term operational layer provide information for the mid-term configuration layer by helping identify the most effective switching and control strategies. In turn, the mid-term configuration defines the operational constraints and performance indicators that guide long-term planning and investment. In the developed formulation, each horizon seeks to minimize a total cost that includes both power losses and possible constraint violations, using decision variables such as flexibility activation, switch positions, tap positions, and asset capacities.

In the following sections, we concentrate on the mid-term and long-term layers. WPs 3 and 4 address the short-term layer by delivering the power profiles of flexible resources. Accordingly, short-term flexibility is represented as distinct operational scenarios within the mid-term optimization problem.

2.5. Treatment of *known* and *unknown* uncertainties

A key aspect of the formulation proposed in deliverable 5.1 is the distinction between *known* and *unknown* uncertainties. *Known* uncertainties are mainly related to operational variability and can be represented through representative scenarios, such as daily and seasonal changes in load, PV generation, and flexible resource behavior. *Unknown* uncertainties are associated with long-term developments, such as future demand growth and DER penetration, which affect strategic reinforcement decisions.

This distinction directly motivates the multi-layer structure of the Dig-A-Plan methodology presented in Figure 1. Primarily, *unknown* uncertainties affect the long-term planning layer, where reinforcement decisions must remain robust against uncertain future developments. By contrast, *known* uncertainties are addressed through the operational and reconfiguration layers, where representative scenarios are used to verify whether the network can be operated safely and efficiently under different operating conditions.

Within this framework, the mid-term operational reconfiguration problem plays an important role in assessing network operation under *known* uncertainties. It provides a scenario-based evaluation of feasible switching, control actions and therefore supports the overall planning methodology. For this reason, the main optimization formulation developed in deliverable 5.1 focuses first on the reconfiguration problem under *known* uncertainties, as described in the next section.

2.6. Mid-term optimization: operational reconfiguration formulation

Based on the treatment of *known* uncertainties described in the previous section, the mid-term optimization focuses on the operational reconfiguration problem. Its objective is to determine the optimal network topology, represented by switch states, and the optimal control settings, represented by transformer tap positions, to ensure safe and efficient operation under representative operating scenarios. These *known* uncertainties mainly arise from the variability of load demand, PV generation, and flexibility resources over representative daily and seasonal conditions.

The reconfiguration problem is formulated as a mixed-integer second-order cone program (MISOCP) based on the convex DistFlow model. The objective is to minimize a total operational cost combining network losses and infeasibility penalties, while satisfying the technical and topological constraints of the distribution grid. The formulation includes:

- Nodal active and reactive power balance,
- Voltage magnitude limits,
- Current limits for lines and transformers,
- Radiality requirements,
- Binary switch-state variables,
- Transformer tap-position variables that remain consistent across scenarios.

This centralized MISOCP formulation provides a detailed representation of grid operation and reconfiguration. However, its application to large-scale distribution grids leads to significant computational challenges, mainly due to the number of binary variables and the scenario-dependent structure of the problem. In particular, the reported tests showed poor scalability in terms of memory use, runtime, and convergence behavior for large feeders. These limitations motivated the investigation of decomposition-based solution approaches, which are presented in the following sections. To address these issues, we developed and evaluated two decomposition approaches:

- *Benders Decomposition* separates discrete (i.e., switching and tap) and continuous (i.e., power flow) decisions into a master (topology/control) and a slave (feasibility) problem. The flowchart of the proposed methodology is presented in Figure 4. In practice, this formulation reduces complexity by letting the master problem handles topology and control logic, while the slave problem validates detailed network operation. However, difficulties were observed, including numerous iterations, weak or unstable cuts due to binary states, and numerical sensitivity in dual variables, resulting in slow convergence and increased runtime at scale.
- *Consensus Alternating Direction Method of Multipliers (ADMM)* is a fully distributed and parallel approach; where each scenario is solved independently, and consensus is enforced on shared variables (i.e., switch and tap positions). This significantly improves scalability for large systems and enables scenario-level parallelization.

2.7. Bender's decomposition formulation

To improve the tractability of the centralized MISOCP reconfiguration model, the problem is reformulated using *Bender's* decomposition. In this approach, the original problem is separated into a master problem, which handles the discrete topology and control decisions, and a slave problem, which performs the detailed operational feasibility check. This decomposition was introduced to manage the nonlinear and mixed-integer structure of the reconfiguration problem more efficiently than the centralized model, whose scalability was limited on large feeders. The Benders approach separates discrete switch and taps decisions from continuous power-flow validation, thereby reducing the complexity of the centralized formulation. However, practical difficulties were also observed, including numerous iterations, weak or unstable cuts due to binary states, and sensitivity of dual variables, which led to slow convergence at scale.

The iterative workflow of the adopted *Benders* approach is illustrated in Figure 4. Starting from an initial switch configuration, the master model proposes a candidate topology and control setting. The slave model then checks the operational feasibility of this configuration and returns information used to refine the master problem. If the slave solution is infeasible, a *Benders* feasibility cut is added; otherwise, an optimality cut is generated. The procedure continues until the master and slave objective values satisfy the convergence criterion.

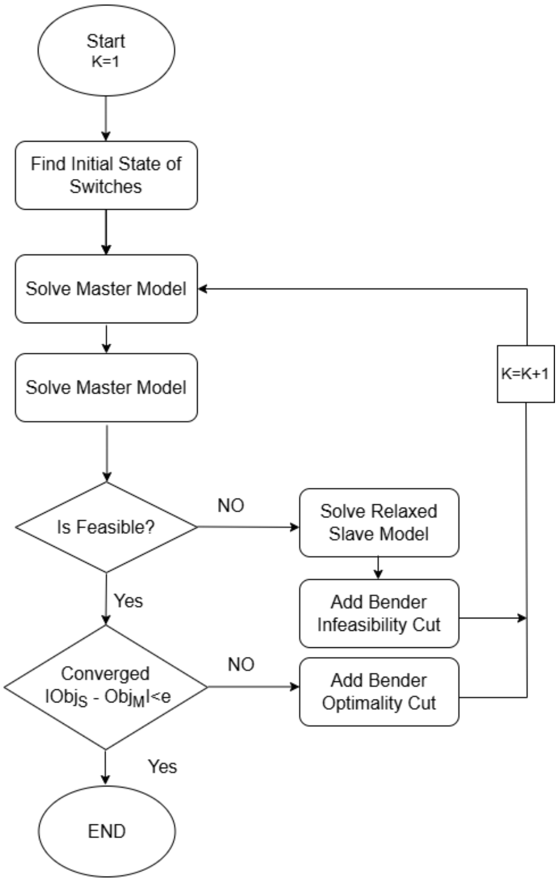

Figure 4: Bender decomposition flowchart.

2.7.1. Master problem

The master problem determines the candidate network configuration through the binary switch-state variables δ_e, the binary tap-selector variables $\zeta_{tr,tap}$, and an auxiliary variable θ representing the best achievable operating cost under the selected configuration. Its objective is:

$$\min_{\delta,\zeta} \theta$$

The master problem is subject to the following groups of constraints.

1) Power-balance constraints

Approximate active and reactive nodal power conservation is imposed, assuming $\Delta p_i = 0$ at the master level:

$$\sum_{j:(i,j)\in\mathcal{E}} \mathrm{P}_{ij,\omega} - \sum_{j:(j,i)\in\mathcal{E}} \mathrm{P}_{ji,\omega} = \mathrm{P}_{i,\omega}^{net}, \quad \forall i \in \mathcal{N}, \forall\omega$$

$$\sum_{j:(i,j)\in\mathcal{E}} \mathrm{Q}_{ij,\omega} - \sum_{j:(j,i)\in\mathcal{E}} \mathrm{Q}_{ji,\omega} = \mathrm{Q}_{i,\omega}^{net} - \sum_{(e,i,j)\in\mathcal{E}} \frac{\mathrm{b}_e}{2} \mathrm{V}_{i,\omega}, \quad \forall i \in \mathcal{N}, \forall\omega$$

with

$$\mathrm{P}_{i,\omega}^{net} = \mathrm{P}_{i,\omega}^{prod} - \mathrm{P}_{i,\omega}^{cons},$$

$$Q_{i,\omega}^{net} = Q_{i,\omega}^{prod} - Q_{i,\omega}^{cons},$$

where $P_{ij,\omega}$ and $Q_{ij,\omega}$ are the active and reactive power flow over the edge i it j under scenario ω. $P_{i,\omega}^{prod}$, $P_{i,\omega}^{cons}$, $Q_{i,\omega}^{prod}$, $Q_{i,\omega}^{cons}$ are active/reactive power production and consumption at node i under scenario ω; $\mathcal{N}$ and $\mathcal{E}$ are the sets of nodes and edges; $j: (i,j) \in \mathcal{E}$ are all the edges starting from node i; $V_{i,\omega}$ is the voltage of node i under scenario ω. Finally, b_e is the susceptance of the edge e because of the capacitance of the line. It is worth mentioning that all variables are in per unit.

2) Linearized voltage drops equations

The master uses simplified LinDistFlow relations for both lines and transformers. The master uses simplified LinDistFlow relations for both lines and transformers. These equations are added in master problem to lead the result into a more feasible solution before the actual equations in the sub-problem.

For distribution branches, the linearized voltage drop relation is

$$V_{i,\omega} - V_{j,\omega} + 2\left(r_e P_{ij,\omega} + x_e Q_{ij,\omega}\right) = 0, \ \forall (e,i,j) \in \mathcal{E}^{(br)}, \ \forall \omega,$$

where r_e and x_e are the resistance and reactance of branch e, $\mathcal{E}^{(br)}$ is the set of distribution branches.

Branch energization is controlled through big-M logic:

$$V_{i,\omega} - V_{j,\omega} \leq M(1-\delta_e), \quad \forall (e,i,j) \in \varepsilon, \forall \omega,$$

$$V_{i,\omega} - V_{j,\omega} \geq -M(1-\delta_e), \quad \forall (e,i,j) \in \varepsilon, \forall \omega,$$

where M is a sufficiently large positive constant and δ_e is a binary variable equal to 1 if branch e is energized and 0 otherwise.

For transformers, the tap-dependent voltage relation is expressed as

$$V_{i,\omega} - V_{j,\omega} + 2\left(r_e P_{ij,\omega} + x_e Q_{ij,\omega}\right) + V_{tap,\omega} = 0, \ \forall (e,i,j) \in \mathcal{E}^{(tr)}, \ \forall \omega$$

where $\mathcal{E}^{(tr)}$ is the set of transformer branches and $V_{tap,\omega}$ is the voltage adjustment introduced by the selected tap position under scenario ω.

Tap position selection is enforced by

$$\left(\frac{tapv - 100}{100}\right) V_{i,\omega} - M\left(1 - \zeta_{tr,tap}\right) \leq V_{tap,\omega} \leq \left(\frac{tap - 100}{100}\right) V_{i,\omega} + M\left(1 - \zeta_{tr,tap}\right).$$

where tap denotes a discrete tap position (expressed in percent), $\zeta_{tr,tap}$ is a binary variable equal to 1 if tap position "tap" is selected for transformer tr and 0 otherwise.

These constraints ensure that exactly one tap position is activated at any time and that the associated voltage shift is applied consistently in the master problem.

3) Radiality constraints

To preserve a tree-like feeder structure and connectivity to the slack bus, the master includes radiality constraints based on auxiliary flow variables $f_{e,ij}$:

$$\sum_{(e,i,j):\, j=n} f_{e,ij} = -\varepsilon, \ \forall n \neq slack,$$

where $f_{e,ij}$ is the auxiliary flow on branch e from bus i to j, ε is a positive constant (typically set to 1) representing a unit artificial demand at each non-slack bus, n denotes a bus in the network, and $slack$ is the reference bus.

$$\sum_{(e,i,j):\, j=slack} f_{e,ij} \geq \varepsilon\,(|\mathcal{N}| - 1),$$

where $|\mathcal{N}|$ is the total number of buses in the network.

$$f_{e,ij} + f_{e,ji} = 0,$$

where $f_{e,ij}$ is the auxiliary flow in the reverse direction of branch e, ensuring antisymmetric of the artificial flow.

$$-\varepsilon|\mathcal{N}|\,\delta_e \le f_{e,ij} \le \varepsilon|\mathcal{N}|\,\delta_e$$

$$\sum_{e\in\mathcal{E}^{(sw)}} \delta_e + \left|\mathcal{E} \setminus \mathcal{E}^{(sw)}\right| = |\mathcal{N}| - 1,$$

where $\mathcal{E}^{(sw)}$ is the subset of switchable branches, and $\left|\mathcal{E} \setminus \mathcal{E}^{(sw)}\right|$ represents the number of permanently closed branches.

These constraints ensure that the final active network remains radial.

4) Operational bounds

The master also imposes admissible bounds on power flows and voltages:

$$-P_e^{max}\,\delta_e \le P_{ij,\omega} \le P_e^{max}\,\delta_e,$$

$$-Q_e^{max}\,\delta_e \le Q_{ij,\omega} \le Q_e^{max}\,\delta_e,$$

$$V_\omega^{slack} - \Delta V \le V_{i,\omega} \le V_\omega^{slack} + \Delta V.$$

$$V_{n,\omega}^{min} \le V_{i,\omega} \le V_{n,\omega}^{max},$$

where ΔV is the relax variable that is minimized in the objective.

5) Discrete control variables

The discrete network decisions are represented by binary variables:

$$\delta_e \in \{0,1\},\ \ \forall e \in \mathcal{E}^{(sw)},$$

$$\zeta_{tr,tap} \in \{0,1\}, \qquad \forall tr, tap$$

$$\sum_{tap} \zeta_{tr,tap} = 1, \forall tr$$

The summation over all admissible tap positions enforces that exactly one tap setting is active for each transformer.

These constraints ensure binary switch selection and one active tap position per transformer.

6) Benders cuts

The coupling between the master and slave models is achieved through optimality and feasibility cuts, which progressively tighten the master relaxation:

- Optimality cut:

$$\theta \ \ge\ \varphi_\omega^{(m)} + \sum_{e\in\mathcal{E}} \pi_{e,\omega}^{(m)}\left(\delta_e - \delta_e^{(m)}\right) + \sum_{tr} \mu_{tr,\omega}^{(m)}\left(\zeta_{tr} - \zeta_{tr}^{(m)}\right),\ \ \forall \omega, m,$$

- Feasibility cut:

$$0 \ \ge\ \psi_\omega^{(m)} + \sum_{e\in\mathcal{E}} \pi_{e,\omega}^{(m)}\left(\delta_e - \delta_e^{(m)}\right) + \sum_{tr} \mu_{tr,\omega}^{(m)}\left(\zeta_{tr} - \zeta_{tr}^{(m)}\right),\ \ \forall \omega, m,$$

where θ is the master auxiliary variable representing the estimated operating cost. $\varphi_\omega^{(m)}$ is the optimal objective value of the slave problem at iteration m under scenario ω. $\pi_{e,\omega}^{(m)}$ is the dual multiplier associated with branch decision δ_e at iteration m and scenario ω. $\mu^{(m)}_{tr,\omega}$ is the dual multiplier associated with transformer tap decision ζ_{tr} at iteration m and scenario ω. δ_e is the current master decision for branch e, $\delta^{(m)}_e$ is the value of δ_e at iteration m. ζ_{tr} is the current master decision variable for transformer tr (aggregated representation of tap selection), $\zeta^{(m)}_{tr}$ is its value at iteration m.

Optimality cuts are generated when the slave problem is feasible and it provides operational cost feedback, ensuring that the auxiliary variable θ remains greater than or equal to the true operating cost. Feasibility cuts are added when the slave problem is infeasible, for example due to voltage or current violations, and they prevent the master from selecting topologies that cannot be operated safely.

2.7.2. Slave problem: feasibility and operational validation

For a fixed topology provided by the master problem, the slave problem performs a second order cone program (SOCP) for full power flow analysis. The objective of the slave problem is to minimize losses and infeasibility penalties:

$$OBJ = \min_{P,Q,V,I,\Delta p} \sum_{(e,i,j)\in\mathcal{E}} r_e I_{ij,\omega} \ + \gamma^{inf} \sum_{i\in\mathcal{N}} |\Delta p_{i,\omega}|,$$

where r_e is the resistance of branch e. $I_{ij,\omega}$ is the squared current magnitude on branch e from bus i to bus j under scenario ω. γ^{inf} is a penalty coefficient for power imbalance or infeasibility. $\Delta p_{i,\omega}$ is the active power mismatch variable at bus i under scenario ω. P and Q denote active and reactive power flow variables, V represents squared voltage magnitude variables at buses, I represents squared current magnitude variables on branches, and ω denotes the operational scenario.

The first term represents total Ohmic losses in the network, while the second term penalizes violations of nodal active power balance to preserve feasibility.

7) Slack bus and propagation of master decisions

The slack bus voltage is fixed as

$$V_{slack,\omega} = V^0_{slack,\omega}, \forall\omega,$$

where $V_{slack,\omega}$ is the voltage magnitude at the designated slack (reference) bus under scenario ω expressed in per unit and $V^0_{slack,\omega}$ is the parameter under scenario ω, which is input of optimization problem. This constraint sets the voltage reference for the entire network and anchors the power flow equations.

The propagation of master decisions into the slave problem is enforced through

$$\delta_e = \delta^{(master)}_e, \ \forall e \in \mathcal{E},$$

where δ_e is the branch status variable used in the slave problem and $\delta^{(master)}_e$ is the corresponding binary decision determined by the master problem.

$$\zeta_{tr,tap} = \zeta^{(master)}_{tr,tap}, \forall tr, tap,$$

where $\zeta_{tr,tap}$ is the transformer tap selection variable in the slave problem and $\zeta^{(master)}_{tr,tap}$ is the tap decision fixed by the master problem.

These constraints ensure that the slave problem evaluates only the network elements that are energized by the master and applies exactly the tap positions selected at the planning level. As a result, the operational feasibility assessment is performed on the precise topology proposed by the master problem.

8) Power balance (with curtailment)

The nodal power balance, including the possibility of active/reactive power curtailment, is expressed as:

$$\sum_{j:(i,j)\in\mathcal{E}} \mathrm{P}_{ij,\omega} - \sum_{j:(j,i)\in\mathcal{E}} \mathrm{P}_{ji,\omega} = \mathrm{P}^{\mathrm{net}}_{i,\omega} + \Delta \mathrm{p}_{i,\omega},\ \ \forall \mathrm{i}, \omega,$$

$$\sum_{j:(i,j)\in\mathcal{E}} \mathrm{Q}_{ij,\omega} - \sum_{j:(j,i)\in\mathcal{E}} \mathrm{Q}_{ji,\omega} = \mathrm{Q}^{\mathrm{net}}_{i,\omega} - \sum_{(e,i,j)\in\mathcal{E}} \frac{\mathrm{b_e}}{2} \mathrm{V}_{i,\omega},\ \ \forall \mathrm{i}, \omega,$$

where $\Delta \mathrm{p}_{i,\omega}$ is a curtailment variable capturing flexibility at each node by allowing small deviations in active power injection, representing curtailed PV generation or reduced load demand.

9) Curtailment bounds

The flexiblity of nodal active power is limited by the following bounds:

$$\Delta p_{i,\omega} = \begin{cases} \left[-p_{i,\omega}^{(nom)}, 0\right], & p_{i,\omega} > 0; \\ \left[0, -p_{i,\omega}^{(nom)}\right], & p_{i,\omega} < 0 \end{cases} \quad \forall\, i, \omega,$$

where $p_{i,\omega}^{(nom)}$ is the nominal active power injection. This constraint limits the degree of flexibility. For generators (P > 0), curtailment cannot exceed total available power. For loads (P < 0), flexibility allows partial load shedding. This ensures realistic operation within physically available bounds.

10) Voltage drop (Full DistFlow)

The voltage drop along an active line or transformer is given by:

$$V_{i,\omega} - V_{j,\omega} + \left[-2\left(r_e p_{i,j,\omega} + x_e q_{i,j,\omega}\right) + (r_e^2 + x_e^2) I_{i,j,\omega}\right] = 0.$$

The first expression enforces the DistFlow voltage drop across each line, where the terms with r_e and x_e model the Ohmic voltage drop caused by active and reactive power flows, while $(r_e^2 + x_e^2) I_{i,j,\omega}$ captures loss-induced effects.

The switch-dependent restriction ensures that the voltage drop relation is applied only when the corresponding line is energized (δ_e=*1*), and relaxed otherwise by:

$$V_{i,\omega} - V_{j,\omega} \le M(1 - \delta_e), \quad \forall (e, i, j) \in \mathcal{E}, \forall \omega,$$

$$V_{i,\omega} - V_{j,\omega} \ge -M(1 - \delta_e), \quad \forall (e, i, j) \in \mathcal{E}, \forall \omega,$$

For transformer branches, an additional variable $V_{tap,\omega}$ accounts for the tap ratio adjustment. The last inequality links this voltage offset to the selected tap position through the binary variable $\zeta_{tr,tap}$ ensuring that only one tap setting is active at a time:

$$\mathrm{V}_{i,\omega} - \mathrm{V}_{j,\omega} + 2\left(\mathrm{r_e} \mathrm{P}_{ij,\omega} + \mathrm{x_e} \mathrm{Q}_{ij,\omega}\right) + (\mathrm{r_e^2} + \mathrm{x_e^2})\, \mathrm{I}_{ij,\omega} + V_{tap,\omega} = 0, \qquad \forall (\mathrm{e}, \mathrm{i}, \mathrm{j}) \in \mathcal{E},\ \forall \omega,$$

$$\left(\frac{tap - 100}{100}\right) V_{i,\omega} - M\left(1 - \zeta_{tr,tap}\right) \le V_{tap,\omega} \le \left(\frac{tap - 100}{100}\right) V_{i,\omega} + M\left(1 - \zeta_{tr,tap}\right), \forall \mathrm{tr}, \mathrm{tap}, \omega,$$

11) SOCP coupling

The convex relaxation linking power flows, voltage, and current is:

$$\mathrm{P}_{ij,\omega}^2 + \mathrm{Q}_{ij,\omega}^2 \ \le\ \mathrm{V}_{i,\omega}\, \mathrm{I}_{ij,\omega},\ \ \forall (\mathrm{i}, \mathrm{j}) \in \mathcal{E},\ \forall \omega.$$

This second-order cone constraint ensures a convex relaxation of the power flow relation between active/reactive flows, voltage, and current.

12) Operational limits

The technical operation constraints are:

$$-\mathrm{M}\delta_e \le \mathrm{P}_{ij,\omega} \le \mathrm{M}\delta_e\,, \qquad \forall (\mathrm{e}, \mathrm{i}, \mathrm{j}) \in \mathcal{E},\ \forall \omega,$$

$$-\mathrm{M}\delta_e \le \mathrm{Q}_{ij,\omega} \le \mathrm{M}\delta_e, \qquad \forall (\mathrm{e}, \mathrm{i}, \mathrm{j}) \in \mathcal{E},\ \forall \omega,$$

$$I_{ij,\omega} \leq I_{ij}^{max}, \qquad \forall(\mathrm{e,i,j}) \in \mathcal{E},\ \forall\omega,$$

$$V_i^{min} \leq V_{i,\omega} \leq V_i^{max}, \qquad \forall i \in \mathcal{N},$$

where I_{ij}^{max} is the rated current capacity of branch (i,j), and V_i^{min}, V_i^{max} are the minimum and maximum voltage limits at bus i.

The abovementioned constraints (7)-(12) impose technical operation boundaries, ensuring that:

- Currents remain below rated line capacities,
- Voltages remain within acceptable limits,
- Active and reactive power flows respect the capacity of energized branches (enabled by δ_e=*1*).

According to the flowchart in Figure 4, the Benders decomposition iteratively alternates between the master and slave problems. The master problem proposes a candidate of network configuration (switch and tap states), while the slave problem verifies feasibility, performs the operational power-flow evaluation, and returns dual information used to refine the master's solution space.

At each iteration, convergence is checked using the relative gap between the master and slave objectives:

$$\mid OBJ_M^{(k)} - OBJ_S^{(k)} \mid < \varepsilon,$$

where $OBJ_M^{(k)}$ and $OBJ_S^{(k)}$ denote the master and slave objective values at iteration k, and ε is a small tolerance (typically 10^{-4}). If this condition is satisfied, the algorithm terminates; otherwise, feasibility or optimality cuts are added, and the process continues with $k \leftarrow k + 1$.

While this decomposition significantly improves scalability compared to the centralized MISOCP, slow convergence was occasionally observed due to weak Benders cuts and instability in dual information when multiple binary configurations were active. To alleviate these issues, a distributed ADMM-based reformulation was later developed, achieving faster convergence and near-linear scalability on networks with many nodes.

2.8. Proposed ADMM formulation

We address the problem of *distribution network reconfiguration* (DNR) under uncertainty, formulated as an MISOCP. The formulation accurately represents power flow physics together with discrete switching and *on-load tap changer* (OLTC) positions. However, its computational complexity increases rapidly with network size, making standard solvers impractical for large or real-world urban distribution systems.

To overcome this challenge, we propose a scalable, consensus-based algorithm that integrates the MISOCP formulation with the ADMM. The algorithm decomposes the DNR problem across multiple scenarios, allowing sub-problems to be solved independently while maintaining global consistency in discrete switching and OLTC decisions. A *loop-based switch-grouping* strategy reduces combinatorial complexity, while an *adaptive penalty update* enhances convergence speed and numerical stability.

Distribution networks are undergoing a profound transformation driven by the rapid proliferation of DERs such as PV systems, *electric vehicle charging stations* (EVCSs), and *heat pumps* (HPs). While these technologies play a pivotal role in advancing the energy transition and enhancing system flexibility, they also introduce substantial uncertainty and temporal variability into network operation. Fluctuating generation and load patterns can induce voltage deviations, thermal overloading of lines and transformers, and increased network losses [3, 4, 5]. Among the various operational strategies available to distribution system operators, DNR has emerged as a practical and effective means of mitigating these challenges. Through the coordinated operation of sectionalizing and tie switches, complemented by the adjustment of OLTC positions, the network topology can be dynamically adjusted to minimize energy losses, reduce power flow congestion, and ensure secure and reliable operation [6, 7]. The reconfiguration intervals can range from seasonal to daily, depending on the degree of grid automation and the availability of controllable switching devices.

A wide range of methodologies has been developed to tackle the DNR problem. Early studies primarily relied on heuristic and metaheuristic optimization techniques, including genetic algorithms [8] and the branch-exchange method [9]. Although such techniques can provide practically acceptable configurations, they lack guaranties of global optimality and often face difficulties in accurately capturing complex operational constraints. To overcome these shortcomings, recent research has increasingly adopted mathematical optimization frameworks, resulting in problem formulations based on *mixed-integer linear programming* (MILP) [10], *mixed-integer nonlinear programming* (MINLP) [7, 11], and various convex relaxations [12, 13]. Second-order cone relaxations of the branch flow, i.e., DistFlow, model [14, 15] and its exact reformulation for radial systems [16] have received considerable attention. These optimization-based formulations provide a systematic means to capture network radiality, voltage limits, and current constraints within a convex framework. However, when extended to incorporate the variability of load and generation across multiple operating scenarios, their computational complexity increases sharply, motivating the need for more scalable solution strategies. Consequently, recent studies have explored scenario-based formulations of the DNR problem that explicitly account for uncertainty in load and generation. Among these, stochastic and robust optimization approaches [7, 17] offer a more realistic representation of uncertainty but at the expense of significantly higher computational effort, particularly as the number of scenarios increases.

To enhance scalability in a multi-scenario setting, several techniques based on decomposition have been explored, particularly for distribution networks with many nodes and operating scenarios. Among these, Bender's decomposition has been applied to the DNR problem for small- and medium-scale networks [18, 19], demonstrating excellent performance in such cases but without fully addressing the computational challenges inherent in large-scale, scenario-based formulations. Other decomposition strategies, including progressive hedging [20] and Lagrangian relaxation [21], have also been investigated in related power system optimization to manage uncertainty. While these methods effectively partition the original formulation into smaller sub-problems, they often exhibit slow convergence or face a combinatorial increase in the sub-problem count as the number of nodes and scenarios grows. Consequently, developing scalable and computationally efficient algorithms for large-scale, uncertainty-aware DNR remains an open and challenging research direction.

A promising direction for tackling this scalability challenge is the ADMM, which offers a natural decomposition for large-scale and multi-scenario formulations of the DNR problem. ADMM decomposes the global optimization problem into independent, scenario-specific sub-problems while iteratively enforcing consensus over shared binary and continuous decisions. This structure is inherently parallelizable, allowing each sub-problem to be solved independently before synchronizing the global variables. Even when executed sequentially, the decomposition substantially reduces per-iteration computational effort and facilitates straightforward scalability to multi-core or distributed computing environments.

Recent research has explored the application of ADMM to a range of power system optimizations, demonstrating its flexibility for distributed computation. For instance, [22] proposes a fully distributed ADMM scheme for the continuous, non-convex AC *optimal power flow* (OPF), focusing exclusively on convexified continuous variables and without modeling discrete switching or OLTC actions. In contrast, [23] develops a non-convex ADMM algorithm for service restoration that incorporates binary reconfiguration decisions through a relax-drive-polish procedure combined with autonomous clustering. Although these studies demonstrate the potential of ADMM for large-scale power system optimization, they neglect discrete operational variables or rely on heuristic treatments for their inclusion. As a result, establishing an ADMM algorithm capable of jointly managing discrete switching operations, OLTC controls, and non-convex power flow constraints in large-scale DNR remains an open problem. Tackling this challenge requires a scalable coordination strategy capable of efficiently handling binary decisions and power flow couplings across multiple operating scenarios. Thus, it provides the motivation for the proposed algorithm presented in this study.

In this section, we present a scalable optimization algorithm for the large-scale, multi-scenario DNR problem. The proposed algorithm uses the ADMM to decompose the global optimization problem into independent scenario sub-problems while enforcing global consistency in discrete operational decisions. The optimization model simultaneously captures continuous power flow constraints and discrete control actions, including switching operations and OLTC adjustments, providing a realistic and comprehensive characterization of network behavior. Additionally, a spatial loop-based switch-grouping mechanism is integrated into the ADMM iterations to enhance numerical stability and accelerate convergence under uncertainty in nodal load profiles. Together, these features enable efficient and reliable reconfiguration of complex distribution networks with numerous nodes and operating conditions.

The main contributions of are summarized as follows:

- A multi-scenario MISOCP formulation for the DNR problem is developed, jointly modeling switch states, OLTC positions, network radiality, and operational constraints.
- A consensus-based ADMM algorithm is proposed to decompose the problem across multiple scenarios, enabling distributed computation while enforcing the non-anticipative constraints.
- A spatial loop-based switch-grouping mechanism is proposed to reduce problem dimensionality, enhance numerical stability, and accelerate convergence in large-scale networks.

2.8.1. DNR Problem as MISOCP Formulation

We consider the DNR problem under multiple operating scenarios. The distribution network is represented as a graph $(\mathcal{N}, \mathcal{E})$, where $\mathcal{N}$ denotes the set of nodes and $\mathcal{E}$ is the set of edges, partitioned into distribution lines $\mathcal{E}^{(line)}$, transformers $\mathcal{E}^{(tr)}$, and controllable switches $\mathcal{E}^{(sw)}$. Each operating scenario $\omega \in \Omega$ corresponds to a particular realization of load and generation, and the network reconfiguration must guarantee feasible operation across all scenarios.

Formally, we define the set of operating scenarios as Ω, and the set of branches, comprising lines and transformers, as $\mathcal{E}^{(br)} = \mathcal{E} \setminus \mathcal{E}^{(sw)}$. Each branch $e \in \mathcal{E}^{(br)}$ is characterized by its electrical parameters: resistance r_e, reactance x_e, apparent power rating F_e, and current limit I_e. At each node $i \in \mathcal{N}$ and scenario $\omega \in \Omega$, the net active and reactives power injections are denoted by p_i^ω and q_i^ω, with generation represented as positive and load as negative. The squared nodal voltage is constrained within the admissible range $[v_i^{(\min)}, v_i^{(\max)}]$, where $v_i^{(\min)}$ and $v_i^{(\max)}$ denote the minimum and maximum allowable squared voltages of node i, respectively. To handle potential infeasibility, curtailed power variables $\Delta\, p_i^\omega$ are introduced and penalized in the objective function with a weighting factor $\gamma^{(\mathrm{inf})}$.

The decision variables are categorized into two classes. The first class includes continuous, scenario-dependent variables:

$$z_\omega = \left\{ \left(P_{ij}^\omega, Q_{ij}^\omega, \ell_{ij}^\omega\right)_{(e,i,j)\in\mathcal{E}^f}, (v_i^\omega, \Delta p_i^\omega)_{i\in\mathcal{N}} \right\},$$

where $\mathcal{E}^f = \{(e,i,j) | e \in \mathcal{E}, i, j \ \ are\ the\ end\ nodes\ of\ \ e\}$, P_{ij}^ω and Q_{ij}^ω are active and reactive power flows from node i to node j, ℓ_{ij}^ω is the squared current magnitude, v_i^ω is the squared nodal voltage, and Δp_i^ω is the curtailed power at node i. The second class includes discrete scenario-independent decision variables:

$$y = \left\{ (\tau_e)_{e\in\mathcal{E}^{(tr)}}, (\kappa_e)_{e\in\mathcal{E}^{(sw)}} \right\},$$

where $\tau_e \in \left\{\tau_e^1, \dots, \tau_e^{N_e}\right\}$ is the tap ratio of transformer e, and $\kappa_e \in \{0,1\}$ denotes the switch state, with $\kappa_e = 1$ for closed and $\kappa_e = 0$ for open state of switch e.

The optimization objective is to minimize energy losses and infeasibility penalties across all scenarios:

$$\min_{\{z_\omega\}_{\omega\in\Omega}, y} \sum_{\omega\in\Omega} h_\omega(z_\omega, y) = \sum_{\omega\in\Omega} \left(\sum_{e\in\mathcal{E}^{(br)}} r_e \ell_e^\omega + \gamma^{(inf)} \sum_{i\in\mathcal{N}} |\Delta p_i^\omega| \right).$$

The problem is subject to the following constraints that capture the physical and operational limits of a distribution network:

1) Active power balance:

At each node, the sum of incoming and outgoing active power flows equals the net nodal injection adjusted by curtailed power:

$$\sum_{\{j:(e,i,j)\in\mathcal{E}f\}} P_{ij}^{\omega} = p_i^{\omega} + \Delta p_i^{\omega}, \qquad \forall i \in \mathcal{N}, \omega \in \Omega.$$

2) Reactive power balance:

Like the active power balance, this equation enforces reactive power balance at each node.

$$\sum_{\{j:(e,i,j)\in\mathcal{E}f\}} Q_{\{ij\}}^{\omega} = q_i^{\omega}, \qquad \forall i \in \mathcal{N}, \omega \in \Omega.$$

3) Voltage drop (DistFlow equations):

For each edge $(e,i,j) \in \mathcal{E}$ and scenario $\omega \in \Omega$, the squared voltage difference is modeled as:

$$v_i^{\omega} - v_j^{\omega} = 2\left(r_e P_{\{ij\}}^{\omega} + x_e Q_{\{ij\}}^{\omega}\right) + (r_e^2 + x_e^2)\ell_{\{ij\}}^{\omega} + \delta V_{\{tr\}}^{(\omega)}.$$

The first two terms represent the Ohmic voltage drop along a line with resistance r_e, reactance x_e. The additional term $\delta V_{\{tr\}}^{(\omega)}$ accounts for transformer tap ratios:

$$\delta V_{\{tr\}}^{(\omega)} = \begin{cases} \tau_e^2 \mathrm{v}_j^{\omega}, & \text{if } e \text{ is transformer,} \quad \mathrm{HV} \rightarrow \mathrm{LV} \\ \dfrac{1}{\tau_e^2} \mathrm{v}_j^{\omega}, & \text{if } e \text{ is a transformer,} \quad \mathrm{LV} \rightarrow \mathrm{HV}, \\ 0, & \text{if } e \text{ is a distribution line.} \end{cases}$$

4) Curtailment bounds:

The available generation or load at each node limit the curtailment variables:

$$\Delta p_i^{\omega} \in \begin{cases} [-\mathrm{p}_i^{\omega}, 0], & \mathrm{p}_i^{\omega} \geq 0, \\ [0, -\mathrm{p}_i^{\omega}], & \mathrm{p}_i^{\omega} < 0, \end{cases} \forall \mathrm{i} \in \mathcal{N}, \omega \in \Omega.$$

5) SOCP current-power relation:

The quadratic constraint linking power flows and current magnitude is relaxed as a second-order cone:

$$\left(P_{\{ij\}}^{\omega}\right)^2 + \left(Q_{\{ij\}}^{\omega}\right)^2 \leq v_i^{\omega} \ell_{\{ij\}}^{\omega}, \forall (e,i,j) \in \mathcal{E}^f, \omega \in \Omega.$$

6) Current and transformer limits:

The line and transformer capacities are enforced through thermal and current limits.

$$\left|P_{\{ij\}}^{\omega}\right| \leq \kappa_e F_e,$$

$$\left|Q_{\{ij\}}^{\omega}\right| \leq \kappa_e F_e,$$

$$\ell_{\{ij\}}^{\omega} \leq \kappa_e I_e^2, \forall (e,i,j) \in \mathcal{E}^f, \omega \in \Omega.$$

7) Voltage limits:

Nodal voltages are constrained within the permissible operating range:

$$v_i^{(\min)} \leq v_i^{\omega} \leq v_i^{(\max)}, \qquad \forall i \in \mathcal{N}, \omega \in \Omega.$$

8) Radiality (artificial-flow model):

The distribution grid, specifically the LV grid is operated in radial mode.

Therefore, in addition to nodal power-balance that enforces Kirchhoff's current law (KCL), we add constraints for grid radiality. To ensure radial topology, an artificial-flow formulation is described below. For each directed arc $(e,i,j) \in \mathcal{E}^f$, an auxiliary flow variable $f_{\{eij\}}$ is defined. A slack node $s \in \mathcal{N}$ is designated, and a small scalar $\varepsilon > 0$ is used to orient the tree. The following constraints are then imposed:

Flow-balance:

$$\sum\nolimits_{(e,i,j)\in\mathcal{E}^{\{f\}}:\, j=n} f_{eij} = -\varepsilon, \qquad \forall\, n \in \mathcal{N}\backslash\{s\};$$

$$\sum_{(e,i,j)\in\mathcal{E}^f, j=s} f_{\{eij\}} \geq \varepsilon(|\mathcal{N}| - 1),$$

Orientation:

$$\sum_{\{(e,i,j)\in\mathcal{E}^f, e=\bar{e}\}} f_{\{eij\}} = 0, \qquad \forall \bar{e} \in \mathcal{E},$$

Switch-propagation:

$$-\varepsilon|\mathcal{N}|\kappa_e \leq f_{\{eij\}} \leq \varepsilon|\mathcal{N}|\kappa_e, \qquad \forall (e,i,j) \in \mathcal{E}^f \text{ with } e \in \mathcal{E}^{(sw)},$$

Spanning-tree size:

$$\sum_{\{\, e\in\mathcal{E}^{(sw)}\}} \kappa_e + \left|\mathcal{E} \setminus \mathcal{E}^{(sw)}\right| = |\mathcal{N}| - 1.$$

The above constraints ensure connectivity, with a unique parent per non-slack node and zero net artificial flow on each physical edge, while last equation fixes the number of active branches to $|\mathcal{N}| - 1$, thereby enforcing radial operation. Unlike alternative formulations based on cycle-elimination constraints or flow-based radiality models, e.g., single-commodity and multi-commodity flow [24], which introduce numerous auxiliary variables and constraints, this scheme attains radiality with a single cardinality equality, yielding a lightweight yet effective representation for large-scale systems.

The proposed formulation defines MISOCP. While mathematically exact, solving this monolithic model is intractable for large-scale networks and many operating scenarios due to the exponential complexity introduced by discrete reconfiguration variables and number of continuous variables. To address this challenge, we adopt a decomposition strategy based on ADMM. For each scenario $\omega \in \Omega$, we create local copies of the operational variables z_ω and discrete decisions: $y_\omega := \left\{ (\tau_e^\omega)_{\{e\in\mathcal{E}^{(tr)}\}}; (\kappa_e^\omega)_{\{e\in\mathcal{E}^{(sw)}\}} \right\}$. This allows scenario sub problems to be solved independently, while the following constraint, i.e., non-anticipative constraint, requires that all y_ω agree with a common global consensus decision vector:

$$y_\omega = y, \forall\, \omega \in \Omega.$$

This consensus formulation provides the foundation for the distributed ADMM scheme proposed in the next subsection.

2.8.2. Consensus-based ADMM Decomposition and Switch-Grouping

The consensus-based ADMM decomposition provides a natural framework for distributed optimization of the multi-scenario DNR problem.

To exploit this, the large-scale DNR problem is decomposed into scenario-specific sub-problems while enforcing non-anticaptivity of the global discrete reconfiguration decisions via consensus. Each scenario $\omega \in \Omega$ maintains a local copy of the switching and tap variables, denoted by $y_\omega^{(sw)}$ and $y_\omega^{(tr)}$, while global consensus vectors $\tilde{y}^{(sw)}$ and $\tilde{y}^{(tr)}$ link these local decisions across scenarios. Within each ADMM iteration, local sub-problems are solved independently with consensus terms fixed, after which the consensus variables and corresponding duals are updated. This alternating procedure gradually reconciles scenario wise decisions and drives the primal-dual residuals to zero, yielding a discrete-consistent and operationally feasible solution.

A primary computational challenge in grid reconfiguration is the large dimensionality of binary switching decisions. Updating all switches simultaneously at every ADMM iteration is computationally intensive and can impede convergence. To address this, we employ a spatial partitioning strategy, dividing the set of controllable switches $\mathcal{E}^{(sw)}$ into G groups:

$$\mathcal{E}^{(sw)} = \bigcup_{\{g=1\}}^{G} \mathcal{E}_g^{(sw)},$$

$$y_\omega^{(sw)} = \left(y_{\{\omega,g\}}^{(sw)}, y_{\{\omega,-g\}}^{(sw)}\right),$$

$$\tilde{y}^{(sw)} = \left(\tilde{y}_g^{(sw)}, \tilde{y}_{-g}^{(sw)}\right).$$

In this formulation, $y_{\{\omega,g\}}^{(sw)}$ denotes the subset of switch variables belonging to the *active* group g for scenario ω, whereas $y_{\{\omega,-g\}}^{(sw)}$ collects the remaining switches that are held fixed during the current update.

The global consensus vector $\tilde{y}^{(sw)}$ is similarly partitioned into active and inactive components. At each iteration, only the active switches $y_{\{\omega,g\}}^{(sw)}$ updated toward their consensus target $\tilde{y}_g^{(sw)}$, while the complementary switches $y_{\{\omega,-g\}}^{(sw)}$ are kept equal to their previous consensus values $\tilde{y}_{-g}^{(sw)}$.

The partitioning logic is rooted in the physical topology of the grid. Specifically, groups are derived from *spatial loops* (fundamental cycles); all switches belonging to a common cycle are assigned to the same group. This ensures that the updates respect the local mesh structures of the network.

In contrast, transformer tap variables are excluded from this grouping strategy and are updated in every iteration. This distinction is based on two key factors:

(i) The number of transformer taps is typically much smaller than the number of switches, so grouping them would not provide any significant computational benefit.

(ii) OLTC positions follow an ordered discrete structure, often modeled via special ordered sets (SOS), e.g., SOS1. Grouping taps would interfere with this ordered structure, potentially violating the adjacency property required by SOS formulations and causing numerical instability. In contrast, switch variables are binary and unstructured, which makes them well suited for grouping without loss of modeling fidelity.

2.8.3. ADMM Iteration Scheme

With the switch-grouping scheme in place, the ADMM procedure alternates between three steps:

(i) local scenario update (x-update),

(ii) consensus averaging (z-update), and

(iii) Dual update of the multipliers.

In the first step, i.e., the x-update, for each scenario $\omega \in \Omega$ and active switch group g at iteration k, we solve a local sub problem that optimizes the operational variables z_ω, the active switch group $y_{\{\omega,g\}}^{(sw)}$, and the transformer $y_{\{g\}}^{(tr)}$, while holding the inactive switches at their consensus values. This step is formulated as:

$$\min_{\{z_\omega, y^{(sw)}_{\{\omega,g\}}, y^{(tr)}_{\{\omega\}}\}} h_\omega\left(z_\omega, y^{(sw)}_{\{\omega,g\}}, \tilde{y}^{(sw),(k-1)}_{\{-g\}}, y^{(tr)}_{\{\omega\}}\right) + \frac{\rho}{2}|y^{(sw)}_{\{\omega,g\}} - \tilde{y}^{(sw),(k-1)}_{\{g\}}|_2^2 + \lambda^{(sw),(k-1)\top}_{\{\omega,g\}}\left(y^{(sw)}_{\{\omega,g\}} - \tilde{y}^{(sw),(k-1)}_{\{g\}}\right)$$
$$+\frac{\rho}{2}|y^{(tr)}_{\{\omega\}} - \tilde{y}^{(tr),(k-1)}|_2^2 + \lambda^{(tr),(k-1)\top}_{\{\omega\}}\left(y^{(tr)}_{\{\omega\}} - \tilde{y}^{(tr),(k-1)}\right),$$

subject to the physical and operational constraints (1)-(8).

Once the local problems are solved, the global consensus step, i.e., the z-update, aggregates the results across all scenarios. The active switch group and transformer taps are averaged over scenarios, while the inactive switches remain fixed at their previous consensus values:

$$y^{(sw),(k)}_g = \frac{1}{|\Omega|}\Sigma_{\{\omega\in\Omega\}} y^{(sw),(k)}_{\{\omega,g\}},$$
$$\tilde{y}^{(sw),(k)}_{\{-g\}} = \tilde{y}^{(sw),(k-1)}_{\{-g\}},$$
$$\tilde{y}\quad(tr),(k) = \frac{1}{|\Omega|}\Sigma_{\{\omega\in\Omega\}} y^{(tr),(k)}_{\{\omega\}}.$$

The dual step then updates the multipliers associated with the active switches and transformer taps, ensuring that local and global variables are gradually aligned:

$$\lambda^{(sw),(k)}_{\{\omega,g\}} = \lambda^{(sw),(k-1)}_{\{\omega,g\}} + \rho\left(y^{(sw),(k)}_{\{\omega,g\}} - \tilde{y}^{(sw),(k)}_{\{g\}}\right),$$
$$\lambda^{(tr),(k)}_{\{\omega\}} = \lambda^{(tr),(k-1)}_{\{\omega\}} + \rho\left(y^{(tr),(k)}_{\{\omega\}} - \tilde{y}^{(tr),(k)}\right).$$

2.8.4. Convergence Criteria

Convergence of the ADMM iterations is assessed by monitoring both the *primal* and dual residuals. The primal residual quantifies violation of the consensus constraints, i.e., the deviation of scenario-specific variables from their consensus values.

$$r^{(k)}_{norm} = \max\left(\max_{\{\omega\in\Omega\}}|y^{(sw)(k)}_{\omega,g} - \tilde{y}^{(sw)(k)}_g|_\infty, \max_{\{\omega\in\Omega\}}|y^{(tr)(k)}_\omega - \tilde{y}^{(tr)(k)}|_\infty\right),$$

In parallel, the dual residual measures the change in the consensus variables between consecutive iterations:

$$s^{(k)}_{norm} = \rho\sqrt{\sum_g |\tilde{y}^{(sw)(k)}_g - \tilde{y}^{(sw)(k-1)}_g|_2^2 + \sum_g |\tilde{y}^{(tr)(k)} - \tilde{y}^{(tr)(k-1)}|_2^2},$$

The algorithm is considered converged once both residuals fall below prescribed thresholds:

$$r^{(k)}_{norm} \le \varepsilon_{(pri)},$$

and

$$s^{(k)}_{norm} \le \varepsilon_{(dual)},$$

where $\varepsilon_{(pri)}$ and $\varepsilon_{(dual)}$ are tolerance values.

To balance progress between primal and dual feasibility, the ADMM penalty parameter ρ is adapted dynamically:

$$\rho^{(k+1)} = \begin{cases} \tau_{\{incr\}}\,\rho^{(k)}, & r^{(k)} > \mu\, s^{(k)}_{norm}, \\ \dfrac{\rho^{(k)}}{\tau_{\{decr\}}}, & s^{(k)} > \mu\, r^{(k)}_{norm}, \\ \rho^{(k)}, & \text{otherwise.} \end{cases}$$

with fixed tuning parameters $\mu > 1$, $\tau_{\{incr\}} > 1$, and $\tau_{\{decr\}} > 1$. This adaptive mechanism balances progress between primal and dual feasibility and is known to improve both stability and efficiency of convergence.

Taken together, the local scenario updates, consensus averaging, dual multiplier adjustments, and residual-based penalty adaptation constitute the complete consensus-based ADMM algorithm, whose overall procedure is summarized in Algorithm 1.

Algorithm 1 Consensus-based ADMM with Switch Grouping

Input: Initial consensus $\tilde{\boldsymbol{y}}^{(0)}$, multipliers $\{\lambda_\omega^{(0)}\}_{\omega\in\Omega}$, penalty $\rho^{(0)}$, switch partition $\mathcal{E}^{(\mathrm{sw})} = \bigcup_{g=1}^{G} \mathcal{E}_g^{(\mathrm{sw})}$, tolerances $\varepsilon_{\mathrm{pr}}, \varepsilon_{\mathrm{du}}$

1: $k \leftarrow 0$
2: **while** $r_{\mathrm{norm}}^{(k)} > \varepsilon_{\mathrm{pr}}$ **or** $s_{\mathrm{norm}}^{(k)} > \varepsilon_{\mathrm{du}}$ **do**
3: **Select group** g; **fix** κ_e for $e \in \mathcal{E}^{(\mathrm{sw})} \setminus \mathcal{E}_g^{(\mathrm{sw})}$ at previous values
4: **for all** $\omega \in \Omega$ **do**
5: **Scenario subproblem (x-update):** solve MISOCP with constraints (2)–(12), penalized consensus as in (14); obtain $(\boldsymbol{z}_\omega^{(k+1)}, \boldsymbol{y}_\omega^{(k+1)})$
6: **end for**
7: **Consensus update** (z-update): update $\tilde{\boldsymbol{y}}^{(k+1)}$ using (15)
8: **Dual update**: update $\lambda_\omega^{(k+1)}$ using (16)
9: **Residuals**: compute $r_{norm}^{(k+1)}$ and $s_{norm}^{(k+1)}$ using (17)–(18)
10: **Penalty update**: adapt $\rho^{(k+1)}$ using (19)
11: $k \leftarrow k+1$
12: **end while**

Output: Consensus reconfiguration $(\tilde{\boldsymbol{y}}^{(\mathrm{sw})}, \tilde{\boldsymbol{y}}^{(\mathrm{tr})})$

2.9. Long-term Optimization: Expansion Planning

The installation of distributed PV generation, EVCSs, and HPs is rapidly growing globally due to the urgent need to address climate change and decarbonization. However, this is challenging for electrical DSOs, as changes in demand configuration in LV and MV grids can lead to voltage violations and grid congestion. To overcome this challenge, we introduce a two-layer optimization framework for planning distribution grid assets, such as lines and transformers. The *upper* layer makes decisions regarding the expansion of grid assets for the upcoming years of the planning horizon, e.g., 5 years, considering the uncertainty in demand configuration. The *lower* layer focuses on the optimal deployment of grid flexibility in daily operations during those years to ensure that nodal voltages, as well as line and transformer currents, remain within safe limits.

A major issue for DSOs in the energy transition is determining how to expand their grid assets during a fundamentally uncertain future. The growth of distributed PV generation, EVCSs, and HPs, and the corresponding surge in *connection requests*[2], which is highly uncertain, as it depends on various unpredictable factors, such as consumer behavior, national policy decisions, and technological

[2] A connection request refers to an application submitted by a consumer to the DSO for connecting new electrical installations, such as PV systems, EVCSs, or HPs, to the grid. Each connection request specifies the desired connection capacity, location, and timing. Based on the grid's technical limits and planned reinforcements, the DSO can approve, either delay, or reject the request.

advancements. Grid reliability is threatened by these uncertainties, which manifest as network congestion and voltage violations.

To overcome this planning difficulty, the planning framework must distinguish between different types of uncertainties rather than treating them identically. A clear distinction must be made between *known* and *unknown* uncertainties based on their predictability. *Known* uncertainties, such as daily solar generation patterns or hourly demand profiles, exhibit well-defined probabilistic behavior that can be reliably characterized using historical data and clustering techniques. In contrast, *unknown* uncertainties, such as future *connection requests* for PV systems, EVCSs, and HPs, lack accurate probabilistic models, as they depend on external and largely uncontrollable factors. This distinction is critical, as it determines which mathematical tools are suitable and at which planning timescale they should be applied.

Current approaches for *distribution network expansion planning* (DNEP) address *known* and *unknown* uncertainties in various ways, as fully reviewed in [25]. Scenario-based stochastic programming is a more realistic framework than deterministic approaches; however, it often leads to infeasible or oversized grid designs because it requires fully specified probability distributions, which are rarely accurate for *unknown* uncertainties. In contrast, robust optimization ensures viability even in worst-case scenarios, but it might be too conservative and economically inefficient [26]. Distributionally robust optimization (DRO) is a more reasonable approach that is robust against *unknown* uncertainty while avoiding extreme conservatism [27-31]. When paired with multistage decision models, DRO is especially effective. Huang et al. [32] established the theoretical foundations by demonstrating that multistage DRO problems can be reformulated as a convex combination of expectation and the *conditional value-at-risk* (CVaR), which allows an efficient solution via *stochastic dual dynamic programming* (SDDP) [33]. Duque and Morton [34] introduced the SDDP with Wasserstein ambiguity sets. The subsequent works have applied this method to diverse optimization problems, e.g., generation dispatch with demand response [35], distributed economic dispatch [36], and energy storage planning [37].

Despite substantial progress, a significant gap remains. Most existing works address DNEP, grid operational flexibility, and operational feasibility as separate problems. This separation creates a critical risk: grid expansion plans that appear optimal and feasible in theory may fail in practice once the demand configuration is realized.

To bridge this gap, we propose a two-layer optimization framework that explicitly differentiates *known* and *unknown* uncertainties according to their time scales, while incorporating operational feasibility directly into the grid expansion decision-making process.

- The *upper* layer addresses the *unknown* uncertainties, including future *connection requests* for distributed PV systems, EVCSs, and HPs. It identifies which line or transformer of the grid should be reinforced or replaced in the coming years. This layer is formulated as SDDP with the Wasserstein ambiguity set to arrive at optimal decisions that are robust against the distribution uncertainty of the demand configuration.
- The *lower* layer addresses the *known* uncertainties, including the demand and generation profile variations on an hourly basis. Once the *upper* layer decisions disclose the available grid capacities, the *lower* layer optimizes grid flexibility, including tap changer positions and switching operations, to handle voltage and current limits under variable demand and generation profiles. An ADMM decomposition is used to maintain computational tractability while respecting the detailed grid model.

Unlike existing approaches that assess feasibility only after grid expansion planning, our proposed two-layer optimization framework integrates operational constraints directly into the long-term grid expansion-planning problem. This ensures that all expansion decisions of the *upper* layer are operationally feasible under varying conditions. The *lower* layer uses an ADMM-based decomposition to maintain scalability for large networks with thousands of nodes. Moreover, by distinguishing between *known* and *unknown* uncertainties, the proposed framework remains robust to ambiguous future *connection requests* while consistently satisfying operational limits.

2.9.1. Proposed Two-Layer Optimization Framework

As illustrated in Figure 5, we propose a two-layer optimization framework that integrates grid expansion decisions under *unknown* uncertainties with grid operational decisions under *known* uncertainties.

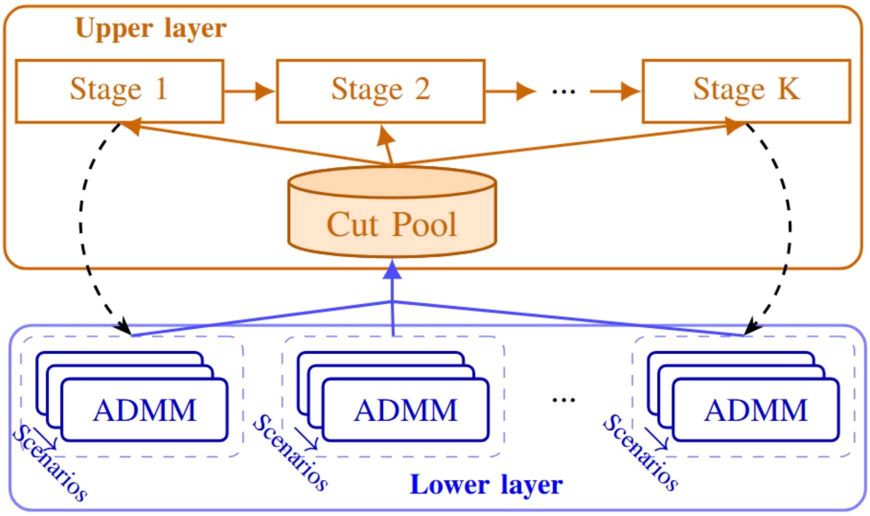

Figure 5: the upper layer handles multistage grid expansion decisions, while the lower layer optimizes grid flexibility ensuring grid operational feasibility. Information is exchanged via a central pool of cuts connecting the two layers.

- The *upper* layer addresses *unknown* uncertainties, such as future *connection requests* for PVs, EVCSs, and HPs, while the *lower* layer deals with *known* operational uncertainties, such as demand and generation variability on an hourly basis.
- The *upper* layer determines the optimal reinforcement of grid assets, such as transformers and lines, while the lower layer optimizes grid flexibility, such as transformer tap and switching positions, ensuring operational grid feasibility across representative operating scenarios.
- The *upper* layer is formulated as a convex multistage stochastic program. It is solved using SDDP, whereas the *lower* layer is formulated as a MISOCP and solved via decomposition using the consensus ADMM.

The interaction between the two layers guarantees that grid expansion decisions are both cost-efficient and operationally feasible. In the following, we provide a detailed description of each layer and their interactions.

1) Upper Layer: Multistage Expansion Planning

Consider a K-stage stochastic optimization model, where each stage $k \in \{1, \dots, K\}$ represents a multi-year period during which grid expansion decisions are made. The formulation of the *upper* layer is built upon three key components: the state vector, the decision vector, and the *unknown* uncertainty vector. Together, these components describe the system's temporal evolution and capture how *unknown* uncertainty affects expansion decisions.

State vector:

$$S_k := (B_k, F_k, U_k, P_k),$$

which aggregates all information carried from stage k to $k+1$,

- B_k is the remaining budget of the DSO for the period of k to $k+1$;
- $F_k := \left(F_{k,e}\right)_{\{e \in \mathcal{E}^{(br)}\}}$ is the vector of apparent power capacities (kVA) of lines and transformers, with $\mathcal{E}^{(br)}$ denoting the set of lines and transformers;

- $U_k := (U_{k,i})_{\{i \in L\}}$ is the vector of accumulated *connection requests* (in kVA) that remain unserved due to grid limitations, with L denoting the set of future *connection requests*, including demands, PVs, HPs, and EVCSs; and
- $P_k := (P_{k,i})_{\{i \in L\}}$ is the vector of accepted *connection requests* in kVA at period k.

Decision vector:

$$X_k := (f_k, u_k, p_k),$$

which specifies expansion actions taken at stage k,

- $f_k := (f_{k,e})_{\{e \in \mathcal{E}^{(br)}\}}$ represents expansion decisions of lines and transformers;
- $u_k := (u_{k,i})_{\{i \in L\}}$ denotes rejected connection requests at node i;
- $p_k := (p_{k,i})_{\{i \in L\}}$ denotes accepted *connection requests* at node i.

Unknown uncertainty vector:

$$\Delta_k := (\delta_k^{(b)}, \delta_k),$$

which represents the ambiguous variables for the period of stage k to $k+1$,

- $\delta_k^{(b)}$ is the realized additional budget of the DSO for this period, and
- $\delta_k := (\delta_{\{k,i\}})_{\{i \in L\}}$ denotes the vector of new *connection requests* for this period.

The evolution of the state vector is governed by the following *state transition* function:

$$S_{k+1} = Tr(S_k, X_k, \Delta_k) := \begin{bmatrix} B_k + \delta_k^{(b)} - C^{(ex)}(f_k) \\ U_k + \delta_k + u_k - p_k \\ F_k + f_k \\ P_k + p_k \end{bmatrix},$$

where $C^{(ex)}(f_k)$ denotes the grid expansion expenses for f_k.

With the *state transition* function defined, the *upper* layer becomes a multistage decision-making problem. To capture the recursive nature of the problem, the DSO selects decisions X_k at each stage k that trade off immediate costs with expected future costs, while the *state transition* function $Tr(\cdot)$ updates the system to the next stage based on current decisions and uncertainties. Formally, the multistage planning problem can be expressed recursively using *Bellman's equation*:

$$V_k(S_k) = \min_{X_k \in Y(S_k)} \{ C_k(X_k, S_k) + R_k[V_{k+1}(S_{k+1})]\},$$

where

- $V_k(S_k)$ is the value function of stage k;
- X_k is the feasible set of decisions given the current state;
- $R_k[.]$ denotes the risk operator applied over the *unknown* uncertainty vector Δ_k; and
- $C_k(X_k, S_k)$ denotes the stage cost, composed of three terms: the grid expansion expenses, the penalty cost for unserved *connection requests*, and the operational expenses. Formally,

$$C_k(X_k, S_k) := C_k^{(ex)}(f_k) + C_k^{(rej)}(U_k) + C_k^{(op)}(F_k, P_k),$$

including expansion expenses, penalties for rejected connection requests, and operational cost, which are defined in following details.

The stage cost function $C_k(X_k, S_k)$ is assumed to be convex in the decision variables. With convex stage costs, convex constraint set $X(S_k)$, and linear state dynamics, the proposed recursive formulation becomes a multistage stochastic problem that could be solved via SDDP through iterative forward and backward passes. In the forward pass, sampled realizations of the uncertainty Δ_k generate state and decision trajectories, yielding an upper bound on the value function. In the backward pass, dual sensitivities with respect to the state variables are used to construct affine cuts, which iteratively refine the approximation of $V_k(S_k)$.

2) Lower Layer: Grid Flexibility and Operational Feasibility

The lower layer objective is to optimize the deployment of grid flexibility, minimizing grid losses and ensuring that power flows, voltages, and thermal limits are satisfied across a range of demand and PV generation scenarios $\omega \in \Omega$. In this layer, the distribution grid flexibility is represented with discrete topology decisions y, including switch statuses and transformer tap positions. In addition, there are scenario-dependent continuous variables z_ω representing power flows, voltages, and other operational quantities across the grid.

Since switching operations and tap adjustments occur infrequently, this problem is typically addressed over a mid-term horizon, e.g., 7 days to 3 months. Variations and uncertainties in demand, PV generation, and voltage levels at the connection points are captured through a set of representative scenarios. By clustering hourly demand and generation profiles, a reduced set of scenarios is constructed to approximate grid operation. These scenarios represent the *known* uncertainty introduced earlier.

To achieve optimal discrete and continuous control actions while satisfying operational constraints, we formulate a MISOCP that captures both the operational limits and the discrete control decisions. The complete formulation is provided in Section 2.6.

Despite the availability of commercial solvers for MISOCP, solving the MISOCP problem becomes computationally intractable for a large-scale distribution grid with numerous operational scenarios. To address this challenge, we decompose the problem across scenarios $\omega \in \Omega$, where each scenario has its own operational variables z_ω and scenario-dependent discrete decisions y_ω. The sub-problems for each scenario are solved in parallel and coordinated through consensus variables that enforce consistency across shared discrete decisions, such as switch statuses and transformer tap positions. The resulting sub-problems for all $\omega \in \Omega$ are solved using the consensus ADMM method as described in Section 2.8.

3) Cut Pool: Information Exchange Between Two Layers

There is a two-way exchange of information between the *upper* and *lower* layers, as illustrated in Figure 5. The first communication path, shown by the dashed black arrows, proceeds from the *upper* to the *lower* layer. After each SDDP iteration, the model generates a set of possible future demand configurations, producing the state vector (F_k, P_k) at each stage k for each expansion scenario[3] $\zeta \in Z$.

The second communication path corresponds to the *cut pool* block in Figure 5. This block serves as a central repository for critical operational constraints that must be respected by the upper layer problem. While the state captures long-term system evolution, each expansion decision must still ensure feasible power flows under the corresponding demand realizations.

Since solving full AC power flows at every stage of the *upper* layer would be computationally intractable, we instead approximate these constraints through *Benders cuts*. These cuts are generated from the ADMM sub-problems solved at each stage k and scenario $\zeta \in Z$. In this way, the cut pool provides a mechanism to feed operational feasibility information, encoded in the dual variables and objective values of the ADMM sub-problems, back into the planning recursion. A generic cut takes the form:

[3] It is important to distinguish between the two types of scenarios used in the two layers. The *upper* layer handles scenarios ζ associated with *unknown* uncertainties, represented by Δ_k. In contrast, the *lower* layer evaluates operational scenarios ω that represent *known* uncertainties, such as daily or seasonal variations in demand and PV generation.

$$\theta_k \geq \sum_{\omega \in \Omega} h^*_{\{k,\omega\}} + \sum_{\{i \in L\}} \mu_{k,i} \cdot \left(P_{k,i} - P^{\circ}_{k,i}\right) + \sum_{\{e \in \mathcal{E}^{(br)}\}} \nu_{k,e} \cdot \left(F_{k,e} - F^{\circ}_{k,e}\right),$$

where $(\cdot)^{\circ}$ denotes the solution point at which the cut is generated; $h^*_{k,\omega}$ is the optimal objective value from the ADMM sub-problem; $\mu_{k,i}$ and $\nu_{k,e}$ are the corresponding dual variables, quantifying the sensitivity of the objective to incremental demand/PV installations and line/transformer capacity expansions, respectively; and $\theta_k \geq 0$ is an auxiliary variable that captures the operational cost.

By aggregating the dual variables $\mu_{k,i}$ and $\nu_{k,e}$ across ADMM sub-problems, associated with demand satisfaction, PV curtailment, and grid capacity limits, the resulting Benders-type cuts directly shape the value function approximation within the SDDP recursion. In this way, operational feasibility is consistently integrated into long-term expansion planning.

Algorithm 2 summarizes the proposed two-layer optimization framework. In each outer iteration, the SDDP forward pass is first executed, where *unknown* uncertainties $\zeta \in Z$ are sampled and the stage problems are solved using the current value function approximation. After completing the forward and backward passes of SDDP, operational feasibility is evaluated by solving ADMM sub-problems for each stage k and scenario $\zeta \in Z$ under multiple operational scenarios $\omega \in \Omega$. Dual multipliers obtained from the ADMM solutions are used to generate Benders-type cuts, which are added to the central cut pool. These cuts are then incorporated into the next SDDP iteration, refining the value function approximation.

The procedure repeats, alternating between SDDP and ADMM, until the gap between the upper bounds (UB) and lower bounds (LB) of operational cost, i.e., θ_k and $\sum_{\{\omega \in \Omega\}} h^*_{k,\omega}$, falls below the convergence tolerance.

Algorithm 2 : multistage expansion planning with operational feasibility

```
Initialization: Set n ← 1; Bounds LB ← −∞, UB ← +∞.
while UB − LB > ε do
    SDDP Pass (Forward and Backward):
    for each stage k in forward order do
        - Sample scenario ζ ∈ Z.
        - Solve stage problem with approximation of V_k(.).
        - Store decision X^ζ_{n,k} and state S^ζ_{n,k}.
    for each stage k in reverse order do
        - Update value function V_k(·) with current cuts.
    Operational Evaluation (ADMM):
    for each stage k and scenario ζ ∈ Z do
        - Solve ADMM presented in Appendix B.
        - Extract (μ^(ζ)_{k,i})_{i∈L} and (ν^(ζ)_{k,e})_{e∈E^(br)}.
        - Add corresponding cuts to the cut pool.
    Convergence Check:
    Update (LB, UB) if UB − LB ≤ ε then
        Terminate
    else
        n ← n + 1 and return to SDDP Pass
```

2.9.2. Objective Function of Upper Layer

Compared to the daily variations in demand and PV generation captured by scenarios $\omega \in \Omega$, there is significantly less information available regarding the distribution of *unknown* uncertainty in the vector Δ_k. While taking the expectation over $\zeta \in Z$ is a natural approach, DSO typically has limited knowledge about Δ_k and therefore tends to be more risk averse. In this section, we present the formulation that explicitly accounts for such risk-averse behavior.

Before introducing the risk-aware formulation, we revisit the per-stage cost function. The stage cost combines three components: expansion expenses, penalties for rejected *connection requests*, and operational cost.

$$C_k^{(ex)}(f_k) = \sum_{\{e \in \mathcal{E}^{(br)}\}} \pi_e^{(br)} f_{k,e},$$

$$C_k^{(rej)}(U_k) = 8760 \cdot N^{(years)} \sum_{\{i \in L\}} \pi_i^{(rej)} U_{k+1,i},$$

$$C_k^{(op)}(F_k, P_k) = 8760 \cdot \frac{N^{(years)}}{n^{cut_{scen}}} \cdot \theta_k,$$

where $\pi_e^{(br)}$ is the expansion expense of grid assets reinforcement, $N^{(years)}$ is the number of years that each planning stage spans, and $\pi_i^{(rej)}$ is the penalty coefficient for rejected connection requests. The factor $8760 \cdot N^{(years)}$ converts per-hour penalties to stage-aggregated costs, while $n^{cut_{scen}}$ normalizes the infeasibility penalty across scenarios.

Stage costs can also be discounted over $N^{(years)}$ years as

$$C_k(\cdot) = (1+r)^{-(k-1)N^{(years)}} \left(C_k^{(ex)} + C_k^{(rej)} + C_k^{(op)} \right),$$

so, all the costs are transformed into *net present value* (NPV), where r is the discount rate.

Having specified the state dynamics, feasibility constraints, and stage costs, we embedded the problem into a multistage stochastic program with distributional robustness. At each stage k, *unknown* uncertainty is represented by a finite set $Z\_k := \left\{\zeta_k^1, \dots, \zeta_k^{\{S_k\}}\right\}$ with nominal probabilities $P_k := \left\{p_k^1, \dots, p_k^{\{S_k\}}\right\}$. In DRO, uncertainty is described by all probability distributions lying within a Wasserstein ball around the nominal distribution P_k. For a generic value function V, the *Wasserstein*-based risk operator can be written as:

$$R_k[V] = \sup_{Q_k \in B_\epsilon(P_k)} \mathbb{E}_{Q_k}[V],$$

where $B_\epsilon(P_k)$ denotes the set of probability distributions within a *Wasserstein* distance ϵ of the nominal distribution. Intuitively, this operator evaluates the worst-case expected cost over all plausible distributions that are ϵ-close to the nominal one.

In addition to the *Wasserstein*-based risk operator, we also consider a risk operator that directly interpolates between the expectation and worst-case realizations:

$$R_k[V] = (1-\alpha) \cdot \mathbb{E}_{P_k}[V] + \alpha \cdot \max_{\zeta \in Z_k} V(\zeta), \qquad \alpha \in [0,1].$$

where $V(\zeta) = V_{\{k+1\}}\big(Tr(S_k, X_k, \Delta_k)\big)$ denotes the *value* function from stage *k+1* onward, which depends on the realized uncertainty $\zeta \in Z_k$ through the transition function $Tr(S_k, X_k, \Delta_k)$. The term $\mathbb{E}_{P_k}[V]$ corresponds to the expected cost under the nominal distribution, while $\max_{\zeta \in Z_k} V(\zeta)$ represents the worst-case realization. This formulation allows a smooth trade-off between the risk-neutral baseline, i.e., $\alpha = 0$, and the fully robust worst-case policy, i.e., $\alpha = 1$.

3 Deliverable 5.2: Technical report containing the validation of the model utilizing appropriate test benches and scenarios in a numerical environment

3.1. Objective and scope

Deliverable 5.2 presents the implementation of the developed planning framework in a numerical environment and its technical validation using appropriate test benches and energy-transition scenarios. Its objective is to demonstrate that:

- We implemented the optimization methodology defined in deliverable 5.1 in a coherent computational workflow.
- We applied to representative distribution-grid studies in a scalable and reproducible manner.

The scope of this deliverable therefore includes the software architecture of the tool, the interaction between long-term planning and operational validation layers, and the numerical studies carried out on benchmark and representative grids.

This deliverable corresponds to the activities carried out under Tasks 5.2 and 5.3, namely:

(i) Building the grid asset planning tool based on the developed formulation in a numerical environment, and

(ii) Simulating the targeted distribution grid for different scenarios of energy transition.

Accordingly, this delivery covers two closely related aspects.

First, it documents the integrated numerical implementation of the multi-layer planning framework.

Second, it reports the validation studies performed on representative networks and scenarios to assess operational feasibility, flexibility use, voltage behavior, and reinforcement needs under different transition pathways.

3.2. Integrated numerical environment

We implemented the planning framework in an integrated computational environment combining a multistage expansion layer and a scenario-based operational layer. The overall structure follows the methodology described in the deliverable 5.1; it is based on a two-level architecture that ensures consistency between long-term investment planning and short-term operational feasibility.

The *upper* layer, implemented in Julia, formulates the long-term expansion problem as a Stochastic Dual Dynamic Programming (SDDP) model. Each stage represents an investment period, such as a year or a multi-year block, and the algorithm iteratively refines value-function approximations through forward simulation and backward recursion. This layer determines optimal reinforcement actions for network assets under *unknown* uncertainties, including future demand growth and DER penetration.

The *lower* layer, implemented in Python using Pyomo, performs detailed operational validation of the expansion decisions under *known* uncertainties, such as load and PV generation variability. This layer relies on the ADMM reformulation to decompose the operational problem across representative daily or seasonal scenarios. Each scenario is solved independently to optimize power flows, switch configurations, and voltage-regulation devices, while consensus constraints enforce coherent grid operation across all scenarios.

As illustrated in Figure 6, both layers are linked through an API-based interface, which enables the iterative exchange of data and cuts:

- The ADMM- based operational model generates cuts that are passed to the SDDP expansion model, updating the value function representation.
- The SDDP expansion layer then updates the investment decisions, which are subsequently re-evaluated by the ADMM layer for operational feasibility.

This two-level integration provides a computationally efficient and scalable coordination between long-term expansion and mid-term operational flexibility. The implementation leverages `SDDP.jl`[4] and the `HiGHS` solver in Julia for the expansion problem, enabling efficient multistage optimization and value function approximation, while `Pyomo` combined with `GUROBI` or `HiGHS` in Python handles the operational feasibility layer, ensuring fast and reliable convergence of the ADMM-based reconfiguration across multiple scenarios.

The architecture illustrated in Figure 6 details the software-level workflow, where:

- The Expansion Model executes the SDDP-based investment iterations (backward and forward passes);
- The ADMM Model performs distributed operational analysis using progressive hedging and consensus updates;
- API middleware coordinates data transfer between both models, managing the iterative cut exchange and grid expansion updates.

This modular and cross-platform design ensures high flexibility, reproducibility, and scalability, making it suitable for complex, large-scale distribution systems.

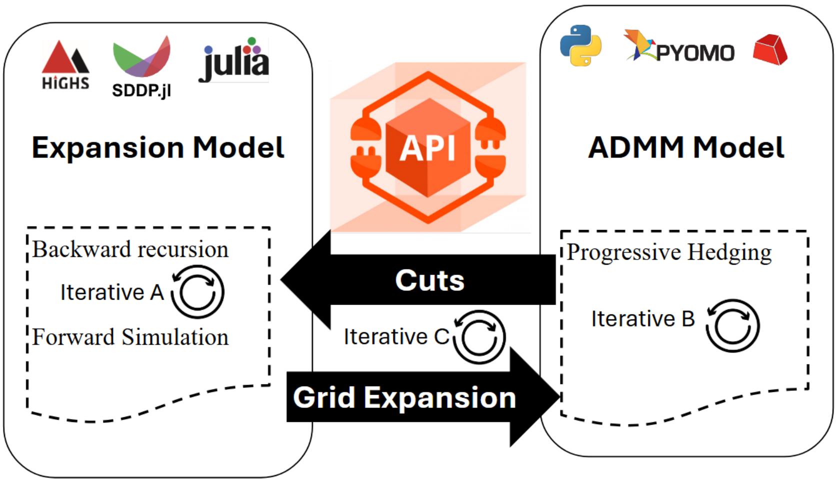

Figure 6: Software-level architecture of the integrated framework, showing the interaction between the Julia-based SDDP expansion model and the Python-based ADMM operational model.

3.3. Validation setup: test bench and scenarios

The technical validation of the developed framework is performed on a benchmark distribution grid. The IEEE 33-node test feeder is used for controlled validation and benchmarking of the optimization methodology.

The analysis is conducted under multiple energy-transition scenarios that reflect different levels of electrification and DER adoption:

- Baseline scenario: current load and generation levels with limited DER integration.
- Sustainable transition: moderate growth in electricity demand and partial deployment of PVs, EVCSs, and HPs.
- Full transition: extensive electrification and high renewable integration, representing a higher-uncertainty future with diverse prosumer behaviors and flexibility potential.

[4] SDDP.jl is a solver for multistage stochastic optimization problems. For more information: https://sddp.dev/stable/tutorial and https://sddp.dev/stable/tutorial/example_milk_producer/.

Each scenario is simulated using representative daily and seasonal profiles to capture the temporal variability of load and renewable generation.

In addition to the benchmark study, as presented in deliverables 2.1 and 2.2, we tested the proposed methodology on two real distribution grids: Estavayer-le-lac operated by Groupe E and Boisy operated by SiL.

The Boisy grid consists of two feeders, Feeder 1 and Feeder 2. The Estavayer-le-Lac grid includes the following feeders: Aumont, Autoroutes, Bel-Air, Centre-Ville, St-Aubin, Tout-vent, Zone-Industrielle.

At present, we executed the proposed methodology independently on each feeder. The aggregation and integrated simulation of all feeders together with the transmission grid are beyond the scope of this project.

3.4. Simulating the targeted distribution under energy transition scenarios

The implementation of this project requires additional analyses beyond the development of the optimization framework and its validation on real-world case studies. System modeling and statistical analysis are used to characterize energy transition pathways and quantify their impact on the daily operation and planning tasks of distribution system operators.

The work is structured in the following steps.

- *First*, future load configurations are estimated at the national level, including the deployment trajectories of photovoltaic systems, electric vehicles, and heat pumps. The distribution grid representation is integrated into the GRIMSEL-FLEX as a nested unit [38], enabling consistent coupling between national-level energy system evolution and local grid constraints.
- *Second*, the GRIMSEL-FLEX model is extended to incorporate alternative tariff designs for prosumers. An iterative calibration procedure is applied to ensure comparable utility revenue levels across tariff schemes.

A scenario-based approach is used to simulate wholesale market evolution up to 2050. This provides consistent long-term trajectories for the penetration of electric vehicles, heat pumps, and photovoltaic systems, as well as estimates of consumer-provided flexibility under different pricing regimes.

The results of Deliverables 3.1 and 3.2 provide annual deployment trends per EGID for photovoltaic systems, heat pumps, electric vehicle charging stations, and baseload demand up to 2050. Deliverables 4.1 and 4.2 provide flexibility activation levels under different pricing scenarios, expressed as hourly power profiles with 8,760 values per EGID per year.

Within Work Package 5, these outputs are combined to construct yearly customer-level load profiles for the Boisy and Estavayer-le-Lac grids from 2025 to 2050. The procedure is as follows.

- *First*, the average annual power per customer is computed to determine the electrification trend under each scenario.
- *Second*, the standard pricing scheme defined in Work Package 4 is applied to derive the corresponding hourly power profile per EGID.
- *Third*, the annual trend component is multiplied by the normalized hourly profile to obtain a full 8,760-hour load profile per EGID for each year in the simulation horizon.

Selected results for the Boisy and Estavayer grids are shown below. Detailed numerical data are not disclosed due to confidentiality constraints.

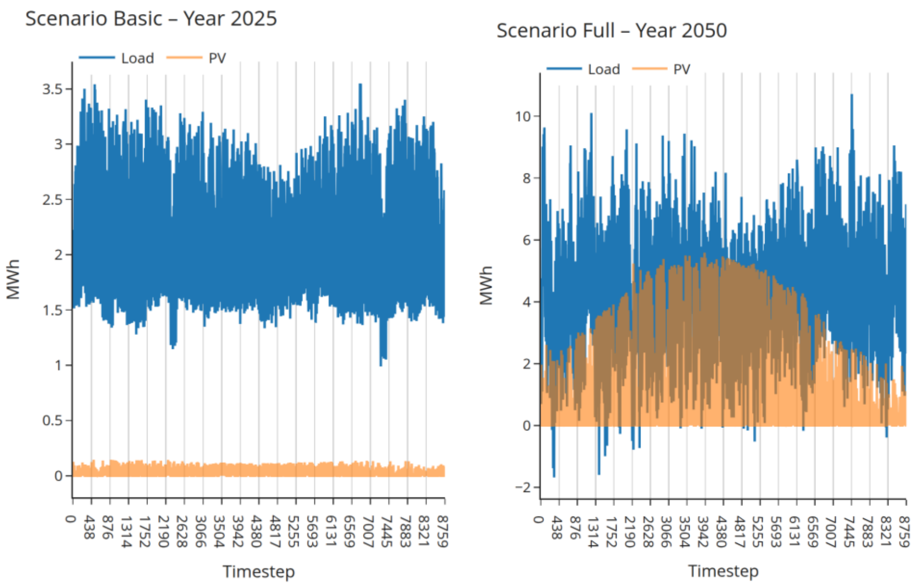

Figure 7: Total Load Power Profile (in kW per EGID), Basic and Full Scenario over the years (Boisy Grid).

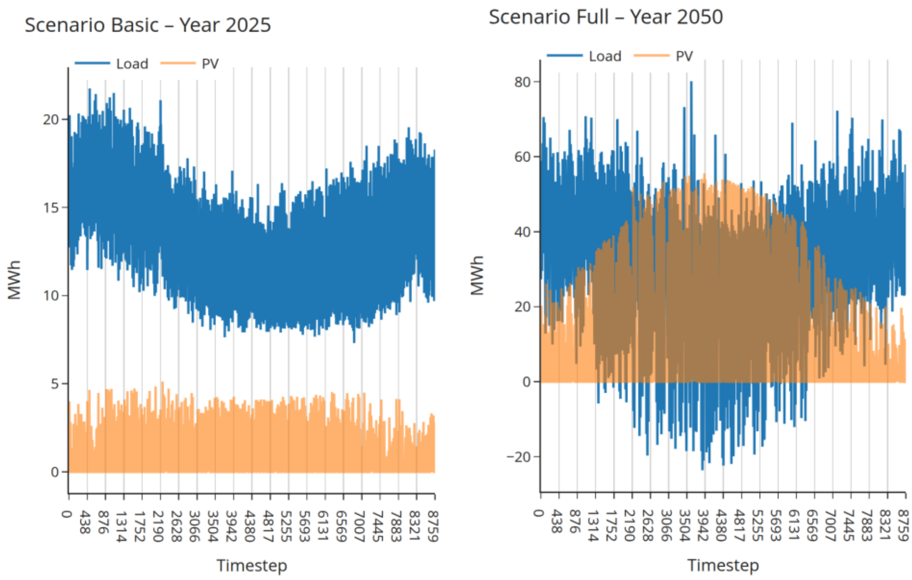

Figure 8: Total Load Power Profile (in kW per EGID), Basic and Full Scenario over the years (Estavayer Grid).

3.5. Numerical Results: Power Flow

Before running the full optimization, power flow simulations are executed for all three scenarios at an hourly resolution over one year. Two case studies are considered: one without network expansion and one with a benchmark expansion applied when required. The benchmark expansion is determined solely by the loading percentage of lines and transformers. If the power flow results show loading above 100 percent, the corresponding line or transformer is reinforced, and the power flow is rerun. This approach does not incorporate flexibility usage, long-term planning considerations, or voltage limitations.

Voltage levels and loading percentages of lines and transformers are evaluated for all feeders in Boisy and Estavayer. The results indicate that voltage constraints, in addition to line and transformer loading, represent a significant limitation. Results for the different feeders are presented in the following figures, with the associated expansion costs reported below each figure. Another conclusion is that the grid of Boisy will have both loading and voltage issues in coming year but the grid of Estavayer is over designed already and the only issue is the voltage limitations.

3.5.1. Boisy Basic scenario

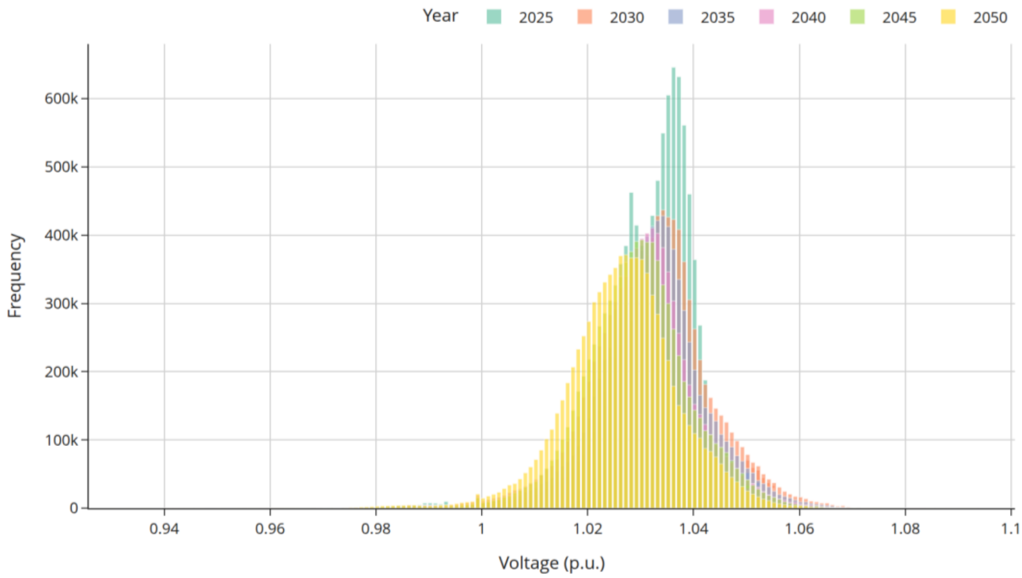

Figure 9: Voltage distribution over the years.

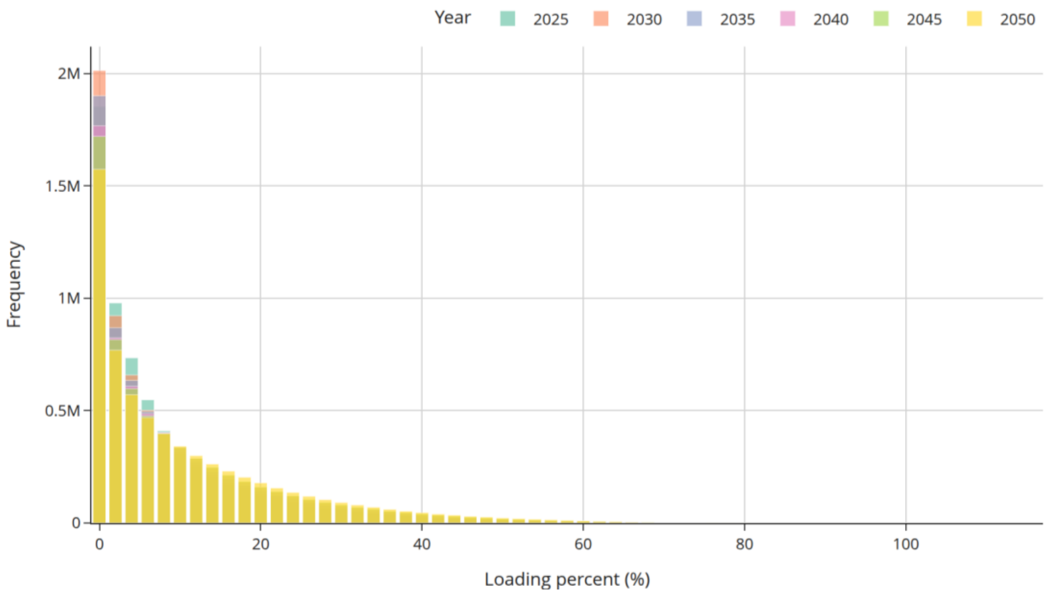

Figure 10: Loading percent distribution of lines over the years.

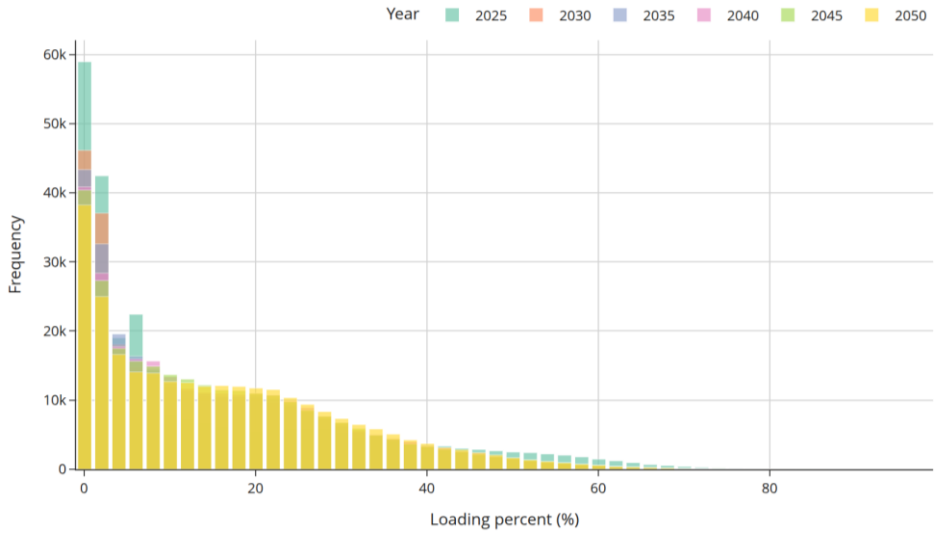

Figure 11: Loading percent distribution of transformers over the years.

The total costs for expansion of lines and transformers are 8.17 MCHF and 13.53 CHF, respectively. When compared with the SDDP-based expansion under a worst-case risk measure, these costs are reduced by approximately half, highlighting the value of forward-looking optimization and CAPEX deferral with flexibility.

3.5.2. Boisy Full scenario

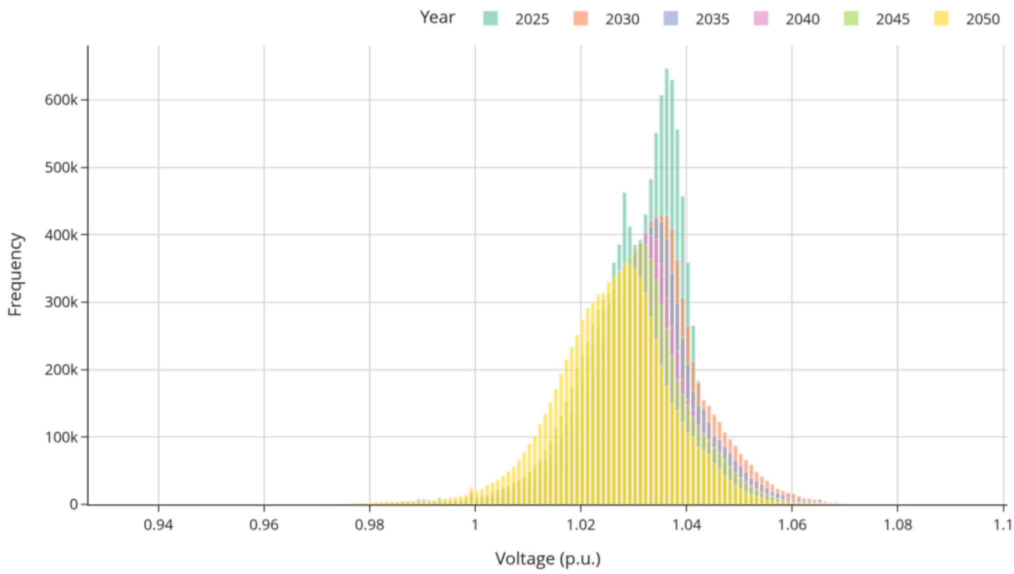

Figure 12: Voltage distribution over the years.

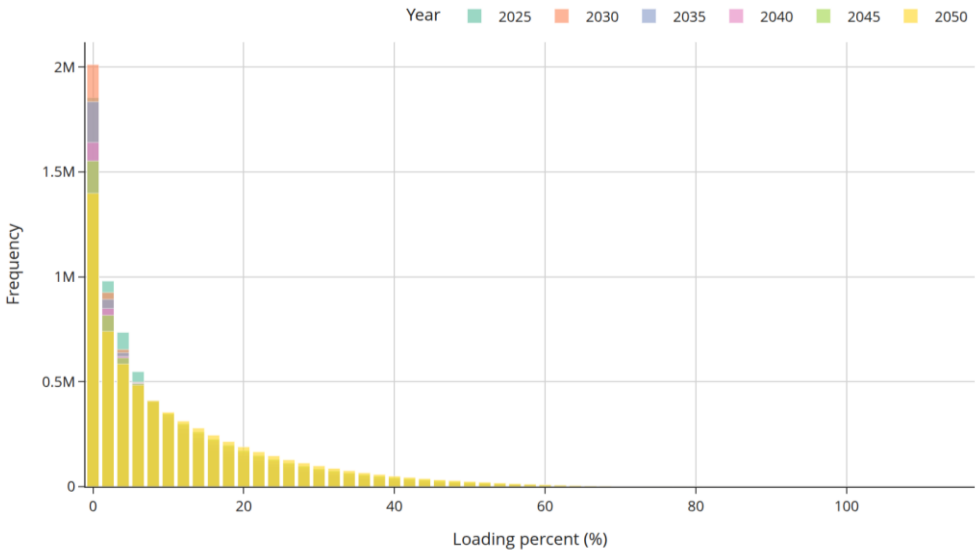

Figure 13: Loading percent distribution of lines over the years.

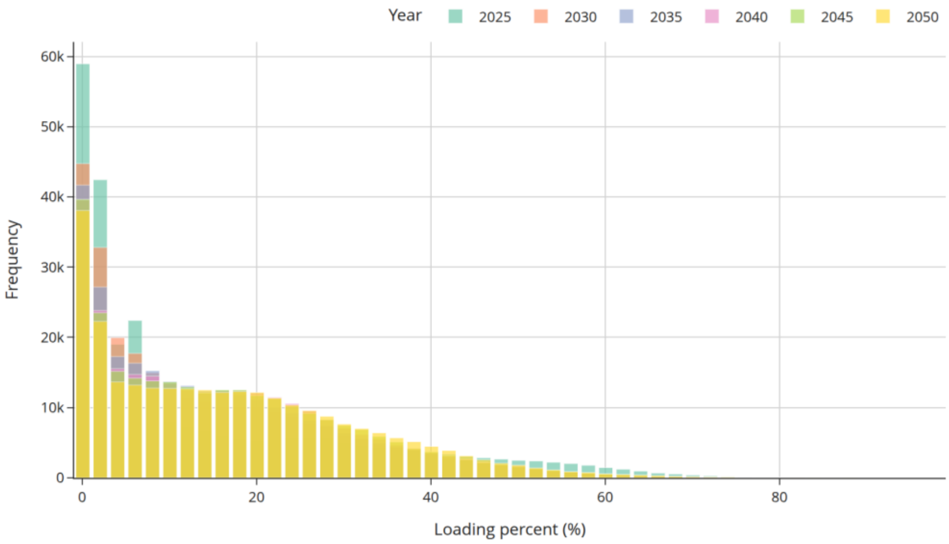

Figure 14: Loading percent distribution of transformers over the years.

The total costs for expansion of lines and transformers are 8.73 MCHF and 14.54 CHF, respectively. When compared with the SDDP-based expansion under a worst-case risk measure, these costs are reduced by approximately half, highlighting the value of forward-looking optimization and CAPEX deferral with flexibility.

3.5.3. Boisy Full scenario without expansion

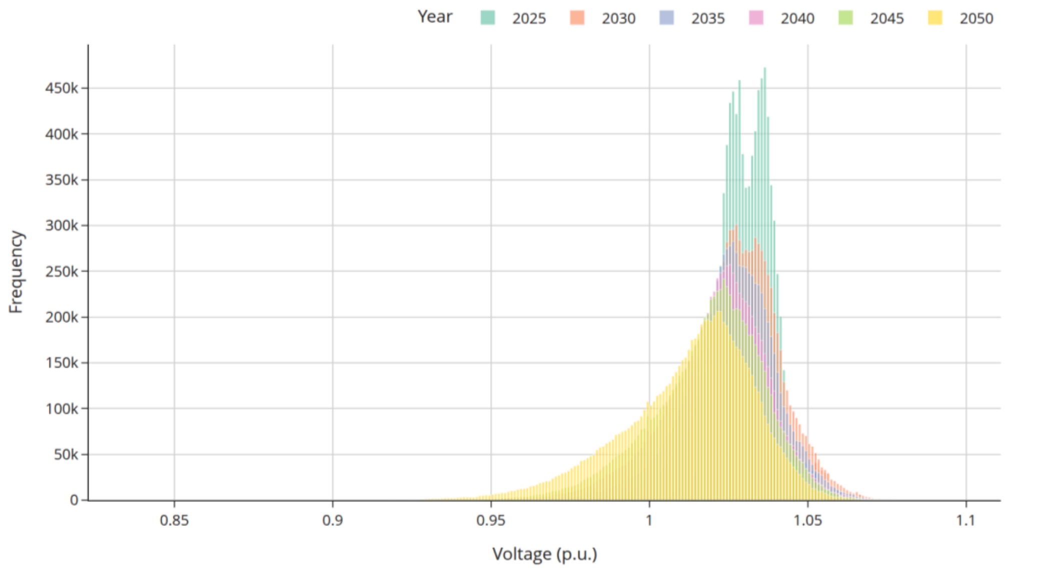

Figure 15: Voltage distribution over the years.

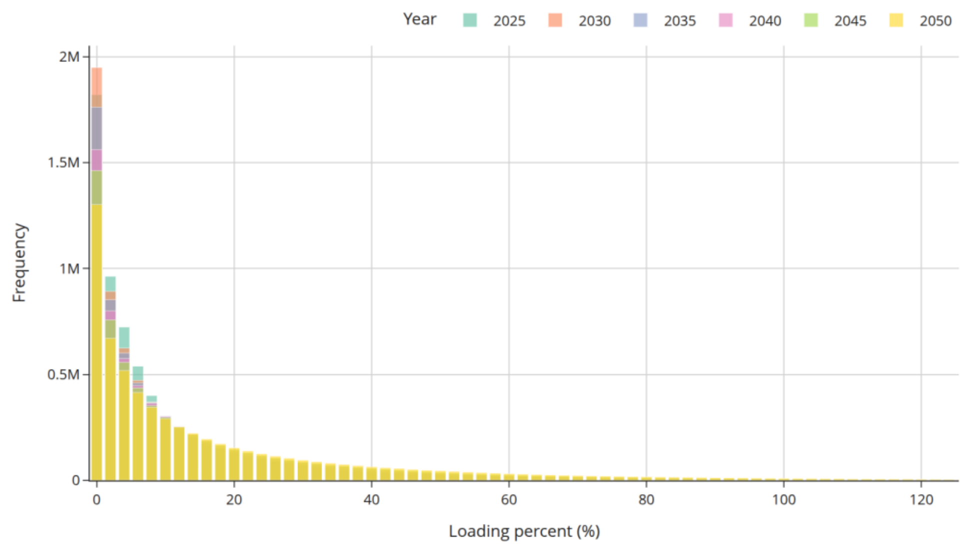

Figure 16: Loading percent distribution of lines over the years.

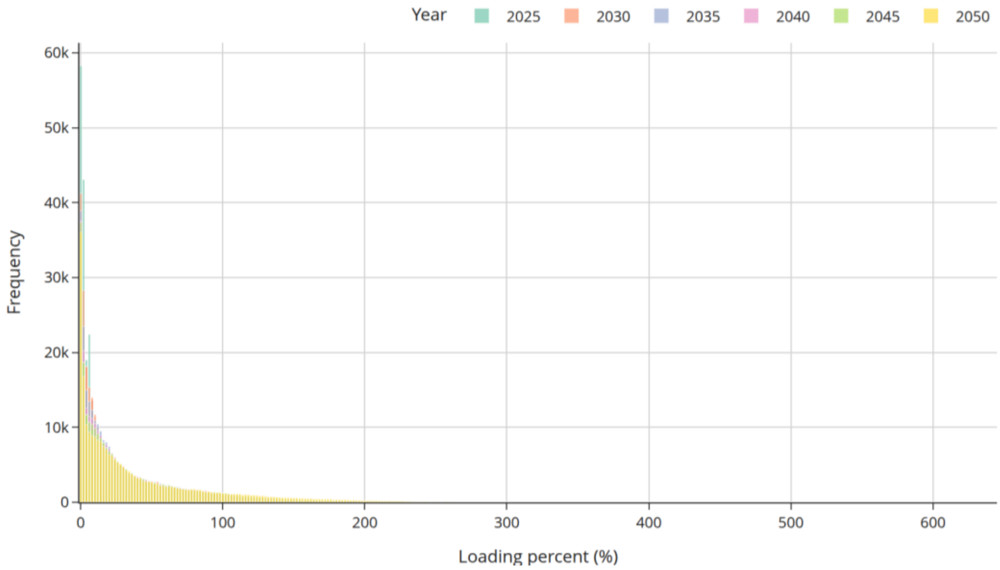

Figure 17: Loading percent distribution of transformers over the years

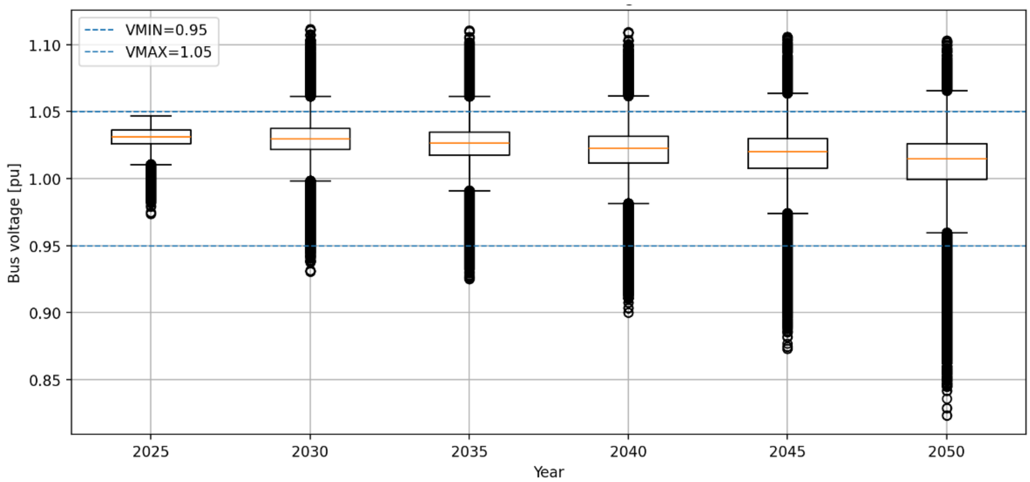

Figure 18: Bus voltage distribution over the years.

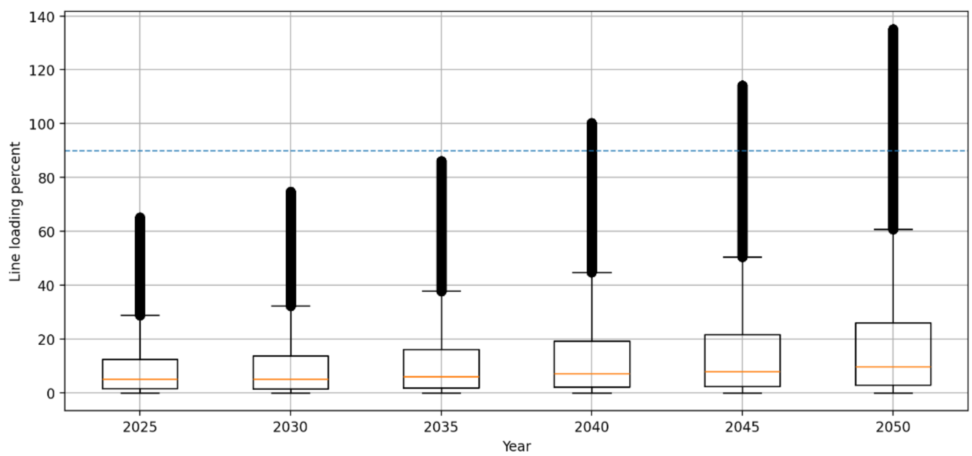

Figure 19: Distribution of line loading over the years.

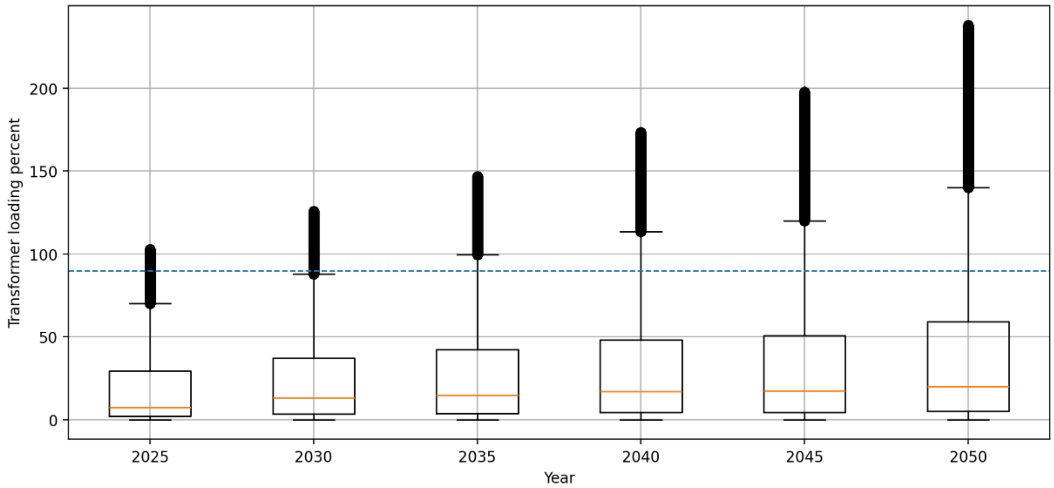

Figure 20: Distribution of transformer loading percent over the years.

Interestingly, the loading of the Boisy is very large for few feeders, indicating that the generated load profiles do not account for LV grid limitations and may therefore lack accuracy. This could be addressed in future work by generating grid wise digital twin of energy consumers.

3.5.4. Estavayer Aumont feeder Full scenario without expansion

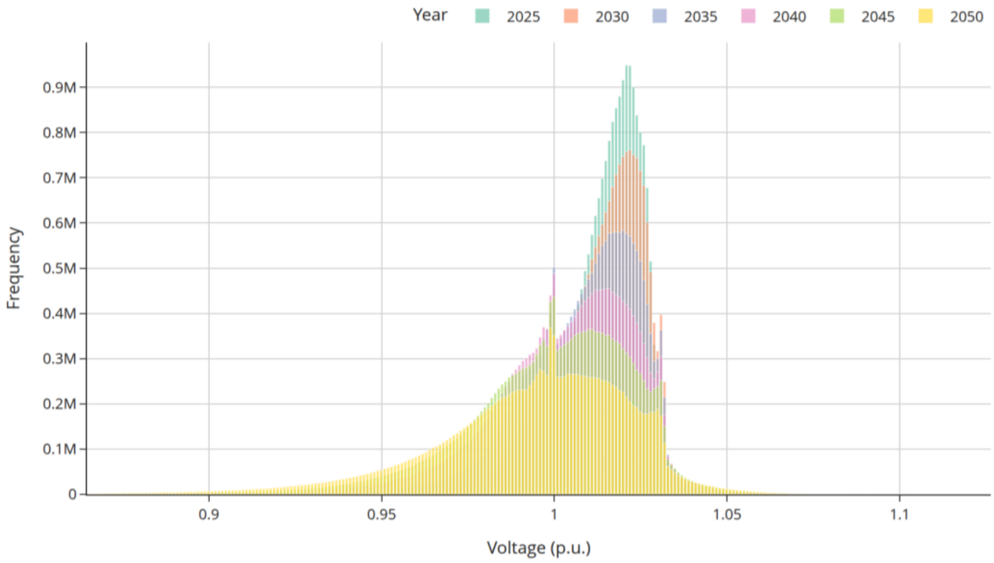

Figure 21: Voltage distribution over the years.

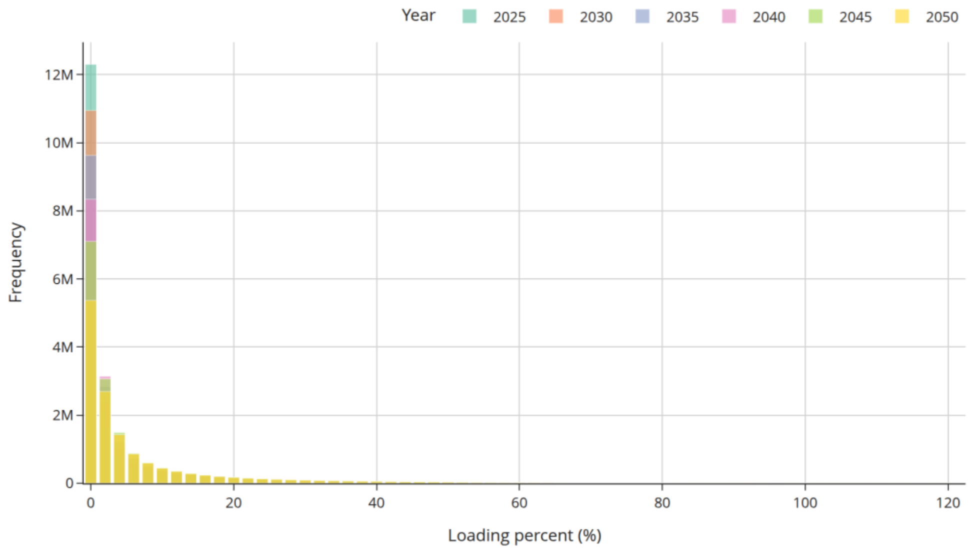

Figure 22: Loading percent distribution of lines over the years.

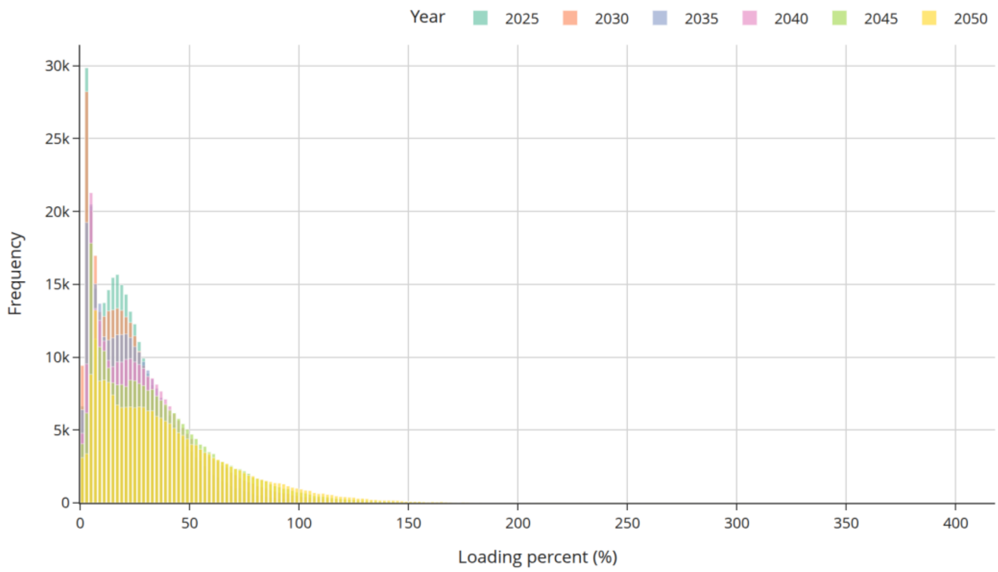

Figure 23: Loading percent distribution of transformers over the years.

Interestingly, the loading of the Estavayer feeders remains relatively low, indicating that the grid is overdesigned. As a result, the benchmark expansion method leads to negligible grid reinforcement, while voltage constraints are not properly maintained. It should be noted, however, that the generated load profiles do not account for LV grid limitations and may therefore lack accuracy.

3.5.5. Estavayer Bel-air feeder Full scenario without expansion

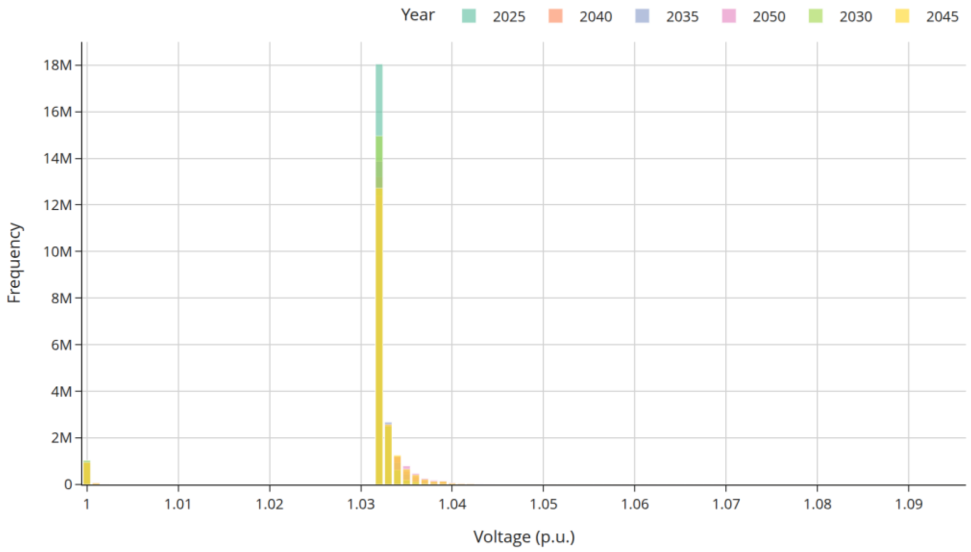

Figure 24: Voltage distribution over the years.

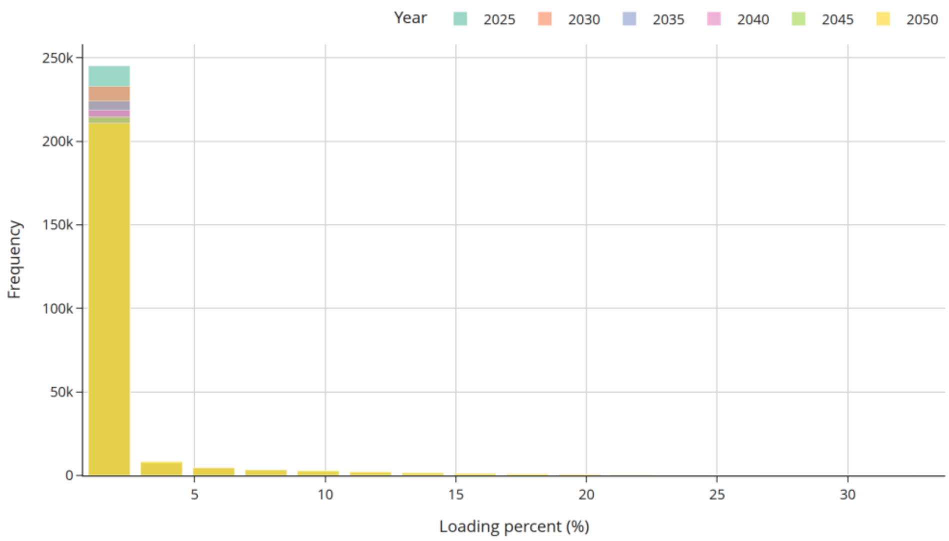

Figure 25: Loading percent distribution of lines over the years.

Interestingly, the loading of the Estavayer feeders remains relatively low, indicating that the grid is overdesigned. As a result, the benchmark expansion method leads to negligible grid reinforcement, while voltage constraints are not properly maintained. It should be noted, however, that the generated load profiles do not account for LV grid limitations and may therefore lack accuracy.

3.5.6. Estavayer Centre-ville feeder Full scenario without expansion

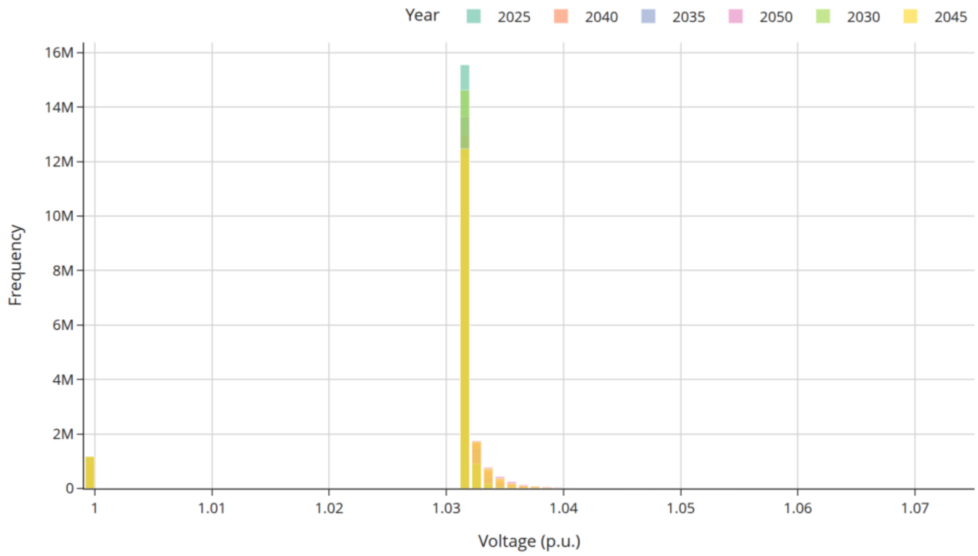

Figure 26: Voltage distribution over the years.

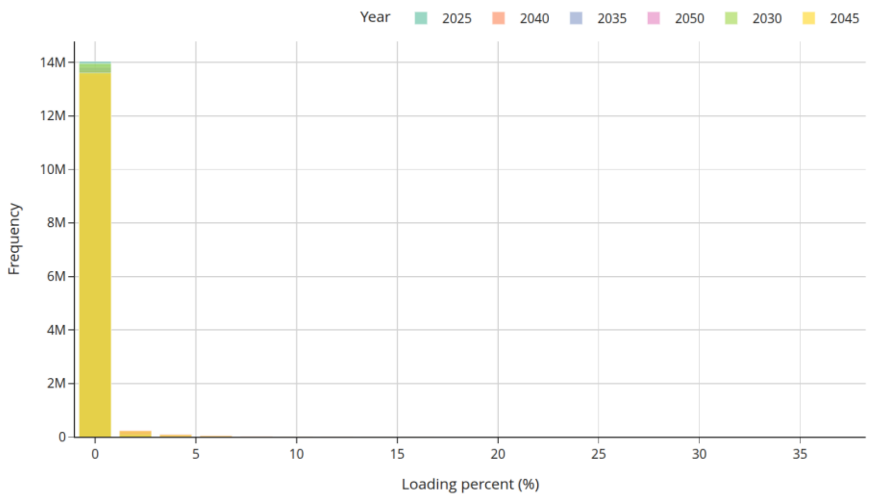

Figure 27: Loading percent distribution of lines over the years.

Interestingly, the loading of the Estavayer feeders remains relatively low, indicating that the grid is overdesigned. As a result, the benchmark expansion method leads to negligible grid reinforcement, while voltage constraints are not properly maintained. It should be noted, however, that the generated load profiles do not account for LV grid limitations and may therefore lack accuracy.

3.6. Numerical Results: Mid-term Optimization for Reconfiguration

3.6.1. Case studies and experimental setup

This section presents ADMM-based operational reconfiguration results on three distribution networks: an IEEE 33-node benchmark, a medium-size simplified MV/LV feeder with 234 nodes constructed by simplifying a large real MV/LV network with 1004 nodes from a district in Lausanne, Switzerland, and the original 1004-node real network itself. For computational tractability, the 234-node surrogate is obtained via graph-based preprocessing that

(i) Aggregates parallel and series switches,

(ii) Simplifies substation representations,

(iii) Clusters LV networks, and

(iv) Aggregates series/parallel lines.

This reduction preserves the essential meshed structure of the network while significantly lowering its dimensionality. Both the original and simplified networks are included in the experiments. The detailed network sizes are reported in the following Table.

Network	Nodes	Lines	Switches	Transformers	Load/PV (MW)
33-nodes (benchmark)	32	17	17	2	4.893 / 0.000
234-nodes (simplified)	234	160	90	19	4.746 / 0.716
1004-nodes (real)	1004	740	281	31	4.746 / 0.716

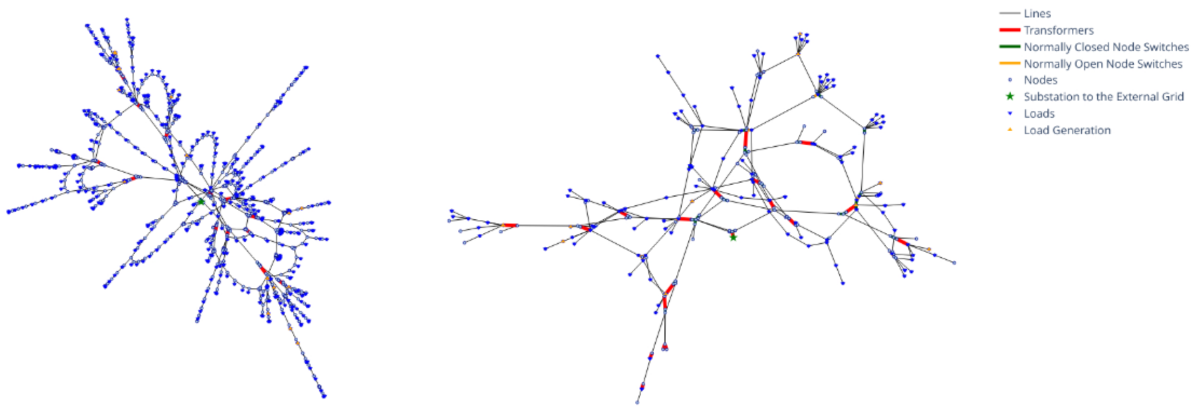

Figure 28: Real network from a Swiss city (left: 1004 nodes) and simplified (right: 234 nodes).

We implemented all proposed optimization models in Pyomo and solved them with `Gurobi` to obtain MISOCP solutions. In our formulation, the power flow equations are enforced via rotated-cone constraints, while the discrete decisions are the switch states $\kappa_e \in \{0,1\}$ and transformer tap positions τ_e. Across all networks, we adopt $S_{base} = 1\ MVA$, enforce voltage limits [0.95,1.05] per unit, and model OLTC with discrete tap ratios in the range of 0.95–1.05 per unit around the nominal value.

3.6.2. Scenario Grouping and Scalability of ADMM

The yearly variability of nodal loads and PV injections is represented through a set of $|\Omega| = 100$ operating scenarios. These scenarios are obtained by applying a clustering-based dimensionality reduction technique to a year of simulated time-series data (Basic scenario in 2025). Specifically, the annual profiles of total load and PV generation are normalized and clustered to obtain 100 representative operating points that reflect typical combinations of load and generation. For every scenario $\omega \in \Omega$, the corresponding active and reactive powers at each node are converted into per-unit values on the system base, forming the input data for the ADMM optimization.

In the ADMM calculations, we need to adopt the grouping settings that are listed in following Table. The grouping is derived from the *spatial loops* of each network. An example is illustrated in Figure 29 for 33-nodes: all switches belonging to the same fundamental cycle are assigned to a common group. The resulting collection of (possibly overlapping) groups covers all controllable switches and serves as the basis for the updates in the ADMM iterations.

Network	$\lvert\Omega\rvert$ (scenarios)	G (groups)
33-nodes	100	5
234-nodes	100	10
1004-nodes	100	40

Computationally, the grouping strategy reduces the dimensionality of each sub-problem, while ADMM decomposes the optimization across the $\lvert\Omega\rvert$ scenario-wise sub-problems. At each iteration, the x-updates for all $\omega \in \Omega$ are solved separately within the sequential workflow, and the subsequent consensus and dual updates ensure coordination across scenarios. All simulations are performed on a single workstation (Intel Core i7-13850HX with 32GB RAM). This decomposition substantially reduces the complexity of each optimization stage compared with the centralized one shot MISOCP, which solves a single monolithic model. While the centralized formulation is competitive for small networks, its runtime increases rapidly with the number of scenarios, whereas the ADMM-based decomposition exhibits much more moderate scaling. The runtime comparison between MISOCP and ADMM for the 33-node network is reported in following table. As shown in Table, the centralized MISOCP is faster at $\lvert\Omega\rvert = 10 - 20$, but a crossover occurs at $\lvert\Omega\rvert = 50$ (ADMM: 378.5s vs. MISOCP: 743.8s), with the gap widening at $\lvert\Omega\rvert = 100$ (ADMM: 861.4s vs. 1973s). For larger scenario sets $\lvert\Omega\rvert \geq 200$, the centralized model did not solve within our limits, whereas ADMM successfully handled. Notably, the ADMM iteration counts remain moderate (6–24) despite increasing $\lvert\Omega\rvert$, and the reported times reflect a sequential implementation—scenario x-updates are independent and thus amenable to parallelization.

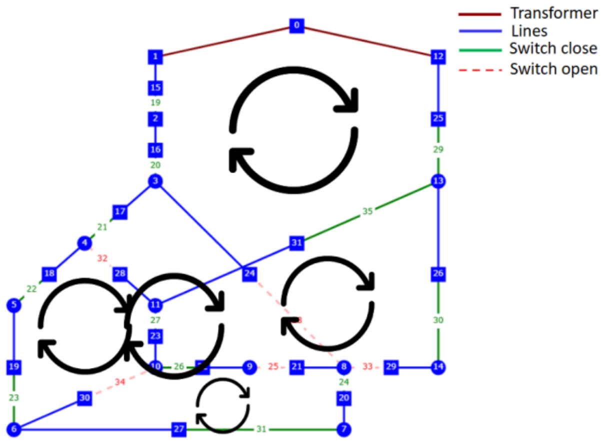

Figure 29: Schematic of the ADMM grouping strategy, illustrated for the IEEE 33 network.

$\lvert\Omega\rvert$ (scenarios)	MISOCP [s]	ADMM [s]	ADMM [iteration number]
10	16.081	33.037	6
20	69.399	84.519	10
50	743.811	378.49	18
100	1972.95	861.44	24
200	Not Converged	1197.182	14
500	Not Converged	2133.306	10
1000	Not Converged	7374.681	18

The runtime comparison highlights the scalability advantage of ADMM over a centralized MISOCP as the number of scenarios increases. Beyond runtime, it is also important to assess the practical convergence behavior of ADMM. Figure 30 plots the evolution of the primal and dual residual norms r_{norm} and s_{norm} over times for the 33-node network with $|\Omega| = 100$ scenarios and $G = 5$ groups. Both residuals decrease steadily and reach small values within a few hundred seconds, indicating stable convergence of the iterative process. The oscillations visible in the primal residual are typical when binary switch decisions are alternately fixed and released across groups; however, the dual residual converges smoothly to near zero, confirming that the consensus mechanism is effective. This behavior is representative across all networks considered, with the time scale primarily governed by network size and scenario count.

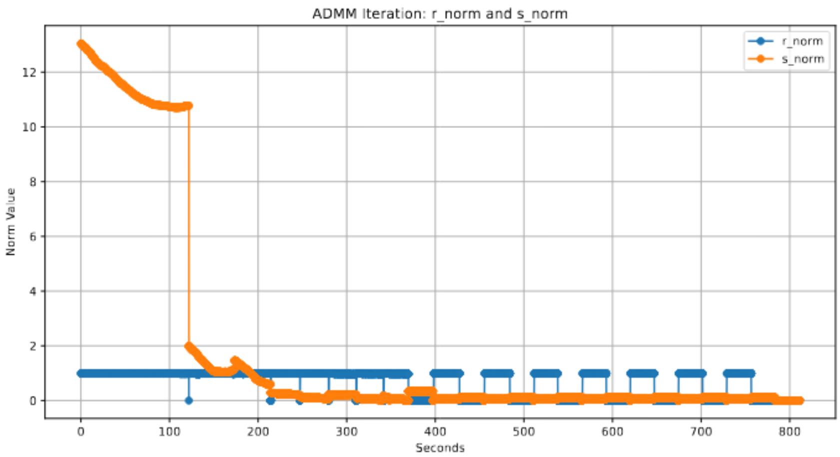

Figure 30: ADMM convergence on the 33-node network with $|\Omega| = 100$ scenarios and $G = 5$ groups: evolution of the primal (r_{norm}) and dual (s_{norm}) residuals over wall-clock time.

To examine factors that influence ADMM convergence, we performed a sensitivity analysis on the adaptive penalty parameters using the benchmark 33-node network. The initial penalty parameter was fixed at $\rho^{(0)} = 2.0$ for all runs, while the augmented Lagrangian scaling parameters $(\mu, \tau_{\{incr\}}, \tau_{\{decr\}})$ were systematically varied between runs. Each configuration used the same grouping and scenario setup ($|\Omega| = 100$ and $G = 5$) to ensure a consistent basis for comparison.

We evaluate how the aggressiveness of the penalty-update rule affects convergence speed, as measured by iteration count and total wall-clock time. The following table summarizes the results, reporting the number of iterations to convergence, the elapsed time, and the final value of ρ attained by the adaptive scheme for each tested configuration.

Run	μ	τ_{incr}	τ_{decr}	Iteration Number	Time [s]	Final ρ
1	10	2.0	2.0	24	861.44	4.0
2	10	4.0	4.0	22	805.12	2.0
3	20	2.0	2.0	22	798.55	2.0
4	20	4.0	4.0	20	750.12	2.0

The results clearly show that larger scaling parameters $(\tau_{\{incr\}}, \tau_{\{decr\}})$ accelerate convergence. For $\mu = 10$, increasing τ from $(2.0{,}2.0)$ to $(4.0{,}4.0)$ reduced the required iterations count from 24 to 22 and the runtime from 861.44s to 750.12s. A similar pattern hold for $\mu = 20$; the configuration $(\mu, \tau_{\{incr\}}, \tau_{\{decr\}}) = (20{,}4{,}4)$ attains the fastest convergence (20 iterations, 750.12s), outperforming $(20{,}2{,}2)$ (22 iterations, 798.55s).

Across all configurations, convergence remained stable and no oscillatory behavior was observed. The results indicate that stronger penalty updates (larger τ values) enhance coordination across sub-problems, improving convergence without sacrificing stability. Among the tested settings, $(\mu, \tau_{\{incr\}}, \tau_{\{decr\}}) = (20{,}4{,}4)$ delivered the best overall performance, achieving the fastest convergence with consistent final accuracy.

In summary, the sensitivity analysis demonstrates that the ADMM adaptive penalty mechanism is robust over a broad range of parameter choices. With appropriately tuned thresholds, it significantly reduces wall-clock time and iteration counts while preserving reliable convergence. These findings support the effectiveness of the adaptive-penalty strategy for large-scale, scenario-based distribution network reconfiguration.

3.6.3. Comparison of Normal Open Baseline Topology with ADMM Results

We next compare the operating states obtained under a *baseline operator topology* (i.e., the normal-open configuration used in routine operations) with those produced by ADMM-based reconfiguration. Figure 31, Figure 32, Figure 33, and Figure 34 illustrate voltage magnitudes and line loadings for the medium (234-node) and large (1004-node) networks, respectively. For the 234-node network, ADMM yields a more symmetric topology, reducing line congestion and distributing flows more evenly. Voltage deviations remain within prescribed limits in both cases, but ADMM leads to fewer heavily loaded edges compared to the baseline case. For the 1004-node network, the performance gap is more pronounced. The baseline topology shows localized overloads and voltage drops near heavily stressed branches, whereas the ADMM reconfiguration successfully redistributes power flows, lowers edge loadings and improves voltage uniformity.

These comparisons indicate that while both strategies satisfy operational constraints, ADMM achieves better utilization of switching flexibility, an effect that becomes more salient in large networks where the space of feasible radial topologies is vast.

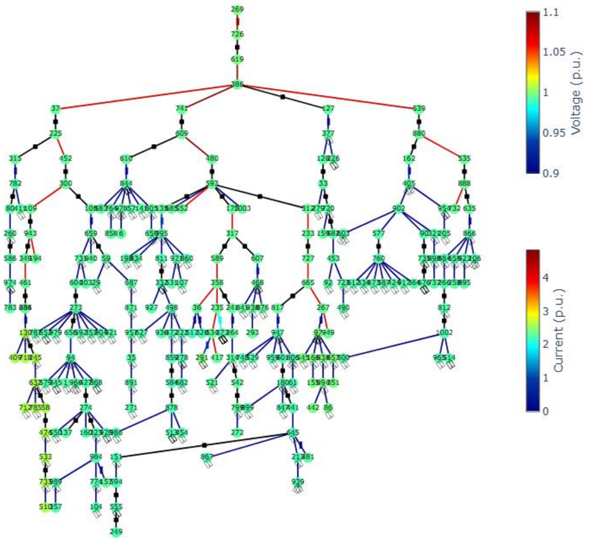

Figure 31: Voltage and current distribution for the simplified Boisy Grid: Proposed ADMM-based reconfiguration.

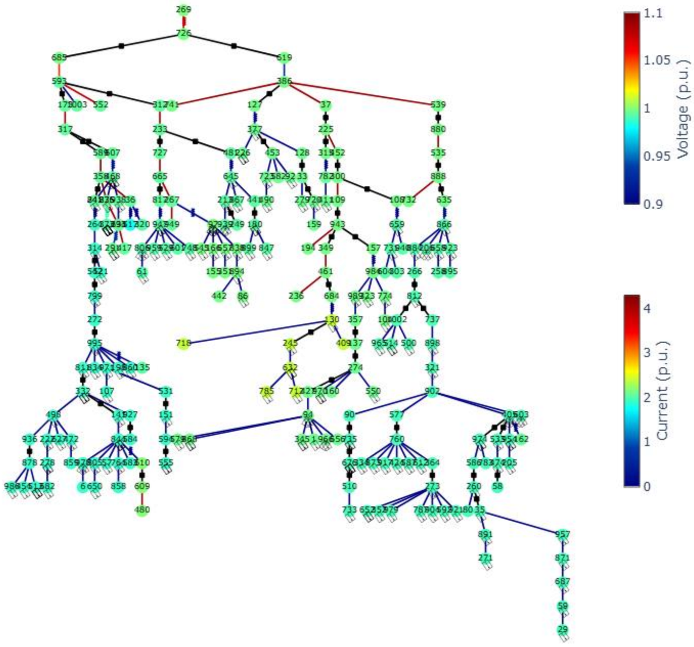

Figure 32: Voltage and current distribution for the simplified Boisy Grid: Norma-open baseline configuration.

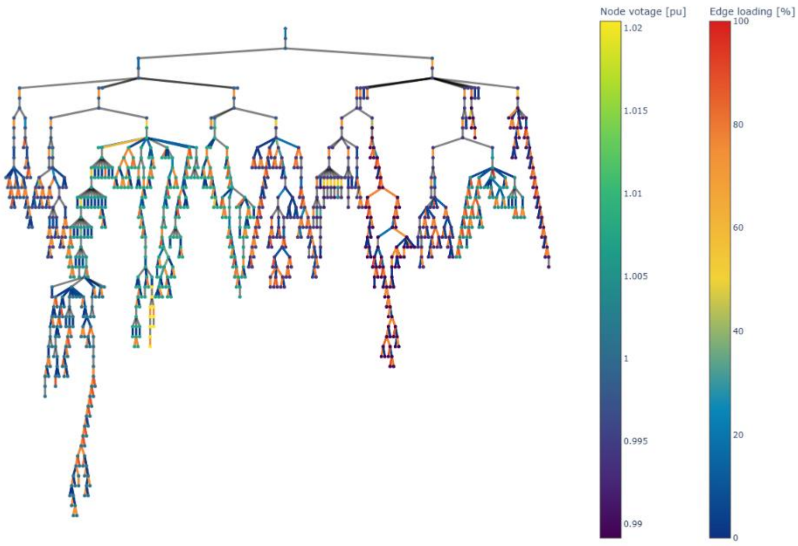

Figure 33: Voltage and current distribution for the actual Boisy Grid: Proposed ADMM-based reconfiguration.

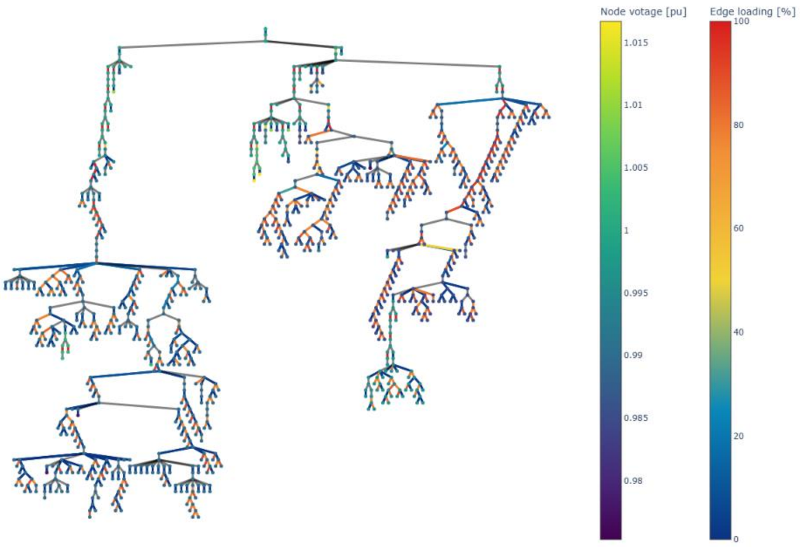

Figure 34: Voltage and current distribution for the actual Boisy Grid: Normal-open baseline configuration.

3.6.4. Statistical Comparison of Loss Distribution

The preceding operating-state analysis suggests consistent benefits from consensus-based ADMM reconfiguration; here we quantify these effects statistically via loss distributions. We compare AC active-power losses, computed with `Pandapower`, for the topology learned by ADMM against a normal open baseline operator topology. To determine the impact of sample size on the robustness of consensus, we vary the number of in-sample scenarios $|\Omega_{\{in-sample\}}| \in \{50,100,150\}$. For each set, ADMM is executed to obtain a fixed consensus switching plan $\tilde{y}^{(sw)}$. We then evaluate performance across three categories:

- In-Sample: AC losses on the same $|\Omega_{\{in-sample\}}|$ scenarios used for training, with switch states fixed to the optimized consensus $\tilde{y}^{(sw)}$.
- Out-of-Sample (OOS): AC losses on an independent set $\Omega_{\{OOS\}}$ of 500 scenarios, using the $\tilde{y}^{(sw)}$ derived from the respective in-sample set $|\Omega_{\{in-sample\}}|$.
- Normal-Open (Baseline): AC losses in the 500 $\Omega_{\{OOS\}}$ scenarios under the operator's static baseline topology.

Figure 35 (log scale) illustrates the resulting boxplots. A key observation is that for all $|\Omega_{\{in-sample\}}|$, the OOS distributions closely mirror their In-Sample counterparts in terms of medians and inter-quartile ranges. This alignment indicates strong generalization: the switching plan optimized for a small subset remains highly effective for unseen operating conditions.

Notably, increasing the training size $|\Omega_{\{in-sample\}}|$ from 50 to 150 scenarios yields only modest incremental improvements in loss reduction, suggesting diminishing returns for this specific feeder and scenario model. This performance plateau is particularly relevant when considering computational overhead: the training time scales linearly with the number of scenarios, meaning that using 100 scenarios instead of 50 effectively doubles the required computation time without offering a proportional benefit in grid efficiency. Consequently, 50 scenarios are sufficiently representative to capture the underlying physics and variability of the feeder while maintaining a favorable computational profile. In contrast, the baseline topology exhibits systematically higher losses and significantly wider dispersion, confirming that even a consensus plan learned from a modest sample size provides a more robust and efficient operating state than the standard configuration.

For each in-sample scenario number $|\Omega_{\{in-sample\}}| \in \{50,100,150\}$, the ADMM-optimized switch configuration $\tilde{y}^{(sw)}$ is evaluated on the corresponding In-Sample scenarios (left box in each pair) and on an out-of-sample set $\Omega_{\{OOS\}}$ with $|\Omega_{\{OOS\}}| = 500$ scenarios (right box). The rightmost box reports the normal-open topology evaluated on the same $|\Omega_{\{OOS\}}| = 500$ scenarios. Boxes show the inter-quartile range (IQR) and median; whiskers extend to $1.5 \times IQR$; circles denote outliers; triangles indicate means.

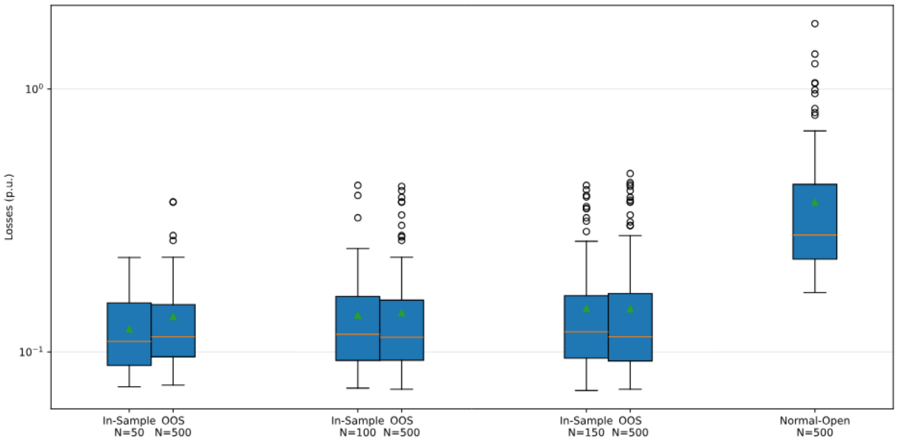

Figure 35: AC active-power loss distributions (per unit) from `Pandapower` for fixed topologies.

3.6.5. Voltage Feasibility and Role of ADMM

The main objective of Proposed ADMM formulation is that the operational feasibility must be guaranteed at the node level, ensuring that voltages remain within acceptable bounds under varying demand and generation conditions. Figure 36 compares the voltage distributions across nodes obtained with the ADMM against a baseline configuration with fixed normal-open switches. The results show that the baseline exhibits frequent violations of the $\pm 5\%$ voltage band, with several nodes operating below 0.95 per unit. In contrast, the proposed ADMM solution maintains all nodal voltages strictly within limits by dynamically optimizing switch states and enforcing radial operation. The box plots further illustrate that the proposed ADMM formulation reduces the spread of voltage variations, leading to a more stable and secure operating profile. These results underscore the essential role of the proposed ADMM formulation: it ensures that the expansion plans produced by the planning layer are operationally feasible, enforcing both radiality and voltage limits across all operational scenarios.

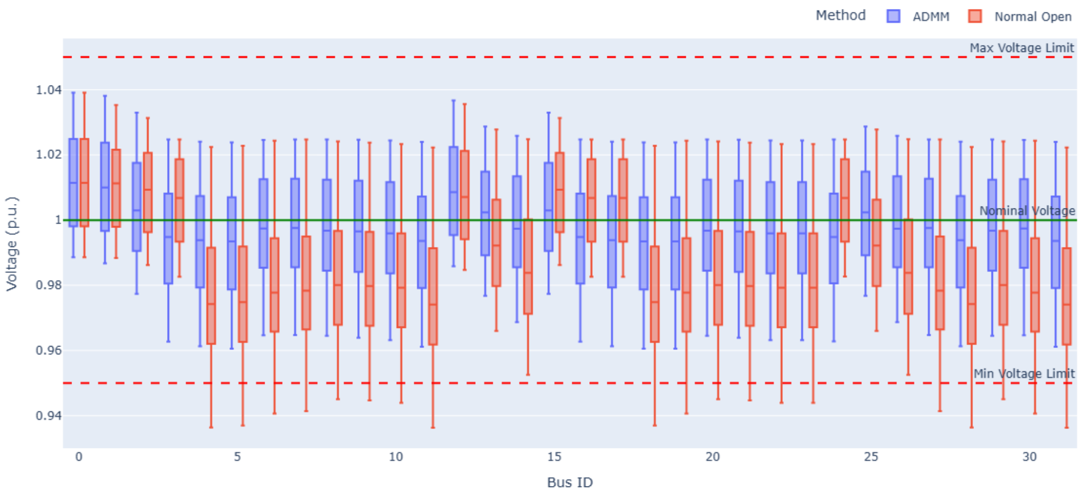

Figure 36: Comparison of Voltage range with ADMM and with Normal-Open Configuration.

3.6.6. Benchmarking and validation against reference power flow solution

The optimization framework is validated by comparing its results with nonlinear AC power flow solutions computed using `pandapower`. The assessment focuses on the maximum deviation in nodal voltage magnitude and branch current. The validation is performed on the IEEE 33-node test feeder and on a simplified Boisy grid. Three approaches are tested: a MISOCP optimal power flow, a Benders decomposition scheme, and an ADMM-based decomposition.

For the 33-bus system, the Benders approach shows a maximum voltage deviation of 3.3×10^{-8} per unit and a current deviation of 5.8×10^{-4} per unit, indicating near-identical results to the AC reference. The MISOCP and ADMM methods yield maximum deviations of 5.3×10^{-3} per unit in voltage and 8.6×10^{-3} per unit in current. These errors are consistent with second-order cone approximations and remain within acceptable engineering tolerances.

The benchmarking confirms that all methods provide feasible solutions, with Benders achieving the highest numerical accuracy on the small test case.

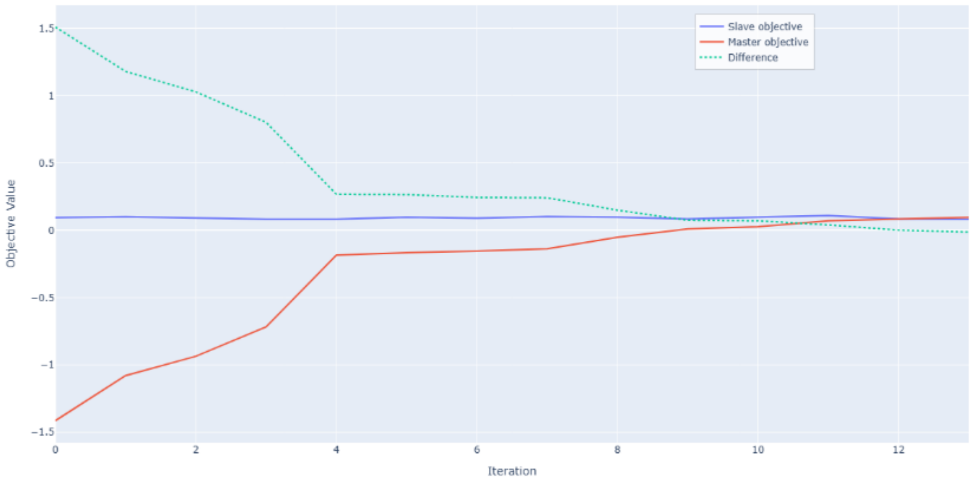

Figure 37: Convergence of Bender decomposition for IEEE33.

Model	Max Voltage Difference with Pandapower	Max Current Difference with Pandapower	33 Buses	Boisy (Simplified)
BENDER	3.3e-08	5.8e-04	y	n
MISOCP	5.3e-03	8.6e-03	y	n
ADMM	5.3E-03	8.6E-03	y	y

3.6.7. Discussion

We present a scalable and distributed optimization framework for multi-scenario DNR based on a consensus formulation of the ADMM. The proposed approach enables the efficient optimization of large-scale distribution network by decomposing a MISOCP into smaller, scenario-specific sub-problems. These sub-problems are solved independently while global consistency of the discrete switching and OLTC decisions is enforced through a consensus mechanism.

A key design choice for tractability and numerical stability is a *spatial–loop* grouping strategy, which updates overlapping groups of switches at each iteration. This grouping reduces the combinatorial complexity per iteration without sacrificing model accuracy. OLTC tap positions are updated in every iteration to respect their ordered discrete structure. Additionally, an adaptive-penalty mechanism dynamically balances the progress of the primal and dual residuals, improving convergence speed and stability in practice.

Comprehensive case studies on small, medium, and large distribution networks demonstrate both scalability and operational benefits. The consensus- based ADMM implementation shows moderate runtime growth with scenario count and remains effective when the centralized MISOCP becomes intractable. The results also show that convergence behavior is sensitive to penalty tuning: reliable convergence was achieved with calibrated $(\mu, \tau_{\{incr\}}, \tau_{\{decr\}}, \rho)$ settings.

From an operational standpoint, the ADMM-optimized topologies reduce line loading and improve voltage uniformity compared to the baseline operator topology. A distributional evaluation using `Pandapower` shows that out of sample power loss distributions closely track their in-sample counterparts, indicating strong generalization of the learned topology. Across all tested networks, the baseline configuration exhibits higher losses and greater variability, whereas the ADMM-derived topology achieves lower median losses with tighter variability.

Users with authorized access to the grid data can execute the optimal reconfiguration experiments directly from the project repository. The corresponding scripts are available at

https://github.com/heig-vd-ie/dig-a-plan-optimization/blob/main/experiments/boisy/01-reconfiguration.py

https://github.com/heig-vd-ie/dig-a-plan-optimization/blob/main/experiments/estavayer/01-reconfiguration.py,

https://github.com/heig-vd-ie/dig-a-plan-optimization/blob/main/experiments/ieee_33/01-reconfiguration.py

To run a specific study case, the input payload must be adapted to the targeted feeder and to the selected power profile.

3.7. Numerical Results: Long-term Optimization for Grid Expansion Planning

Known and *unknown* uncertainties are modeled at two different time scales, aligned with the architecture of our proposed two-layer framework. At the *upper* layer, representing *unknown* uncertainties, we consider $K = 5$ stages, each spanning $N^{\{years\}} = 5$ years, with 100 long-term scenarios per stage (demand and PV variations based on determined power profiles in section 3.4). At the *lower* layer, representing *known* uncertainties, each representative day is perturbed by 100 short-term scenarios. These operational scenarios are solved in parallel to ensure feasibility. To address the combinatorial complexity of discrete switch decisions, we adopt a grouping strategy within the *lower* layer. The set of switches is partitioned into five groups. At each iteration, the switch states in one group are fixed, while the remaining four groups are optimized. This rotation continues across all groups, ensuring that the final solution explores feasible radial topologies without incurring the prohibitive computational cost of optimizing all switch states simultaneously.

The *upper* layer runs 100 SDDP iterations with 5000 forward simulations. The initial budget of DSO is considered 500,000 with a 5% discount rate. Expansion costs are assumed 0.2 kVA/km (lines) and 0.15 kVA (transformers). Unless otherwise specified, results are reported using Expectation risk measure. A fixed random seed (42) is used for reproducibility.

For the *lower* layer, we use the `Gurobi` solver via `Pyomo`, which supports MISOCP and efficiently handles the nonlinearities and discrete decisions involved in grid operation. For the *upper* layer, the implementation is carried out in Julia using `SDDP.jl` package with HiGHS solver, which efficiently handles large-scale convex programs within the SDDP framework. The interaction between Python and Julia environments is managed through a dedicated API, enabling seamless data exchange between layers. In our implementation, we also utilize the risk operators provided by the SDDP.jl library.

From a computational standpoint, the ADMM-based operational computations for different *unknown* scenarios are distributed across two machines: one equipped with a 13th Gen Intel® Core™ i7-13850HX and 32GB of RAM, and the other with an Intel® Core™ i7-2600K@3.40GHz and 16GB of RAM. Parallel execution and resource allocation across a total of 34CPU cores are managed using the Ray framework, which enables efficient scheduling and memory usage. The overall wall-clock time for the simulations was approximately 1.8 hours for IEEE33, corresponding to roughly 60 core-hours of CPU time.

The following figures present the performance results of the proposed solution across the different case studies when they are run on only second computer with an Intel® Core™ i7-2600K@3.40GHz and 16GB of RAM.

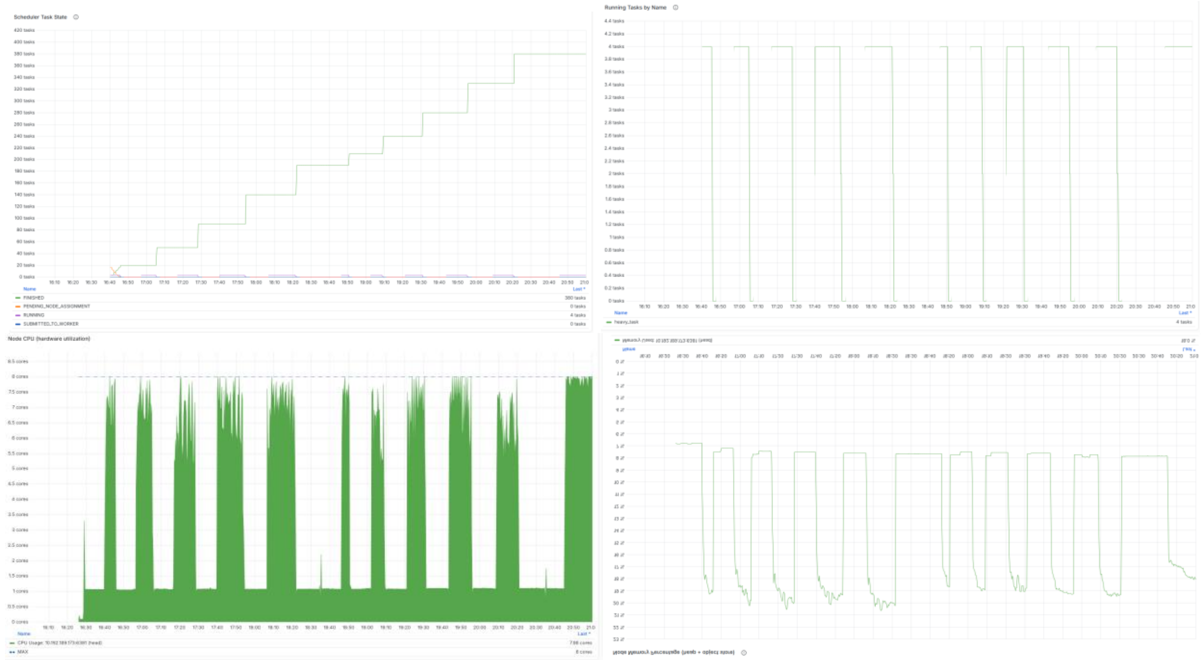

Figure 38: Performance of four consecutive runs on IEEE33 (results from Prometheus service on ray framework).

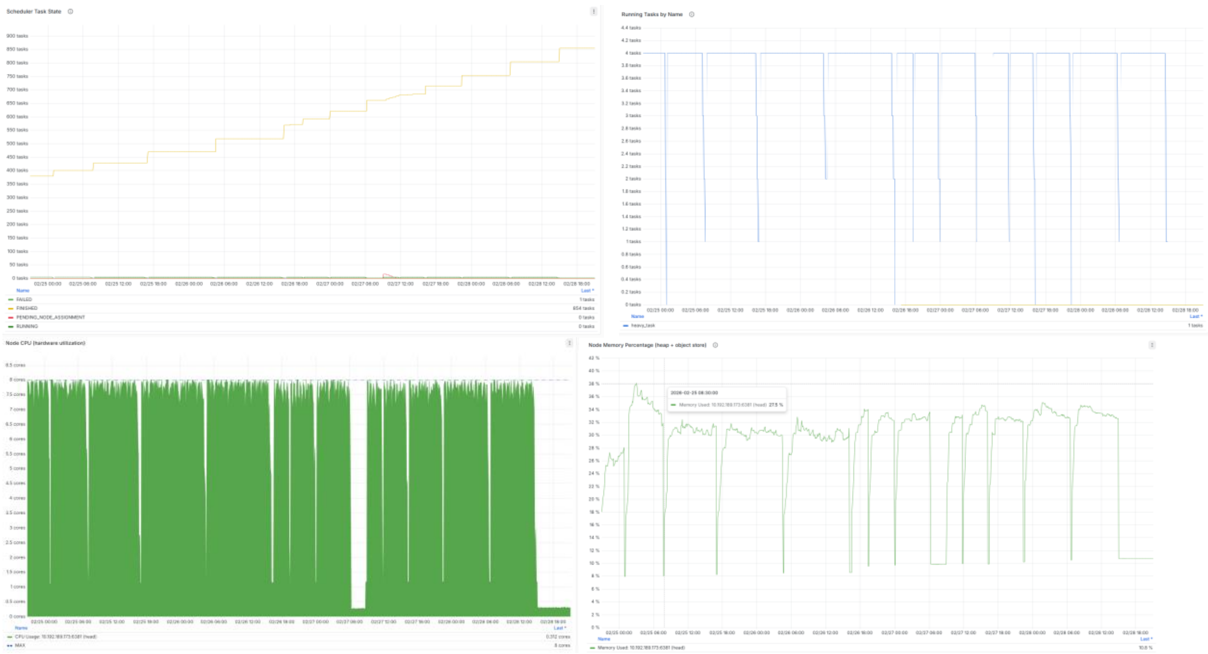

Figure 39: Performance of four consecutive runs on Boisy (results from Prometheus service on ray framework).

Job ID	Submission ID	Entrypoint	Status	Status message	Duration	Tasks	Actions	StartTime	EndTime	Driver Pid
08000000	-	/usr/local/bin/python3.12 /usr/local/bin/uvicorn main:a...	SUCCEEDED	-	6m 58s		Log Stack Trace (Driver) CPU Flame Graph (Driver) Memory Profiling (Driver)	2026/02/24 18:01:59	2026/02/24 18:08:57	7
07000000	-	/usr/local/bin/python3.12 /usr/local/bin/uvicorn main:a...	SUCCEEDED	-	4m 27s		Log Stack Trace (Driver) CPU Flame Graph (Driver) Memory Profiling (Driver)	2026/02/24 17:45:55	2026/02/24 17:50:22	7
06000000	-	/usr/local/bin/python3.12 /usr/local/bin/uvicorn main:a...	SUCCEEDED	-	15m 20s		Log Stack Trace (Driver) CPU Flame Graph (Driver) Memory Profiling (Driver)	2026/02/24 17:06:18	2026/02/24 17:21:38	7
05000000	-	/usr/local/bin/python3.12 /usr/local/bin/uvicorn main:a...	SUCCEEDED	-	14m 29s		Log Stack Trace (Driver) CPU Flame Graph (Driver) Memory Profiling (Driver)	2026/02/24 16:39:44	2026/02/24 16:54:14	7
04000000	-	/usr/local/bin/python3.12 /usr/local/bin/uvicorn main:a...	SUCCEEDED	-	11m 44s		Log Stack Trace (Driver) CPU Flame Graph (Driver) Memory Profiling (Driver)	2026/02/24 16:16:33	2026/02/24 16:28:17	7
02000000	-	/usr/local/bin/python3.12 /usr/local/bin/uvicorn main:a...	SUCCEEDED	-	9m 5s		Log Stack Trace (Driver) CPU Flame Graph (Driver) Memory Profiling (Driver)	2026/02/24 15:56:29	2026/02/24 16:05:35	7
01000000	-	/usr/local/bin/python3.12 /usr/local/bin/uvicorn main:a...	SUCCEEDED	-	5m 49s		Log Stack Trace (Driver) CPU Flame Graph (Driver) Memory Profiling (Driver)	2026/02/24 15:39:53	2026/02/24 15:45:42	7

Figure 40: The logs from the Ray dashboard for the first run on the IEEE 33-node test feeder are shown below. The table reports the execution time of each expansion planning iteration.

Another identified limitation is related to the `Gurobi` license, which allows only three concurrent active sessions. As a result, increasing parallelism beyond three computational nodes does not lead to a significant performance improvement.

Users with authorized access to the grid data can execute the optimal expansion planning experiments directly from the project repository. The corresponding execution scripts are available at https://github.com/heig-vd-ie/dig-a-plan-optimization/blob/main/scripts/run-all.sh. To run a specific study case, the input payload must be adapted to the targeted feeder and to the selected power profile.

3.7.1. IEEE 33

This section reports the numerical results for the 33-node medium voltage test system and provides a detailed interpretation of all figures, including those appended at the end of this section. This test system corresponds to the IEEE 33 bust distribution system (Figure 29) including 17 lines, 2 transformers, 17 switches, and 7 tap positions per transformer. This system base power is assumed to be $S_{base} = 1MVA$, voltage limits are set to [0.95,1.05] per unit, and discrete transformer tap positions from 0.95-1.05 per unit. Candidate investments include line upgrades and transformer reinforcements. The *lower* layer enforces radiality and operational feasibility by jointly optimizing switch states and transformer taps under voltage and current constraints, thereby ensuring that all *upper*-layer expansion decisions are physically realizable.

1) Capital expenditure distribution under different risk operators

Figure 41 summarizes the distribution of CAPEX under three risk operators, *expectation*, *worst-case*, and *Wasserstein* ($\alpha = 0.1$), combining a density histogram with inset box plots. The *lower* layer optimizes switch configurations and transformer tap positions considering their combinatorial complexities: it determines which switches should remain open or closed so that the resulting grid is radial and simultaneously satisfies voltage and current limits. The *lower* layer ensures that expansion plans remain both feasible and consistent with realistic distribution grid operation. Having established feasibility through the *lower* layer, we next analyze how the proposed two-layer optimization framework affects long-term planning outcomes. We first examine the distribution of *cumulative capital expenditures* (CAPEX) under different risk attitudes, followed by the temporal evolution of expansion trajectories across stages of the *upper* layer and the operational voltage profiles across nodes.

The histogram highlights the overall shape of each distribution. The risk-neutral *expectation* policy (green) produces most outcomes between 60k and 1.5MCHF, but it also shows a wider spread with a lower tail. The conservative worst-case policy (orange) shifts the entire distribution upward, with CAPEX concentrated around 250kCHF and 1.45MCHF, reducing risk at the expense of higher costs. The *Wasserstein* policy (blue) lies between the two, preserving efficiency close to *expectation* while extending protection against costly outcomes through a heavier right tail. The box plots in the insect complement the density view by emphasizing medians, inter-quantile ranges, and outliers. *Expectation* shows the lowest median but the widest variability; worst-case narrows the spread but raises the median; and Wasserstein balances both, keeping the median close to *expectation* while tightening the upper range. Together, the histogram and box plots reveal the trade-off between cost efficiency and robustness: *expectation* minimizes average expansion but risks; *worst-case* ensures resilience at high expense; and *Wasserstein* offers a balanced compromise by partially accounting for distributional ambiguity.

The figure also indicates that lower-layer optimization of switch configurations and tap settings has limited influence on aggregate CAPEX. Differences in final expansion cost across risk operators are primarily driven by upper-layer planning decisions rather than by operational reconfiguration, suggesting that network topology adjustments do not materially alter total expansion requirements.

The load and generation time-series profiles used in this study are available in the public repository at https://github.com/heig-vd-ie/dig-a-plan-optimization/tree/main/examples/ieee_33.

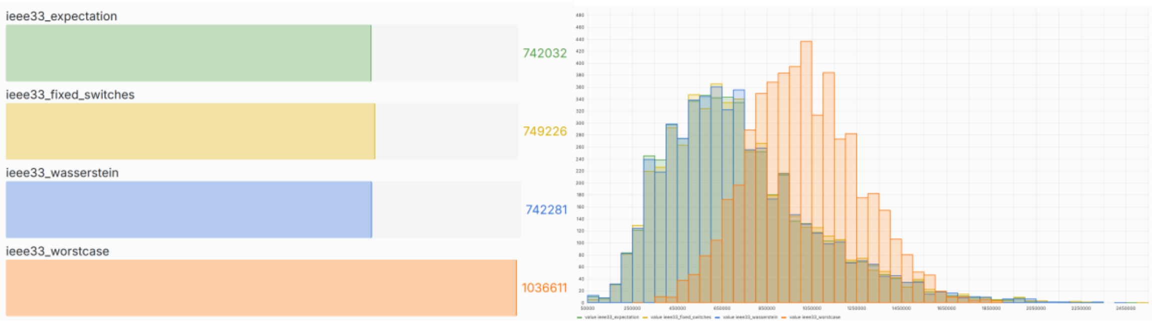

Figure 41: CAPEX distribution under different risk measure and fixed switches configuration.

2) Normalized expansion trajectories across planning stages

Figure 42 illustrates normalized expansion cost trajectories over the 25-year horizon. Each trajectory corresponds to one scenario, and costs are normalized by the mean expectation-policy cost. Under *Wasserstein* policy, trajectories cluster tightly around unity across all stages. This indicates that reinforcement timing and magnitude remain close to the risk-neutral baseline, but variability across scenarios is controlled. In contrast, the *worst-case* policy produces uniformly higher and earlier reinforcements, shifting trajectories upward across all scenarios. This behavior reduces variability but results in consistently higher capital expenditures. These results highlight a key trade-off: while *expectation*-based policies risk delays or insufficient expansions, *worst-case* policies ensure feasibility at the excessive cost. In contrast, the *Wasserstein* approach strikes a balance, achieving stable, cost-efficient, and robust expansion trajectories over time.

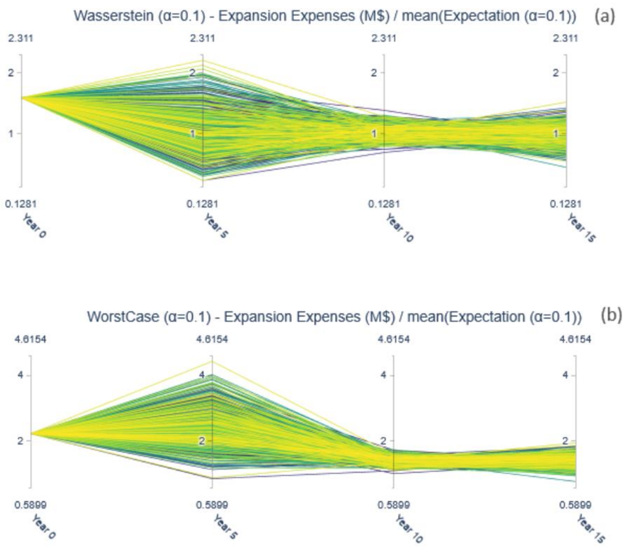

Figure 42: Normalized expansion cost trajectories under different risk attitudes, shown across planning stages (Years 0-15). Each line represents a scenario trajectory, normalized by the mean *expectation* policy cost.

3) Spatial Expansion Pattern over Stages

Figure 43 visualizes how reinforcement actions propagate through the network over time (comparing stage 1, i.e., year 0, with stage 5, i.e., year 25). Although node coordinates are randomly generated for visualization, the figure reveals structural expansion patterns.

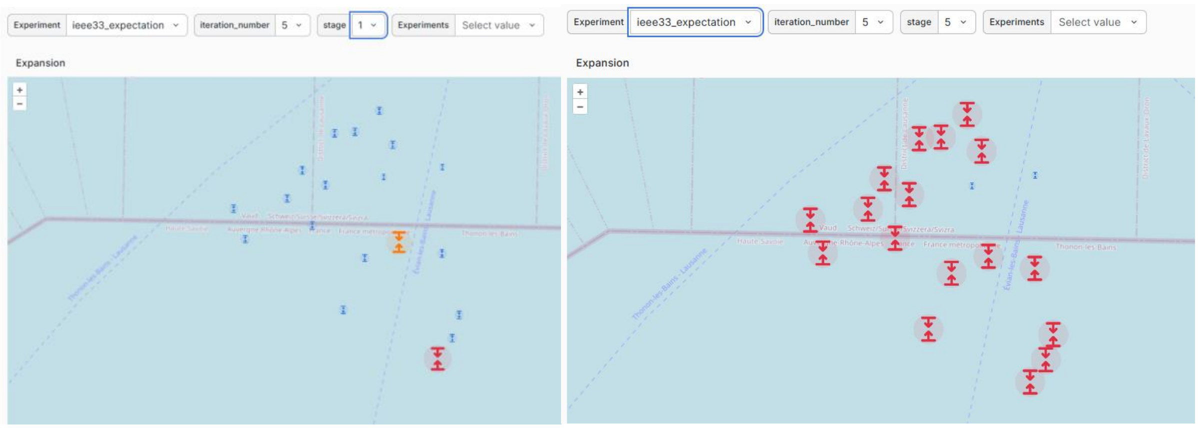

Figure 43: Spatial Expansion Pattern over Stages (geolocations are randomly generated).

4) In sample and Out-of-Sample Comparison

The in-sample versus out-of-sample comparison figure evaluates generalization performance. The gap between in-sample and out-of-sample objective values is small for both Wasserstein and Expectation operators, indicating stable decisions under unseen realizations.

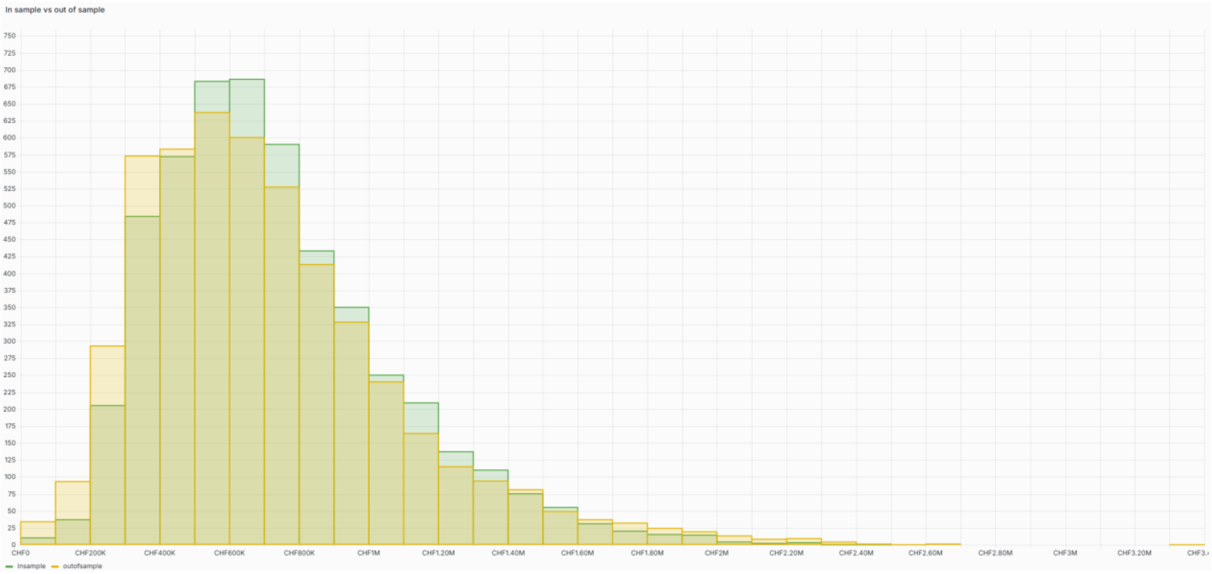

Figure 44: In-sample and out-of-sample distribution for expansion planning based on *expectation* risk measure.

5) Convergence behavior

The convergence plot of the objective value across the outer iterations shows monotonic stabilization of the two-layer algorithm. The objective rises quickly during the initial iterations as major reinforcement decisions are updated and then improves more gradually as the solution is refined. If the optimization were run for additional iterations, this refinement would continue until the convergence tolerance is satisfied. However, the rate of improvement diminishes significantly after the initial rapid increase, indicating that most of the significant adjustments have already been made.

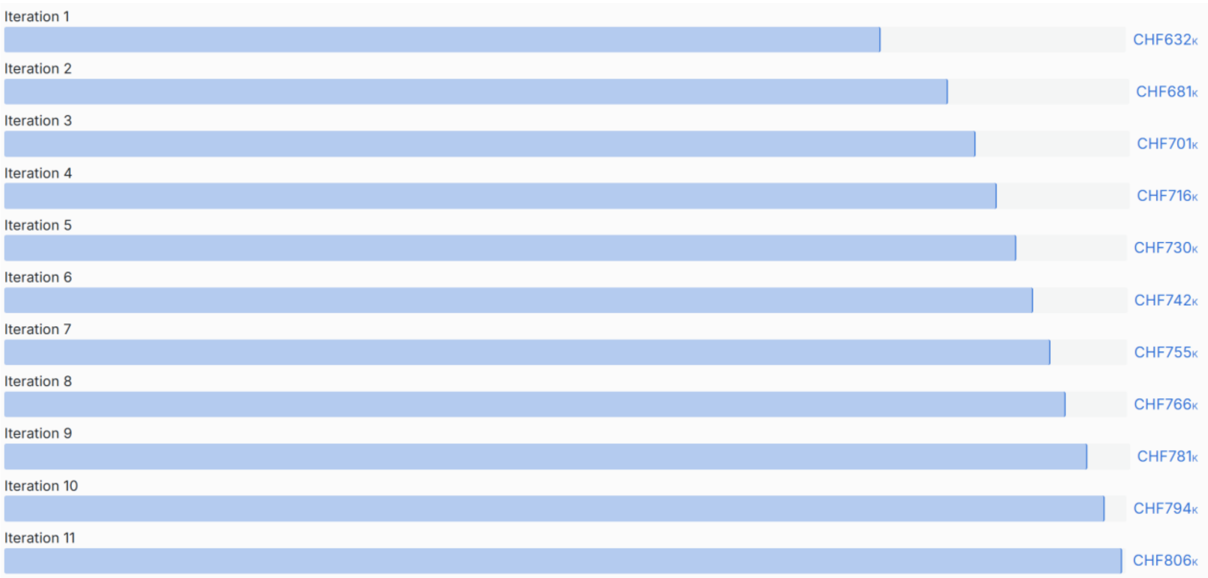

Figure 45: The convergence plot of objective value across the outer iterations.

6) Stage wise total cost comparison

The figure reporting total cost over stages compares *expectation*, *worst-case*, *Wasserstein*, and a fixed-switch benchmark. The worst-case policy exhibits significantly higher early-stage investments, confirming front-loaded expansion. In contrast, expectation and Wasserstein show similar cumulative trajectories, with differences becoming visible only under adverse realizations. The fixed-switch case results in higher operational penalties in later stages due to limited reconfiguration flexibility, demonstrating the economic value of jointly optimizing switches and taps in the lower layer.

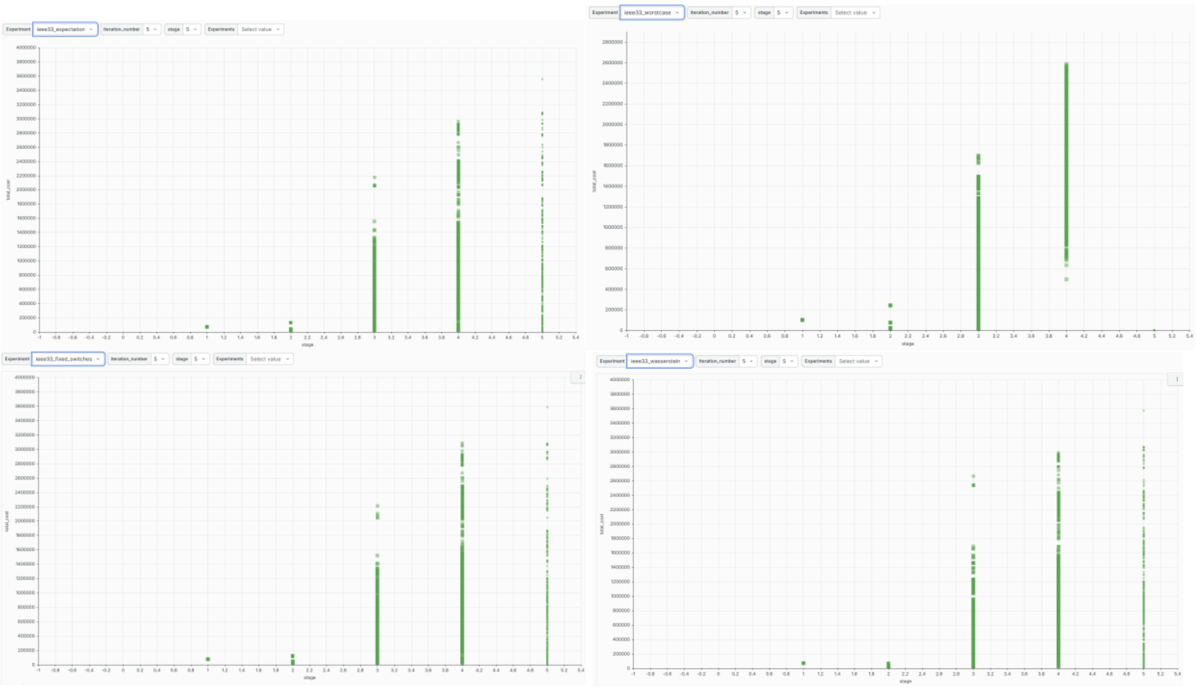

Figure 46: Stage wise comparison of total cost for *expectation*, *worst-case*, *Wasserstein*, and fixed switches.

7) Overall Interpretation

The figure showing the objective values for the four risk measures confirms that expectation yields the lowest average objective, worst-case the highest, and Wasserstein remains close to expectation but with reduced dispersion. The corresponding objective distribution plot further highlights that worst-case compress the distribution at higher cost levels, while Wasserstein reduces the probability mass of extreme high-cost realizations without significantly increasing the median.

For the IEEE 33-node system, representing a medium-voltage feeder supplying approximately 2.423 MW (roughly 200 typical customers), and considering a 25-year planning horizon with cumulative CAPEX of around 749kCHF, the average annual expansion cost per customer is approximately 265CHF (assuming a 5% interest rate). Under a worst-case expansion strategy, this cost increases to roughly 367CHF per customer per year.

In terms of policy behavior, expectation-based planning minimizes average expenditure but allows higher variability and can delay necessary reinforcements. Worst-case planning ensures robustness by front-loading investments, leading to consistently higher costs. The Wasserstein-based approach provides a balanced trade-off, achieving near risk-neutral efficiency while limiting exposure to adverse scenarios. Importantly, the lower layer of the framework guarantees that all expansion trajectories remain radial and maintain voltage compliance, ensuring operational feasibility throughout the planning horizon.

3.7.2. Boisy Grid

In the Boisy distribution grid, we analyzed two feeders to evaluate the impact of operational flexibility on long-term expansion planning. Figure 47 and Figure 48 illustrate the spatial evolution of grid reinforcement for the two feeders over 25 years planning horizon. It is worth mentioning that the icons represent reinforcement action, where both the color and the size are scaled relative to the magnitude of the investment in that specific year. This visualization is intended only to illustrate the spatial progression of investments; absolute numerical values are not disclosed for confidentiality reasons.

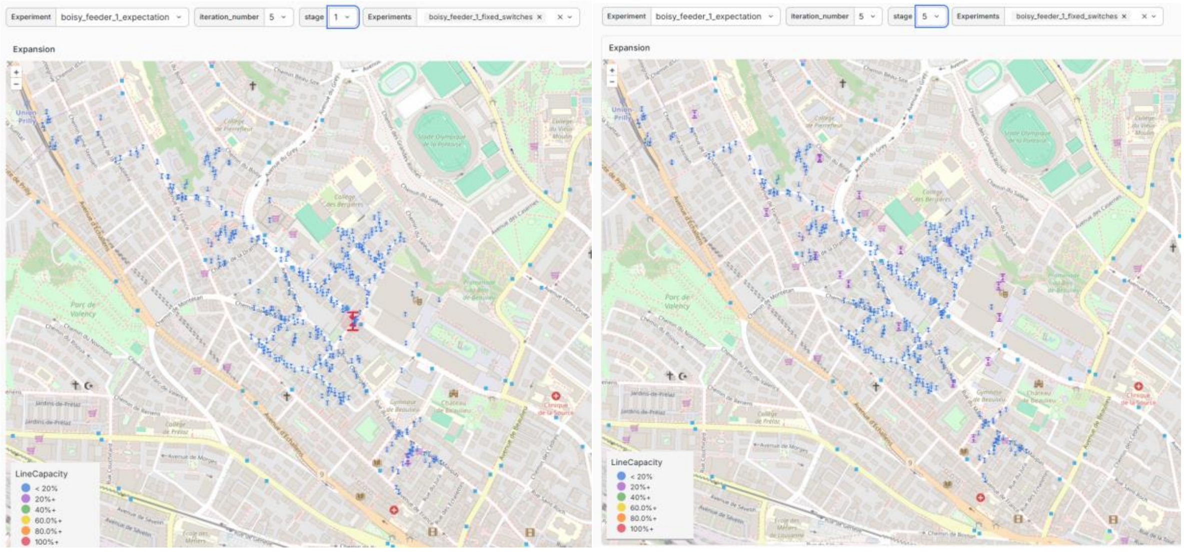

Figure 47: The expansion trajectory for Feeder 1. The left panel shows the network at the initial stage, while the right panel illustrates the configuration at Stage 5.

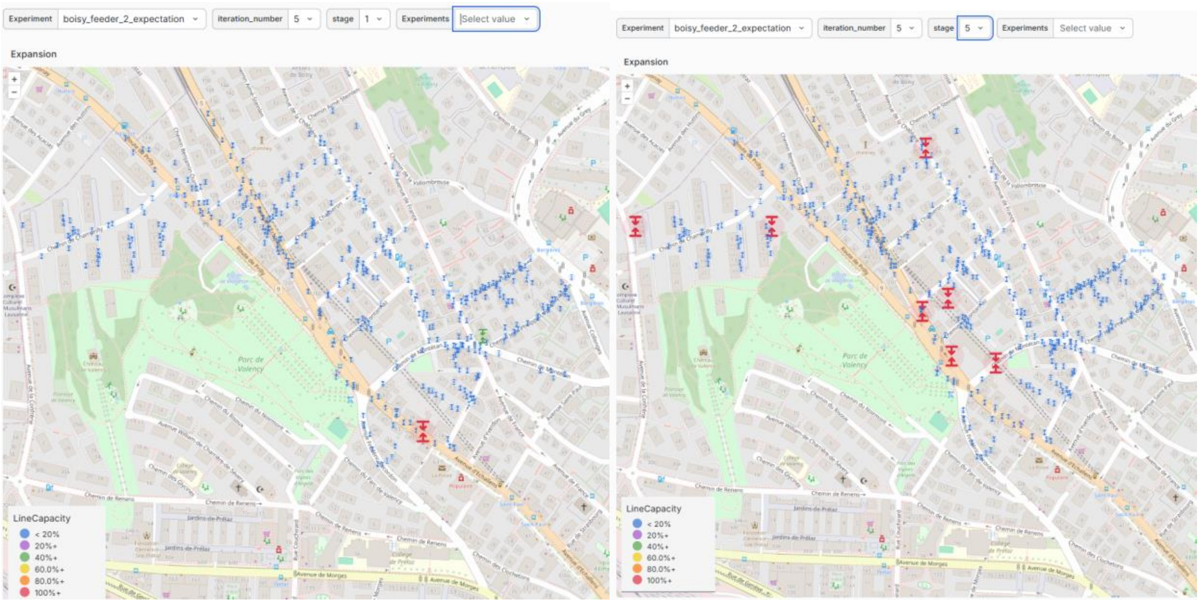

Figure 48: The expansion trajectory for Feeder 2. The left panel shows the network at the initial stage, while the right panel illustrates the configuration at Stage 5.

The convergence behavior of the optimization algorithm is summarized in
Figure 49 and

Figure 50. The individual histograms and iteration trackers indicate that the model converges consistently within six iterations of the outer optimization loop. For feeder 1, the objective values stabilize between approximately 1.68MCHF and 1.81MCHF, while feeder 2 converges to slightly lower values between about 1.65MCHF and 1.66MCHF. The close alignment between in-sample and out-of-sample values indicates that the solutions obtained are stable and statistically reliable.

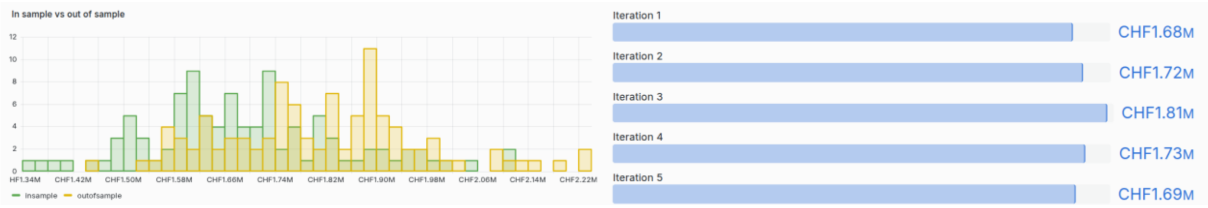

Figure 49: In sample and out-of-sample comparison for feeder 1 together with the convergence of the outer iteration loop.

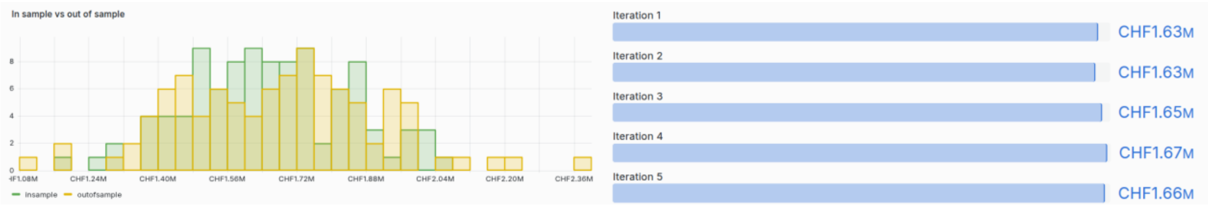

Figure 50: In sample and out-of-sample comparison for feeder 2 together with the convergence of the outer iteration loop.

The economic impact of operational flexibility is summarized in

Figure 51. The horizontal bar chart compares the aggregate performance of two operational strategies: the expectation case, in which switch states can be optimized dynamically, and the fixed-switch configuration, where switches remain static. For feeder 1, the expectation model produces a total cost of approximately 1.69MCHF, while the fixed switch configuration increases the cost about 1.70MCHF. For feeder 2, the two values remain much closer to each other, indicating that switching flexibility has much smaller impact.

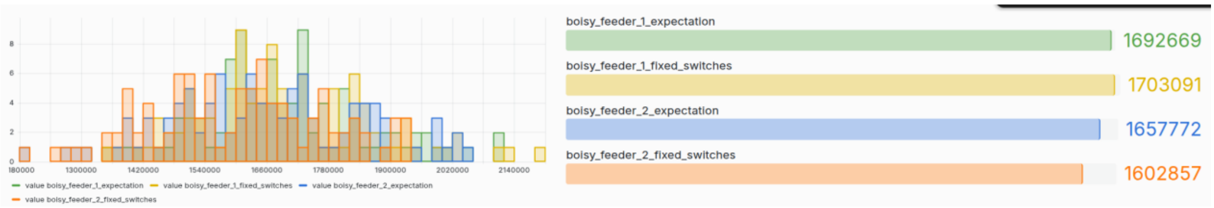

Figure 51: The comparison of results for feeders 1, 2, and fixed switches versus the expectation risk measure.

The distribution plots in the same figure provides additional insight. For the feeder one there is a clear horizontal shift between the green distribution corresponding to the expectation case and the yellow distribution corresponding to fixed switches. The fixed configuration shifts the distribution toward higher cost values, demonstrating that restricting switch operations reduces the system's ability to manage congestion efficiently. For feeder 2, however, the blue distribution representing the expectation case and the orange distribution representing the fixed-switch configuration almost completely overlap, indicating that dynamic switching does not significantly change the cost outcomes.

These results reflect the structural differences between the two feeders. Feeder 1 contains a more interconnected topology with several alternative paths for power flow. Dynamic switching therefore plays an important role in identifying efficient routing configurations and in reducing overall expansion costs. When switches are forced to remain fixed, this operational flexibility disappears, leading to higher investment requirements. In contrast, Feeder 2 exhibits a more linear and constrained topology with limited alternative routing options. Because power flows cannot be easily redirected, dynamic switching provides little additional benefit, and the performance remains almost identical to the fixed-switch configuration.

Considering both feeders together, which supply roughly 1500 customers, and assuming a 25-year planning horizon with cumulative expansion costs of approximately 1.6–1.7MCHF per feeder, the average annual expansion cost per customer is about 260CHF when a discount rate of 5 percent is applied. This value provides a practical interpretation of the investment scale required to maintain reliable operation of the network over the long-term planning horizon.

3.7.3. Estavayer-le-Lac

This section presents the results for the Estavayer distribution grid. The analysis is reported separately for each feeder, and the corresponding figures are provided for every case. For each feeder, three types of results are included: the spatial evolution of grid expansion over the planning horizon, the convergence behavior of the optimization algorithm per feeder, and the stage wise evolution of voltage profiles across scenarios.

The expansion figures illustrate how reinforcement decisions evolve over the planning horizon for each feeder. These maps provide a qualitative representation of where reinforcement actions occur over time. The figures are intended primarily to illustrate the spatial progression of investments rather than to disclose absolute numerical values. The convergence plots show the evolution of the objective value across iterations of the outer planning loop. Unlike the previous case studies, the optimization has not fully converged after five iterations. Nevertheless, the reduction in the objective value between successive iterations becomes progressively smaller, indicating that the algorithm is approaching a stable solution. Although full convergence is not reached within the reported iterations, the remaining variation in cost is limited. Voltage evolution plots are also presented for each feeder. In several scenarios, the voltage magnitude falls outside the usual operational range of 0.95–1.05 per unit. This occurs because switching actions alone are not sufficient to eliminate all voltage violations in this network. In some configurations the available switching actions, or “cuts,” do not significantly change the electrical structure of the feeder and therefore cannot effectively correct voltage deviations.

It is important to note that reliability plays a central role in the planning philosophy of the Estavayer network. However, reliability criteria are not explicitly included in the optimization formulation used in this study. As a result, the reinforcement decisions presented here should be interpreted primarily in terms of cost and operational feasibility rather than reliability performance.

The results also show that network reconfiguration provides limited economic benefit for this grid. The feeders are largely radial and contain only a small number of switching points that can be used for reconfiguration. Because the network is not strongly meshed, dynamic switching offers little opportunity to reroute power flows or significantly reduce investment needs.

Another important observation is that the grid appears to be relatively overdesigned with respect to the demand levels considered in the study. Therefore, the required expansion investments remain small compared with the other case studies. When expressed on a customer basis, the resulting expansion cost per customer per year is therefore relatively low. However, this should not be interpreted as evidence that the network is fully prepared for future demand conditions toward 2050. The low investment requirement mainly reflects the current capacity margin of the existing infrastructure rather than a guarantee that no major reinforcements will be required in the long term.

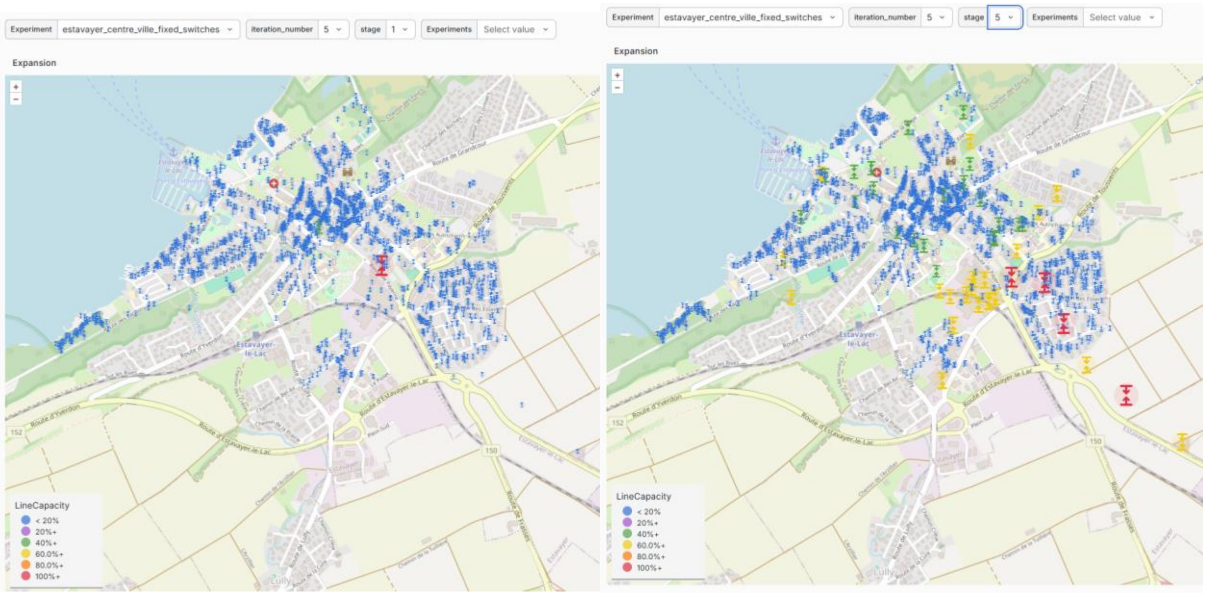

Figure 52: The expansion trajectory for Estavayer centre-ville. The left panel shows the network at the initial stage, while the right panel illustrates the configuration at Stage 5.

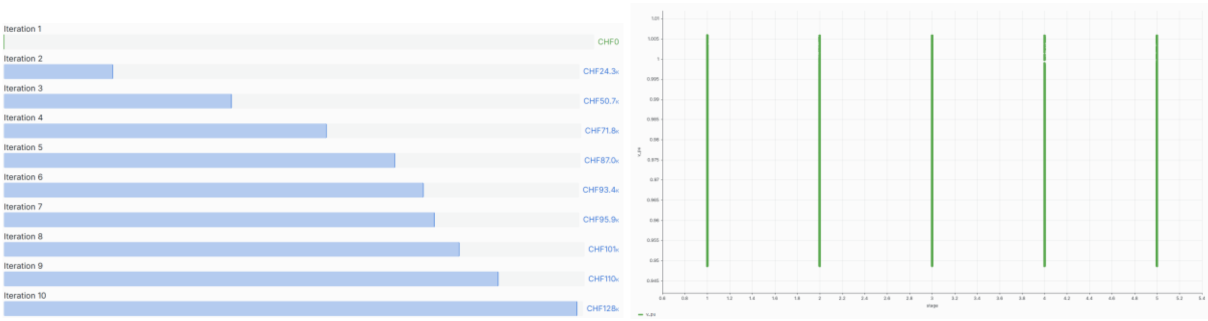

Figure 53: The convergence plot together with stage wise comparison of voltage variation of Feeder Centre-Ville.

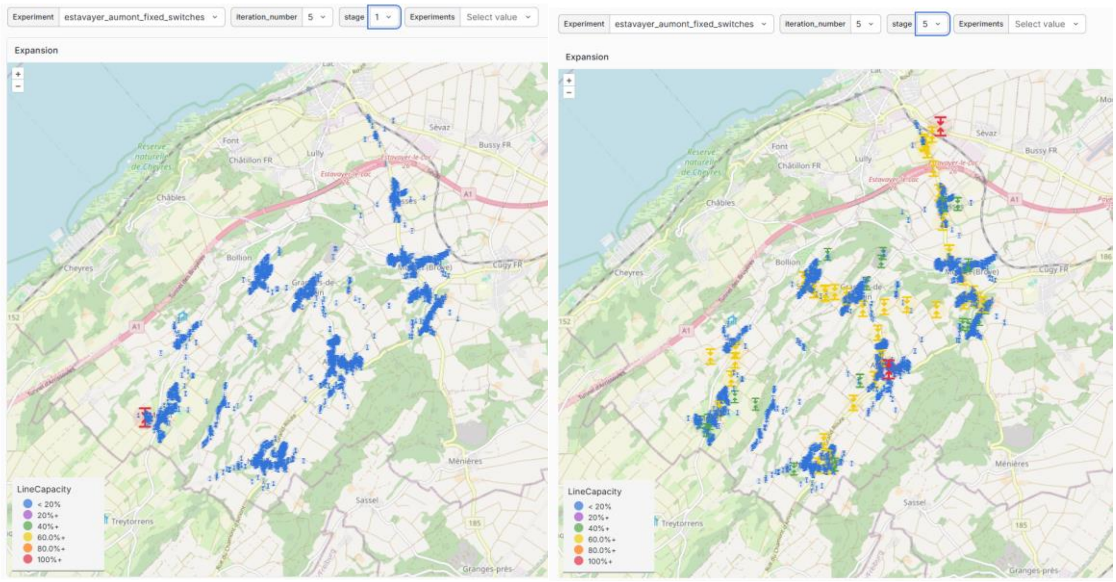

Figure 54 The expansion trajectory for Estavayer Aumont. The left panel shows the network at the initial stage, while the right panel illustrates the configuration at Stage 5.

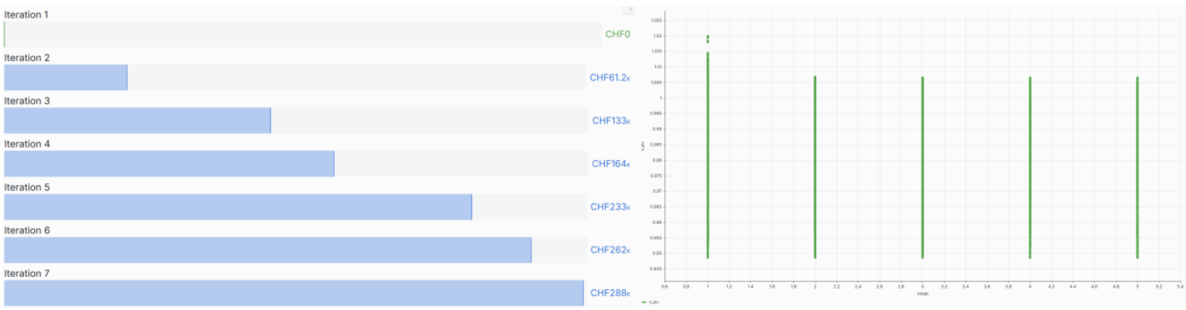

Figure 55: The convergence plot together with stage wise comparison of voltage variation of Feeder Aumont.

3.7.4. Discussion and Conclusion

This works proposes a two-layer optimization framework for distribution network expansion planning under uncertainty. The proposed methodology links long-term investment decisions with short-term operational flexibility. The *upper* layer models planning decisions over multiple stages and incorporates *unknown* uncertainty with different risk attitudes, e.g., *expectation*, *worst-case*, and *Wasserstein*, The *lower* layer enforces radiality and voltage and current limits through consensus-based coordination of grid flexibility including switch and tap positions.

An important contribution of the framework is the integration of operational constraints within the planning process. The *lower* layer guarantees that all candidate expansion plans remain operationally feasible by enforcing radial network structures and maintaining voltage limits across the grid. This coordination between planning and operation allows the model to capture the value of operational flexibility such as switching and tap control while avoiding infeasible expansion strategies.

Several directions for future work emerge from this study. First, a more advanced decomposition strategy could improve scalability and computational efficiency. An ADMM-based formulation could enable a geographical decomposition of the network into separate feeders, allowing each feeder to be optimized independently while maintaining consensus on shared variables such as boundary flows and switching states.

Second, additional benchmarks could provide further insight into the value of the proposed approach. Comparing the framework with simpler planning rules, such as reinforcement triggered only when congestion appears, would help quantify the benefit of anticipatory planning under uncertainty.

Finally, reliability considerations should be integrated explicitly into the optimization model. Reliability is a critical planning criterion in many real distribution systems, as illustrated by the Estavayer network, where operational reliability strongly influences infrastructure design. Incorporating reliability constraints or reliability-based cost metrics would provide a more comprehensive representation of real-world planning objectives.

4 Deliverable 5.3: Release of proposed asset planning tool

The source code, including instructions for local deployment, is available at the following repository: https://github.com/heig-vd-ie/dig-a-plan-optimization.

The full technical documentation is accessible at https://heig-vd-ie.github.io/dig-a-plan-optimization/.

5 References

[1] Park, Jangho, and Güzin Bayraksan. "A multistage distributionally robust optimization approach to water allocation under climate uncertainty." European Journal of Operational Research 306, no. 2 (2023): 849-871.

[2] Birge, John R., and Francois Louveaux. *Introduction to stochastic programming*. New York, NY: Springer New York, 1997.

[3] P. Lopes, N. Hatziargyriou, J. Mutale, P. Djapic, N. Jenkins, Integrating distributed generation into electric power systems: A review of drivers, challenges and opportunities, Electric power systems research 77 (9) (2007) 1189–1203. doi:10.1016/j.epsr.2006.08.016.

[4] S.-E. Razavi, E. Rahimi, M. S. Javadi, A. E. Nezhad, M. Lotfi, M. Shafiekhah, J. P. Catalão, Impact of distributed generation on protection and voltage regulation of distribution systems: A review, Renewable and Sustainable Energy Reviews 105 (2019) 157–167. doi:10.1016/j.rser.2019.01.050.

[5] A. Navarro-Espinosa, L. F. Ochoa, Probabilistic impact assessment of low carbon technologies in lv distribution systems, IEEE Transactions on Power Systems 31 (3) (2015) 2192–2203. doi:10.1109/TPWRS.2015.2448663.

[6] M. E. Baran, F. F. Wu, Network reconfiguration in distribution systems for loss reduction and load balancing, IEEE Transactions on Power delivery 4 (2) (2002) 1401–1407. doi:10.1109/61.25627.

[7] M. Lavorato, J. F. Franco, M. J. Rider, R. Romero, Imposing radiality constraints in distribution system optimization problems, IEEE Transactions on Power Systems 27 (1) (2011) 172–180. doi:10.1109/TPWRS.2011.2161349.

[8] J. Z. Zhu, Optimal reconfiguration of electrical distribution network using the refined genetic algorithm, Electric power systems research 62 (1) (2002) 37–42. doi:10.1016/S0378-7796(02)00041-X.

[9] Q. Peng, S. H. Low, Optimal branch exchange for feeder reconfiguration in distribution networks, in: 52nd IEEE conference on Decision and Control, IEEE, 2013, pp. 2960–2965. doi:10.1109/CDC.2013.6760333.

[10] F. Llorens-Iborra, J. Riquelme-Santos, E. Romero-Ramos, Mixed-integer linear programming model for solving reconfiguration problems in large-scale distribution systems, Electric Power Systems Research 88 (2012) 137–145. doi:10.1016/j.epsr.2012.02.013.

[11] E. M. Carreno, R. Romero, A. Padilha-Feltrin, An efficient codification to solve distribution network reconfiguration for loss reduction problem, IEEE Transactions on Power Systems 23 (4) (2008) 1542–1551. doi:10.1109/TPWRS.2008.2002178.

[12] Q. Peng, Y. Tang, S. H. Low, Feeder reconfiguration in distribution networks based on convex relaxation of opf, IEEE Transactions on Power Systems 30 (4) (2014) 1793–1804.

[13] X. Cao, J. Wang, J. Wang, B. Zeng, A risk-averse conic model for networked microgrids planning with reconfiguration and reorganizations, IEEE Transactions on Smart Grid 11 (1) (2019) 696–709.

[14] M. Farivar, S. H. Low, Branch flow model: Relaxations and convexification—part i, IEEE Transactions on Power Systems 28 (3) (2013) 2554–2564. doi:10.1109/TPWRS.2013.2255317.

[15] M. Farivar, S. H. Low, Branch flow model: Relaxations and convexification—part ii, IEEE Transactions on Power Systems 28 (3) (2013) 2565–2572. doi:10.1109/TPWRS.2013.2255318.

[16] L. Gan, N. Li, U. Topcu, S. H. Low, Exact convex relaxation of optimal power flow in radial networks, IEEE transactions on automatic control 60 (1) (2014) 72–87. doi:10.1109/TAC.2014.2332712.

[17] M. E. Khodayar, L. Wu, M. Shahidehpour, Hourly coordination of electric vehicle operation and volatile wind power generation in scuc, IEEE Transactions on Smart Grid 3 (3) (2012) 1271–1279. doi:10.1109/TSG.2012.2186642.

[18] H. Khodr, J. Martinez-Crespo, M. Matos, J. Pereira, Distribution systems reconfiguration based on opf using benders decomposition, IEEE Transactions on Power Delivery 24 (4) (2009) 2166–2176. doi:10.1109/TPWRD.2009.2027510.

[19] A. S. Kahnamouei, S. Lotfifard, M. Rostami, Optimized distribution systems reconfiguration considering protection devices constraints, IEEE Transactions on Power Delivery (2025). doi:10.1109/TPWRD.2025.3542817.

[20] P.-L. Carpentier, M. Gendreau, F. Bastin, Long-term management of a hydroelectric multireservoir system under uncertainty using the progressive hedging algorithm, Water Resources Research 49 (5) (2013) 2812–2827. doi:10.1002/wrcr.20254.

[21] B. Singh, B. Knueven, Lagrangian relaxation based heuristics for a chance-constrained optimization model of a hybrid solar-battery storage system, Journal of Global Optimization 80 (4) (2021) 965–989. doi:10.1007/s10898-021-01041-y.

[22] T. Erseghe, Distributed optimal power flow using admm, IEEE Transactions on Power Systems 29 (5) (2014) 2370–2380. doi:10.1109/TPWRS.2014.2306493.

[23] R. R. Nejad, W. Sun, Scalable distributed non-convex admm-based active distribution system service restoration, arXiv preprint arXiv:2008.03778 (2020).

[24] S. Lei, C. Chen, Y. Song, Y. Hou, Radiality constraints for resilient reconfiguration of distribution systems: Formulation and application to microgrid formation, IEEE Transactions on Smart Grid 11 (5) (2020) 3944–3956.

[25] A. Rastgou, “Distribution network expansion planning: An updated review of current methods and new challenges,” Renewable and Sustainable Energy Reviews, vol. 189, p. 114062, 2024.

[26] N. Amjady, A. Attarha, S. Dehghan, and A. J. Conejo, “Adaptive robust expansion planning for a distribution network with DERs,” IEEE Trans. Power Systems, vol. 33, no. 2, pp. 1698–1715, 2017.

[27] Y. Zhang, S. Shen, and J. Mathieu, “Distributionally robust chance-constrained optimal power flow with uncertain renewables and uncertain reserves provided by loads,” IEEE Trans. Power Systems, vol. 32, no. 2, pp. 1378–1388, 2016.

[28] C. Duan, W. Fang, L. Jiang, L. Yao, and J. Liu, “Distributionally robust chance-constrained approximate AC-OPF with Wasserstein metric,” IEEE Trans. Power Systems, vol. 33, no. 5, pp. 4924–4936, 2018.

[29] A. Zare, C. Chung, J. Zhan, and S. O. Faried, “A distributionally robust chance-constrained MILP model for multistage distribution system planning with uncertain renewables and loads,” IEEE Trans. Power Systems, vol. 33, no. 5, pp. 5248–5262, 2018.

[30] S. Babaei, R. Jiang, and C. Zhao, “Distributionally robust distribution network configuration under random contingency,” IEEE Trans. Power Systems, vol. 35, no. 5, pp. 3332–3341, 2020.

[31] R. S. Pinto and C. Unsihuay-Vila, “A data-driven distributionally robust expansion planning model for ADNs with multi-microgrids considering energy trading strategy based on game theory,” Sustainable Energy, Grids and Networks, vol. 39, p. 101431, 2024.

[32] J. Huang, K. Zhou, and Y. Guan, “A study of distributionally robust multistage stochastic optimization,” https://arxiv.org/abs/1708.07930, 2017.

[33] M. V. Pereira and L. Pinto, “Multi-stage stochastic optimization applied to energy planning,” Mathematical programming, vol. 52, no. 1, pp. 359–375, 1991.

[34] D. Duque and D. P. Morton, “Distributionally robust stochastic dual dynamic programming,” SIAM Journal on Optimization, vol. 30, no. 4, pp. 2841–2865, 2020.

[35] Y. Huang, W. Huang, N. Tai, C. Li, R. Li, and M. Yu, “A multistage distributionally robust optimization approach for generation dispatch with demand response under endogenous and exogenous uncertainties,” IET Generation, Transmission & Distribution, vol. 17, no. 22, pp. 5041– 5061, 2023.

[36] J. Zhu, W. Zhu, J. Chen, H. Liu, G. Li, and K. Zeng, “A DRO-SDDP decentralized algorithm for economic dispatch of multi microgrids with uncertainties,” Systems Journal, vol. 17, no. 4, pp. 6492–6503, 2023.

[37] J. Feng, Z. Hu, X. Duan, S. Cai, and P. Zhang, “A multistage DRO-SDDP approach for planning multi-type energy storage systems and flexible resources in high-penetration renewable power systems,” IEEE Trans. Industry Applications, 2025.

[38] Rinaldi, Arthur, Selin Yilmaz, Martin K. Patel, and David Parra. "What adds more flexibility? An energy system analysis of storage, demand-side response, heating electrification, and distribution reinforcement." *Renewable and Sustainable Energy Reviews* 167 (2022): 112696.